

DESIGNING CLUSTERS FOR EFFICIENT CATALYTIC ACTIVITY AT A REALISTIC CONDITION FROM FIRST-PRINCIPLES SIMULATION

SHIKHA SAINI



DEPARTMENT OF PHYSICS
INDIAN INSTITUTE OF TECHNOLOGY DELHI
SEPTEMBER 2020

© Indian Institute of Technology Delhi (IITD), New Delhi, 2020

DESIGNING CLUSTERS FOR EFFICIENT CATALYTIC ACTIVITY AT A REALISTIC CONDITION FROM FIRST-PRINCIPLES SIMULATION

by

SHIKHA SAINI

Department of Physics

Submitted

in fulfillment of the requirements of the degree of Doctor of Philosophy

to the



INDIAN INSTITUTE OF TECHNOLOGY DELHI

SEPTEMBER 2020

Dedicated to all in one
(Teacher, Father, Brother, Friend)

Professor Saswata Bhattacharya

Certificate

This is to certify that the thesis entitled “**Designing Clusters for Efficient Catalytic Activity at a Realistic Condition from First-Principles Simulation**” being submitted by **Shikha Saini**, to the Indian Institute of Technology Delhi, for the award of the degree of **Doctor of Philosophy** in Physics is a record of bonafide research work carried out by her under my supervision and guidance. She has fulfilled the requirements for the submission of the thesis, which to the best of my knowledge has reached the required standard. The material contained in the thesis has not been submitted in part or full to any other University or Institute for the award of any degree or diploma.

Prof. Saswata Bhattacharya

Department of Physics,
Indian Institute of Technology Delhi,
Hauz Khas, New Delhi 110016, India.

Date: September 2020

Place: New Delhi

Acknowledgments

Firstly, I would like to take this opportunity to express my heartfelt gratitude to my thesis supervisor Professor Saswata Bhattacharya, for his continuous support, expert guidance, patience, and motivation. He made me able to take initial steps in research, just like parents make their baby able to take the first steps of their life. I am extremely thankful to him for the exhilarating discussions on matters of physics, research skills, leading quality, philosophy, and much more, which have not only enriched my understanding in physics but have also assisted me to become a well rounded and an inquisitive person. I am largely indebted to him for the generous support and instilling courage when the going got tough. He has always inspired me by his infectious enthusiasm, passion for physics, dynamic nature and desire to accomplish big goals. I am humbly thankful to him for always trusting my abilities and motivating me to pursue my career in research.

My sincere thanks to all my colleagues and collaborators from our DISCERE group: Pooja Basera, Ekta Arora, Manish Kumar, Arunima Singh, Deepika Gill, Manjari Jain, Preeti Bhumla and Sajjan Sheoran for their constant help and support during my Ph. D. days. I have spent many lively moments discussing physics with them. I am very grateful to Arunima for her guiding words, respectful nature and moral support (particularly “Are you fine Di?”) during difficult situations. My heartiest best wishes to all my juniors.

I am also thankful to my other collaborators: Professor Santanu Ghosh, Professor Sreedevi Upadhyayula, Professor M. Ali Haider, Dr. Debraj Chandra, Parswajit Kalita, Shailesh Pathak and Sonit Balyan for the fruitful collaborations and discussions.

I thank the Indian Institute of Technology Delhi, New Delhi for providing all facilities for my research activities and travel grant. I would like to thank the Council for Scientific and Industrial Research (CSIR) for funding my research. Additionally, I acknowledge the Science & Engineering Research Board (SERB) for providing me financial assistance to travel.

I would like to thank the rest of my student research committee: Professor Sankalpa Ghosh,

Professor Sunil Kumar and Professor M. Ali Haider, for intriguing questions and insightful suggestions.

A special thanks to my friends - Zakiya Shireen, Priyanka Lochab, Sonal Singhal, Madhu Choudhary, Soumik Adhikary for being with me through times thick and thin and always showing care.

I am highly grateful to my family and cousins, without their constant support this thesis would not have been possible. I shall forever be indebted to my parents for showering boundless blessings and love on me. Without their wishes, inspiration, and emotional support, I might not be the person I am today. They have felt every moment of my success or failure as their own. I especially want to remember my uncle, I wish he could see me that I am about to get the highest degree of the study, and fulfilling the incomplete dream of his life. I am greatly thankful to Sethu for exciting discussions on various topics of science and life and for being the guiding light in my life.

Lastly, I bow my head in reverence to Almighty to give me five senses and showering unfailing love on me - Thank you!

Shikha Saini

Abstract

The ultimate goal of research in heterogeneous catalysis is to engineer the efficient and optimized catalyst for wide range of catalytic processes. The meaningful strategy to find suitable catalysts is to think what really limits the utility of existing catalysts. Basically, the development and rational design of catalytic materials largely depend on the ability to grasp the knowledge of targeted functionality at atomistic level. Usually, under realistic conditions catalytic materials come into contact with reactive molecules of surrounding phase. This induces the changes in local structure, composition and morphology of the catalyst. The newly formed configurations can account for the observed activity of catalyst. Moreover, it is often considered that an operating catalyst is a static entity or in equilibrium state with surrounding, though it is in dynamic nature thus situation becomes more elusive under operating conditions. Hence, complementary in situ modeling is an essential prerequisite to provide the novel insights for designing promising catalyst. The first principles methods such as density-functional theory (DFT) combined with concepts from thermodynamics have become stand tools for the accurate description of underlying factors that drive the activity of catalyst in operating conditions. Therefore, the aim of our work is to design the metal/metal-oxides nanoclusters for catalytic applications (e. g. C–H bond activation, overall water splitting, reduction and hydrogenation) and thoroughly explore their electronic and catalytic properties at finite temperature and pressure. Further, the performance of clusters are enhanced by mixing/doping different add-atoms, charge defect, changing the shape and tuning the morphology of support. The significant efforts have been dedicated for efficient designing of metastable structures and their role in catalysts' performance. The calculations that I have carried out for designing efficient catalytic materials are: (a) clusters designing via property based cascade genetic algorithm (b) ground state geometry, electronic structure (c) stability using *ab initio* atomistic thermodynamics, fundamental gap using GW approximation (d) transition state and reaction pathways using the Nudge Elastic Band method.

विषम उत्प्रेरक में अनुसंधान का अंतिम लक्ष्य उत्प्रेरक प्रक्रियाओं की विस्तृत श्रृंखला के लिए कुशल और अनुकूलित उत्प्रेरक अभियंता करना है। उपयुक्त उत्प्रेरक खोजने के लिए सार्थक रणनीति, यह सोचना है कि वास्तव में मौजूदा उत्प्रेरकों की उपयोगिता को क्या सीमित करता है। असल में, उत्प्रेरक सामग्री का विकास और तर्कसंगत रचना काफी हद तक परमाणु स्तर पर लक्षित कार्यक्षमता के ज्ञान को समझने की क्षमता पर निर्भर करता है। आमतौर पर, यथार्थवादी परिस्थितियों में उत्प्रेरक सामग्री आसपास के चरण के प्रतिक्रियाशील अणुओं के संपर्क में आती है। यह उत्प्रेरक की स्थानीय संरचना, संरचना और आकारिकी में परिवर्तन को प्रेरित करता है। नवगठित कॉन्फ़िगरेशन उत्प्रेरक की परिगणित गतिविधि के लिए जिम्मेदार हो सकता है। इसके अलावा, यह अक्सर माना जाता है कि एक परिचालन उत्प्रेरक एक स्थिर इकाई है या आसपास के साथ संतुलन की स्थिति में है, हालांकि यह गतिशील प्रकृति में है इसलिए परिचालन परिस्थितियों में स्थिति कठिन हो जाती है। अतः, पूरक "इन सीटू मॉडलिंग" एक आवश्यक शर्त है होनहार उत्प्रेरक रचनाओं में अंतर्दृष्टि प्रदान करने के लिए। पहले सिद्धांत तरीके जैसे घनत्व-कार्यात्मक सिद्धांत ("डीएफटी"), "थर्मोडायनामिक्स" की अवधारणाओं के साथ मिलकर अंतर्निहित कारकों के सटीक विवरण के लिए मानक उपकरण बन गए हैं जो परिचालन परिस्थितियों में उत्प्रेरक की गतिविधि को चलाते हैं। इसलिए, हमारे काम का उद्देश्य धातु/धातु-आक्साइड नैनो समूहों को उत्प्रेरक अनुप्रयोग के लिए रचना करना है (उदाहरण, सी-एच बांड सक्रियण, समग्र जल विभाजन, कमी और हाइड्रोजनीकरण) और परिमित तापमान और दबाव पर उनके "इलेक्ट्रॉनिक" और उत्प्रेरक गुणों का पूरी तरह से पता लगाना है। इसके अलावा, समूहों के प्रदर्शन को विभिन्न जोड़-परमाणुओं के मिश्रण/डोपिंग, आवेश दोष, आकृति में परिवर्तन और समर्थन की आकृति विज्ञान को बदलकर बढ़ाया जाता है। "मेटास्टेबल" संरचनाओं के कुशल रचनाओं और उत्प्रेरक के प्रदर्शन में उनकी भूमिका के लिए महत्वपूर्ण प्रयासों को समर्पित किया गया है। मैंने कुशल उत्प्रेरक सामग्री रचना करने के लिए जो गणनाये की हैं वह इस प्रकार हैं: (ए) गुण आधारित समूहों की रचना "कैसकेड आनुवंशिक एल्गोरिथ्म" के माध्यम से, (बी) "ग्राउंड स्टेट ज्योमेट्री", इलेक्ट्रॉनिक संरचना, (सी) "ऐब-इंसियो एटोमिस्टिक थर्मोडायनामिक्स" का उपयोग करके स्थिरता, "जी-डब्लू सन्निकटन" का उपयोग करके मौलिक अंतर और (डी) "नज़ इलास्टिक बैंड" विधि का उपयोग करके परिवर्तन स्थिति और प्रतिक्रिया पाथवे।

Contents

Certificate	i
Acknowledgements	ii
Abstract	iv
List of Figures	ix
List of Tables	xvii
1 Introduction	1
1.1 A brief introduction to catalysis and historical aspects	1
1.2 Applications of catalysts for mankind	2
1.3 What is a catalyst?	2
1.4 Recent progress in development of catalyst	5
1.5 Nanomaterial as a catalyst	7
1.6 Metal-oxide nanoclusters	7
1.7 Noble metal based nanoclusters	8
1.8 Governing factors for catalytic activity	9
1.9 Problems and challenges	11
1.10 A short overview	15
2 Theoretical methodology	18
2.1 Computer simulation	18
2.2 First principles calculation	19
2.3 Introduction of theoretical framework	20
2.4 Wavefunction	23

2.5	Schrödinger equation	24
2.6	Born-Oppenheimer approximation	25
2.7	The Hartree approximation	26
2.8	The Hartree-Fock approximation	28
2.9	Functional	29
2.10	Density Functional Theory	29
2.10.1	The Thomas-Fermi Model	31
2.10.2	Hohenberg and Kohn Theorem	31
2.10.2.1	Kohn-Sham equations	35
2.10.3	Exchange and correlation energy	37
2.11	Basis set	41
2.11.1	The Plane wave basis set	42
2.11.2	Numeric atom-centered basis functions	43
2.11.3	Plane wave pseudopotential method	44
2.11.4	Norm-conserving pseudopotential	45
2.11.5	Vanderbilt Ultrasoft pseudopotential	45
2.11.6	Projector augmented-wave method (PAW)	46
2.12	GW method	48
2.13	Geometry optimization	53
2.14	Nudged Elastic Band method (NEB)	54
2.15	Cascade genetic algorithm	56
2.16	<i>Ab initio</i> atomistic thermodynamics (<i>aiAT</i>)	59
2.16.1	Thermodynamic potentials	60
2.16.2	Free energy of formation	60
2.16.3	Partition function	62
3	Thermodynamic stability and electronic properties of neutral bimetallic oxide $\text{TM}_x\text{Mg}_y\text{O}_z$ clusters	66
3.1	Introduction	66
3.2	Methodology	68
3.3	Results and Discussions	70
3.3.1	Global minimum (GM) structures of $\text{TM}_x\text{Mg}_y\text{O}_z$ clusters	70

3.3.2	Determination of Gibbs free energy of formation as function of temperature and pressure via <i>ab initio</i> atomistic thermodynamics	70
3.3.3	Validation of functional	73
3.3.4	Determination of the stable phases of $\text{TM}_x\text{Mg}_y\text{O}_z$ clusters	74
3.4	Conclusion	80
4	Electronic structures and catalytic activity of charged bimetallic oxide clusters	81
4.1	Introduction	81
4.2	Methodology	83
4.3	Results and Discussions	84
4.3.1	Determination of the stable phases of $[\text{TM}_x\text{Mg}_y\text{O}_z]^{+/0/-}$ clusters	84
4.3.2	Identification of the active center to abstract first C–H bond from CH_4	87
4.3.3	Correlation of fundamental gap (E_g) vs C–H bond activation barrier (E_a) of a catalyst	89
4.3.4	E_g is a descriptor for catalytic activity	92
4.3.5	Structural analysis: Radial distribution function of $\text{TM}_x\text{Mg}_y\text{O}_z$ clusters	94
4.4	Conclusion	96
5	Effect of nitrogen doping on the stability and electronic properties of (meta-)stable $(\text{TiO}_2)_n$ clusters	97
5.1	Introduction	97
5.2	Methodology	99
5.3	Results and Discussions	100
5.3.1	VEA, VIP and Relative energy of pristine $(\text{TiO}_2)_n$ clusters	100
5.3.2	Density of states for undoped $(\text{TiO}_2)_{10}$ cluster	101
5.3.3	Structural details to form $(\text{N})_O$, $(\text{NO})_O$ and $(\text{N}_2)_O$ in $(\text{TiO}_2)_n$ clusters	102
5.3.4	Thermodynamic stability of $(\text{N})_O$, $(\text{NO})_O$ and $(\text{N}_2)_O$ in $(\text{TiO}_2)_n$ clusters	103
5.3.4.1	2D phase diagrams	104
5.3.4.2	3D phase diagrams	105
5.3.5	Fundamental gap and excitation energy of (un)doped $(\text{TiO}_2)_n$ clusters	106
5.3.6	VIP and VEA of (un)doped clusters with respect to the water redox potentials	108
5.3.7	Electronic structure of doped $(\text{TiO}_2)_{10}$ clusters	111

5.3.8	Evaluation of OER and HER	114
5.3.9	Electrochemical phase (Pourbaix) diagram and phase probability analysis	118
5.3.9.1	Thermodynamic energies	118
5.3.9.2	Electrochemical reaction paths and chemical potentials of re- action	119
5.4	Conclusion	122
6	Shape dependent catalytic activity of Ru nanoparticles	124
6.1	Introduction	124
6.2	Methodology	125
6.3	Results	126
6.3.1	Elucidating the role of catalyst's shape for reductive amination of furfural	126
6.3.1.1	Interaction of reactants with catalyst	126
6.3.1.2	Determination of activation barrier	128
6.3.2	Role of support on catalytic activity of Ru nanoclusters	132
6.3.3	Role of charge state on catalytic activity of Ru nanoclusters	133
6.4	Conclusions	137
7	Conclusions and future aspects	138
A	Appendix	142
	Author's Bio-data	184

List of Figures

1.1	(a) The contribution of catalytic processes to the industry and (b) the contribution of heterogeneous catalysts in comparison to others [1].	2
1.2	(a) Potential energy diagram of a heterogeneous catalytic reaction. (b) The catalyzed reaction comprises a sequence of elementary steps: reactants (A, B) bind to the catalyst, then react to form the product (P), after that the product liberates from the catalyst so that it can be used for next cycle. Note that the activation barrier of catalytic path is much lower than the noncatalytic route, thus, the latter has to overcome a high energy barrier [2].	4
1.3	(a) Activation energy on Maxwell Boltzmann distribution. As the activation energy of a reaction decreases, the number of particles with at least this much energy increases as indicated by orange shaded area. (b) At a higher temperature, more particles have kinetic energy greater than the E_a , as illustrated by the red shaded area.	4
1.4	(a) The key factors such as particle size and shape, composition, structure, surface area and support etc. are shown that govern the catalytic performance [3].	12
1.5	(a) Conceptual visualization of the problem and approach.	14
2.1	Multi-scale simulation in different length and time scales.	19
2.2	(a) The spherical polar coordinates for system with spherical symmetry, (b) The surface of a sphere is covered with twirling half arc that allows θ to range from 0 to π , and a full whirling around the sphere by allowing ϕ to range from 0 to 2π [4].	24
2.3	Schematic flowchart Hartree-Fock method for the solution of many electron system.	30

2.4	Illustration of interacting and non-interacting many-electron systems having same ground state electron density.	36
2.5	Schematic diagram of Jacob's ladder of density functional theory with different approximations for exchange-correlation energy.	39
2.6	Schematic illustration of self-consistent loop for the solution of the Kohn-Sham equations.	40
2.7	Schematic diagram of an all-electron wavefunction (solid line) and the corresponding pseudo wavefunction (dashed line) and together with the respective pseudopotential and external Coulomb potential [5].	44
2.8	Representation of spectral function for non-interacting single particle excitation and interacting many particles excitation.	49
2.9	The representation of excitation peaks for the noninteracting particle and the quasiparticles.	50
2.10	The Hedin's pentagon. The vertex function (Γ) is ignored in <i>GW</i> approximation.	52
2.11	Schematic diagram to show the various forces acting on the elastic band during the optimization [6].	55
2.12	Flow chart of cascade genetic algorithm.	57
2.13	Illustration of crossover and mutation operators. A and B represent the different types of species in the structure.	58
2.14	Schematic representation of the system: a cluster in gas phase environment of oxygen.	61
3.1	The GM structures in PES of $\text{TM}_x\text{Mg}_y\text{O}_z$ clusters are scanned via. cGA. In $\text{TM}_x\text{Mg}_y\text{O}_z$ clusters, TM = Cr, Fe, Co and Ni and $x, y = (1,2)$, $Z = (1..8)$. The geometries are optimized with PBE+vdW, and J is calculated using HSE06+vdW.	71
3.2	In Figure (a), the formation energy (ΔG_f) of globally optimized clusters ($\text{Ni}_1\text{Mg}_1\text{O}_x$) is varied with $\Delta\mu_{\text{O}}$ at $T = 300$ K. The top axis represents the pressure scale at 300 K. The black dotted lines indicate O-poor and O-rich limit. In Figure (b), ΔG_f is varied with T at 1 atm pressure of O_2 . Total energies are calculated using HSE06+vdW [13]. Colored areas are for the guideline to identify which phase is the most stable for the different range of pressure (a) and temperature (b).	72

- 3.3 3D phase diagram is constructed for most stable $\text{Ni}_1\text{Mg}_1\text{O}_x$ clusters at various T and p_{O_2} under thermodynamic equilibrium. The top black line represents the O-rich limit: beyond this limit O_2 molecules start to condense on the clusters. The rectangular box represents the ambient conditions ($T = 300$ K, $p_{\text{O}_2} = 1$ atm), and the dashed-dotted lines indicate the normal conditions in the phase diagram. The vibrational free energy is calculated under harmonic approximations. 72
- 3.4 In Figure (a) and (c), ΔG_f varies as a function of chemical potential of oxygen at 300 K. Total energy of geometries are calculated using PBE+vdW and HSE06+vdW, respectively. Colored areas identify the stable phases. In Figure (b) and (d), 3D phase diagrams are shown corresponding to the 2D phase diagrams of $\text{Ni}_1\text{Mg}_2\text{O}_x$ clusters. 74
- 3.5 The most stable $\text{TM}_x\text{Mg}_y\text{O}_z$ clusters at various temperatures and pressures under thermodynamic equilibrium. In $\text{TM}_x\text{Mg}_y\text{O}_z$ clusters, TM = Cr (a), Co (b), Ni (c) and Fe (d). The geometries are optimized with PBE+vdW, and the electronic energy is calculated using HSE06+vdW. The vibrational free energy is computed under harmonic approximations. 75
- 3.6 (a) VIP vs VEA for the low energy isomers stable at an experimentally achievable environmental condition for all different cluster sizes ($x + y \leq 3$). The symbols represent the nature of the TM atoms in the clusters, while the colour is set as per the amount of oxygen content (as shown by the colour bar) in the cluster. The loci of constant E_g are indicated by diagonal lines. (b) E_g vs oxygen content (z) is plotted for all the stable isomers at realistic conditions (see text for details). 76
- 3.7 Histogram of vibrational frequencies ranging from $1000\text{--}1200\text{ cm}^{-1}$ for clusters (i) gap > 4 eV (top panel) (ii) gap ≤ 4 eV (bottom panel). 77
- 3.8 Atom-projected spin polarised density of states of different $\text{TM}_x\text{Mg}_y\text{O}_z$ clusters. The corresponding *spin multiplicity* (J) is also given in the respective plots. Oxygen atoms responsible for lowering the fundamental gap of a particular cluster are marked by dark green circle. 78

- 3.9 T - p_{O_2} phase diagram (see text) of Ni_4 clusters under oxygen atmosphere with (right) and without (left) MgO substrate. The red, navyblue, and green spheres represent O, Ni and Mg respectively. 79
- 4.1 2D view of 3D phase diagrams obtained for neutral and ionic $[\text{TM}_2\text{Mg}_2\text{O}_z]^{+/0/-}$ clusters in the reactive atmosphere of O_2 . Coloured regions show the most stable compositions in wide range of pressures and μ_e under thermodynamic equilibrium. In $(\text{TM}_2\text{Mg}_2\text{O}_z)^{+/0/-}$ clusters, TM = Cr (a), Fe (b), Co (c) and Ni (d). The top axis is representing the pressure of oxygen at $T = 300$ K. 86
- 4.2 Structure of $\text{Ni}_1\text{Mg}_2\text{O}_3$ cluster with methane before optimization (left one) and after optimization (right one). 87
- 4.3 Structure of the global minimum (GM) for $\text{Ni}_1\text{Mg}_2\text{O}_3$, $\text{Ni}_1\text{Mg}_2\text{O}_8$ and $\text{Ni}_2\text{Mg}_2\text{O}_5$ clusters in (a), (b), (c), respectively. In (d) and (e), meta-stable structure of $\text{Ni}_2\text{Mg}_2\text{O}_5$ cluster with the charge corresponding to each atom. The partial charge density on each atom is calculated from the Hirshfeld charge analysis. 88
- 4.4 Potential energy surfaces for first C–H bond activation by $\text{Ni}_1\text{Mg}_2\text{O}_3$ cluster at the O-atom site with the higher negative charge (a), and the lesser negative charge (b). 89
- 4.5 Electronic structures of $\text{Ni}_2\text{Mg}_2\text{O}_5$ cluster (global minimum (a), meta-stables (b) and (c)). Coloured surface represents the hirshfeld charge density in the cluster. 90
- 4.6 Minimum energy pathway of first C–H bond activation of methane on GM of neutral $(\text{Ni}_2\text{Mg}_2\text{O}_5)^0$ cluster (a), negatively charged $(\text{Ni}_2\text{Mg}_2\text{O}_5)^-$ (b), meta-stable structure of $(\text{Ni}_2\text{Mg}_2\text{O}_5)$ cluster in neutral state (c and e), and meta-stable structure of $\text{Ni}_2\text{Mg}_2\text{O}_5$ cluster in negatively charge state (d and f). Reaction coordinate of initial (R), final (P), transition state (TS) and intermediates are shown. Activation barriers (E_a) for all cases are also indicated in the respective graphs in kJ/mol. The fundamental gap E_g of the clusters in all cases are shown in eV. 91
- 4.7 E_g ($G_0\text{W}_0@PBE0$) of all the charged and neutral $[\text{TM}_x\text{Mg}_y\text{O}_z]^{0/-}$ clusters of the dataset are shown for TM = Cr (a), Fe (b), Co (c) and Ni (d) as a function of the oxygen content (z), which is varied from 1..13. 93

- 4.8 The radial distribution function for $\text{TM}_x\text{Mg}_y\text{O}_z$ [TM = Cr (a), Fe (b), Co (c) and Ni (d) using all the data for all possible combination of x and y with $x + y \leq 5$ and $z=1..11$] set of clusters. 95
- 5.1 VIP vs VEA for the low-energy isomers of (a) $(\text{GA})_E$, (b) $(\text{GA})_P^{\text{EA}}$ and (c) $(\text{GA})_P^{\text{IP}}$ based clusters. The color bar represents the relative energy. The single point energy is calculated with PBE0+vdW, whereas VIP and VEA are determined with G0W0@PBE0. 101
- 5.2 TDOS and PDOS for $(\text{TiO}_2)_{10}$ cluster. 101
- 5.3 Energetically preferable position of different types of defects in N-doped $(\text{TiO}_2)_{10}$ cluster: (a) N_O , (b) $(\text{NO})_O$ and (c) $(\text{N}_2)_O$ 102
- 5.4 2D phase diagrams of N-doped $(\text{TiO}_2)_{10}$ clusters at $T = 300$ K and $p_{\text{O}_2} = 1$ atm. The formation free energy is shown as a function of the chemical potential of an electron (μ_e). The upper, middle and lower panel represent the phase diagrams of $(\text{GA})_E$, $(\text{GA})_P^{\text{EA}}$ and $(\text{GA})_P^{\text{IP}}$ based clusters, respectively, for size: (a, e, i) $n = 5$, (b, f, j) $n = 10$, (c, g, k) $n = 15$, (d, h, l) $n = 20$ 104
- 5.5 2D view of 3D phase diagrams obtained for N-doped $(\text{GA})_E$ [upper panel], $(\text{GA})_P^{\text{EA}}$ [middle panel] and $(\text{GA})_P^{\text{IP}}$ [lower panel] clusters in different charge states for size $n = 5$ (a, e, i), 10 (b, f, j), 15 (c, g, k) and 20 (d, h, l). Colored regions show the most stable defect states at realistic conditions (T , p_{O_2} and μ_e). The top axes are representing the pressure scale of O_2 at $T = 300\text{K}$ and 600K 105
- 5.6 (a) Fundamental gap (E_g) vs. excitation energy (E_x) (G0W0@PBE0) for all the (un)doped $(\text{TiO}_2)_n$ [$n = 4 - 10, 15, 20$] clusters. (b) In the schematic, yellow lines refer to the vertical ionization potential and vertical electron affinity of the neutral cluster (NP), while the green line refers to the vertical ionization potential of negatively charged cluster. The dashed green lines define VIP' (the energetic cost of extracting an electron from the HOMO-1 level of the NP^{-1}) and AIP (adiabatic ionization potential corresponds to the HOMO level of the NP^{-1}). 107

- 5.7 (a) The schematic diagram shows how the (standard) reduction potentials (VIP and VEA) of the ideal photocatalyst (cluster) straddle the HER and OER potentials. The schematic shows the free charge carriers scenario, where the excited electron and hole are spatially separated within the particle due to negligible coulombic interaction. $h\nu$ defines the energy of the photon absorbed by the cluster. e^- and h^+ stand for electron and hole, respectively. VIP refers to the cluster's ground-state ionization potential, whereas VEA to the ground-state electron affinity. VIP and VEA for doped clusters: (b) N_O , (c) $(NO)_O$, and (d) $(N_2)_O$. The dashed green and red lines represent the standard redox potentials for water reduction (H^+/H_2) and oxidation potential (O_2/H_2O) at $pH = 0$, respectively. 110
- 5.8 TDOS and PDOS of $(GA)_P^{EA}$ based doped $(TiO_2)_{10}$ clusters: (a) N_O , (b) $(NO)_O$, (c) $(N_2)_O$. The respective electronic configuration of doped state is shown below the DOS. Double headed arrows are representing the HOMO–LUMO gap. 112
- 5.9 IR spectra of $(GA)_E$ (left column) and $(GA)_P^{EA}$ (right column) based $(TiO_2)_{10}$ clusters: (a, b) undoped, (c, d) N_O , (e, f) $(NO)_O$ and (g, h) $(N_2)_O$ 113
- 5.10 (a, b) Geometries, electron density profile and binding energies of single H-atom and water molecule adsorbed on $(NO)_O$ doped $(TiO_2)_{10}$ cluster, respectively. 115
- 5.11 (a, b) OER cycles on two different Ti-sites of $(NO)_O$ doped $(GA)_P^{EA}$ based $(TiO_2)_{10}$ cluster. In Fig. 5.12, we have shown the OER cycles on other configurations. (c, d) Reaction free energy diagrams of the OER and HER on N-doped $(TiO_2)_{10}$ clusters at an electrode potential $E_{SHE} = 0$ V, respectively. At zero potential, $(H^+ + e^-)$ can be expressed as $\frac{1}{2}H_2$ 116
- 5.12 OER cycles on different configurations of $(GA)_E$, $(GA)_P^{EA}$ and $(GA)_P^{IP}$ based $(TiO_2)_{10}$ clusters. 117
- 5.13 (a) Pourbaix diagram with aqueous ion concentration of 10^{-6} mol/L is obtained using PBE0 functional including vibrational contributions. The two inclined parallel black dashed lines show the electrode potentials for the water oxidation ($2H_2O - 4e^- \rightarrow O_2 + 4H^+$, upper one) and reduction ($2H_2O + 2e^- \rightarrow H_2 + 2OH^-$, lower one). (b, c) Logarithm of concentration (in %) of various configurations with respect to E_{SHE} ($pH = 12$) and pH ($E_{SHE} = 0$ V). 121

- 6.1 Side view of DFT-optimized adsorption configurations of reactants and products on flat-shaped fcc (upper panel) and spherical-shaped hcp clusters (lower panel). Bond lengths are labelled in Å. 127
- 6.2 Side and top view of DFT-optimized adsorption configurations of furfural on flat-shaped fcc Ru nanocluster (a, b) and spherical-shaped hcp Ru nanocluster (c). The adsorption energy of furfural and hirshfeld charge density of O-atom (in yellow color) in carbonyl are shown with respective configuration. (d) Optimized geometry structure, and (e) hirshfeld charge density for isolated furural molecule. The dashed lines represent the bond lengths (labelled in Å). 129
- 6.3 Illustration of elementary steps for reductive amination of furfural. 129
- 6.4 Reaction profiles of first elementary step with side and top view of initial state (IS), transition state (TS) and final state (FS) on flat-shaped fcc nanocluster by considering flat (a) and bent (b, c) configuration. The dashed lines represent the bond lengths (labeled in Å). 130
- 6.5 Reaction profile of furfural conversion to furfurylamine over flat-shaped (upper panel) and spherical-shaped (lower panel) Ru nanocluster. The side and top view of initial state (IS), transition state (TS) and final state (FS) structures of all the elementary steps on flat-shaped fcc nanocluster are shown. The dashed lines represent the bond lengths (labeled in Å). 131
- 6.6 Optimized geometry structure and hirshfeld charge density for (a) standalone and (b) supported hcp Ru nanocluster. (c) The side view of DFT-optimized structure of hcp Ru nanocluster on N-carbon support. 132
- 6.7 Side and top view of DFT-optimized adsorption configurations of quinoline (1a) on neutral Ru nanocluster (a, b, c) and negatively charged $\text{Ru}^{\delta-}$ nanocluster (d, e, f). The adsorption energy (E_{ad}) of 1a is shown with respective configuration. 134
- 6.8 (a, b) Side view of DFT-optimized adsorption configuration of H_2 molecule, and (c) transition state of H_2 dissociation step on flat-shape Ru nanocluster. . . 134
- 6.9 Reaction profile of quinoline conversion to 1,2,3,4-tetrahydroquinoline over flat-shaped hcp Ru and $\text{Ru}^{\delta-}$ nanocluster. The side view of initial state (IS), transition state (TS) and final state (FS) structures of all the elementary steps are shown. 135

-
- 6.10 (a, b) Side view of initial state (IS), transition state (TS) and final state (FS) for second step of hydrogenation on negatively charged $\text{Ru}^{\delta-}$ and neutral Ru nanocluster, respectively. 136
- 6.11 Schematic representation of reaction processes for hydrogenation of quinoline over Ru catalyst. The electron rich site is highly active to initialize the hydrogenation process. The detailed configurations for full reaction paths on flat-shaped hcp Ru and $\text{Ru}^{\delta-}$ nanoparticles are illustrated in Figure 6.9. 136

List of Tables

5.1	Theoretically calculated excitation energy (E_x), experimental excitation energy (E_{exp}) [7], singlet transition energy (E_{TD}) [8], and HOMO-LUMO energy E_{HL} [9, 10] corresponding to $(\text{TiO}_2)_n$ clusters. All the values are in eVs.	108
6.1	Hirshfeld charge density of furfural molecule.	128
6.2	Activation barrier (E_a) of elementary reaction steps for the reductive amination of furfural.	130
6.3	Activation barrier (E_a) of elementary reaction steps for hydrogenation of quinoline (1a) on Ru and $\text{Ru}^{\delta-}$ nanoclusters.	135

Introduction

1.1 A brief introduction to catalysis and historical aspects

The catalyst term was coined in 1835 by J. J. Berzelius to determine the property of materials that facilitate the rate of chemical reactions without itself being consumed in the process [2, 11]. In 1909, Wilhelm Ostwald received the Nobel Prize for his pioneering work in catalysis including investigations of the fundamental principles that govern the chemical equilibria and rates of reaction [12]. Subsequently, in 1912, Paul Sabatier was awarded Nobel Prize for his work on the hydrogenation of ethylene and CO over Ni and Co catalysts [2, 11]. In 1918, the Haber process to convert the atmospheric nitrogen and hydrogen into ammonia using a metal catalyst began the true revolution in catalysis industry [13]. Afterwards, Langmuir – Hinshelwood mechanism, suggested by Irving Langmuir in 1921 and further developed by Cyril Norman Hinshelwood in 1926, paved the way to study the catalytic mechanisms [2]. The advent of spectroscopy, followed by various characterization techniques for catalyst and research in surface science allowed one to investigate the surface structure, adsorbed species, reactivity patterns and correlate the catalytic properties with configuration and structure of materials. By the end of 20th century, computational study became an ultimate tool in this emerging field which enables to have a deeper insight of rate governing factors viz. shape, size, electronic structure, metal-support interaction, defects, active sites, reaction path and fundamental properties of catalyst material at the atomistic level. However, the rational designing of efficient catalyst is still a long-standing challenge in terms of cost-effective production.

1.2 Applications of catalysts for mankind

In chemical industry, around 85–90 % (see Figure 1.1) of the products are obtained through catalyzed processes [1]. Therefore, catalysts are known as workhorses for many valuable chemical transformations in industry. The primary aim is to control the rates of reaction to enhance the chemical processes. This control is generally acquired by a catalyst that can promote a chemical reaction and determine its selectivity. A catalyst provides an alternative way to carry out the reaction processes under practically feasible conditions of pressure and temperature. Catalysts become indispensable tools as they have huge impact in our day to day life:

1. For the production of transportation fuels.
2. Manufacturing the bulk and fine chemicals in industry of chemicals.
3. Preclusion of pollution by suppressing the formation of unwanted byproducts.
4. Remediation of pollution that is produced from automotive and industrial exhaust.

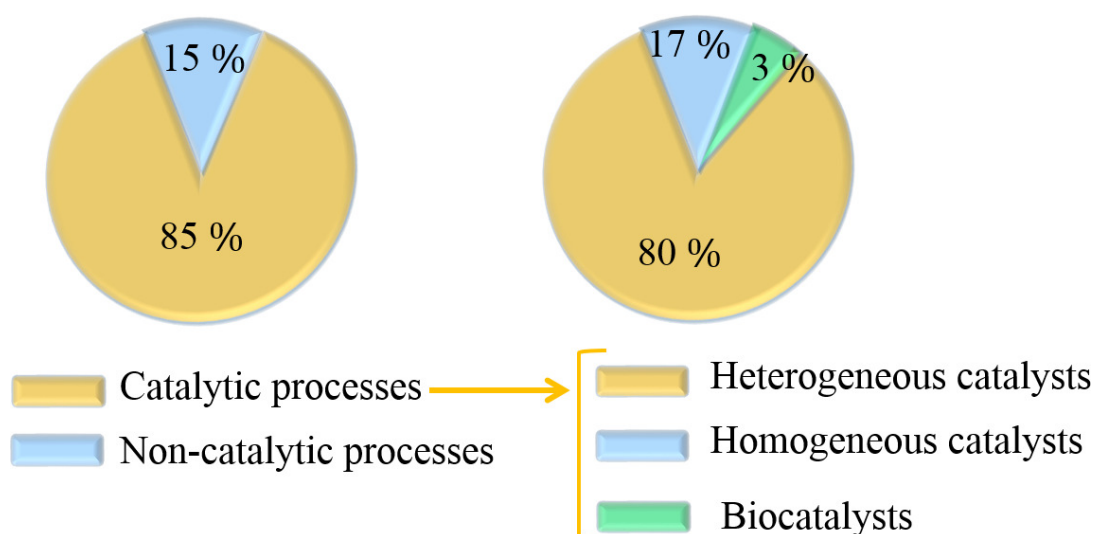


Figure 1.1: (a) The contribution of catalytic processes to the industry and (b) the contribution of heterogeneous catalysts in comparison to others [1].

1.3 What is a catalyst?

A catalyst is a substance that accelerates the rate of a chemical reaction, but remains unconsumed in the process, therefore, at the end of the reaction catalyst can be recovered in its original form [2]. Traditionally, the catalysts are mainly categorized into three parts:

1. Homogeneous
2. Heterogeneous
3. Enzymes and biocatalysts

Homogeneous catalysts exist in the same phase as reactants and products. Contrary to this, heterogeneous catalysts operate in a different phase from the reactants or products. Usually, catalysts exist in solid phase and reactants in gas phase or liquid form. Enzyme catalysts are made mainly of proteins. The main advantage of heterogeneous catalysts is that they are easily separable from the reactants and products and can be reused. In addition, heterogeneous catalysts are enduring under extreme operating conditions, therefore, heterogeneous catalysts are preferred in industry for large scale production. The main concern in catalysis is the impact of the catalyst on the rate of a reaction or the product distribution, which is determined by the relative rates of the elementary steps of reaction path. The rate constant (k) of an elementary reaction is often expressed by Arrhenius equation. Based on the van't Hoff equation (see the appendix for details), Svante Arrhenius in 1889, unified the activation energy and the Boltzmann distribution law [2, 14]. The Arrhenius equation

$$k = A \times \exp\left(-\frac{E_a}{RT}\right) \quad (1.1)$$

Where, A is the pre-exponential factor (frequency of collisions in the correct orientation), T is the absolute temperature, E_a is the activation energy for the reaction, R is the universal gas constant, RT is the average kinetic energy and $\exp\left(-\frac{E_a}{RT}\right)$ energy factor. E_a and T affect the rate of a reaction exponentially. E_a is the maximum energy that is required to start any chemical reaction and it depends on the nature of the chemical reaction. For an example, if we perform the same reaction (having higher potential barrier) with and without using the catalyst [14]. The reaction which occurs in the absence of catalyst has a lower rate because of high activation energy of path to achieve the product from reactants. But, in the presence of a catalyst the efficiency or rate of the particular reaction increases substantially (as shown in Fig. 1.2a and 1.2b); because a catalyst provides an alternative route with a lower activation energy. It is important to note that catalyst does not reduce the activation energy of a reaction, rather it provides an easier path for the same. A heterogeneous catalytic reaction involves the sequence of elementary steps: adsorption of reactants onto a catalyst surface, surface reaction of adsorbed entities, and finally desorption of products as depicted in Figure 1.2b. Clearly,

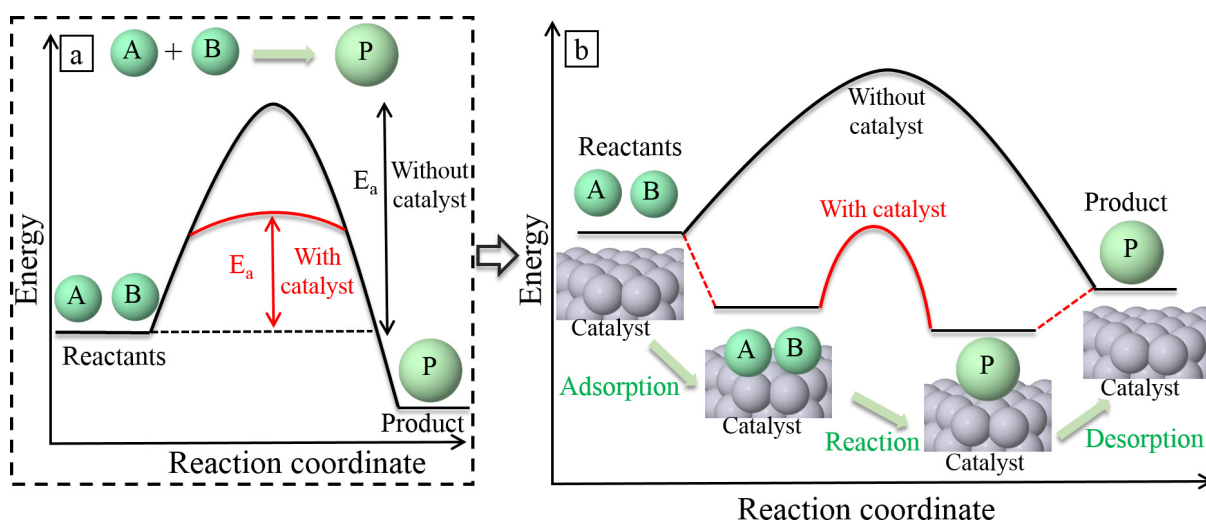


Figure 1.2: **(a)** Potential energy diagram of a heterogeneous catalytic reaction. **(b)** The catalyzed reaction comprises a sequence of elementary steps: reactants (A, B) bind to the catalyst, then react to form the product (P), after that the product liberates from the catalyst so that it can be used for next cycle. Note that the activation barrier of catalytic path is much lower than the noncatalytic route, thus, the latter has to overcome a high energy barrier [2].

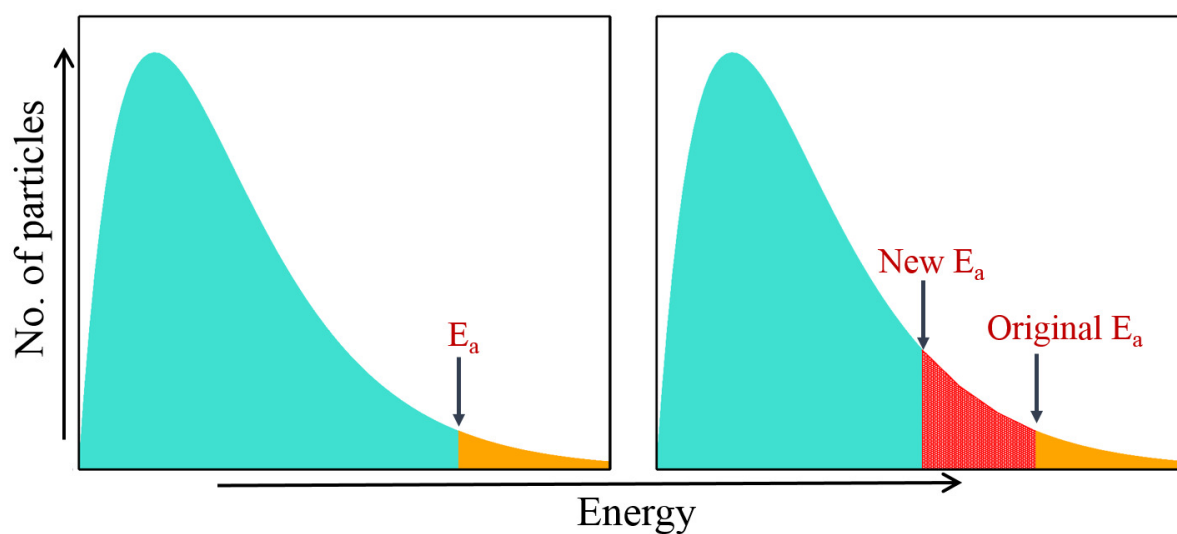


Figure 1.3: **(a)** Activation energy on Maxwell Boltzmann distribution. As the activation energy of a reaction decreases, the number of particles with at least this much energy increases as indicated by orange shaded area. **(b)** At a higher temperature, more particles have kinetic energy greater than the E_a , as illustrated by the red shaded area.

the role of catalyst is providing an alternative path with lesser activation barrier to accomplish the significant increment in rate of reaction. The significance of lower activation barrier for a reaction can be understood by Maxwell-Boltzmann distribution by locating the E_a position as shown in Figure 1.3. To proceed a chemical reaction at a reasonably fast rate, there should

exist an appreciable number of particles which possess kinetic energy equal or greater than the activation energy. In Figure 1.3a, only those particles which are represented by the area to the right of the E_a will react when they collide. The majority of particles do not have enough energy to react in absence of catalyst. To increase the rate of a reaction, the number of successful collisions must be increased. One possible way of doing this is to provide an alternative way for the reaction to happen which has a lower activation energy. In other words, to move the activation energy to the left on the graph as shown in Fig. 1.3b. Arrhenius equation is based on empirical observations, which does not consider any mechanistic aspect. Later, in 1935, Eyring, Evans, and Polanyi independently developed the transition state theory (absolute rate theory), to describe both the parameters, the pre-exponential factor (A) and the activation energy (E_a) of chemical reactions. Eyring–Polanyi equation follows from the transition state theory explains the rates of elementary reactions by assuming the chemical equilibrium (quasi-equilibrium) between the reactants and activated complex (transition state) [see the appendix for derivation] [15, 16]. Transition state is the slowest step in the bond breaking/forming process, this chemical configuration is neither a reactant nor a product, but is called an intermediate between the reactant and product. The amount of energy requires to form the transition state, is called the activation energy (E_a) [15].

$$k = \frac{k_B T}{h} \times \exp(-\Delta G_{TS}^\ddagger / k_B T) \quad (1.2)$$

where $\Delta G_{TS}^\ddagger = \Delta E_{TS}^\ddagger - T\Delta S_{TS}^\ddagger = E_a - T\Delta S_{TS}^\ddagger$ is the standard Gibbs free energy of activation (difference between TS and reactant state). The term $\frac{k_B T}{h} \times \exp(\Delta S_{TS}^\ddagger / k_B)$ is the prefactor A in the Arrhenius expression.

1.4 Recent progress in development of catalyst

A sustainable future calls for the development of efficient catalytic processes to meet the necessity of fuels, energy and many useful products over the coming years. This can be attained if we design the potential catalysts that can utilize sunlight, renewable sources and raw materials to synthesize fuels and produce valuable things from plastics to fertilizers [2]. In addition to this, it also requires the high selectivity for catalytic reactions and efficient catalysts prepared from earth-abundant materials. Nowadays, this approach also refers as “green” if it utilizes raw materials efficiently so that consumption of toxic and hazardous reagents and products can

be minimized [2]. In addition, the formation of waste materials should be avoided. Moreover, catalysts act as a best remedy against water, air and soil pollutants. An efficient catalyst that provides high stability, high activity and high selectivity is highly desirable for green production at large scale. An enormous progress has been made in modeling and studying the reactions at solid surfaces due to remarkable development of spectroscopic techniques and of computational methods. The scanning tunnelling microscope enables to probe the active sites and to capture the surface diffusion of adsorbates [17]. Likely, more advanced 4D electron microscopy allows us to analyze the motion of single atoms in the timescale of femtoseconds. X-ray absorption spectroscopy (XAS) permits to determine local structure of catalysts under reaction conditions [18]. Moreover, it has unveiled that active sites show dynamical behavior under operative conditions, hence, their properties continuously change during catalytic reaction. Furthermore, the advanced in-situ optical, Raman, and infrared spectroscopies provide the electronic and structural details at the molecular level of modeled catalysts [19, 20]. Recently developed environmental transmission electron microscopy (ETEM) and multiscale structure reconstruction (MSR) model help to characterize and explain the equilibrium shapes of nanoparticles in reactive environments under atmospheric pressure [21]. Using advanced methods, it is possible to realize the single-atom and subnanometric clusters formed by few atoms and to observe the dynamic behavior of active sites.

Although tremendous progress has been made in the field of heterogeneous catalysis but still in terms of knowledge we are quite lagging in the practical uses of cost-effective catalysts. A clear understanding of the fundamental properties of materials can assist us to accelerate the functionality of designed catalysts. In practice, the chemical reactions are performed at the surface of materials. First-principles based methods enable us to explore the atomic-level understanding of the catalysts' surface and the mechanism of chemical reaction. The catalysis science involves many length scales [18]. The Monte Carlo and Molecular Dynamics simulations are used to model the porous structures and corresponding surfaces as well as to gain the understanding of adsorption and diffusion processes of reactants and products inside the pores. The electronic modeling regime can be dealt with quantum chemical approaches to determine active sites and to describe the bond-breaking and bond-forming phenomena on these active sites. In the present thesis work, we have mainly focused on exploring the subnanometre regime.

1.5 Nanomaterial as a catalyst

The discovery of the nanomaterials has sparked a boom in the realm of science and industry, owing to their extraordinary electronic, optical, magnetic and catalytic properties [22, 23, 23, 24, 25]. These nanomaterials are considered as bridge between atomic and bulk materials, and also exhibit a variety of distinct physiochemical properties than their bulk counterparts [23]. Specifically, in heterogeneous catalysis, the major breakthrough happened with the dramatic finding of Haruta. In 1987, Haruta et al. disclosed that the gold nanoparticles smaller than 5 nm show catalytic properties, whereas previously it was considered inactive material [22]. Since then, designing an optimized catalyst (high activity, high selectivity, high stability and low-cost) for commercial purposes remains the most challenging area of active research. As a consequence, a wealth of studies have been carried out to design new catalysts and enhance the performance of existing ones. Especially, metal clusters and nanoparticles dispersed across a high-surface-area support material, are widely used as catalyst for wide range of chemical processes including fine chemical synthesis, energy conversion, oil refining and petrochemicals, along with having applications in medical field. Typically, a cluster (e.g. Au, Pd, Pt, Ru, Ni, Fe) refers to a small agglomerate of atoms and molecules, varying from few to thousands of units, having diameters in nanometer scale whereas the diameter range of nanoparticle varies from some nanometers to hundreds of nanometers [26, 23, 24, 25, 27, 28]. Moreover, metal nanoparticles possess the continuous band of electronic energy levels with well defined Fermi surface, whereas the small clusters exhibit discrete energy levels with higher energy gap between the highest occupied molecular orbital and lowest unoccupied molecular orbital levels. The reactant molecules can readily exchange electron to and from metal cluster with less amount of energy due to their molecular character.

1.6 Metal-oxide nanoclusters

In heterogeneous catalysis, metal-oxides (silica, alumina, TiO₂, MgO, zeolites, ZnO, perovskites and mixed oxides etc.) became prominent materials for catalytic applications because of their half-filled d orbitals giving rise to multiple oxidation states [25, 29, 30, 31, 32, 33, 34]. In particular, the metal-oxide nanoclusters (containing small number of atoms) have largely covered the catalytic domain that are involved in wide variety of chemical reactions like oxida-

tion, photocatalysis, hydrogen production, hydrogenation, dehydrogenation, biomass transformation and acid-base reactions [35, 36, 37, 38, 39, 40, 41, 42, 43, 44]. In selective oxidation of various hydrocarbons, coke formation and cluster sintering are the prime causes to degrade the catalytic performance. Coking blocks the active sites and sintering of clusters reduces the population of small clusters resulting in minimization of surface energy. Moreover, in complete oxidation the single metal-oxides show low activity and selectivity. Doping and mixing with other metal atoms are widely used strategies to overcome these issues [45, 46, 47, 48, 49, 50]. These metal-oxides families are not limited to mono and bimetallic nanoclusters, also they can be extended to ternary particles that reflect the superior catalytic properties than their component oxides analogues [51, 52, 53]. It has been suggested that the trace amounts of noble metal can drastically enhance the properties (structural, electronic, catalytic and magnetic) of metal-oxides due to synergistic effect of multiple atoms [54, 55, 56, 57, 58]. However, the increased complexity associated with composition arise new challenges to understand the structure, stability and role of individual species in reaction mechanism at atomistic level. It is therefore of profound interest to understand the explicit role of different metals in these composite oxide systems. At the same time, an in-depth knowledge of driving factors (size, structure, stoichiometry, oxidation and charge state) is essential to elucidate the molecular level mechanisms.

1.7 Noble metal based nanoclusters

Among the myriad of available catalysts, noble metals (Pt, Pd, Ru, Rh, Ag, Au, Ir and their alloys, etc.) have attracted substantial attention owing to their extraordinary physico-chemical properties and diversity in applications such as petrochemical industry, environmental protection, medicine, photochemistry, electronics and energy conversion [26, 23, 24, 25, 27, 28]. However, the high cost and low abundance minimize their use at industrial level. Consequently, noble metal catalysts could not able to meet the increasing demands of chemical industry. Hence, high catalytic performance with low per metal is extremely desired at present scenario to improve the sustainability of sparse noble metal-based catalysts. For enhancing the mass-specific activity and lowering the expenditure, the robust strategy is to reduce the particle size. Moreover, the shape-controlled modeling privileges us to expose specific phase with abundant active sites. For instance, the hcp Co has been found more active towards CO dissociation step than that of fcc Co [59, 60, 61]. Unlike Co catalysts, fcc Ru has shown higher activity towards

CO oxidation as compared to hcp Ru due to abundant active (111) facets [62]. Further, discovery of single-atom catalyst provides the great opportunity in reducing the cost of catalyst, especially for noble-metals. The stability of single-atom catalyst is crucial factor because when metal catalyst is dispersed into tinier particles, the surface energy increases. Subsequent studies reveal that single-atoms tend to accumulate during the catalytic process. For instance, Pt ensembles have shown higher activity and stability than their single-atom counterpart for catalyzing low-temperature CO oxidation in oxygen-rich environment [63]. Therefore, modeling of efficient single-atom catalysts and probing their structure remain main issues. Modern electronic structure methods like density functional theory (DFT) coupled with *ab initio* atomistic thermodynamics allow us to accurately predict the active centers/phases and determine their stability under practical conditions of varying temperatures and pressures [64, 65].

1.8 Governing factors for catalytic activity

In previous reports, it has been revealed that many factors such as size, shape, composition, surface area, coordination number, metal-support interaction, and so forth, significantly influence the catalytic properties of metal catalysts. [3, 66, 67, 23, 24, 25, 27, 28, 45]. Metal catalysts with different sizes (single atoms, nanoclusters, and nanoparticles) possess different catalytic properties for various valuable chemical reactions including CO oxidation, water-gas shift, hydrogenation, partial oxidation of methane, carbon-carbon bond formation, electrochemical reactions in fuel cells, abatement of exhaust gases and so forth [23, 26]. It has been uncovered that exposing faces of metal surface usually constitutes different active centers (namely edges, corners, terraces, steps, kinks and facets) having different coordination number [23, 68]. Each site shows relatively different catalytic activity with different coordination numbers of the surface atoms. For instance, G.A. Somorjai has reported that step and kink sites are very active in cleaving C-H and C-C bonds in hydrocarbon molecules [69]. Similarly, G. Ertl and co-workers have found that steps are the active sites to dissociate the NO on Ru(001) surface [70]. The size of nanoparticles is one of the pertinent criteria to dictate catalytic performance [23]. The role of particle size on activity and selectivity of supported metal nanoparticles has been examined extensively by Haruta et al. [71, 72]. Since then, reducing the particle size to attain larger surface area has gained tremendous research interest and still a rapidly growing topic. The surface area of metal nanoparticle usually increases with decreasing size of particle.

In practice, the most of chemical reactions happen on surface of the catalyst, thus nanoparticles show higher catalytic activity with decreasing size [73]. Lopez et al. reported that particle size is the prime factor to affect the selectivity and catalyst performance [74]. On size reducing path, supported single-atom catalysts have received great attention lately, which not only provide optimal active sites but also maximize atomic efficiency of noble metals [75, 76, 26]. However, precise synthesis and accurate prediction of active sites of these catalysts remains unresolved issue. A well hand shake between chemists and physicists could make it possible to rationally design superior catalysts for sustainable production of energy and other valuable products at reasonable cost. Doping is the pragmatic approach to modify the electronic structure, stability and promote the catalytic activity.

Moreover, a designed bimetallic Ni–Au catalyst for steam reforming process has shown the excellent resistance toward carbon formation [68]. It has been widely investigated that bimetallic catalyst (alloy or inter-metallic compounds, core-shell structures or cluster-in-cluster) exhibit significantly higher activity and selectivity as compared to mono-metallic counterpart [77]. The inclusion of additional metal generate a synergistic effect which alters the electronic configuration and thus improves the catalytic activity. Alloy and bimetallic nanocatalysts can also enhance the thermal stability in certain chemical reactions [78]. It is noted that incorporating the other type of metal not only enhances the performance but also prevents the catalyst from poisoning and deactivation. For instance, gold alone is not sufficient to oxidize formic acid, it requires additional Pd active sites to facilitate the oxidation of formic acid. Moreover, in case of platinum-based nano-catalysts, the selectivity of nanocatalysts can be improved by lowering the fraction of Pt by including another metal [79]. However, it further increases the complexity of nanoparticles to clearly understand their geometrical structure and electronic properties. A support material and its morphology can have a significant influence on the performance of a cluster via charge transfer. For instance, F-center defects, present on MgO surfaces, transfer charge to supported gold clusters. The latter is responsible to activate the molecular O₂, which facilitates the oxidation of CO to CO₂ [80]. In addition, the lattice defects and strain effects in nanoparticles are also preminent factors to influence the geometric structures while considering the catalytic properties. Furthermore, the electronic properties and stability of nanoclusters can be tunned by protecting it with monolayer or ligands [24]. Recently, it has been suggested that dynamic change in shape of nanoparticles occurs under the operating conditions, that impedes for fully elucidate the catalytic phenomena at the atomic

level [14]. Therefore, enormous studies have been devoted on regulating the shape of nanoparticles in order to gain the high performance. These studies highlight the necessity to properly account the effect of reactive environment while modeling and characterizing the equilibrium shape of nanoparticles. Gao and co-workers have suggested a quantitative model for predicting the accurate equilibrium shape of nanoparticles in real conditions [81]. T

As a whole, small nanoclusters are highly desirable for catalysis, because they exhibit higher amount of coordinatively unsaturated active sites. The reactivity of the clusters is highly dependent on the electronic configuration. In subnanometer regime every atom counts, therefore it opens a wide scope for designing new efficient catalysts and tailoring the functionality of existing ones. In this regime, the slighter changes in cluster sizes i.e. differing by only single atom, can result in huge variation in reactivity. In general, the reactivity of all nanoclusters is much higher as compared to their bulk counterpart because of their higher surface to volume ratio. There is a plethora of applications of clusters like in microelectronics, magnetic-storage, optical data storage, spintronics, sensors, transducers, chemical reactors and of-course in catalysis. In the evolving field of heterogeneous catalysis, TM nano-particles (typically clusters consisting well-defined number of atoms) exhibit significant variations as a function of size in their physico-chemical nature and electronic properties. In the presence of a realistic reactive atmosphere, clusters change their stoichiometry by adsorbing the ligands from the environment, under certain conditions [82]. This new composition (with specific active sites) may work as active (functional) material. Therefore, one has to understand the functional properties of clusters in a technologically relevant atmosphere. Advanced theoretical methods serve us the major motivation to further improve our fundamental understanding of structure-activity correlations that hopefully, lead to rational design of superior catalysts. identification and characterization of key intermediates are important for proposing the mechanism of a particular reaction. However, it remains challenging as the catalyst's structure is prone to change during the reaction. Therefore, it is desirable to incorporate the robust methods that can include the effect of environmental conditions in simulation studies.

1.9 Problems and challenges

It is appreciable that much knowledge has been accumulated on metal catalysts from theoretical and experimental studies. However, to develop a unified theory that is able to explain

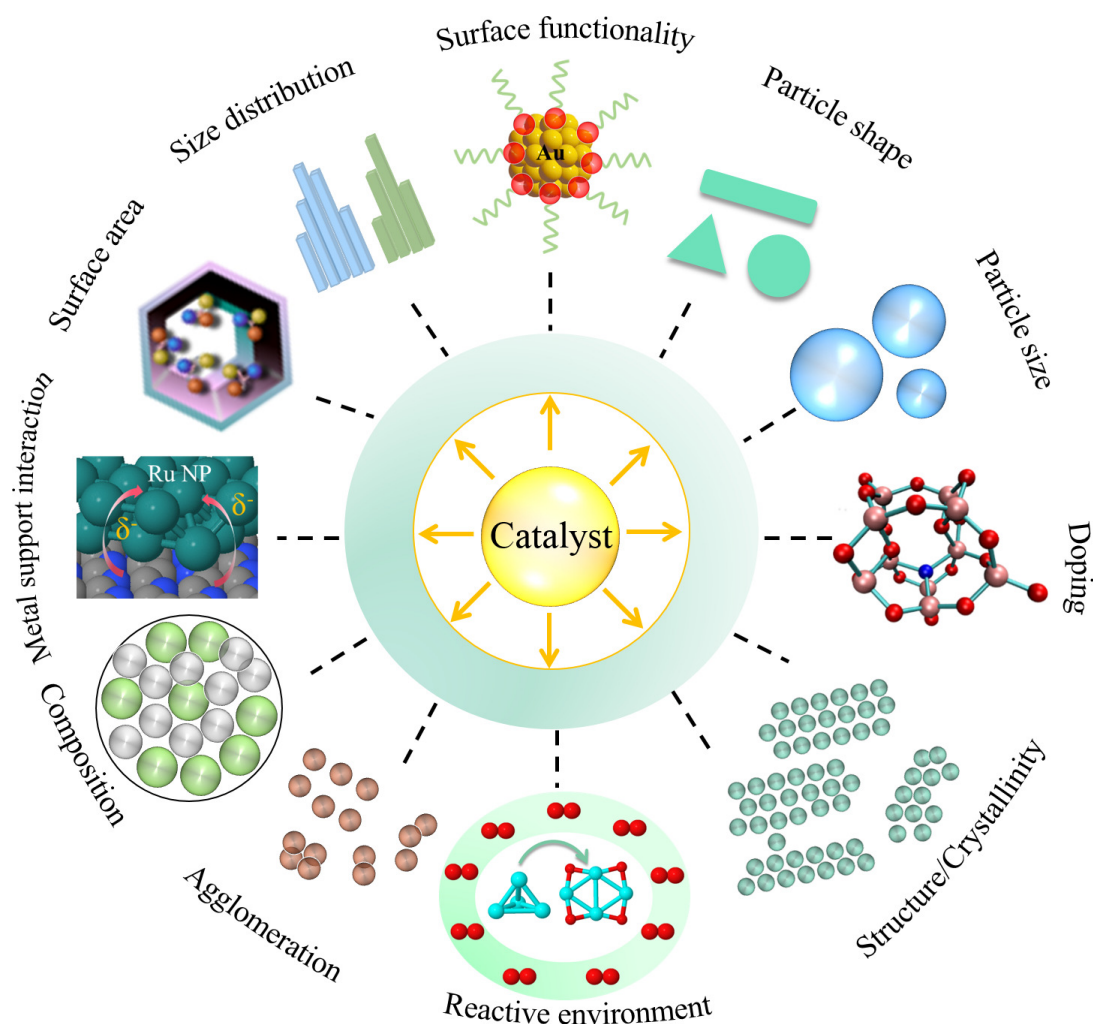


Figure 1.4: (a) The key factors such as particle size and shape, composition, structure, surface area and support etc. are shown that govern the catalytic performance [3].

and predict the catalytic properties and to describe the behavior of different metal catalyst for various catalytic processes is still an open challenge. Moreover, the situation becomes more complex when we go below 1nm (clusters and nanoparticles), where the electronic properties of clusters highly change due to the overlapping of orbital among metal atoms. For instance, in case of Au clusters, the fundamental gap of Au species varies largely with the atomicity up to size of 30 atoms, whilst above 70 atoms the fundamental gap remains constant on increasing the atomicity. The continuous band forms in the larger metal nanoparticles (>2 nm) [83]. The geometric shape of clusters containing fewer atoms also gets changed from planar to 3D. Notably, for metal nanoclusters such as Au, Ag, and Cu, their plasmonic and optical properties are strongly size-dependent, which further influence their catalytic performance in photocatalysis [84]. More importantly, in clusters with size less than 20 atoms, the geometric structures becomes quite flexible and vulnerable in the reactive environment. Thus, subnanometric clusters

shows distinct behavior and activity as compared to the larger nanoclusters. It is worth to mention that cluster with specific stoichiometry can have many possible structural configurations that depend on various factors like support, reactant, and operando conditions. Especially, the support morphology serves great impact on shape and size of clusters, which further determines the performance of catalyst. The geometric structure and charge density of clusters get alter by gaining the extra charge from support, which govern the catalytic properties of catalyst. For instance, Ru nanoparticles supported on electride, show the higher electron density as compared to those supported on conventional supports, and this increment in electron density attribute to higher activity for ammonia production [85]. Also, the simulation studies reveal that the shape of Au₃ cluster can vary from linear to triangular by changing the charged states from Au₃⁻ and Au₃⁺ [86].

Furthermore, determining the catalyst structures, under reaction conditions, is very challenging as well as demanding task to acquire the unequivocal understanding of active sites for rational design of efficient catalysts [87, 88, 89]. Since, nanoclusters show the dynamical behavior when they are exposed to realistic conditions, it is quite difficult to probe the catalyst' structures even with modern experimental methods at operating conditions [18]. Though the most stable structures have higher probability of occurrence at finite temperature but it is not necessary that the observed activity will be mainly accounted by the global minimum structure. The metastable structures also become energetically accessible under reaction conditions, and can play a vital role in determining the overall catalytic activity. For instance, the metastable structures of H covered Pt₁₃ clusters govern the observed activity due to their distinct electronic and structural properties than the most stable structure [88]. Hence, the global minimum structure alone is not sufficient to accurately describe the observed activity. The concept of metastability triggered activity opens a new avenue for understanding and designing new catalysts. Subsequently, it is needed to thoroughly explore the low energy isomers in simulation modeling rather than merely targeting the global minimum structure. Recently, some groups have addressed the modified global optimization methods to efficiently predict the low energy isomers on potential energy surface [90, 88, 87]. In the present thesis work, we have employed the robust property based genetic algorithm to search global minimum along with low energy structures. This approach allows us to systematically address the impact of metastable structures in catalysis. However, the unambiguous identification of active sites, detailed insight of elementary steps of that reaction process, the selectivity and the stability of

intermediate products are sometimes a daunting task due to the complexity involved in catalytic processes. Theory and computation have played an important role in understanding and

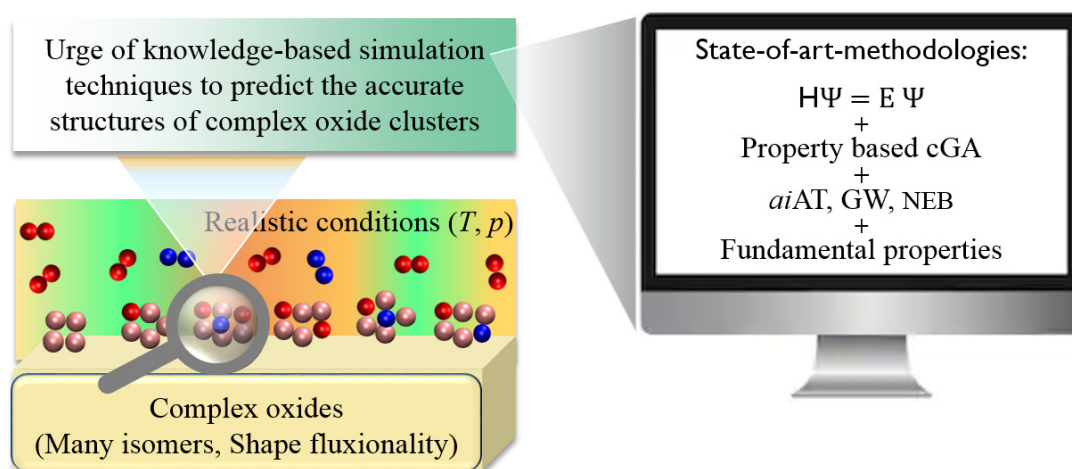


Figure 1.5: (a) Conceptual visualization of the problem and approach.

predicting chemical reactivity of various TM-oxide catalysts at nanoscale. Gas phase metal clusters have been considered to be versatile model systems to explore the basic principles of catalytic reaction mechanisms at a molecular level. Previous reports have identified a direct correlation between the products yielded in gas phase cluster calculations and condensed phase catalytic reactions [91, 92]. For instance, oxidation of ethylene by $V_2O_5^+$ and $V_4O_{10}^+$ clusters is in exact agreement to that occurring over Vanadia surfaces [91]. Similarly, the reaction mechanism of oxidation of methanol by $Mo_xO_y^+$ clusters is found in direct correspondence to reaction which occur over their bulk-surface counterpart [92]. Therefore, in last decades, there has been an increasing interest in understanding the physico-chemical properties of gas-phase clusters [93, 94, 95, 96, 97, 49, 98]. Detailed knowledge of structures of active sites is indispensable for meaningful modeling of efficient, optimize and cost-effective catalyst. First principles simulations (see Figure 1.5) allow us to gain the fundamental insights beyond the experimental limitations. Moreover, this helps us to answer the following questions: How does the electronic structure of adsorbed molecule modifies in the intermediate state and what is the structure of the intermediate configuration? How does intermediate complex affect the reactivity and determine the yielding of product during the catalytic reaction? What is the correlation between intermediate and properties of active centres. What is the role of steric and electronic factors to determine the catalytic path? What is the structure-activity relation? What is the best descriptor?

1.10 A short overview

- **Chapter 2 :** This chapter describes the theoretical methods used in this work. It presents a brief overview of first principles based density functional theory (DFT), Cascade genetic algorithm, *ab initio* atomistic thermodynamics, GW approximation and Nudged elastic band method that are used to obtain structural, stability, electronic properties and catalytic activity of the designed clusters.
- **Chapter 3 :** In this chapter, the composition, atomic structure, and electronic properties of $\text{TM}_x\text{Mg}_y\text{O}_z$ clusters (TM = Cr, Ni, Fe, Co, $x + y \leq 3$) at realistic temperature T and partial oxygen pressure p_{O_2} conditions are explored using the *ab initio* atomistic thermodynamics approach. The low-energy isomers of the different clusters are identified using a massively parallel cascade genetic algorithm at the hybrid density-functional level of theory. On analyzing a large set of data, we find that the fundamental gap E_g of the thermodynamically stable clusters are strongly affected by the presence of Mg-coordinated O_2 moieties. In contrast, the nature of the transition metal does not play a significant role in determining E_g . Using E_g of a cluster as a descriptor of its redox properties, our finding is against the conventional belief that the transition metal plays the key role in determining the electronic and therefore chemical properties of the clusters. High reactivity may be correlated more strongly with oxygen content in the cluster than with any specific TM type.
- **Chapter 4 :** In this chapter, a large data set is generated on $[\text{TM}_x\text{Mg}_y\text{O}_z]^{+/0/-}$ clusters (TM = Cr, Ni, Fe, Co, $x + y \leq 5$) using a massively parallel cascade genetic algorithm (cGA) approach at the hybrid density functional level of theory. The low energy isomers are further analyzed via *ab initio* atomistic thermodynamics to estimate their free energy of formation at a realistic temperature T and partial pressure of oxygen p_{O_2} . A thermodynamic phase diagram is drawn by minimizing Gibbs free energy of formation to identify the stable phases of neutral and charged $[\text{TM}_x\text{Mg}_y\text{O}_z]^{+/0/-}$ clusters. From this analysis, we notice that neutral and negatively charged clusters are stable in the wide range of (T, p_{O_2}) . The negatively charged clusters are more effective as a catalyst to lower the C–H bond activation barrier for oxidation of methane. We find that the nature of TM atoms towards controlling the activation barrier is less important. However, the TM gives rise

to different structural motifs in the cluster, which may act as active centres for catalysis.

- **Chapter 5** : In this chapter, we report a strategy, by taking a prototypical model system for photocatalysis (viz. N-doped $(\text{TiO}_2)_n$ clusters), to accurately determine low energy metastable structures that can play a major role with enhanced catalytic reactivity at a realistic condition. In free energy potential energy surface (PES) consisting plenty of isomers, computational design of specific metastable photocatalysts with enhanced activity is never been easy. This requires fixing various parameters viz. (i) favorable formation energy, (ii) low fundamental gap, (iii) low excitation energy and (iv) high vertical electron affinity (VEA) and low vertical ionization potential (VIP) to drive the hydrogen evolution reaction (HER) and oxygen evolution reaction (OER) for water splitting. We validate here by integrating several first principles based methodologies that consideration of the global minimum structure alone can severely underestimate the activity. As a first step, we have used a suite of genetic algorithms [viz. searching clusters with conventional minimum total energy $((\text{GA})_E)$; searching clusters with specific property i.e. high VEA $((\text{GA})_P^{\text{EA}})$, and low VIP $((\text{GA})_P^{\text{IP}})$] to model the N-doped $(\text{TiO}_2)_n$ ($n = 4 - 10, 15, 20$) (meta)stable clusters. Following this we have identified its free energy using *ab initio* thermodynamics to confirm that the metastable structures are not too far from the free energy global minima so that it can never be experimentally feasible to synthesis. By analyzing a large dataset, of different N-doped $(\text{TiO}_2)_n$ clusters, we find that N-substitution $((\text{N})_O)$ prefers to reside at highly coordinated oxygen site to maximize its coordination, whereas N-interstitial $((\text{NO})_O)$ and split-interstitial $((\text{N}_2)_O)$ favor the dangling oxygen site. $(\text{NO})_O$ and $(\text{N}_2)_O$ doped states are thermodynamically stable at realistic conditions (e.g. temperature (T) , oxygen partial pressure (p_{O_2}) , doping). Interestingly, we notice that each types of defect (viz. substitution, interstitials) reduce the fundamental gap and excitation energy substantially. However, $(\text{N}_2)_O$ doped clusters are found to be less probable in the pourbaix phase diagram, whereas $(\text{N})_O$ and $(\text{NO})_O$ doped metastable clusters show significant contribution near the phase boundaries in the probability profile. The latter ensure higher electrocatalytic activity for water splitting than the stable configurations.
- **Chapter 6** : In this chapter, we have investigated the role of shape in determining the catalytic activity of Ru nanoparticles. The flat-shaped Ru nanoparticles (NPs) show higher

activity for reductive amination of furfural to fufurylamine than that of spherical-shaped NPs. The high activity of Ru NPs can be attributed to the active sites with weak electron donating ability that prevail on the (111) facets of flat-shaped fcc Ru NPs. We have also addressed that thoroughly benchmarking of adsorption energy is crucial step to get the preliminary idea of active sites on the modeled catalysts. The weaker adsorption drives the selective transformation of carbonyl and imine compounds into other valuable derivatives. For the first time, the charge transfer from the N-carbon support to Ru catalyst is demonstrated by DFT calculations. This transferred charge leads to enhance the electron donating capacity of Ru catalyst. Our results reveal that the low activation barriers for hydrogenation steps of N-heterocyclic ring of quinoline is ascribed to the strong electron donating power of flat-shaped hcp Ru NPs. Moreover, weak adsorption energies are noticed for quinoline on electron-rich Ru surface that lead to prevent the poisoning caused by its adsorption. The weak binding of N-containing ring on flat-shaped hcp Ru catalyst facilitate the selective hydrogenation of quinoline. Hence, we suggest that the shape-controlled synthesis and designing of Ru nanocatalysts might significantly improve the efficiency and selectivity in various industrial chemical processes.

- **Chapter 7 : Conclusion**

This chapter concludes the thesis and present some future directions to be explored.

Theoretical methodology

2.1 Computer simulation

Computer simulation is defined as a comprehensive method which largely helps to simulate an abstract model of a particular system. The essence of the computer simulations is driven via mathematical models. In recent time, simulation methods are widely accepted in diverse fields of study such as physics, mathematics, chemistry, material science, biology, medical science, human systems in economics, psychology, social science and engineering science. Simulation methods allows us to explore and gain new insights into new technology innovation. Moreover, they enable us to predict the properties, performance, and behavior of the system of interest for a wide range of conditions. In the present time, with the accessibility of very fast computers, rapid progress in the development and comprehensive knowledge of efficient algorithms, simulations methods have become prevalent in any field of research. Fast parallelized computer systems enable us to tackle the problem of any length scale (nano \rightarrow meso \rightarrow micro). Computer simulations are not only a bridging link between analytical theory and experiment, allowing to examine theories, but they are also used as guiding research tool under physical conditions, that are not feasible in a laboratory. Moreover, rapidly evolving computational power is meeting the level that allows one to account and predict how the functioning of an entire system may be influenced by altering individual components within that system. Thus, the computational simulation has established a new, interdisciplinary research area which is known as “Computational Materials Science”. The multi-scale simulation in physics is aimed to determine the material properties and system behavior on one level using information or models from different levels. These levels are classified as: level of quantum mechanical models (account the information of the electrons explicitly), molecular dynamics models (information about individual atoms is involved), mesoscale or nano level (information about groups of atoms and

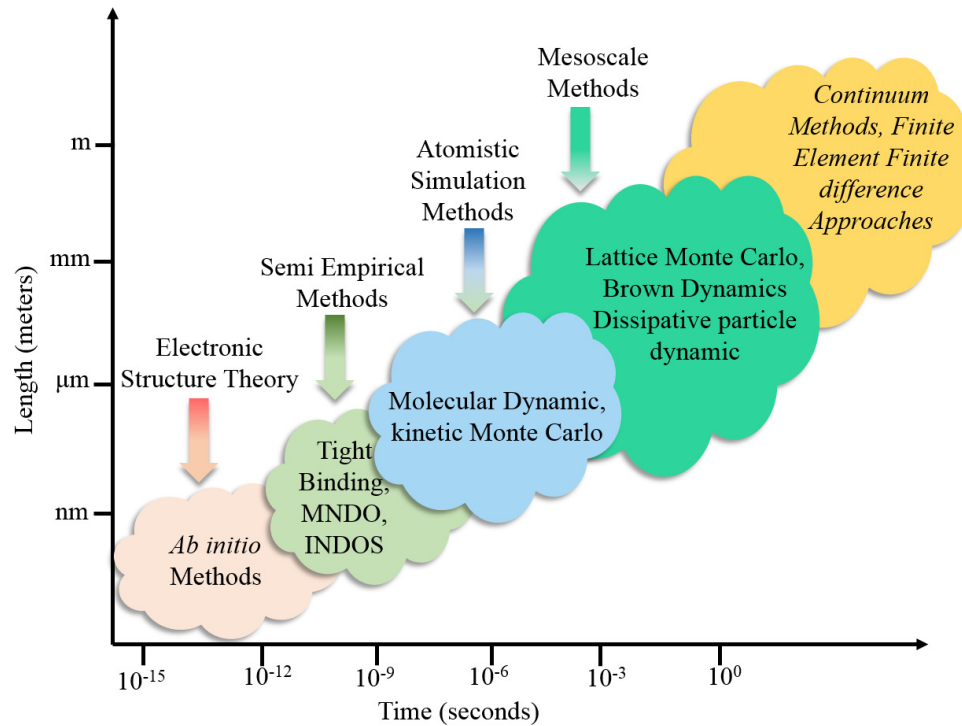


Figure 2.1: Multi-scale simulation in different length and time scales.

molecules is included), continuum models and device models. Each level addresses a phenomenon over a specific window of length and time scale. Multi-scale modeling is particularly important in integrated computational materials engineering since it allows predicting material properties or system behavior based on knowledge of the atomistic structure and properties of the elementary processes. Computational methods help to describe the geometries, energies, band gaps, vibrational modes and optical spectra. Prior to start the simulation, it is essential to know which phenomena and properties one is interested to investigate and accordingly the classified models can be adopted to the respective problem. In the present thesis work, the first principles electronic structure methods are used for simulation and designing of complex clusters that are efficient for catalysis purpose.

2.2 First principles calculation

This chapter describes the theoretical methods and concepts behind the methods, that are employed to perform the electronic structure calculations in this thesis. The world around us is made of condensed matter i.e., matter whose energy is low enough that it has condensed to form stable systems of atoms and molecules, usually in solid or liquid phases. The atoms are made of a positively charged nucleus and a number of negatively charged electrons and

these fundamental constituents of atoms determine the nature of the matter such as molecules, condensed matter and man-made structures. The nature of chemical and molecular bonding, mainly depends upon the interactions of their constituent electrons and nuclei. Hence, all of the physics of condensed matter systems emerges from these fundamental interactions. If we are able to model these interactions precisely, then all of the complex physical phenomena should appear naturally in our calculations. The physics that explains the interaction of electrons and nuclei in condensed matter is relatively simple. There are only two different types of particle included, and the behavior of these particles is mainly governed by basic quantum mechanics. What makes first principles calculations difficult is not the complexity of the physics but rather the size of the problem in terms of a numerical formulation.

The famous scientist of quantum mechanics, Paul Dirac, wrote “*The underlying physical laws necessary for the mathematical theory of a large part of physics and the whole of chemistry are thus completely known, and the difficulty is only that the exact application of these laws leads to equations much too complicated to be solved.*”

Therefore, the development of accurate and efficient theoretical methods and the computational techniques to deal with many-body problem is therefore the focus of ongoing research in this realm.

2.3 Introduction of theoretical framework

ab initio methods are rigorously used to solve the many-body system. Schrödinger equation is the initial point of these methods. However, due to many-electron in the system, the analytical solution of Schrödinger equation becomes impossible except some simple cases; such as H-atom, He^+ , harmonic oscillator etc. Therefore, *ab initio* methods are employed to solve the system numerically. However, in practice, numerical solution is also not feasible for more than a handful of electrons due to the limited speed and memory of computers. When exact solution of a particular problem becomes an acutely complex or computationally daunting task, the common strategy is to approximate it to a closely related problem, for which the exact solution is feasible. Then the difference between these two, which is considered to be small, is treated as a perturbation to the exactly solvable problem. Therefore, the quantitative calculations on many-electron systems include the approximations. The first level of approximation is associated with the much slower motion of nuclei as compared to the electrons. According to

Born-Oppenheimer approximation [99], the motion of nuclei can be decoupled from that of the electrons, hence, the electronic and ionic part of the wavefunction can be written as the product of the electronic and the nuclear wavefunctions. This approximation effectively reduces the dimension of the wavefunction, despite of this, due to the electron-electron interaction the dimension still remains too large. The first quantitative calculations on many-electron systems have been carried out on atoms by D. R. Hartree. He treated each electron independently, where each electron is considered to be moving in a average potential due to all other electrons and the nucleus [100, 101]. Hartree's work set the footing for many of the numerical methods, which are still in use today. The main draw back of the Hartree approximation is that, the wavefunction of system has been considered to be symmetric in nature. Since electrons are fermions, and they follow the Pauli's exclusion principle, therefore, the wavefunction should be antisymmetric in nature. Later, Fock modified the Hartree method, by incorporating the antisymmetric constraint to the independent electron Hartree approach by using a Slater determinant as wavefunction [102]. Slater determinant satisfies the Pauli exclusion principle that each electron has to be described by a different wave function. However, it complicates equations compared to Hartree method and introduces a new term, *electron exchange*. Hence, the combined efforts of Hartree and Fock developed a method to find the best single determinant wavefunction for the system, known as the Hartree-Fock method. This method is quite successful for geometries, but it fails miserably to describe the chemical and physical properties of the systems due to neglecting the electron-electron correlation energy. To account the correlation energy, one has to go thoroughly to correlated methods, which use multi-determinant wave functions as the total wavefunction of two-body Coulomb interactions, that is not well represented by a single Slater determinant. Many methods are proposed to incorporate this correlation energy very accurately viz. Møller-Plesset (MP) perturbation theory, Configuration Interaction (CI), Coupled Cluster (CC) methods, multiconfiguration self-consistent field (MCSCF) and Quantum Monte-Carlo (QMC) methods. However, in practice, these methods are computationally too expensive to tackle calculation even for a moderate cluster.

There is a justified interest for possible development of practical use of independent-particle approaches that incorporates effect of interactions and correlations among the particles. The approach of Hohenberg and Kohn [103] is to formulate density functional theory (DFT) as an exact theory of many-body system of interacting particles in an external potential including any problem of electrons and fixed nuclei. They proposed that many properties of a system includ-

ing total energy can be written as a functional of electron density and this energy is at minimum, if the density is an exact ground state density of many-body interacting system. These concepts laid the foundation of all the modern methods based on DFT. Later, Kohn and Sham [104] proposed that the exact ground state density of a many-body system can be represented by the ground state density of an auxiliary system of non-interacting particles. And Kohn-Sham method involves an auxiliary hamiltonian with usual kinetic energy term and an effective local potential, which incorporate exchange and correlation effects approximately. This method has led to be very successful approach for quantitative calculations on realistic problems and is by far the most widely used approach to treat the ground state. Density functional theory is a phenomenally exemplary approach to solve the fundamental equation that describes the quantum behavior of atoms and molecules. The fundamental remark of DFT is that any property of a many-electrons system can be determined as a functional of the ground state density; which is a scalar function of position and contains all the information of the system. The DFT is accurate, if we know how to derive necessary relations between density and energy. Unfortunately, energy functionals that relate electronic density to energy are unknown, and there is no general way to improve them, beside trying to implement it with suitable approximation. In fact the DFT results are in many cases surprisingly good if one takes into account even one of the conceptually simplest approximations on which some of them are based. DFT offers a good balance between the qualitative description of the electronic structure and the computational costs. Therefore, DFT became one of the widely popular and successful quantum mechanical methods to describe the ground state electronic properties of materials.

However, DFT results are valid and accurate only at 0 K. To include environmental effects, one needs to compute the free energy of formation using *ab initio* atomistic thermodynamics [105, 106, 107, 82]. In this approach, we approximate the configurational free energy of the potential energy surface in order to determine the compositions and the structures that minimize the free energy of formation at given external conditions, i.e., temperature and pressure of the reactive atmosphere. Experimentally, to probe the accurate structure of the clusters is a daunting task and cost effective due to expensive techniques. In simulation, evolutionary methods are used to predict the accurate structures of the clusters. In the present work, the low-energy structures (including the global minimum) are generated from an exhaustive scanning of the potential energy surface using a massively parallel cascade genetic algorithm (cGA) [108, 82, 90]. Nudged elastic band method has been employed to determine the min-

imum energy path between a given initial and final state of a transition process, which is an efficient method for finding the minimum energy path [109].

2.4 Wavefunction

In quantum mechanics, the state of system can be defined by wavefunction, $\Psi(\mathbf{r}_1, \mathbf{r}_2, \dots, \mathbf{r}_i, \dots; \mathbf{R}_1, \mathbf{R}_2, \dots, \mathbf{R}_I, \dots)$, where \mathbf{r}_i and \mathbf{R}_I are the positions of i^{th} electron and I^{th} nucleus. If we know the wave function of a system at an instant, corresponding position, momentum, kinetic energy, etc. can also be determined at that instant. Necessary conditions for the wavefunction to be physically acceptable are:

1. It should be continuous everywhere.
2. Its derivatives should be exist and continuous everywhere.
3. Its should be square integrable.
4. They should vanish at infinity (finite system).
5. The expectation value of any power of position and momentum should be finite.

Once we know the wave function Ψ for a given state of the system, we are at position to calculate the expectation value of any physical quantity (E) having an operator. The eigenvalues of the observables has to be real number.

$$E = \frac{\int \int \dots \int \Psi^*(\mathbf{r}_1, \mathbf{r}_2, \dots, \mathbf{r}_N) \hat{H} \Psi(\mathbf{r}_1, \mathbf{r}_2, \dots, \mathbf{r}_N) d\mathbf{r}_1 d\mathbf{r}_2 \dots d\mathbf{r}_N}{\int \int \dots \int \Psi^*(\mathbf{r}_1, \mathbf{r}_2, \dots, \mathbf{r}_N) \Psi(\mathbf{r}_1, \mathbf{r}_2, \dots, \mathbf{r}_N) d\mathbf{r}_1 d\mathbf{r}_2 \dots d\mathbf{r}_N} \quad (2.1)$$

In can be written in more convenient way using Dirac *bra* and *ket* notation:

$$E = \frac{\langle \Psi | \hat{H} | \Psi \rangle}{\langle \Psi | \Psi \rangle} \quad (2.2)$$

If wavefunction is normalized, $\langle \Psi | \Psi \rangle = 1$. Notably, the wavefunction Ψ does not have any physical meaning but its square ($|\Psi(\mathbf{r}_1, \mathbf{r}_2, \dots, \mathbf{r}_N)|^2$) determines the probability to find electron 1 at the space point \mathbf{r}_1 , electron 2 at the point \mathbf{r}_2 , and so on. For the system having only one electron, $|\Psi(\mathbf{r})|^2 d\mathbf{r}$ determines the probability to find the electron in the volume $d\mathbf{r}$ at the point \mathbf{r} . If wavefunction is normalized, then the integration of probability over all the space for all the variables must be 1, which means the probability of finding electron anywhere in the space is equal to 1.

$$\int \Psi(\mathbf{r})^* \Psi(\mathbf{r}) d\tau = \int_0^\infty \int_0^\pi \int_0^{2\pi} \Psi(\mathbf{r})^* \Psi(\mathbf{r}) r^2 \sin\theta dr d\theta d\phi = 1 \quad (2.3)$$

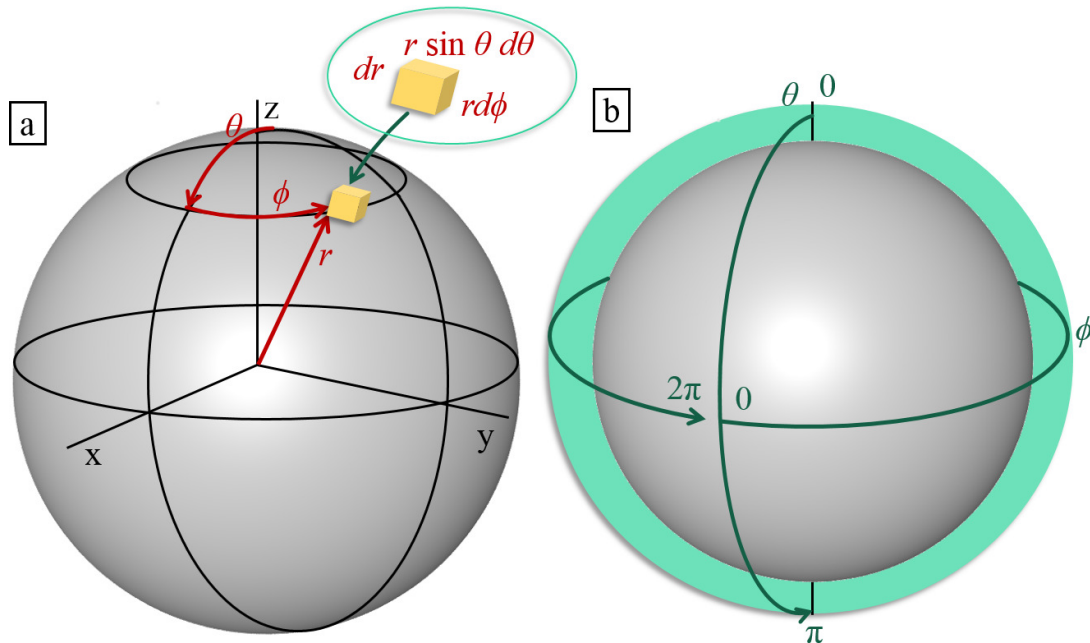


Figure 2.2: (a) The spherical polar coordinates for system with spherical symmetry, (b) The surface of a sphere is covered with twirling half arc that allows θ to range from 0 to π , and a full whirling around the sphere by allowing ϕ to range from 0 to 2π [4].

2.5 Schrödinger equation

The solution of stationary Schrödinger equation for a many-body system gives the information about its physical and chemical properties at microscopic level.

$$\hat{H}\Psi(\mathbf{r}_1, \mathbf{r}_2, \dots, \mathbf{r}_i, \dots; \mathbf{R}_1, \mathbf{R}_2, \dots, \mathbf{R}_I, \dots) = E\Psi(\mathbf{r}_1, \mathbf{r}_2, \dots, \mathbf{r}_i, \dots; \mathbf{R}_1, \mathbf{R}_2, \dots, \mathbf{R}_I, \dots) \quad (2.4)$$

here, \hat{H} is the operator of the total energy for the system and has a special name Hamiltonian. To calculate the total energy (E) of the system, one needs to construct its Hamiltonian (\hat{H}) that can be expressed in the atomic units ($\hbar = m_e = e = 1$) as:

$$\hat{H} = -\frac{1}{2} \sum_i \nabla_i^2 - \sum_{i,I} \frac{Z_I}{|\mathbf{r}_i - \mathbf{R}_I|} + \frac{1}{2} \sum_{i \neq j} \frac{1}{|\mathbf{r}_i - \mathbf{r}_j|} - \sum_I \frac{1}{2M_I} \nabla_I^2 + \frac{1}{2} \sum_{I \neq J} \frac{Z_I Z_J}{|\mathbf{R}_I - \mathbf{R}_J|} \quad (2.5)$$

where \mathbf{r}_i denotes the position of i^{th} electron, \mathbf{R}_I and Z_I are the position and atomic number of I^{th} nucleus, respectively. ∇_i^2 is the Laplacian operator. $|\mathbf{r}_i - \mathbf{R}_I|$ is the distance between i^{th} electron and I^{th} nucleus. $|\mathbf{r}_i - \mathbf{r}_j|$ is the distance between i^{th} and j^{th} electrons. $|\mathbf{r}_i - \mathbf{R}_I|$ and $|\mathbf{r}_i - \mathbf{r}_j|$ can be written in cartesian coordinates:

$$|\mathbf{r}_i - \mathbf{r}_j| = \sqrt{(x_i - x_j)^2 + (y_i - y_j)^2 + (z_i - z_j)^2}$$

$$|\mathbf{r}_i - \mathbf{R}_I| = \sqrt{(x_i - X_I)^2 + (y_i - Y_I)^2 + (z_i - Z_I)^2}$$

We can write it in more simplified form:

$$\hat{H} = \hat{T}_e + \hat{V}_{ext} + \hat{U}_{ee} + \hat{T}_{nucl} + \hat{U}_{nucl} \quad (2.6)$$

where, $\hat{T}_e \rightarrow$ kinetic energy of electrons.

$\hat{V}_{ext} \rightarrow$ external potential experienced by electrons from nuclei.

$\hat{U}_{ee} \rightarrow$ electrostatic repulsion between electrons.

$\hat{T}_{nucl} \rightarrow$ kinetic energy of nuclei.

$\hat{U}_{nucl} \rightarrow$ interaction energy of nuclei.

However, the exact solution of Schrödinger equation for bigger systems (having large number of electrons and nuclei) becomes impractical as it involves a large number of variables. Therefore, there is an urge to include the approximation to deal easily with many body problem.

2.6 Born-Oppenheimer approximation

The physical motivation behind the first level of simplification is that the mass of nuclei (M_I) is much heavier than that of electrons (m_e) (a proton is 1836 times heavier as compared to electron). With the same amount of kinetic energy, the motion of nuclei is much more slower than the electrons. Consequently, electrons instantly adjust to their ground states whenever nucleus change its position. We can therefore distinct the dynamics of electrons and nuclei with the assumption that the motion of electrons depends on positions of nuclei in a parametric way (considered nuclei as static). In mathematical terms, under this approximation the electronic and nuclear wavefunctions can be decoupled.

$$\begin{aligned} \Psi_{total} &= \psi_{electronic} \times \psi_{nuclear} \\ \Psi(\mathbf{r}_1, \mathbf{r}_2, \dots, \mathbf{R}_1, \mathbf{R}_2, \dots) &= \psi(\mathbf{r}_1, \mathbf{r}_2, \dots; \mathbf{R}) \times \psi(\mathbf{R}_1, \mathbf{R}_2, \dots) \end{aligned} \quad (2.7)$$

It is important to note that the electronic wavefunction $\psi(\mathbf{r}_1, \mathbf{r}_2, \dots; \mathbf{R})$ has parametric dependence on the ionic positions. It allows one to separate the Hamiltonian operator into electronic (H_{el}) and nuclear terms (H_{nucl}), so that the decoupled systems can be solved more efficiently.

The nuclear Hamiltonian of the many-body system:

$$\hat{H}_{nucl} = \hat{T}_{nucl} + \hat{U}_{nucl} \quad (2.8)$$

Here, the kinetic energy of nuclei can be omitted as the nuclei is much more heavier than the electrons. The second term is the electrostatic ion-ion interaction, which is a classical additive

term and can be calculated by Ewald summation method [110]. The electronic Hamiltonian of the many-body system:

$$\hat{H}_{el} = \hat{T}_e + \hat{V}_{ext} + \hat{U}_{ee} \quad (2.9)$$

We can rewrite the electronic Hamiltonian as:

$$\hat{H}_{el} = \sum_{i=1}^N \hat{h}_i + \hat{U}_{ee} \quad (2.10)$$

Here, $\hat{h}_i = -\frac{1}{2}\nabla_i^2 + \hat{v}_i$, only depends on coordinates of i^{th} electron. Indeed, significant reduction in the dimensionality of the total wavefunction has been achieved using Born-Oppenheimer approximation [99]. Despite this approximation, still exact solution requires to deal with $3N$ variables due to electron-electron interaction (\hat{U}_{ee}). Hence, solving N -electron system remains impractical and calls for further approximations.

2.7 The Hartree approximation

Hartree have found an independent-electron approximations [100, 101], which assumes that electrons are not correlated with each other individually, but with the averaged density of electrons. In this approach, the wavefunction of many-electron system Ψ can be approximated by product of each electron's function ($\phi_i(\mathbf{r}_i)$):

$$\Psi_{\mathbf{r}_1, \mathbf{r}_2, \dots, \mathbf{r}_N} = \phi_1(\mathbf{r}_1)\phi_2(\mathbf{r}_2)\dots\phi_N(\mathbf{r}_N) \quad (2.11)$$

We can determine densities corresponding to each electron:

$$\rho_i(\mathbf{r}) = |\phi_i(\mathbf{r})|^2 \quad (2.12)$$

The total density of the electrons in the system will be:

$$\rho_{total}(\mathbf{r}) = \sum_{i=1}^N \rho_i(\mathbf{r}) = \sum_{i=1}^N |\phi_i(\mathbf{r})|^2 \quad (2.13)$$

However, if we want to write the density to which the k^{th} electron will interact, we have to exclude its own density from the total density:

$$\rho^k(\mathbf{r}) = \rho_{total}(\mathbf{r}) - \rho_k(\mathbf{r}) = \left(\sum_{i=1}^N \rho_i(\mathbf{r}) - |\phi_k(\mathbf{r})|^2 \right) = \sum_{i=1, i \neq k}^N |\phi_i(\mathbf{r})|^2 \quad (2.14)$$

Now, we need to evaluate the interaction of an electron which is located at point \mathbf{r} , with electron density of rest electrons:

$$\hat{g}_k(\mathbf{r}) = \int \rho^k(\mathbf{r}') \frac{1}{|\mathbf{r} - \mathbf{r}'|} d\mathbf{r}' \quad (2.15)$$

Hence, by using this assumption, we can write:

$$\hat{U}_{ee} \approx \sum_{i=1}^N \hat{g}_i(\mathbf{r}) \quad (2.16)$$

(Note that, one discrepancy still remains, since we doubly count interaction, we will deal it later) Now, all the terms containing by \hat{H}_{el} are one-electron operator:

$$\hat{H}_{el} \approx \sum_{i=1}^N \left(-\frac{1}{2} \nabla_i^2 + \hat{v}_i + \hat{g}_i(\mathbf{r}) \right) \quad (2.17)$$

and Schrödinger equation for many electron system can be resolved into N independent one electron equations:

$$\left(-\frac{1}{2} \nabla_i^2 + \hat{v}_i + \hat{g}_i(\mathbf{r}) \right) \phi_i(\mathbf{r}) = \epsilon_i \phi_i(\mathbf{r}) \quad (2.18)$$

ϵ_i is the energy of the i^{th} electron. In beginning, we start from approximate orbitals ϕ_i (e.g. from H-atom). We obtain the better ϕ_i 's by solving the N equations. In next iteration, we use these new orbitals as a starting point. At a point, when no improvement is noticed in orbitals from one iteration to another iteration, we can consider that the self-consistent field orbitals are converged. Then we construct the wavefunction Ψ from these orbitals to calculate the total energy E of the ground state. The total energy is obtained from expectation value of the Hamiltonian \hat{H}_{el} . In order to find the ground state wavefunction, we minimize the total energy of the system using variational principle. It says that if E_0 is the ground state energy of the system, for any wavefunction Ψ :

$$\frac{\langle \Psi | \hat{H} | \Psi \rangle}{\langle \Psi | \Psi \rangle} \geq E_0 \quad (2.19)$$

We count twice to evaluate Coulomb interactions between electrons. Therefore, the correct total energy can be written as:

$$E = \sum_{i=1}^N \epsilon_i - \sum_{i=1}^{N-1} \sum_{j=i+1}^N J_{ij} \quad (2.20)$$

where, J_{ij} are known as Coulomb integrals and are defined as:

$$J_{ij} = \int \int \frac{\rho_i(\mathbf{r}_1) \rho_j(\mathbf{r}_2)}{|\mathbf{r}_1 - \mathbf{r}_2|} d\mathbf{r}_1 d\mathbf{r}_2 = \int \int |\phi_i(\mathbf{r}_1)|^2 \frac{1}{|\mathbf{r}_1 - \mathbf{r}_2|} |\phi_j(\mathbf{r}_2)|^2 d\mathbf{r}_1 d\mathbf{r}_2 \quad (2.21)$$

Hartree's work is the foundation for subsequent developments in approximations and methods to solve the many-body system efficiently (with sufficient accuracy). However, the main drawback of Hartree approximation is that the form of the wavefunction does not hold the antisymmetry nature of fermions. In case of electrons (fermions), two or more electrons can not be described by the same quantum state, this is known as the Pauli's exclusion principle in quantum mechanics.

2.8 The Hartree-Fock approximation

After few years, Fock [111] and independently Slater [112] suggested some modification to the Hartree method. Since electrons are fermions, the wavefunction of many-electron system should be antisymmetric under the interchange of any set of electrons.

$$\hat{P}_{1,2}\Psi(\mathbf{r}_1, \mathbf{r}_2, \dots, \mathbf{r}_N) = -\Psi(\mathbf{r}_2, \mathbf{r}_1, \dots, \mathbf{r}_N) \quad (2.22)$$

where, $\hat{P}_{1,2}$ is the parity operator. The antisymmetric wavefunction is the sum of all the products which can be obtained by interchanging electron labels. However, this way becomes very tedious to generate a wavefunction. Slater suggested the more convenient way to construct the wavefunction as a single Slater determinant with single electron states as elements of the matrix, which exhibits the antisymmetric nature.

$$\Psi(\mathbf{r}_1, \mathbf{r}_2, \dots, \mathbf{r}_N) = \frac{1}{\sqrt{N!}} \begin{vmatrix} \phi_1(\mathbf{r}_1) & \phi_2(\mathbf{r}_1) & \dots & \phi_N(\mathbf{r}_1) \\ \phi_1(\mathbf{r}_2) & \phi_2(\mathbf{r}_2) & \dots & \phi_N(\mathbf{r}_2) \\ \phi_1(\mathbf{r}_3) & \phi_2(\mathbf{r}_3) & \dots & \phi_N(\mathbf{r}_3) \\ \cdot & \cdot & \cdot & \cdot \\ \cdot & \cdot & \cdot & \cdot \\ \cdot & \cdot & \cdot & \cdot \\ \phi_1(\mathbf{r}_N) & \phi_2(\mathbf{r}_N) & \dots & \phi_N(\mathbf{r}_N) \end{vmatrix} \quad (2.23)$$

For the sake of ease, let us consider the case of two electrons system:

$$\Psi(\mathbf{r}_1, \mathbf{r}_2) = \frac{1}{\sqrt{2}} \begin{vmatrix} \phi_1(\mathbf{r}_1) & \phi_2(\mathbf{r}_1) \\ \phi_1(\mathbf{r}_2) & \phi_2(\mathbf{r}_2) \end{vmatrix} = \frac{1}{\sqrt{2}} [\phi_1(\mathbf{r}_1)\phi_2(\mathbf{r}_2) - \phi_2(\mathbf{r}_1)\phi_1(\mathbf{r}_2)] \quad (2.24)$$

By changing the labels $1 \rightarrow 2$ and $2 \rightarrow 1$, we obtain:

$$\Psi(\mathbf{r}_2, \mathbf{r}_1) = \frac{1}{\sqrt{2}} \begin{vmatrix} \phi_1(\mathbf{r}_2) & \phi_2(\mathbf{r}_2) \\ \phi_1(\mathbf{r}_1) & \phi_2(\mathbf{r}_1) \end{vmatrix} = \frac{1}{\sqrt{2}} [\phi_1(\mathbf{r}_2)\phi_2(\mathbf{r}_1) - \phi_2(\mathbf{r}_2)\phi_1(\mathbf{r}_1)] \quad (2.25)$$

$$\Psi(\mathbf{r}_1, \mathbf{r}_2) = -\Psi(\mathbf{r}_2, \mathbf{r}_1) \quad (2.26)$$

If we consider that two electrons are defined by the same spin-orbital ($\phi_1 = \phi_2 = \phi$) we obtain:

$$\Psi(\mathbf{r}_2, \mathbf{r}_1) = \frac{1}{\sqrt{2}} \begin{vmatrix} \phi(\mathbf{r}_2) & \phi(\mathbf{r}_2) \\ \phi(\mathbf{r}_1) & \phi(\mathbf{r}_1) \end{vmatrix} = \frac{1}{\sqrt{2}} [\phi(\mathbf{r}_2)\phi(\mathbf{r}_1) - \phi(\mathbf{r}_2)\phi(\mathbf{r}_1)] = 0 \quad (2.27)$$

Hence, the wavefunction and the probability of finding such electrons are zero. To find the best single determinant wavefunction that minimize the total energy for the interacting Hamiltonian is called Hartree-Fock method. Note that the solution steps of Hartree-Fock methods are summarized in Figure 2.3. Slater determinant ensures the Pauli's principle since (1) If two rows are same the determinant comes out to be zero, which means each electron has to be defined by a different state, (2) sign change on interchanging two rows (columns), (3) determinant is zero if any row(column) is zero. This inclusion introduces a new term *electron exchange* in an exact manner to Hartree method. However, it neglects electron-electron Coulomb correlation energy, which is the energy difference between the exact energy and Hartree-Fock energy of the system. This correlation energy ($E_{corr.} = E_{exact} - E_{HF}$) plays the vital role to describe the physical and chemical properties of atoms, molecules and solid systems. There have been proposed many correlated methods that account the correlation energy such as MP2 or MP4, CI, CC methods and QMC. These methods include multi-determinant wave functions and are quite accurate. However, these methods are computationally very expensive. Therefore, more rigorous approach is needed to solve the interacting many-body problem. DFT allows to treat the much larger system by providing a good balance between accuracy and computational cost.

2.9 Functional

A function takes one or more number as inputs and yields another number as an output. Unlike function, functional takes a function as its argument and provides a number as an output. In usual notation, the function is written in square brackets as $F[f] = a$. Functionals can also have derivatives, which behave similarly to traditional derivatives for functions. The differential of the functional is defined as:

$$\partial F[f] = F[f + \partial f] - F[f] = \int \frac{\partial F}{\partial f(x)} \partial f(x) dx \quad (2.28)$$

Moreover, the functional derivatives have properties similar to traditional function derivatives.

2.10 Density Functional Theory

Density Functional Theory (DFT) is the widely accepted method in the condensed matter physics, material science and computational chemistry. This theory is largely applicable to

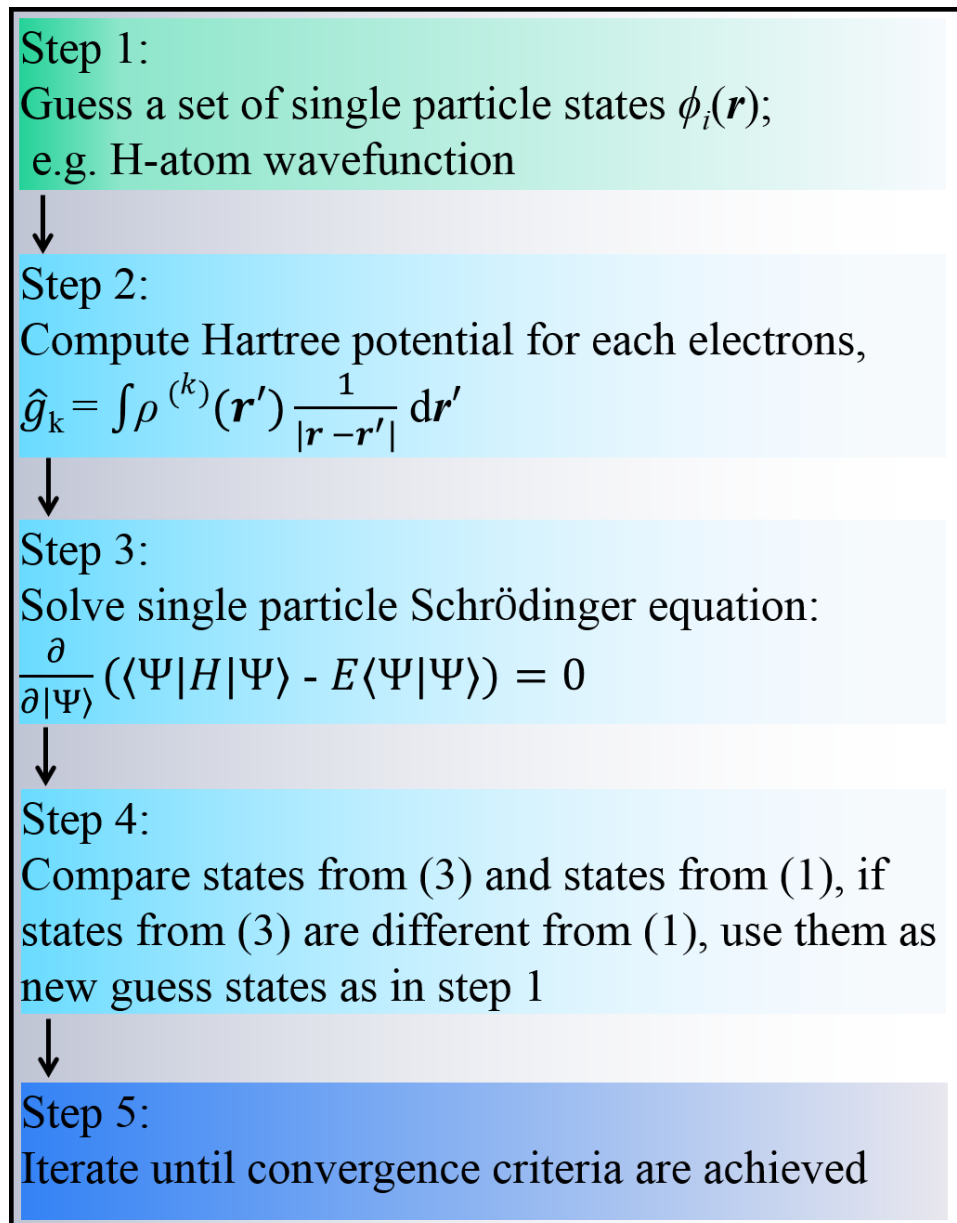


Figure 2.3: Schematic flowchart Hartree-Fock method for the solution of many electron system.

describe the ground state properties of many-body systems, e.g. atoms, molecules, and solids. The core assumption of DFT is to use the ground state electron density as the fundamental variable. Electron density is a scalar function of position and possesses all the information of the system. Using an electron density rather than wavefunction can remarkably simplify the many-body problem by reducing the degrees of freedom from $3N$ to 3 . Hence, under the framework of DFT, the solution of Schrödinger equation becomes tractable for the interacting system with desired accuracy at reasonable computational cost. The idea of electron density already used by Thomas and Fermi in 1927 to propose the Thomas-Fermi model. The modern formulation of DFT has been established by Hohenberg and Kohn (1964). Walter Kohn awarded Noble

prize in Chemistry in 1998 for his contribution in the foundation of DFT. The development of DFT is described in the next sections.

2.10.1 The Thomas-Fermi Model

Thomas-Fermi method is the oversimplified approach to provide the total energy of the system in terms of electron density [113, 114]. In this model, the distribution of electrons is approximated uniformly in an atom. The Thomas-Fermi kinetic energy functional is written as a function of the local density:

$$T_{TF}[\rho(\mathbf{r})] = \frac{3}{10}(3\pi^2)^{2/3} \int \rho^{5/3}(\mathbf{r}) d^3\mathbf{r} \quad (2.29)$$

This expression is also used in the local density approximation (LDA). Combining the other interactions, the Thomas-Fermi equation to obtain the total energy of an atom is given by:

$$E^{TF}[\rho(\mathbf{r})] = \frac{3}{10}(3\pi^2)^{2/3} \int \rho^{5/3}(\mathbf{r}) d^3\mathbf{r} - \int \frac{\rho(\mathbf{r})}{\mathbf{r}} d^3\mathbf{r} + \frac{1}{2} \int \frac{\rho(\mathbf{r}_1)\rho(\mathbf{r}_2)}{\mathbf{r}_{12}} d^3\mathbf{r}_1 d^3\mathbf{r}_2 \quad (2.30)$$

where, the second and third terms are the potential energy (nucleus-electron) and the Hartree energy, respectively. The total energy and electron density of the ground state can be obtained by minimizing this functional. This model is a crude approximation to describe the energy of an atom, as the kinetic energy is not calculated accurately as well as the exchange-correlation effects are not taken into consideration. However, in 1930 Dirac [115] included the exchange term to the Thomas-Fermi model, which is known as the Thomas-Fermi-Dirac model. Still, these models remained inaccurate for molecular systems.

2.10.2 Hohenberg and Kohn Theorem

In 1964 Hohenberg and Kohn laid the foundation of DFT by introducing two fundamental theorems based on electron density $\rho(\mathbf{r})$ of electrons in an external potential [103, 104].

Theorem I: *For a system of interacting particles in an external potential, $\hat{V}_{ext}(\mathbf{r})$ can be uniquely determined by its ground state electron density $\rho(\mathbf{r})$ within an additive constant.* Thus the ground state density determines the full Hamiltonian, except for a constant shift of the energy. Hence, all properties of the many-body electronic system such as its total energy, kinetic energy, and potential energy are also functional of the ground state electron density $\rho(\mathbf{r})$. Electronic density for a system of N electrons, with an exact wavefunction, is defined by:

$$\rho(\mathbf{r}) = N \sum_{\mathbf{s}_1} \dots \sum_{\mathbf{s}_N} \int d\mathbf{r}_2 \dots \int d\mathbf{r}_N |\Psi(\mathbf{r}_1, \mathbf{s}_1, \mathbf{r}_2, \mathbf{s}_2, \dots, \mathbf{r}_N, \mathbf{s}_N)|^2 \quad (2.31)$$

where \mathbf{r}_i denotes the spatial coordinates of the electrons and s_i represents their spin coordinates.

$$N = \int \rho(\mathbf{r}) d\mathbf{r} \quad (2.32)$$

The electron density, $\rho(\mathbf{r})$ denotes the probability of finding the electron at the space point (\mathbf{r}) . Electron density gives the total number of electrons by integrating it all over the space. It provides all the information of the system and only depend on three variables. If we know the electron density of the system, we can compute most of the properties and is more tractable than the wave function.

Let's consider that for a given density $\rho(\mathbf{r})$ there exist two potentials $\hat{V}_{ext}(\mathbf{r})$ and $\hat{V}'_{ext}(\mathbf{r})$, which correspond to two different Hamiltonians \hat{H}_{el} and \hat{H}'_{el} , respectively. They produce two distinct wavefunctions, Ψ and Ψ' . The expectation values of energy for Ψ and Ψ' correspond to \hat{H}_{el} and \hat{H}'_{el} : $E_0 = \langle \Psi | H | \Psi \rangle$ and $E'_0 = \langle \Psi' | H' | \Psi' \rangle$, respectively. Here, it is considered that the ground state is nondegenerate. According to the variational theorem, except Ψ no wavefunction can give an energy that is less than the energy E_0 with the Hamiltonian \hat{H}_{el} :

$$E_0 = \langle \Psi | H | \Psi \rangle < \langle \Psi' | H | \Psi' \rangle \quad (2.33)$$

$$\langle \Psi' | H | \Psi' \rangle = \langle \Psi' | H' | \Psi' \rangle + \langle \Psi' | H - H' | \Psi' \rangle \quad (2.34)$$

$$E_0 < E'_0 + \int \rho(\mathbf{r}) [\hat{V}_{ext} - \hat{V}'_{ext}] d\mathbf{r} \quad (2.35)$$

Similarly, variational theorem are used for second wavefunction Ψ' and we obtain:

$$E'_0 = \langle \Psi' | H' | \Psi' \rangle < \langle \Psi | H' | \Psi \rangle \quad (2.36)$$

$$\langle \Psi | H' | \Psi \rangle = \langle \Psi | H | \Psi \rangle + \langle \Psi | H' - H | \Psi \rangle \quad (2.37)$$

$$E'_0 < E_0 - \int \rho(\mathbf{r}) [\hat{V}_{ext} - \hat{V}'_{ext}] d\mathbf{r} \quad (2.38)$$

Adding equations 2.35 and 2.38, we get:

$$E_0 + E'_0 < E_0 + E_0 \quad (2.39)$$

equation 2.39 is contradictory, which implies that there cannot be two potentials corresponding to a ground state density $\rho(\mathbf{r})$.

Theorem II: *A universal functional for the energy $E[\rho(\mathbf{r})]$ can be described in terms of the density $\rho(\mathbf{r})$, which is accepted for any external potential $V_{ext}(\mathbf{r})$. For any particular $V_{ext}(\mathbf{r})$, the exact ground state energy is the global minimum value of this functional and the density $\rho(\mathbf{r})$ that minimizes this functional is the ground state density $\rho_0(\mathbf{r})$.*

$\rho_0(\mathbf{r})$ uniquely determines the external potential of the system, which leads to the ground state wavefunction. Moreover, all the observable properties of ground state such as kinetic energy can be determined. Thus, the total ground state energy can be written as a functional of the density:

$$E[\rho] = T_e[\rho] + V_{ext}[\rho] + U_{ee}[\rho] \quad (2.40)$$

$$E[\rho] = \int \rho(\mathbf{r}) \hat{V}_{ext}(\mathbf{r}) d\mathbf{r} + F_{HK}[\rho] \quad (2.41)$$

The F_{HK} is a universal functional independent of the particular system, which operates only on density. The system dependent part is involved in the external potential V_{ext} . Note that we have used “hat” above the operators and no “hat” above the corresponding energy terms. The correct density that minimizes the functional is the exact ground state density $\rho_0(\mathbf{r})$.

$$E_0 = E[\rho_0(\mathbf{r})] \quad (2.42)$$

According to the variational principle, an arbitrary (trial) electron density $\tilde{\rho}(\mathbf{r})$ will give a higher energy:

$$E_0 \leq E[\tilde{\rho}(\mathbf{r})] \quad (2.43)$$

There is an important issue concerning the, so called, v -representability question. v -representable density is associated with a non-degenerate ground state in the external potential, V_{ext} . Levy and Lieb [116, 117] have shown that all density distributions are not v -representable, i.e., they do not correspond to any external potential. There is a possibility that the energy minimization leads to a non v -representable density and fails to converge to the physical ground state density. It is important to note that in the Hohenberg-Kohn theorems, during the minimization, we use trial densities by assuming that these remain v -representable, i.e., each trial density $\tilde{\rho}$ is associated with a Hamiltonian \hat{H}_{el} . From the Hamiltonian we can obtain the corresponding wavefunction $\tilde{\Psi}$ for the ground state defined by this Hamiltonian ($\tilde{\rho} \rightarrow \hat{H}_{el} \rightarrow \tilde{\Psi}$). As per variational theorem, this wavefunction is not a ground state for the actual Hamiltonian of the system \hat{H}_{el} .

$$\langle \tilde{\Psi} | H | \tilde{\Psi} \rangle = E[\tilde{\rho}] \geq E[\rho_0] \equiv E_0 \quad (2.44)$$

where $\rho_0(\mathbf{r})$ is the exact ground state density of the system. The ground state energy can be found by minimizing the energy with respect to density $\rho(\mathbf{r})$, and the density that minimizes the energy is the true ground state density. In order to minimize the energy functional, it requires to be constrained by the N -representability of density that is optimized. The constrained minimization is performed by assuming that the trial density can be found from an antisymmetric wavefunction, which means, density is N -representable. The Lagrange's method of undetermined multipliers is a viable way to conduct the constrained minimization. The constraints are defined in such a way that their value is exactly zero when they are satisfied. The N -representability constraint can be expressed as:

$$\text{constraint} = \int \rho(\mathbf{r})d\mathbf{r} - N = 0 \quad (2.45)$$

These constraints are added to a minimized functional by after multiplied by an undetermined constant (μ).

$$E[\rho(\mathbf{r})] - \mu \left(\int \rho(\mathbf{r})d\mathbf{r} - N \right) \quad (2.46)$$

Now, to obtain the minimum of above expression:

$$\partial \left[E[\rho(\mathbf{r})] - \mu \left(\int \rho(\mathbf{r})d\mathbf{r} - N \right) \right] = 0 \quad (2.47)$$

Differential of the functional,

$$\partial E = \int \frac{\partial E[\rho(\mathbf{r})]}{\partial \rho(\mathbf{r})} \partial \rho(\mathbf{r})d\mathbf{r}$$

and using the fact that differential and integral signs can be interchanged, we get:

$$\int \frac{\partial E[\rho(\mathbf{r})]}{\partial \rho(\mathbf{r})} \partial \rho(\mathbf{r})d\mathbf{r} - \mu \int \partial \rho(\mathbf{r})d\mathbf{r} = 0 \quad (2.48)$$

which gives the value of the Lagrange multiplier at minimum.

$$\frac{\partial E[\rho(\mathbf{r})]}{\partial \rho(\mathbf{r})} - \mu = 0 \quad (2.49)$$

Using equation 2.41, we can obtain the expression in terms of external potential:

$$\mu = \frac{\partial E[\rho(\mathbf{r})]}{\partial \rho(\mathbf{r})} = \hat{V}_{ext}(\mathbf{r}) + \frac{\partial F_{HK}\rho(\mathbf{r})}{\partial \rho(\mathbf{r})} \quad (2.50)$$

Lagrange multiplier (μ) has a physical meaning, which is called the chemical potential. For detail review, see the Parr & Yang (1989) chapters 4 and 5. These theorems tell us that a unique energy functional can construct a many-body interacting system, that depends only on the electron density. Further, by minimizing this functional with respect to the density, we can obtain

the ground state density and energy of our system. However, these theorems do not provide any mathematical expression of universal functional F_{HK} in terms of density with significant (satisfactory) accuracy. Therefore, to solve the Schrödinger equation is still difficult. The Kohn-Sham equations provide the framework for finding the exact density and energy of the ground state of a many-body electron problem using standard independent-particle methods. These methods have proven to be very successful in many problems and are by far the most widely used approach for quantitative calculations on realistic problems. In 1965, Kohn and Sham [104] proposed a way to approximate exchange and correlation effects, which enables to represent the exact ground state density of an interacting system to a ground state density of a fictitious system of non-interacting particles. This method provides a set of independent particle equations that can be solved numerically.

2.10.2.1 Kohn-Sham equations

In 1965, Kohn and Sham [104] proposed that the exact ground state density of an interacting many-body system can be represented with ground state density of an auxiliary system of independent-particles as shown in Figure 2.4. The auxiliary Hamiltonian (\hat{H}_{KS}) consists of single particle energy term and an effective single particle local potential $V_{eff}(\mathbf{r})$. The form of equations for non-interacting particles, which are known as the Kohn-Sham equations:

$$\hat{H}_{KS}\phi_i = \left[-\frac{1}{2}\nabla_i^2 + \hat{V}_{eff}(\mathbf{r}) \right] \phi_i^{KS}(\mathbf{r}) = \epsilon_i \phi_i(\mathbf{r})^{KS} \quad (2.51)$$

where the effective potential is:

$$\begin{aligned} \hat{V}_{eff}(\mathbf{r}) &= \hat{V}_{ext}(\mathbf{r}) + \hat{V}_H(\mathbf{r}) + \hat{V}_{xc}(\mathbf{r}) \\ &= \sum_{\alpha} \frac{-Z_{\alpha}}{|\mathbf{R}_{\alpha} - \mathbf{r}|} + \frac{\rho(\mathbf{r}')}{|\mathbf{r} - \mathbf{r}'|} d\mathbf{r}' + \frac{\partial E_{xc}[\rho(\mathbf{r})]}{\partial \rho(\mathbf{r})} \end{aligned} \quad (2.52)$$

here, \hat{V}_H is the Coulomb potential (Hartree term) from all electrons and \hat{V}_{xc} is the exchange correlation potential that is defined as functional derivative of exchange correlation energy (E_{xc}). This potential consists of all many-body effects, which are not accounted in the classical Hartree interaction term. Expression of equation 2.51 is quite similar to the Hartree-Fock method, but in more simplified form. The Kohn-Sham operator rests upon \mathbf{r} , and not on the index of the electron. It is same for all electrons. The Kohn-Sham orbitals $\phi_i(\mathbf{r})^{KS}$ are easily obtained from equation 2.51, that are further used to compute the total density:

$$\rho(\mathbf{r}) = \sum_{i=1}^N |\phi_i^{KS}(\mathbf{r})|^2 \quad (2.53)$$

Subsequently, the improved potential $\hat{V}_{eff}(\mathbf{r})$ can be determined by knowing the electron den-

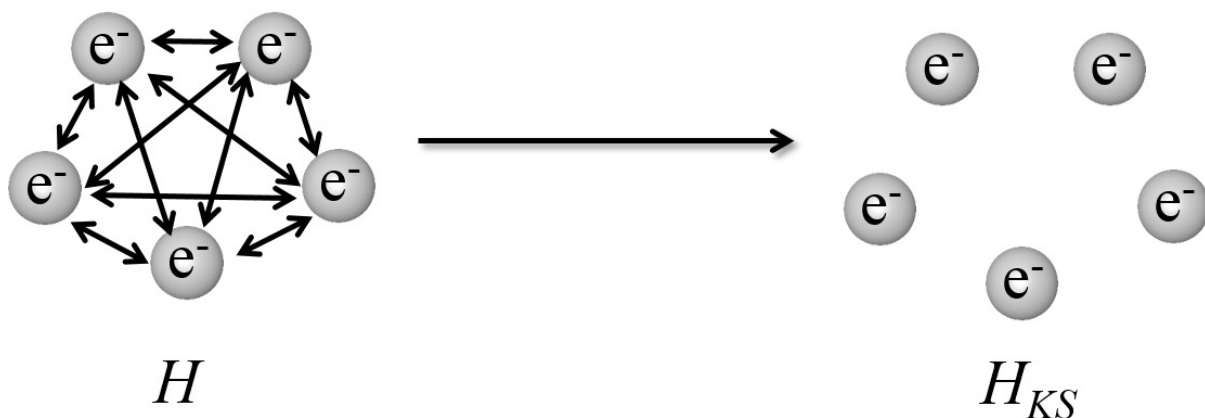


Figure 2.4: Illustration of interacting and non-interacting many-electron systems having same ground state electron density.

sity following the self-consistent cycles. The initial electron density can be considered as a superposition of atomic densities. To incorporate the spin-related effects, the total density is defined as the sum of the spin-up and spin-down densities $\rho(\mathbf{r}) = \rho_{\uparrow}(\mathbf{r}) + \rho_{\downarrow}(\mathbf{r})$. Density is also used to evaluate the total energy as follow:

$$E[\rho] = T_0[\rho] + \int [\hat{V}_{ext}(\mathbf{r}) + \hat{V}_H(\mathbf{r})]\rho(\mathbf{r})d\mathbf{r} + E_{xc}[\rho] \quad (2.54)$$

The kinetic energy $T_0[\rho]$ is obtained from the corresponding orbitals instead of density.

$$T_0[\rho] = \frac{1}{2} \sum_{i=1}^N \langle \phi_i^{KS} | \nabla_i^2 | \phi_i^{KS} \rangle \quad (2.55)$$

and the remaining of the energy as:

$$V_{eff}[\rho] = \int \hat{V}_{eff}(\mathbf{r})\rho(\mathbf{r})d\mathbf{r} \quad (2.56)$$

$E_{xc}[\rho]$ contains all the energy contributions, which are not taken into account in rest of the terms:

1. Electron exchange
2. Electron correlation
3. An amount of the kinetic energy that is required to add in $T_0[\rho]$ to get true kinetic energy of a real system $T_e[\rho]$
4. Correction for self-interaction included in the classical coulomb potential

E_{xc} is vital to understand the chemical bonds, which determines the accuracy of methods using Khon-Sham equations.

2.10.3 Exchange and correlation energy

Since the analytical form of exchange-correlation energy is not known, various approximations are proposed for the exchange-correlation (xc) functional to find the desired balance between accuracy and computational cost. These approximations can be categorized into two main parts: (1) local and semi-local approximations viz. local density approximation (LDA) [118], generalized gradient approximation (GGA) and meta-GGA, (2) non-local approximations, i.e. hybrid functionals and random phase approximation. In the limit of homogeneous electron gas, the exchange-correlation energy becomes a local functional. Hence, the first simplest exchange correlation functional of the Kohn-Sham method is the local density approximation (LDA). Here, it is assumed that density varies slowly with position. As a result, the exchange-correlation energy per electron depends solely on electron density only, where its derivatives are not taken into consideration. To include spin polarization in the system, it is essential to consider both spin densities: spin up $\rho_{\uparrow}(\mathbf{r})$ and spin down $\rho_{\downarrow}(\mathbf{r})$, we call it local spin density approximation (LSDA). The exchange-correlation energy comprises of two parts: the exchange energy, and the correlation energy.

$$E_{xc}[\rho] = E_x[\rho] + E_c[\rho] \quad (2.57)$$

Exchange energy: This term occurs due to antisymmetric nature of electronic wavefunction. According to the Pauli's exclusion principle, two electrons cannot reside in the same state, as a result, electrons having same spin repel each other. Consequently, a spatial separation is introduced between electrons, which leads to the reduction in Coulomb energy. This reduction in energy is called the exchange energy. In the technical terms, it is energy difference between the Hartree and Hartree-Fock energy. The exchange energy in LDA is approximated within the homogeneous electron gas, where $\alpha = \frac{2}{3}$ [119].

$$E_x[\rho] = -\frac{9}{4}\alpha \left(\frac{3}{4\pi}\right)^{\frac{1}{3}} \int [\rho_{\uparrow}^{\frac{4}{3}}(\mathbf{r}) + \rho_{\downarrow}^{\frac{4}{3}}(\mathbf{r})] d\mathbf{r} \quad (2.58)$$

Correlation energy: Electrons being negatively charged avoid each others, which is the origin of correlation energy. In this part significant portion is added from the kinetic energy difference ($T_e - T_0$) between the non-interacting and the interacting systems. It can be defined as the energy difference between exact energy of the system and the Hartree-Fock energy:

$$E_c = E_{exact} - E_{HF} \quad (2.59)$$

The correlation energy is given by:

$$E_c[\rho] = \int \rho(\mathbf{r}) \epsilon_c[\rho_\uparrow(\mathbf{r})\rho_\downarrow(\mathbf{r})] d\mathbf{r} \quad (2.60)$$

where $\epsilon_c[\rho_\uparrow(\mathbf{r})\rho_\downarrow(\mathbf{r})]$ is the correlation energy per electron of a homogeneous electron gas with density $\rho(\mathbf{r})$, and its exact form is not known analytically. The constant efforts have devoted to improve it on the basis of quantum Monte Carlo simulations [120], and fitted to analytical expansion. LDA works well for system close to homogeneous gas such as metals, whereas fails for inhomogeneous ones i.e. atoms, molecules etc.. Using this, the atomic structures, elastic and vibrational properties can be described for a wide range of systems. However, it is unsuccessful to predict the accurate energetics of chemical bonds, binding energy, heats of reaction and activation energy barriers.

In further improvement of exchange-correlation energy, both the electronic density and the gradient of density at a given point have been taken into account. This semi-local approximation is known as the generalized gradient approximation (GGA) [121, 122]. Here, the exchange-correlation energy is expressed as a function of both:

$$E_{xc}^{GGA}[\rho(\mathbf{r})] = \int \rho(\mathbf{r}) \epsilon_{xc}^{GGA}(\rho(\mathbf{r}), |\nabla\rho(\mathbf{r})|) d\mathbf{r} \quad (2.61)$$

This improves the accuracy of the calculations such as to calculate the bond lengths and lattice constants of the systems. However, It fails to predict the properties of large atoms (5d transition elements). In the next step of development is to include the fourth-order gradient expansion of the exchange-correlation energy. This can be achieved by incorporating the additional semi-local information via the Laplacian of the electronic density. This improvement is called as meta-GGA. The local and semi-local functional underestimate the band gap results, since these approximations unable to completely resolve the self-interaction error in the Hartree term. There exists more advanced functional, where the improved accuracy of the calculations comes at the cost of computational time. To construct the hybrid functionals, some fraction of exact exchange from Hartree-Fock theory is combined with the exchange-correlation energy that comes from LDA/GGA [118]. This approach helps to correct the self-interaction error. The exchange-correlation energy can be written as:

$$E_{xc}^{hyb} = \alpha E_x^{HF} + (1 - \alpha) E_x^{DFT} + E_c^{DFT} \quad (2.62)$$

where α denotes the fraction of the exact exchange that comes from Hartree-Fock theory and the rest from a local/semi-local functional. In hybrid functional, the Coulomb interaction term

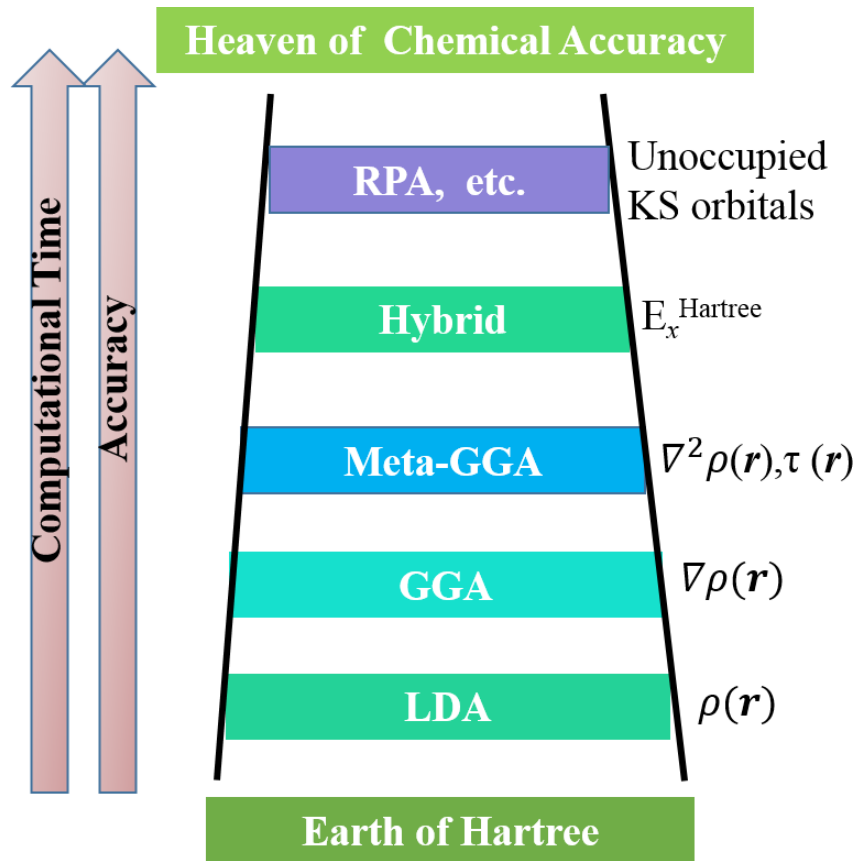


Figure 2.5: Schematic diagram of Jacob's ladder of density functional theory with different approximations for exchange-correlation energy.

involves the short-range and long-range parts, which demands more computational resources. To conquer this problem, Heyd, Scuseria, and Ernserhof (HSE) [123] have proposed that the exact exchange term can be determined for short-range interactions (where they are most difficult) and come to the local/semi-local functional for longer ranges. A screening mechanism is introduced to speed up the calculation of the Hartree-Fock exchange.

$$\frac{1}{r} = \underbrace{\frac{1 - \text{erf}(\omega r)}{r}}_{\text{SR}} + \underbrace{\frac{\text{erf}(\omega r)}{r}}_{\text{LR}} \quad (2.63)$$

where screening parameter ω represents the range of the interactions and the error function is:

$$\text{erf}(\omega r) = \frac{2}{\sqrt{\pi}} \int_0^{\omega r} e^{-x^2} dx \quad (2.64)$$

In case of PBE0 functional [124], $\omega = 0$, where the long-range (LR) term vanishes and the short-range (SR) term is exactly the full Coulomb potential. The HSE functional becomes the purely (semi)local approximation at very high values of ω . In HSE06, the PBE [121] correlation is considered and the exchange-correlation energy can be expressed by:

$$E_{xc}^{HSE} = \alpha E_x^{HF,SR}(\omega) + (1 - \alpha) E_x^{PBE,SR}(\omega) + E_x^{PBE,LR}(\omega) + E_c^{PBE} \quad (2.65)$$

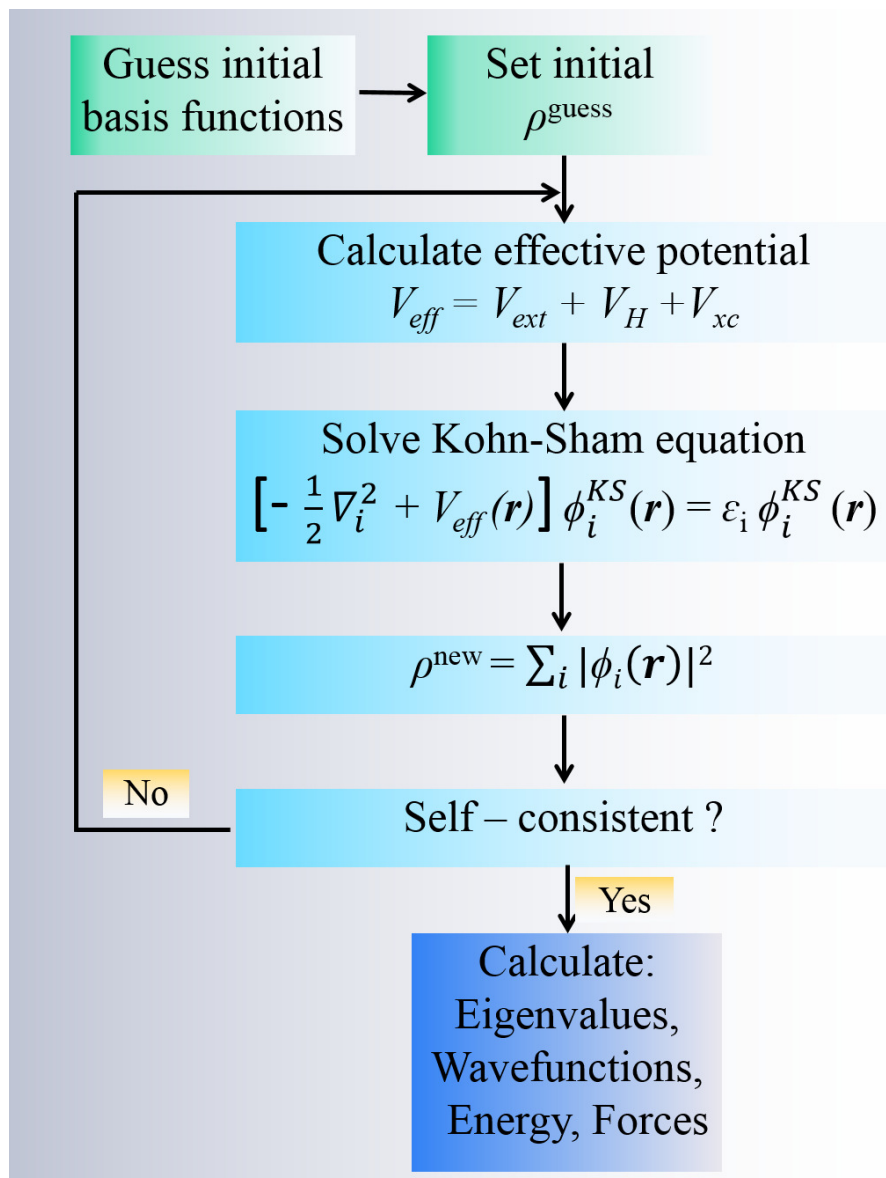


Figure 2.6: Schematic illustration of self-consistent loop for the solution of the Kohn-Sham equations.

In case of HSE calculation, $\alpha = \frac{1}{4}$ and $\omega = 0.11 \text{ bohr}^{-1}$ have been suggested as the good choice to obtain the band gaps for small band gap and metallic systems. We have used these values for the calculations. The different approximations to the exchange-correlation energy are shown in terms of accuracy and computational time in Figure 2.5. In the present thesis work, we have used the semi-local (Perdew-Burke-Ernzerhof (PBE) version of GGA [121]) and non-local (hybrid, PBE0, GW [125]) functionals to perform the calculations. The single particle-like Kohn-Sham equations are solved self-consistently by evaluating the effective potential $V_{eff}(\mathbf{r})$ starting from the initially guessed electron density $\rho(\mathbf{r})$ as an input. The scheme to solve the Kohn-Sham equations is summarized in Figure 2.6. There are many codes available to perform the DFT calculations. In present work, FHI-aims [126] (Fritz Haber Institute

ab initio molecular simulations) and VASP (Vienna *Ab initio* Simulation Package) codes are employed [127, 128, 129]. Particularly, FHI-aims code is efficient for molecular systems and nanostructures with high numerical accuracy.

2.11 Basis set

As discussed earlier, we enable to map some observables of the many-body problem to correspond observables in an effective single-particle problem. However, there is the question of handling of an infinite number of non-interacting electrons moving in the static potential of an infinite number of nuclei. Therefore, a wavefunction must be calculated for each of the infinite number of electrons in the system, and, since each electronic wavefunction extends over the entire solid, an infinite basis set is required to expand each wavefunction. Both these problems can be taken care of by performing calculations on periodic systems and applying Bloch's theorem to the electronic wavefunction. This section briefly describes (i) pseudopotentials in combination with the plane wave basis set and (ii) the projector augmented wave (PAW) method. Three main categories of methods based on the basis sets are:

1. Localized Atomic like orbitals

- Semi-empirical Tight Binding Method
- Linear Combination of Atomic Orbital [LCAO]
- Linear Combination of Gaussian Orbital [LCGO]
- Numerical Approach [Order-N methods]

2. Plane Waves and Grids

- Pseudopotential Methods
- Orthogonalized Plane Wave Method (OPW)
- Projector Augmented Wave (PAW)

3. Augmentation of Muffin-Tin or Atomic Sphere Method

- Augmented Plane Wave Method
- Green's Function Approach or Multiple Scattering Approach, e.g. KKR approach

- Linearized Method; LMTO, LAPW, ASW

In practice, to solve the many-body problem, one needs to select one-electron orbitals (basis functions) to form the electronic wavefunctions using linear combination of these functions. The efficiency and accuracy of a method highly depend on the choice of basis functions. Computationally, the plane wave based approach is much more efficient to calculate for periodic systems.

2.11.1 The Plane wave basis set

Bloch theorem enables us to solve the Schrödinger equation for the periodic systems. The most common approach is to use the plane wave based basis set for periodic systems. The plane wave function based on Bloch theorem can be written as follows:

$$\Psi_k(r) = u_k(\mathbf{r})e^{i\mathbf{k}\cdot\mathbf{r}} \quad (2.66)$$

$$\rho(\mathbf{r}) \approx \sum_k |\Psi_k(\mathbf{r})|^2 \quad (2.67)$$

where $u_k(r)$ represents a basis set function having the same periodicity as the supercell.

$$u_k(\mathbf{r} + n_1\mathbf{a}_1 + n_2\mathbf{a}_2 + n_3\mathbf{a}_3) = u_k(\mathbf{r}) \quad (2.68)$$

here, n_1, n_2, n_3 can be any integers. Thus, using periodicity, it is possible to solve the Kohn-Sham equations for each value of \mathbf{k} independently. The space of \mathbf{k} vector is known as the reciprocal space (also called momentum space or \mathbf{k} -space). The values of \mathbf{k} are set to be within primitive cell of the reciprocal lattice, which is named as first Brillouin zone (BZ). BZ can be divided for the \mathbf{k} -mesh in different ways. In this thesis, Monkhorst-Pack grid is used for defining the \mathbf{k} -point grid in the BZ [130]. The reciprocal of a reciprocal lattice vector is the real space lattice vector. Kohn-Sham orbitals are expanded in the plane wave basis set as follow:

$$u_{nk}(\mathbf{r}) = \sum_{\mathbf{G}} C_{nk,\mathbf{G}} e^{i\mathbf{G}\cdot\mathbf{r}} \quad (2.69)$$

where \mathbf{G} represents the reciprocal lattice vectors of the system. n and k denote the band index and wavevector in the first Brillouin zone, respectively. The electronic wavefunctions can be represented as sum of plane waves:

$$\phi_{nk}(\mathbf{r}) = \sum_{\mathbf{G}} C_{nk,\mathbf{G}} e^{i(\mathbf{k}+\mathbf{G})\cdot\mathbf{r}} \quad (2.70)$$

where, $C_{nk,G}$ is the expansion coefficient, which decreases as $|\mathbf{G}|^2$ increases. Therefore, the infinite series in equation 2.70 can be truncated to include the plane waves up to the cutoff energy (E_{cut}) according to equations 2.71. In practice, one needs to perform the convergence tests in order to find extent of E_{cut} that is sufficient to compute the ground state energy and density with desired accuracy and efficiency. The disadvantage of using plane waves is that it requires rapid oscillation of the wave function near the core region. One can choose different types of basis set to expand the u_{nk} function.

$$\frac{|\mathbf{k} + \mathbf{G}|^2}{2} \leq E_{cut} \quad (2.71)$$

The number of plane waves (N_{PW}) needed for the expansion of a wavefunction is largely depend on E_{cut} :

$$N_{PW} = \frac{V E_{cut}^{\frac{3}{2}}}{6\pi^2} \quad (2.72)$$

where V denotes the volume of the real space lattice.

2.11.2 Numeric atom-centered basis functions

In FHI-aims [126], the form of basis functions are considered to be numeric atom-centered orbitals (NAOs):

$$\phi_i(\mathbf{r}) = \frac{u_i(r)}{r} Y_{lm} \quad (2.73)$$

where the radial shape $u_i(r)$ is numerically tabulated part, due to this the basis functions become very flexible. The numerical solutions of Schrödinger-like radial equations can be determined as follow:

$$\left[-\frac{1}{2} \frac{d^2}{dr^2} + \frac{l(l+1)}{r^2} + v_i(r) + v_{cut}(r) \right] u_i(r) = \epsilon_i u_i(r) \quad (2.74)$$

where potential $v_i(r)$ determines the main behavior of $u_i(r)$ (such as free-atom like, Hydrogen-like, free-ions, Gaussians-like), and a confining potential $v_{cut}(r)$ ensures the smooth decay of each radial function, which should be zero outside a cutoff radius. This helps to prevent slowing down of the calculations due to irrelevant tails of the function, and allows to construct the element-dependent basis sets, which are tightly packed while retaining transferability. Each radial function $u_i(r)$ is strictly localized inside the given radius. Y_{lm} is the angular momentum part. To compose the minimal basis set in FHI-aims, the numerical solutions of a Schrödinger-like equation for spherically symmetric free atoms are used. These minimal basis sets consider

the wavefunction oscillations around the nucleus, thereby they facilitate the all-electron treatment greatly. It is preferable for bigger basis sets to consist of all smaller ones to guarantee accurate convergence. Bigger basis sets in FHI-aims are constructed by starting from smaller basis sets and expanding these by addition of basis functions from a large pool of radial functions.

2.11.3 Plane wave pseudopotential method

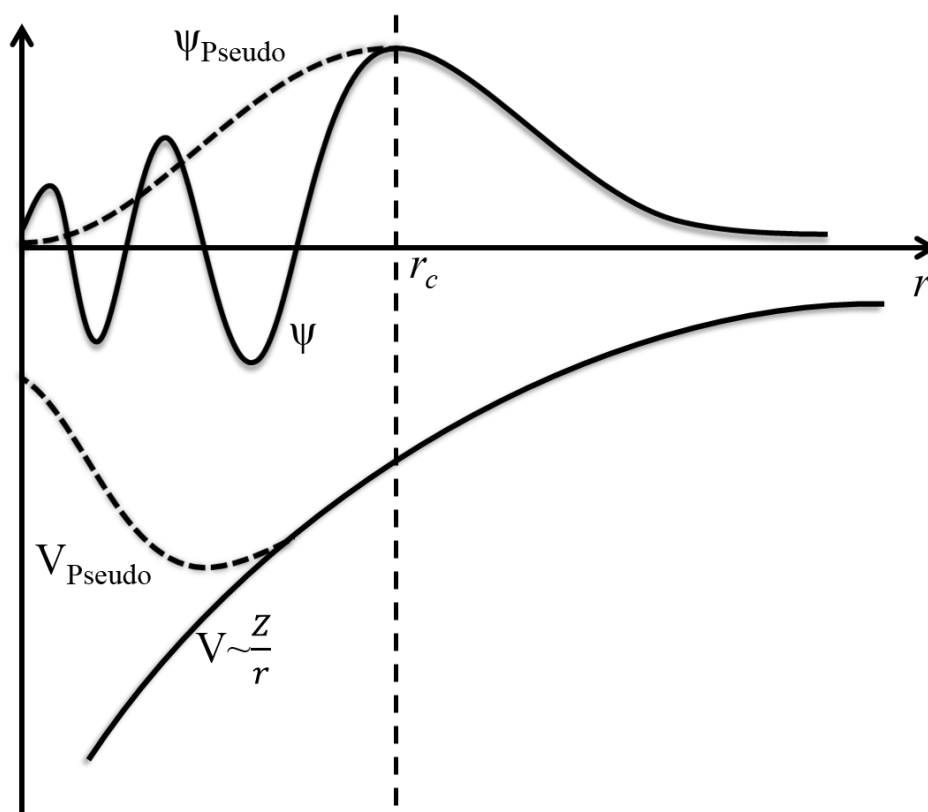


Figure 2.7: Schematic diagram of an all-electron wavefunction (solid line) and the corresponding pseudo wavefunction (dashed line) and together with the respective pseudopotential and external Coulomb potential [5].

In spite of the tremendous progress that have been made for solving the Kohn-Sham equations, obtaining a solution still remains computationally very challenging, since the wavefunction requires to be known for each of the N electrons. Moreover, the valence wavefunctions of the core region of atoms oscillate rapidly due to highly localized nature of the core states. This implies that the kinetic energy corresponding to these valence states are very high. Therefore, the large number of plane waves and a large E_{cut} are essential for good representation of these

fast oscillations, which make calculations very expensive. The computational cost can be alleviated significantly by using the pseudopotential approximation. The underlying fact is that the most of the physical properties of solids are mainly ascribed to the valence electrons. Under this assumption, the core electrons are not considered explicitly in the calculation. The effect of the strong core potential is approximated by the pseudopotential (V_{Pseudo}). Here, the electrons are separated into core and valence electrons by defining a core radius \mathbf{r}_c as shown in Figure 2.7. The extent of core radius determines the hardness and softness of the pseudopotential. Small \mathbf{r}_c leads to hard pseudopotential and large core radius results to ultrasoft potentials. Here, the valence wavefunctions in the core region are also substituted by a set of pseudo wavefunctions (Ψ_{Pseudo}) and V_{Pseudo} works on Ψ_{Pseudo} rather than the true all-electron wavefunctions [122, 118, 131]. The Ψ_{Pseudo} and all-electron wavefunction become identical beyond the cutoff radius \mathbf{r}_c . A further advantage of pseudopotentials is that relativistic effects can be implemented easily into the potential while treating the valence electrons non-relativistically. There are various types of pseudopotentials used in DFT calculations, which are discussed below.

2.11.4 Norm-conserving pseudopotential

In norm-conserving pseudopotential, the pseudopotential (and wavefunctions) are formed to be equal to the actual potential (and wavefunctions) outside the core radius. Inside \mathbf{r}_c , the pseudo wavefunctions are not same as the true wavefunctions, whereas the norm is restricted to be equal.

$$\int_0^{\mathbf{r}_c} \mathbf{r}^2 \Psi^{PS*}(r) \Psi^{PS}(r) d\mathbf{r} = \int_0^{\mathbf{r}_c} \mathbf{r}^2 \Psi^*(\mathbf{r}) \Psi(\mathbf{r}) d\mathbf{r} \quad (2.75)$$

The wavefunctions and eigenvalues differ for different angular momenta, l , which implies that the pseudopotential has to be l dependent. This potential is often called semi-local. Particularly, the norm-conserving condition ensures the transferability of the pseudopotential, which enables to describe the scattering properties of an ion in different chemical environments [132].

2.11.5 Vanderbilt Ultrasoft pseudopotential

In Ultrasoft pseudopotentials the norm-conserving constraint has been relaxed to reduce the basis-set size. In this scheme, the pseudo wavefunctions should be similar to the all-electron wavefunctions beyond the cutoff radius (\mathbf{r}_c). However, inside \mathbf{r}_c , they are considered as soft as possible, thereby the constraint of norm-conservation is eradicated to accomplish this. In-

stead of representing the full valence wavefunction by plane waves, only a small portion of the wavefunction is calculated within this pseudopotential scheme. This substantially reduces the cutoff energy of plane wave. The extent of cutoff radius can be increased without sacrificing the transferability of the ultrasoft pseudopotential. An intriguing feature of this pseudopotential is that in the self-consistent cycles, the contribution of the augmenting charge inside the sphere ($< \mathbf{r}_c$) evolves along with the wavefunctions. This charge contributes to the potential used in the Kohn-Sham equations. The evolution of the augmenting charge during the calculation and its contribution to the potential allow to use relatively large values of \mathbf{r}_c in the Vanderbilt construction [133]. This results in very soft pseudopotentials, without loosing the accuracy of the calculation.

2.11.6 Projector augmented-wave method (PAW)

Projector augmented wave (PAW) method has been developed by Peter Böchl in 1994, which combines the pseudopotential and linear augmented plane wave methods into a unified description [134]. Since the valence wavefunctions oscillate rapidly near the nucleus to accomplish the requirement of being orthogonal to core states, many Fourier components are needed to construct the wavefunctions accurately. Moreover, the orthogonal condition for wavefunctions assures that Pauli principle is being satisfied to have the unique and independent wavefunctions. The PAW method replaces the fast oscillating wavefunctions with smooth wavefunctions, that helps in reducing the computational workload. In this method, the wavefunction is divided into two portions as the partial wave in a sphere around the atom known as the augmentation region and outside the sphere as the interstitial region. In PAW potentials, the \mathbf{r}_c is smaller, hence it requires higher E_{cut} energy and larger basis sets, which increase the computational demand, but provide the better description of the many-body system as they reproduce the nodes in the core area. Let us suppose the Hilbert space of all wavefunctions, that are orthogonal to the core states. Since it is tough to treat the core region numerically due to rapid oscillations, we can assume the pseudo-Hilbert space that includes functions without any rapid variations. The linear transformation operator (T) links both the spaces. Using this operator, the true wavefunction ($|\Psi\rangle$) can be mapped to pseudo wavefunction ($|\tilde{\Psi}\rangle$):

$$|\Psi\rangle = T|\tilde{\Psi}\rangle \quad (2.76)$$

We can write the operator T in the form:

$$T = 1 + T_0 \quad (2.77)$$

where T_0 works in the augmentation region around the atom. Let's consider a set of functions $|\phi_i\rangle$ and $|\tilde{\phi}_i\rangle$ to represent the all-electron partial waves and pseudo partial waves, respectively. Since both the wavefunctions are complete within the augmentation region, we can define the operator T as follow:

$$|\phi_i\rangle = (1 + T_0)|\tilde{\phi}_i\rangle \quad (2.78)$$

From equation 2.78, we can deduce that outside the augmentation region both all-electron and pseudo partial waves will be equal, as T_0 acts only within the augmentation region. The set of pseudo partial waves is complete in the augmentation region, therefore, each pseudo wavefunction ($\tilde{\Psi}$) can be written in terms of the pseudo partial waves ($\tilde{\phi}_i$):

$$|\tilde{\Psi}\rangle = \sum_i c_i |\tilde{\phi}_i\rangle \quad (2.79)$$

where c_i 's are the expansion coefficients. This pseudo wavefunction is then mapped by T into:

$$T|\tilde{\Psi}\rangle = |\Psi\rangle = \sum_i c_i |\phi_i\rangle \quad (2.80)$$

by subtracting the equation 2.79 from equation 2.80, we can obtain the all-electron wavefunction:

$$|\Psi\rangle = |\tilde{\Psi}\rangle = \sum_i c_i (|\phi_i\rangle - |\tilde{\phi}_i\rangle) \quad (2.81)$$

Due to linear operator T , the coefficients c_i should be linear functionals of $|\tilde{\Psi}\rangle$. Projector functions probe the character of the wavefunction viz. s, p, and d-type. The general form of a linear function can be expressed as the scalar product with some constant function. This function is represented by ($\langle\tilde{p}_i|$) that refers as a projector function. Thus, we can write:

$$c_i = \langle\tilde{p}_i|\tilde{\Psi}\rangle \quad (2.82)$$

The pseudo partial waves form a complete basis, hence:

$$c_i = \langle\tilde{p}_i|\tilde{\phi}_j\rangle = \delta_{ij} \quad (2.83)$$

Now, the projection operator T can be written as:

$$T = 1 + \sum_i [|\phi_i\rangle - |\tilde{\phi}_i\rangle] \langle\tilde{p}_i| \quad (2.84)$$

The expectation value of any local operator O can be defined in terms of pseudo functions $\langle \tilde{\Phi}_i | \tilde{O} | \tilde{\Phi}_i \rangle$, where \tilde{O} is pseudo operator:

$$\tilde{O} = T^\dagger O T = O + \sum_{ij} |\tilde{p}_i\rangle [\langle \phi_i | O | \phi_j \rangle - \langle \tilde{\phi}_i | O | \tilde{\phi}_j \rangle] \langle \tilde{p}_j| \quad (2.85)$$

Employing these approximations, the numerical solution of the many-body problem becomes doable. The smooth pseudo wavefunctions can be expressed with a small set of plane waves. Further, the integrations for rapidly varying partial waves can be performed on a radial grid as these functions are the product of a radial function and a spherical harmonic. In this thesis, electronic structure calculations have been performed using the PAW method and these calculations are performed using Vienna *Ab initio* Simulation Package (VASP) [127, 128, 129].

2.12 GW method

Density functional theory (DFT) is a powerful tool to predict the ground state properties of the existing and new materials. However, it fails to describe the excited state properties of the many-body system. Therefore, to investigate the excited state properties of the system, one needs to go beyond the single particle approach. Usually, the electronic properties are examined by the photoemission and inverse photoemission spectroscopies, which include the addition/removal of an electron to/from the system. There is no direct theorem to link the Kohn-Sham orbitals' energies to the energies of electron addition and removal. In the process of photoemission or inverse photoemission, electrons in excited states are strongly interacting particles. The single-particle Green's function describes the propagation of a removal or an addition of an electron in the system. In many-body perturbation theory, the Green's function is described by the self-energy which is complex, non-local and energy dependent. The real part of the self-energy describes the energy change of the electron/hole moving through the system from one point to another and the imaginary part of the self-energy describes the lifetime of the particle. The solution of the quasiparticle equation leads to the eigenfunctions and the eigenvalues of the single-particle excitations [125, 135, 136]. The following equation describes the Quasiparticle behavior:

$$\left(-\frac{\nabla^2}{2} + V_{ext} + V_H\right)\Psi_{QP}(r) + \int dr' \Sigma_{xc}(r, r'; \epsilon_{QP})\Psi_{QP}(r') = \epsilon_{QP}\Psi_{QP}(r) \quad (2.86)$$

In GW method the reference Hamiltonian is most commonly used Kohn-Sham orbitals as the

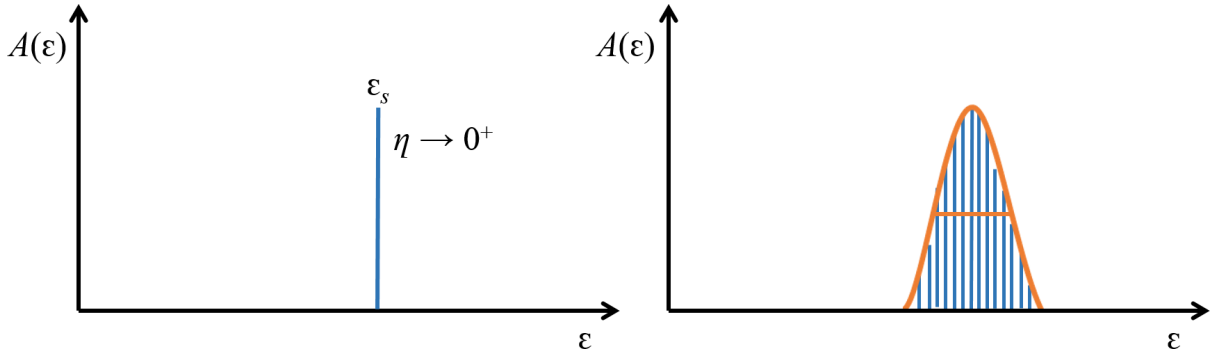


Figure 2.8: Representation of spectral function for non-interacting single particle excitation and interacting many particles excitation.

starting input. The Lehmann (spectral) representation of the green function (G):

$$G(r, r'; \epsilon) = \lim_{\eta \rightarrow 0^+} \sum_s \frac{\Psi_s(r) \Psi_s^*(r')}{\epsilon - \epsilon_s + i\eta \text{sgn}(\epsilon_s - \mu)} \quad (2.87)$$

where ϵ_s is the charged excitation energies of the system having N -electron.

$$\epsilon_s = \begin{cases} E^{N+1} - E^N & \text{if } \epsilon_s > \mu \\ E^N - E^{N-1} & \text{if } \epsilon_s < \mu \end{cases}$$

The imaginary part of the Green's function defines the spectral function, which describes all the probabilities to reach the final state.

$$A(\epsilon) = \frac{-1}{\pi} \int dr \lim_{r' \rightarrow r} \text{Im} G(r, r'; \epsilon) \quad (2.88)$$

$$A(\epsilon) = \text{Im} G_k(\epsilon) \approx \frac{Z_k}{\epsilon - (\epsilon_k + i\Gamma_k)} \quad (2.89)$$

Electron's lifetime is infinite during the process of electronic excitation as it does not decay. Therefore, we observe a delta function that corresponds to each transition. However, contrary to this, in experimental observations the peak is observed with certain broadening, as shown in Figure 2.8. This can be explained as, many electrons are excited rather than a single electron in the process and each excitation contributes a delta function with closely spaced energetics. This gives rise to a peak that has finite width. This peak seems a single particle-like and we called it quasiparticle peak as shown in the right panel of Figure 2.8. Hence, we can attribute the three fundamental factors from the excited spectrum; we called quasiparticle energy (ϵ_k) to the peak position, inverse of the life-time (Γ_k) is defined by width of peak and Z_k is quasiparticle weight. The another perspective to see the quasiparticle is illustrated in Figure 2.9.

When we bring the sample in light and kick out an electron from it, then this electron creates a hole behind it. Over the time when system evolves, the negative charge will screen out the positive charge. Hence, the combination of hole and its surrounding charge form an entity, that we identify as a quasiparticle (QP) and now this whole entity will move through the system. The QP weakly interacts with the rest of system via screened Coulomb potential (W). QP energies are evaluated by Green's function methods within the many-body perturbation theory [17]. Where the concepts of polarization and screening are described. In particular, the polarization

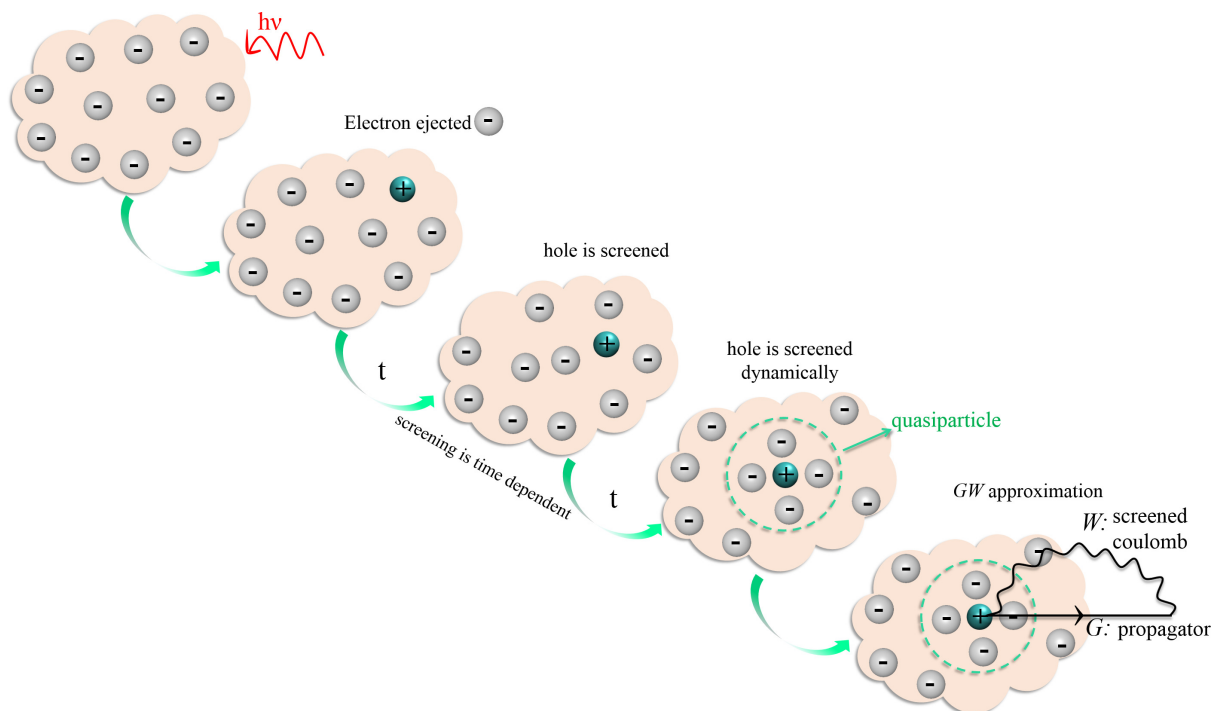


Figure 2.9: The representation of excitation peaks for the noninteracting particle and the quasiparticles.

will be translated to polarization response function and screening will be represented by the dielectric function. The exact Green's function contains two parts: the interacting and non-interacting Green's function. The non-interacting function is evaluated from DFT. Then the Dyson equation relates self-energy with non-interacting function thereby achieving full interacting function. The relation between the interacting and the non-interacting Green's function is given by Dyson's equation as follow:

$$G^{-1} = G_0^{-1} - \Sigma \quad (2.90)$$

The Dyson equation is used to describe all the scattering processes during the excitations and the self energy defines the sum of all possible single scattering processes. If an electron is removed or added to the system, the rest of the electrons try to adjust themselves to the new

state, where the self energy plays the crucial role. Moving electron feels a repulsion from the other electrons which in turn polarizes and changes the potential. During the excitation process the infinite number of scattering occurs in the system and it becomes arduous to determine the self energy. In 1965 Hedin proposed a set of equations to perform GW , whose self-consistent solution can provide the exact self-energy of the interacting problem. Although, the exact solution of Hedin's equations are not tractable even for the simplest homogeneous electron gas system. However, by knowing the exact theory we can make the systematic improvable approximations. The most simplest one is the GW approximation.

Exact solution-Hedin's Equations:

$$P(12) = -i \int d(34)G(13)G(41^+)\Gamma(342) \quad (2.91)$$

$$\Sigma(12) = i \int d(34)G(14^+)W(13)\Gamma(423) \quad (2.92)$$

$$\Gamma(123) = \delta(12)\delta(13) + \int d(4567) \frac{\delta\Sigma(12)}{\delta G(45)} G(46)G(75)\Gamma(673) \quad (2.93)$$

$$W(123) = v(12) + \int d(34)W(13)P(34)v(42) \quad (2.94)$$

Dyson equation to relate the Green's function (G) and the self-energy (Σ_{xc}) as given:

$$G(12) = G_{KS}(12) + \int d(34)G_{KS}(13)\Sigma(34)G(42) \quad (2.95)$$

where P , G , Σ and Γ are the polarizability, Green's function propagator, self energy and vertex function. The vertex function which includes the derivative of self-energy w.r.t green function, makes the solution prohibitively expensive and, also demands huge memory. Therefore, in the GW approximation, the vertex corrections are excluded to make the equations solvable.

$$\Gamma(123) = \delta(12)\delta(13) \quad (2.96)$$

$$\begin{aligned} \Sigma &= iGW = \Sigma_x + \Sigma_c \\ &= iGv + iG(W - v) \end{aligned} \quad (2.97)$$

The irreducible polarizability is derived using random phase approximation (RPA):

$$P(r, r', \epsilon) = \frac{i}{2\pi} \int d\epsilon' e^{i\omega\eta} G(r, r', \epsilon + \epsilon') G(r, r', \epsilon) \quad (2.98)$$

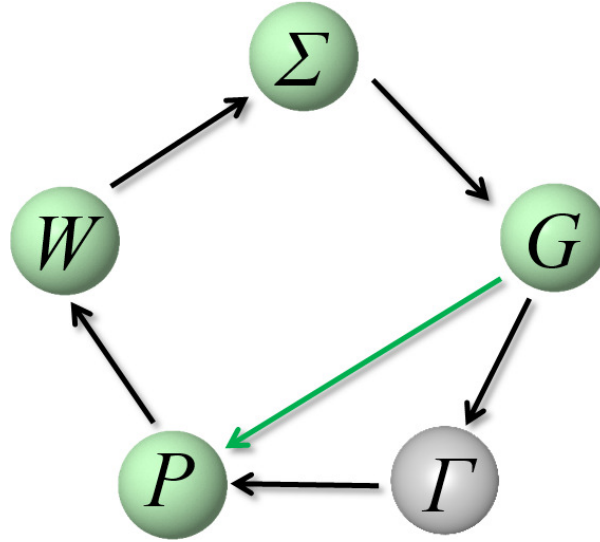


Figure 2.10: The Hedin's pentagon. The vertex function (Γ) is ignored in GW approximation.

The dielectric constant is obtained by:

$$\epsilon(r, r', \epsilon) = \delta(r - r') - \int dr'' \frac{P(r, r'', t)}{|r'' - r'|} \quad (2.99)$$

If we know the dielectric function (ϵ) then we can determine the W . This describes how the quasiparticle interact with rest of the system via screened coulomb interaction. The screened coulomb interaction:

$$W(r, r', t) = \int dr'' \frac{\epsilon^{-1}(r, r'', t)}{|r'' - r'|} \quad (2.100)$$

In GW approximation the self-energy can be obtained as:

$$\Sigma^{GW}(r, r', \epsilon) = -\frac{i}{2\pi} \int d\epsilon' e^{i\epsilon'\eta} G(r, r', \epsilon + \epsilon') W(r, r', \epsilon) \quad (2.101)$$

Here, Green's function $G(r, r', \epsilon)$ is propagator to describe the motion of quasiparticle, and $W(r, r', \epsilon)$ is the screened interaction. Self-energy is the energy that the quasiparticle feels due to its own presence. That is energy contribution induced by the presence of the particle itself. By knowing all the building blocks, we can now calculate the quasiparticle energies by solving the equation 2.86. The GW self-energy can be used to perturbatively correct the DFT or HF eigenvalues by means of the quasi-particle equation: The quasi-particle energies are evaluated perturbatively on top of a preceding DFT, therefore GW method highly depends on the starting point calculations.

$$\epsilon_i^{QP} = \epsilon_i^{KS} - \langle \psi_i^{KS} | V_{xc}^{KS} - \Sigma_c^{GW}(\epsilon_i^{QP}) - \Sigma_x | \psi_i^{KS} \rangle \quad (2.102)$$

where Σ_x denotes exact-exchange operator, Σ_c^{GW} is the correlation part of the GW self-energy. V_{xc}^{KS} represents the exchange-correlation potential of the preceding DFT calculation, there cor-

responding eigenvalues and eigenvectors are ϵ_i^{KS} and ψ_i^{KS} . The most common scheme is the single-shot G_0W_0 , which gives the band gap/fundamental gap the system that is in good agreement with the experimental results [137, 138].

2.13 Geometry optimization

Geometry optimization is performed to search the equilibrium configuration of a system from an arbitrary starting geometry in which all the atoms are arranged in the ground state. Achieving the lowest energy structure is the primary step in the modeling of materials. The atoms within the unit cell/supercell move as per the Hellmann Feynman forces until the total energy is minimized [139]. The local energy minimum is achieved when the force on each atom is equal to zero or lower than a given threshold value. The Hellmann-Feynman force acting on the I^{th} atom is given by the following expression:

$$F_I = -\frac{\partial E}{\partial \mathbf{R}_I} \quad (2.103)$$

where E is the total energy of the system. \mathbf{R}_I denotes the position of I^{th} atom.

$$\begin{aligned} F_I &= -\frac{\partial}{\partial \mathbf{R}_I} \langle \Psi | H | \Psi \rangle \\ &= -\langle \Psi | \frac{\partial H}{\partial \mathbf{R}_I} | \Psi \rangle - \langle \frac{\partial \Psi}{\partial \mathbf{R}_I} | H | \Psi \rangle - \langle \Psi | H | \frac{\partial \Psi}{\partial \mathbf{R}_I} \rangle \end{aligned} \quad (2.104)$$

Here, Ψ is an eigenfunction of H .

$$\begin{aligned} F_I &= -\langle \Psi | \frac{\partial H}{\partial \mathbf{R}_I} | \Psi \rangle - E \langle \frac{\partial \Psi}{\partial \mathbf{R}_I} | \Psi \rangle - E \langle \Psi | \frac{\partial \Psi}{\partial \mathbf{R}_I} \rangle \\ &= -\langle \Psi | \frac{\partial H}{\partial \mathbf{R}_I} | \Psi \rangle - E \frac{\partial}{\partial \mathbf{R}_I} \langle \Psi | \Psi \rangle \end{aligned} \quad (2.105)$$

Since Ψ is normalized ($\langle \Psi | \Psi \rangle = 1$), the last term in the above expression vanishes, the force on the I^{th} atom can be expressed as:

$$F_I = -\langle \Psi | \frac{\partial H}{\partial \mathbf{R}_I} | \Psi \rangle \quad (2.106)$$

There are two main factors which affect the use of aforementioned method. One is the errors due to non self-consistency and another is the explicit dependence of the basis functions on the position of ions. The latter gives rise to the Pulay forces. These issues must be treated to avoid the additional errors in the calculations. The detailed discussion can be found in Ref. [118].

2.14 Nudged Elastic Band method (NEB)

The NEB method is used to find the saddle points and minimum-energy path (MEP) between two known local minima: the reactant and product of a reaction step [140, 109]. The MEP defines the reaction coordinate for transition process, e.g. chemical reactions, diffusion processes, atomic exchange processes and changes in conformation of molecules [141]. A saddle point is the maximum along the MEP, which determines the activation energy barrier. This quantity has central role for calculating the transition rate within harmonic transition state theory. Once, the local minima (reactant and product) are known, a set of images are constructed by a linear interpolation between them. These images are linked together with a spring interaction (forming an elastic band) to form a path, and then the energy of each image is minimized to obtain the correct MEP. There are two major issues in the traditional elastic band (EB) method: the sliding-down and the corner-cutting problem [142, 143]. The first problem occurs due to smaller spring constant, where true force along the path slides away the images from the barrier region towards the minima, thereby reducing the resolution around the saddle point region. In case of higher spring constant the spring forces perpendicular to path tend to prevent the images from the true MEP, thereby the saddle point cannot be located accurately. Hence, the convergence of saddle point highly depends on the choice of spring constant. Therefore, “nudging” scheme has been proposed, where the parallel component of the true force and the perpendicular component of the spring force have been eliminated. Subsequently, the total force on each image is the sum of the true force perpendicular to the local tangent and the spring force along the local tangent. Let’s consider an elastic band with $N+1$ images [$\mathbf{R}_0, \mathbf{R}_1, \mathbf{R}_2, \dots, \mathbf{R}_N$], where the end points, \mathbf{R}_0 and \mathbf{R}_N , are the local minima correspond to initial and final states. The forces acting on image i are shown in Figure 2.11 and can be expressed as follow:

$$\mathbf{F}_i = \mathbf{F}_i^s|_{\parallel} - \nabla E(\mathbf{R}_i)|_{\perp} \quad (2.107)$$

The converged configuration of the images which lie on the MEP satisfies the following condition: $\nabla E(\mathbf{R}_i)|_{\perp} = 0$. The true force is:

$$\nabla E(\mathbf{R}_i)|_{\perp} = \nabla E(\mathbf{R}_i) - \nabla E(\mathbf{R}_i) \cdot \hat{\tau}_i \quad (2.108)$$

where E denotes the energy of system, which is the function of all the atomic coordinates. $\hat{\tau}_i$ represents the normalized local tangent for image i . The spring force is given by:

$$F_i^s \parallel = k(|\mathbf{R}_{i+1} - \mathbf{R}_i| - |\mathbf{R}_i - \mathbf{R}_{i-1}|)\hat{\tau}_i \quad (2.109)$$

where k depicts the spring constant. If the spring constant of each spring is equal then images

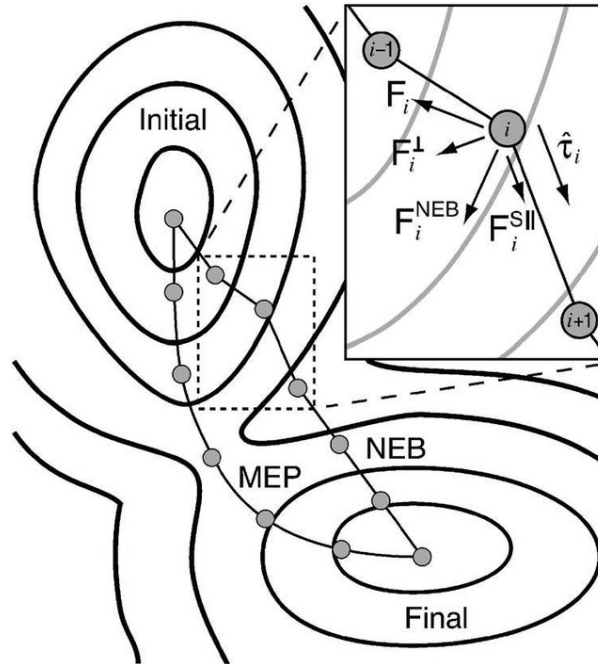


Figure 2.11: Schematic diagram to show the various forces acting on the elastic band during the optimization [6].

converge to the MEP with same spacing. The variable spring constants can be adopted to attain more resolution in the MEP near the saddle point as compared to the end points. The idea to do so, is that the spring constant depends on the energy of the images. Images with low energy can be connected via weaker spring constant, whereas the images close to the saddle point will be linked with stronger spring constant [37]. However, NEB method have resolved both the shortcomings caused by the EB method, there still exists a major drawback that the transition state is not always captured in the MEP. Hence, further modification is done to the NEB method for finding the exact transition state and obtaining the precise barrier, that is called the climbing image NEB (CI-NEB) method. Moreover, this improvement does not increase any computational cost significantly. In this scheme, after running few iterations of the regular NEB, the image with the highest energy i_{max} is identified. At this image the forces act differently. This image does not experience any spring force and the true force acts along the inverted direction of elastic band. This image is known as the climbing image. The force

acting on i_{max} image can be given by:

$$\begin{aligned} \mathbf{F}_{i_{max}} &= -\nabla E(\mathbf{R}_{i_{max}}) + 2\nabla E(\mathbf{R}_{i_{max}})|_{\parallel} \\ &= -\nabla E(\mathbf{R}_{i_{max}}) + 2\nabla E(\mathbf{R}_{i_{max}}) \cdot \hat{\tau}_i \hat{\tau}_i \end{aligned} \quad (2.110)$$

Due to this reversed force, the climbing image becomes the energy maximum along the path and energy minimum in all directions perpendicular to the path. Hence, CI-NEB ensures the accurate convergence of the MEP and locate the saddle point precisely. Therefore, CI-NEB is more appropriate choice to opt for searching transition state of chemical reactions. Further, the activation energy of the transition can be determined by taking the energy difference between the reactants and the transition state.

2.15 Cascade genetic algorithm

The Genetic Algorithm (GA) is an optimization technique based on the natural evolution process, which is widely used in science and technology to determine the global minima [144, 145, 146, 147, 148]. In this thesis work, we have used a massively parallel cascade genetic algorithm (cGA) to thoroughly scan the potential energy surface (PES) to locate all possible low-energy structures (including the global minimum) of metal oxide clusters [82]. In cGA approach, successive steps employ increasingly more accurate level of theories and each of the next level takes information obtained from its immediate lower level. This way, structural information is passed between steps of the cascade, and certain unfit structures are filtered out to speed up the scanning. The general steps involved in cGA are shown in the Figure 2.12. In the first step of employed algorithm, a random pool is formed by creating the random structures with the constraint that the closest distance between neighbor atoms should be larger than 1.21 Å. The further step consists of local optimization which is computationally expensive and time consuming part of the algorithm, in particular at the ab initio level, where several energy and force optimization takes place. Therefore, the local optimization of initial pool is performed with the semi-local functionals using lower-level settings to alleviate the computational cost. The best fitted structures within the energy of 2.5 eV from the first level are passed to next level of cascade, where selected structures are relaxed with higher-level settings. Subsequently, their single point energies are evaluated by using hybrid functionals with higher-level settings. Using these energetics, the normalized fitness value ρ_i is assigned to each i th cluster which is

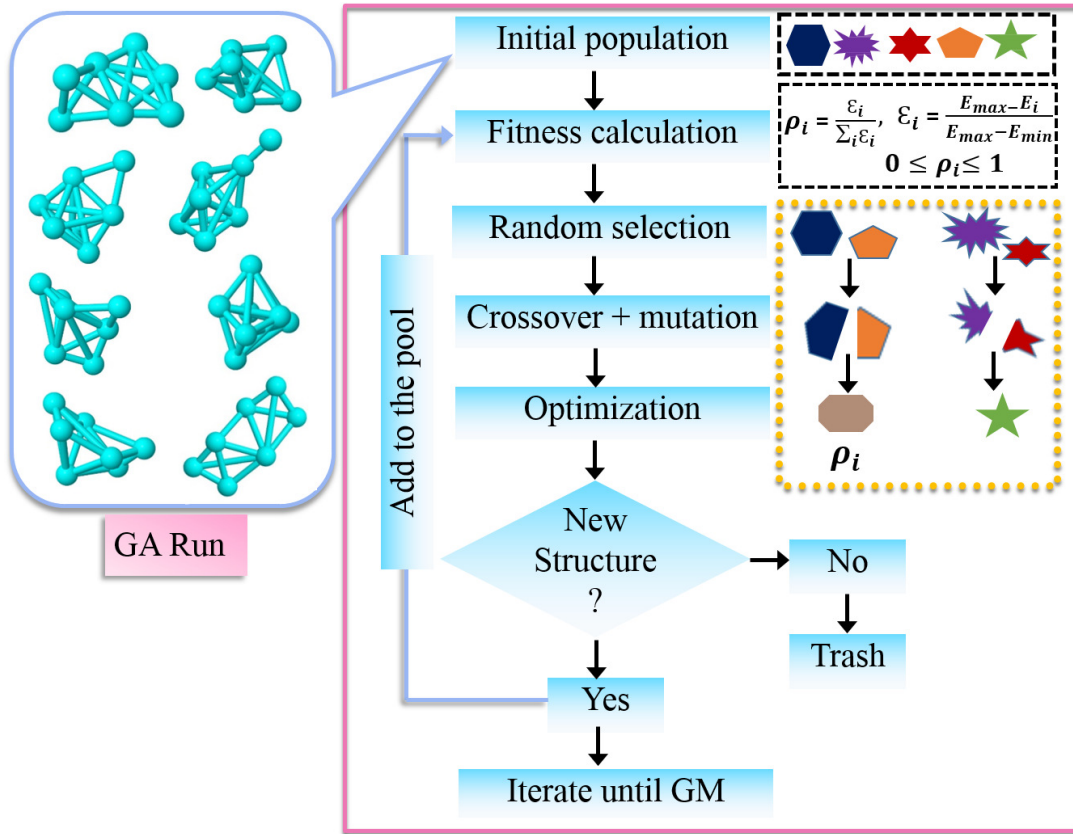


Figure 2.12: Flow chart of cascade genetic algorithm.

determined as follows:

$$\rho_i = \frac{\epsilon_i}{\sum_i \epsilon_i} \quad (2.111)$$

where ϵ_i is the relative energy of the i^{th} cluster. It is defined as:

$$\epsilon_i = \frac{E_{max} - E_i}{E_{max} - E_{min}} \quad (2.112)$$

where E_i is the total energy of the i^{th} cluster of the population. The E_{min} and E_{max} represent the lowest and highest total energies in the population pool, respectively. According to the above condition, it is clear that low energy (i.e. more negative value) clusters have high fitness and clusters with high energy (less negative value) have low fitness.

$$0 < \rho_i < 1$$

If $E_i = E_{max}$, then the corresponding $\rho_i = 0$ which means poor fitness. On the basis of the fitness function, two structures are selected from the pool for crossover and mutation. Higher the fitness function, higher is the probability of selection of the structure from the pool. The validation of efficiency and accuracy for different level of theory as well as setting (w.r.t more

advanced theory) for cGA is discussed in details in Ref [82]. Note that the accurate choice of functional for estimation of fitness function is essential for a meaningful scanning of the PES. The fitness function determines the selection probability of structures from the pool for mating operators (crossover and mutation) to generate structures of next generation. A particular structure with higher fitness value has the higher possibility to be selected from the pool which increase the probability of retaining the winning structural features during the evolutionary process. The performance of cGA highly depend on the selected crossover operators. Here, we have incorporated three types of crossover to get the optimum results as early as possible in the minimum scanning time. Each crossover operator has some advantages and disadvantages under different conditions. In first crossover scheme, two selected individuals are randomly rotated around their center of geometry, which is fixed at the origin of the coordinate axes. After the random reorientation, we select a plane to cut the parents in such way that each halve (above and below the plane) has equal number of atoms (as shown in Figure 2.13). The new

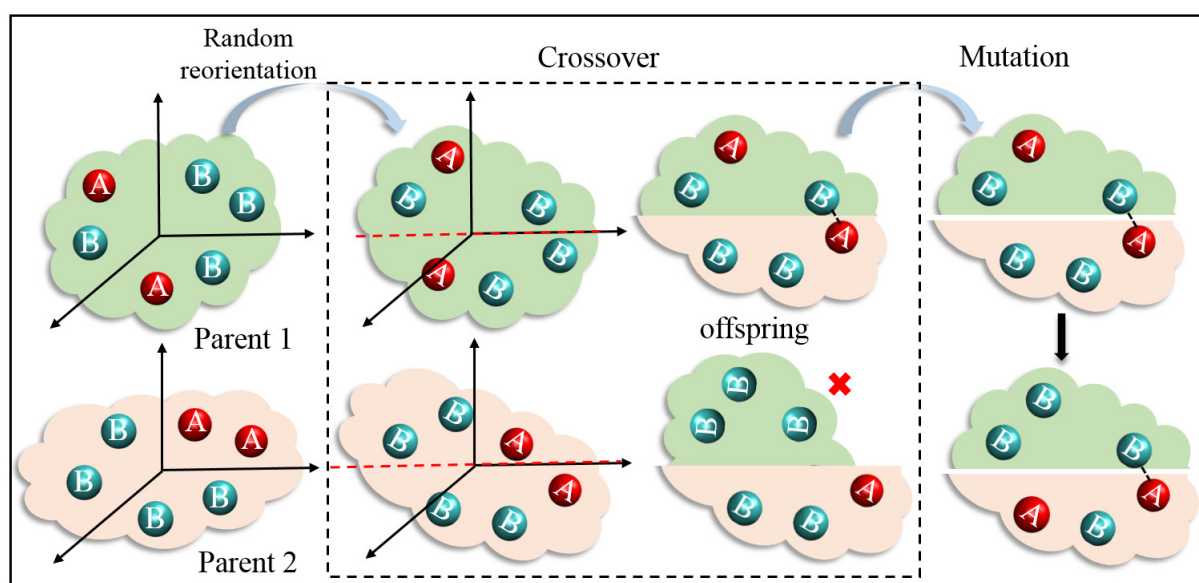


Figure 2.13: Illustration of crossover and mutation operators. A and B represent the different types of species in the structure.

structure is formed by combining the upper fragment of one parent with the lower fragment of another parent. After assemblage, the mutation operator (translation) is applied to avoid interatomic distances that are too close between two atoms. Note that we have used two types of mutation operators: (a) a rigid translation of the two halves, (b) an exchange of the atom species without altering their coordinates. The latter one is used to preserve the stoichiometry of the newly assembled structure as well as to maintain diversity into the genetic pool. This

crossover scheme is efficient in generating new candidates with the correct composition. Second type of crossover is similar to the Deaven and Ho cut-and-splice crossover operator [149]. After the reorientation, the parents are cut by random plane, then the complementary halves are combined together. The stoichiometry of newly formed offspring is checked, if it is not preserved, we reject it and select new parents, and follow the operation until the offspring contains required stoichiometry. The main advantage of this operator is to transfer the winning features of the parents in the newly generated structure. However, it takes many attempts to obtain an optimum candidate due to many rejecting trials. In third crossover scheme, we take one type of atoms from one parent and other atoms from another parent. This crossover introduce more diversity into the population.

Following this, we also allow few selection of structures with high ρ_i for mating operators to prevent the pre-convergence to a local minimum of GA scheme. After performing local optimization for the offspring with higher-level settings, energies and radial distribution function are used to examine the uniqueness of newly assembled structure against the existing structures, to avoid filling of duplicate candidates in the pool. Note that, new candidate is skipped if its copy already exists otherwise it is included in the pool by optimizing at higher-level settings. This process continues until the convergence criteria is achieved. Note that there is not any particular criteria to decide the convergence limit of a global scanning. An operative criteria is to run the cGA for a long time until no significant improvements in the fitness value is achieved than the current optimal one. In our case, we have scanned for at least double the time needed to find the actual GM. Further, if new updated lowest minima has not seen in the process, we can assume that the global minimum have obtained in the scanning. More details on benchmark and validation of the cascade GA can be found in Ref [82]. In cGA, the fitness criteria is decided by calculating the energetics at the hybrid level, therefore, its gives the more reliable scanning of all low energy isomers.

2.16 *Ab initio* atomistic thermodynamics (*aiAT*)

DFT has become a standard tool for electronic structure calculations to understand the ground state properties at zero-temperature and zero-pressure, and using the DFT results can provide detailed information in the microscopic regime. The results from DFT are then combined with the concepts of thermodynamic and statistical mechanics to study the properties of materials in

meso- and macroscopic regime. Hence, *ab initio* atomistic thermodynamics bridges the connection between the microscopic and macroscopic regimes [105, 150]. The key idea to employ the *ab initio* atomistic thermodynamics is to describe the materials properties at finite temperature and pressure. From the DFT inputs, we aim to evaluate appropriate thermodynamic potential functions namely the Gibbs free energy and Helmholtz free energy. We are able to describe the macroscopic properties of the system using the concept of thermodynamics, if we know any one of the free energies. The main advantage of this methodology is that we can apply it to the larger systems by dividing it into smaller subsystems that hold the equilibrium condition with each other. In thermodynamic equilibrium, subsystem can be described with thermodynamic quantities of internal energy (E), entropy (S), volume (V), the number of particles (N), and the chemical potential (μ).

2.16.1 Thermodynamic potentials

There are four thermodynamic potentials, which are defined as: (i) Internal energy, U (ii) Helmholtz free energy, $F = U - TS$ (iii) Enthalpy, $H = U + pV$ (iv) Gibbs free energy $G = U + pV - TS = H - TS = F + pV$. In thermodynamics, these four potentials U , F , H and G play the same role as the potential energy has in mechanics. We use Helmholtz free energy, F , to describe a system with constant T , V , and N . Whereas Gibbs free energy, G , is used to address the system at constant T , p , and N . The Gibbs free energy is minimum for a system in equilibrium.

2.16.2 Free energy of formation

In real life situations, any catalytic process takes place at a finite temperature and pressure of the reactant gases. In reactive atmosphere (composed of gas phase molecules), clusters (catalyst) adsorb the ligands which in turn form the new stable phases. The resulting configurations will depend on the conditions at which the experiment is performed, viz. the temperature and partial pressure of the gas phase reactants. By using the concept of *ab initio* atomistic thermodynamics, we can predict which phase will be favorable by determining the formation free energy of each configuration as a function of T and p . Theoretical studies of the environmental effects (T , p) on the stability of materials have already been developed and employed for bulk semiconductors [105, 150], to study the adsorption on metal-oxide surfaces [151, 152, 106, 107]. We call it the *ab initio* atomistic thermodynamics. This methodology has been extended for gas-phase clusters placed in an reactive environment as well [108, 82, 153].

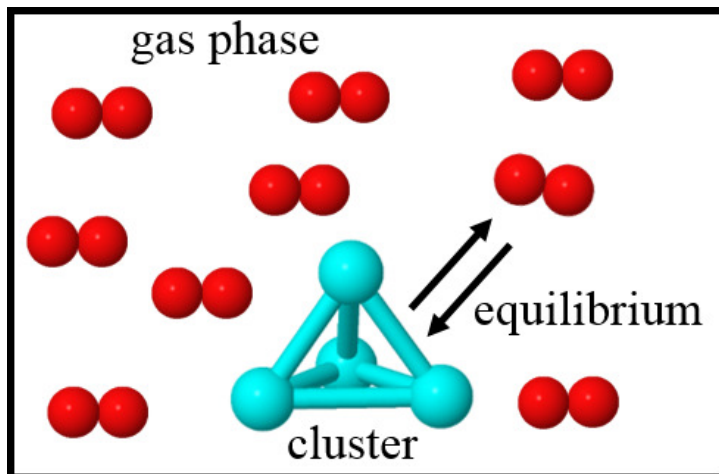


Figure 2.14: Schematic representation of the system: a cluster in gas phase environment of oxygen.

The application of *aiAT* proceeds along the following steps:

- Calculate the free energy of structures that are found in the cGA-scan.
- Compare the relative thermodynamical stability of those structures as a function of (T, p) , i.e. construct phase diagrams.
- Identify the most relevant structures, that comes out to be the most stable at a given experimental condition.
- Find the chemical connections between them.

In our work, *ab initio* atomistic thermodynamics yields phase diagrams, which assist us to identify the structures that are probably relevant for catalysis at the realistic temperature and pressure of interest.

$$\Delta G_f(T, p_{O_2}) = F_{cluster+ligands}(T) - F_{cluster}(T) - z\mu_O(T, p_{O_2}) \quad (2.113)$$

where, $F_{cluster+ligands}$ and $F_{cluster}$ are the free energies of the cluster+ligands and of the pristine cluster, μ_O is the chemical potentials of oxygen and z represents the number of oxygen atoms in the cluster. The chemical potential of oxygen is $\mu_O = \frac{1}{2}\mu_{O_2}$. By minimizing the Gibbs free energy of formation ($\Delta G_f(T, p_{O_2})$) for each configuration using the concept of *aiAT*, we can determine which composition will be formed preferentially at different T and p_{O_2} . To evaluate $\Delta G_f(T, p_{O_2})$ from equation 2.113, we need to calculate the free energies of the cluster+ligands and of the pristine cluster and also the chemical potential of oxygen. The free energies of the cluster+ligands and pristine cluster are obtained from their partition functions including translational, rotational, vibrational, electronic, and configurational degrees of freedom [45,46]. The

chemical potentials of O₂ is also obtained from their partitions functions. Using equation 2.113 we find out which compositions are the most stable (lowest free energy) ones at given environmental conditions (T, p_{O_2}). The concept of *ab-initio* atomistic thermodynamics enables us to plot the phase diagrams.

2.16.3 Partition function

Partition function (q_N) tells that how much energy is distributed or partitioned among the various energy levels. The average energy (U), Helmholtz free energy (F), Gibbs free energy (G), chemical potential (μ), entropy (S), and pressure (p) can be obtained from partition function or its derivatives. For example: $U = -\frac{\partial}{\partial \beta}(\ln q_N)$, $F = -k_B T \ln q_N$, $G = F + pV$, $\mu = \frac{G}{N}$. Partition function for discrete system:

$$q_N = \sum_i e^{\beta E_i} \quad (2.114)$$

where, $\beta = \frac{1}{k_B T}$, i is the index for the microstates, E_i is the total energy of the system in the respective microstate. Partition function for continuous system:

$$q_N = \frac{1}{h^f} \int e^{\beta E_i} d^f q d^f p \quad (2.115)$$

where, h is the Planck constant, f is the degree of freedom. A molecule with N atoms has $3N$ degrees of freedom. Amongst $3N$ degrees of freedom, three are rotational and the remaining $3N-6$ are vibrational for non-linear molecules. Linear molecules have two rotational degrees of freedom and $3N-5$ vibrational degrees of freedom. If particles are indistinguishable:

$$q_N = \frac{1}{h^f N!} \int e^{\beta E_i} d^f q d^f p \quad (2.116)$$

Partition function of an ideal gas composed of N indistinguishable molecules:

$$q_N = \frac{1}{N!} [q]^N \quad (2.117)$$

For distinguishable molecules:

$$q_N = [q]^N \quad (2.118)$$

If $N = 1$ (single molecule), q is the partition function of a single molecule. The different modes of motion viz. translation (trans), rotational (rot), vibrational (vib), configurational (conf), electronic (elect) and nuclear (nucl) contribute to the total energy of a molecule.

$$q = \sum_{i(\text{all-states})} e^{-\beta E_i^{\text{trans}} - \beta E_i^{\text{rot}} - \beta E_i^{\text{vib}} - \beta E_i^{\text{conf}} - \beta E_i^{\text{elect}} - \beta E_i^{\text{nucl}}} \quad (2.119)$$

$$q = \left(\sum_{i(\text{trans})} e^{-\beta E_i^{\text{trans}}} \right) \left(\sum_{i(\text{rot})} e^{-\beta E_i^{\text{rot}}} \right) \left(\sum_{i(\text{vib})} e^{-\beta E_i^{\text{vib}}} \right) \left(\sum_{i(\text{conf})} e^{-\beta E_i^{\text{conf}}} \right) \left(\sum_{i(\text{elect})} e^{-\beta E_i^{\text{elect}}} \right) \left(\sum_{i(\text{nucl})} e^{-\beta E_i^{\text{nucl}}} \right) \quad (2.120)$$

Hence, the partition function of a single molecule is the factorization of individual contributions, which means that we can calculate each part separately. The nuclear/electronic part can be decoupled from the vibrational/rotational part due to Born-Oppenheimer approximation. Further, the vibrational and rotational terms are also decoupled as both the motions happen on different time scales.

$$q = q^{\text{trans}} \times q^{\text{rot}} \times q^{\text{conf}} \times q^{\text{vib}} \times q^{\text{elect}} \times q^{\text{nucl}} \quad (2.121)$$

The different contributions as functions of temperature and pressure (T, p):

$$q^{\text{trans}} = \left(\frac{2\pi m k_B T}{h^2} \right)^{\frac{3}{2}} V = \left(\frac{2\pi m k_B T}{h^2} \right)^{\frac{3}{2}} \frac{k_B T}{p} \quad (2.122)$$

where, m is the mass of the molecule and we have considered the ideal gas approximation. The nuclear state is rarely changed during the chemical processes, and therefore q^{nucl} term does not contribute to the thermodynamical changes.

$$\begin{aligned} q^{\text{rot}} &= \frac{8\pi^2 I_A k_B T}{h^2}, \text{ for linear molecules and} \\ q^{\text{rot}} &= 8\pi^2 \left(\frac{2\pi k_B T}{h^2} \right)^{\frac{3}{2}} (I_A I_B I_C)^{\frac{3}{2}}, \text{ for non-linear molecules} \\ q^{\text{vib}} &= \prod_i \left[e^{-\frac{h\nu_i}{2k_B T}} \left(1 - e^{-\frac{h\nu_i}{k_B T}} \right)^{-1} \right] \\ q^{\text{conf}} &= \frac{1}{\sigma} \\ q^{\text{elect}} &= \sum_i \left(\mathcal{M}_i e^{-\frac{E_i}{k_B T}} \right) \approx \mathcal{M} e^{-\frac{E^{\text{DFT}}}{k_B T}} \end{aligned} \quad (2.123)$$

I_A, I_B, I_C are the moment of inertia of the molecule, and ν_i are the vibrational frequencies of the molecule. Note that, we have assumed the harmonic approximation to account the vibrational modes. σ is the number of symmetry operations according to the symmetry point group, which represents the number of indistinguishable orientations of the molecule. In case of diatomic molecules, $\sigma = 1$ for heteroatomics and $\sigma = 2$ for homoatomics. E^{DFT} is the ground state energy, and \mathcal{M} is the spin multiplicity. Here, we have considered no interaction between the first excited state and ground state.

The chemical potential of molecular oxygen as a function of temperature and pressure is calculated as: $\mu_{\text{O}_2} = -k_B T \ln q + pV$

$$\begin{aligned} \mu_{\text{O}_2}(T, p_{\text{O}_2}) = & -k_B T \ln \left[\left(\frac{2\pi m}{h^2} \right)^{\frac{3}{2}} (k_B T)^{\frac{5}{2}} \right] + k_B T \ln p_{\text{O}_2} - k_B T \ln \left(\frac{8\pi^2 I_A k_B T}{h^2} \right) \\ & + \frac{h\nu_{\text{OO}}}{2} + k_B T \ln \left[1 - \exp \left(-\frac{h\nu_{\text{OO}}}{k_B T} \right) \right] + E^{\text{DFT}} - k_B T \ln \mathcal{M} + k_B T \ln \sigma \end{aligned} \quad (2.124)$$

The μ scales do not correspond to absolute chemical potentials, but rather to the change in free energy at (T, p) with respect to the absolute zero temperature and standard pressure: $\Delta\mu_{\text{O}}(T, p) = \mu_{\text{O}}(T, p) - \mu_{\text{ref}}(T, p)$ with $\mu_{\text{ref}}(T, p) = \frac{1}{2}(E^{\text{DFT}} + E^{\text{ZPE}})$. See the appendix for the full derivation.

The Helmholtz free energy can be obtained from the partition function as follow:

$$\begin{aligned} F(T) = & -k_B T \ln q \\ = & F^{\text{trans}}(T) + F^{\text{rot}}(T) + F^{\text{vib}}(T) + F^{\text{symmetry}}(T) + F^{\text{spin}}(T) + E^{\text{DFT}} \end{aligned} \quad (2.125)$$

Where,

$$\begin{aligned} F^{\text{trans}}(T) = & -\frac{3}{2} k_B T \ln \left[\left(\frac{2\pi m k_B T}{h^2} \right) \right] \\ F_{\text{non-linear}}^{\text{rot}}(T) = & -k_B T \ln \left[8\pi^2 \left(\frac{2\pi k_B T}{h^2} \right)^{\frac{3}{2}} \right] - \frac{1}{2} k_B T \ln(I_A I_B I_C) \\ F_{\text{linear}}^{\text{rot}}(T) = & -k_B T \ln \left(\frac{8\pi^2 I_A k_B T}{h^2} \right) \\ F^{\text{vib}}(T) = & \sum_i \frac{h\nu_i}{2} + \sum_i k_B T \ln \left[1 - \exp \left(-\frac{h\nu_i}{k_B T} \right) \right] \\ F^{\text{symmetry}}(T) = & k_B T \ln \sigma \\ F^{\text{spin}}(T) = & -k_B T \ln \mathcal{M} \end{aligned}$$

Here, a term $\ln V$ (V is a reference volume), which comes in F^{trans} , is dropped, because it cancels out when taking the difference $F_{\text{cluster+ligands}}(T) - F_{\text{cluster}}(T)$ to calculate the formation free energy.

Limiting conditions on chemical potential

We see from derivations below, the μ_{O} variation ($\Delta\mu_{\text{O}}$) is restricted to a finite range. There are two limits on $(\Delta\mu_{\text{O}})$ (i) O-poor limit and (ii) O-rich limit. If $(\Delta\mu_{\text{O}})$ is less than the ‘‘O-poor limit’’ the oxide will decompose into cluster and oxygen. Therefore, the oxide is only stable if

the following relation is satisfied:

$$F_{cluster+ligands}(T) < F_{cluster}(T) + z\mu_{\text{O}}(T, p_{\text{O}_2}) \quad (2.126)$$

We can rewrite μ_{O} with respect to μ^{ref} as below:

$$z\mu_{\text{O}} = z(\mu_{\text{O}} - \mu^{\text{ref}} + \mu^{\text{ref}}) = z(\Delta\mu_{\text{O}} + \mu^{\text{ref}}) \quad (2.127)$$

where $\mu^{\text{ref}} = \frac{1}{2}(E_{\text{O}_2}^{\text{DFT}} + E_{\text{O}_2}^{\text{ZPE}})$, and $E_{\text{O}_2}^{\text{ZPE}} = \frac{h\nu_{\text{OO}}}{2}$, is the expression for zero point energy.

Thus, equation (3) becomes:

$$z\Delta\mu_{\text{O}} > F_{cluster+ligands}(T) - F_{cluster}(T) - \frac{z}{2}(E_{\text{O}_2}^{\text{DFT}} + E_{\text{O}_2}^{\text{ZPE}}) \quad (2.128)$$

The ‘‘O-rich limit’’ $\Delta\mu_{\text{O}} = 0$, is a condition where oxygen gas is in equilibrium with O_2 droplets, therefore O_2 droplets condensed on the clusters. Thus, another restriction on $\Delta\mu_{\text{O}}$ range:

$$\Delta\mu_{\text{O}} < 0 \quad (2.129)$$

Combining the equations (5) and (6), we get the range of $\Delta\mu_{\text{O}}$:

$$F_{cluster+ligands}(T) - F_{cluster}(T) - \frac{z}{2}(E_{\text{O}_2}^{\text{DFT}} + E_{\text{O}_2}^{\text{ZPE}}) < z\Delta\mu_{\text{O}} < 0 \quad (2.130)$$

$$\begin{aligned} \Delta\mu_{\text{O}} &= (\mu_{\text{O}} - \mu^{\text{ref}}) \\ \Delta\mu_{\text{O}} &= \frac{1}{2}(\mu_{\text{O}_2} - \mu^{\text{ref}}) \\ \Delta\mu_{\text{O}}(T, p_{\text{O}_2}) &= \frac{1}{2}\left(\mu_{\text{O}_2}(T, p_{\text{O}_2}) - E_{\text{O}_2}^{\text{DFT}} - \frac{h\nu_{\text{OO}}}{2}\right) \end{aligned}$$

We see from above expression, that the oxygen condensation limit depends on the temperature and pressure.

Thermodynamic stability and electronic properties of neutral bimetallic oxide $\text{TM}_x\text{Mg}_y\text{O}_z$ clusters

3.1 Introduction

Transition-metal (TM) nanoparticles/clusters are used as catalysts for a variety of important chemical processes [154, 155, 156, 157, 158]. At nanoscale, the particles acquire unique properties not found in the bulk TMs. The size of the nanoparticles is an additional parameter that affects their electronic and chemical properties and can be used to control the activity and selectivity of the catalyst. Moreover, the particles containing two or more transition or other metals can be synthesized, which tremendously increase the possibilities for tuning their functional properties. Together with these possibilities, new challenges arise for the design of more efficient and stable nano-catalysts. In particular, due to the increased complexity, the atomic structure and the stability of nanoparticles is harder to determine. Moreover, the particles usually operate in a reactive atmosphere, containing molecules of oxygen for instance. The interaction of the particles with oxygen will eventually result in their partial or complete oxidation, whether it is intended or not [82]. In fact, in some applications [159], the particles are created by a reduction of the oxide in hydrogen. Thus, both oxidized and reduced metal atoms are usually present at the surface, with their relative concentrations depending on the temperature and oxygen partial pressure. Disentangling the role of different oxidation states in a catalytic process is extremely challenging.

In view of the above discussion, it is important to provide theoretical guidance to experiment and technology on the composition and atomic structure of metal particles in a reactive atmosphere, in particular in the ubiquitous presence of oxygen. Stability being a key factor for the desired functioning of a catalyst, it is a prerequisite to know the most stable phase of a

particle/cluster in the reactive atmosphere. There are both experimental and theoretical reports stating the existence of particular phases viz. Ni_4O_5 clusters (on top of MgO substrate) under oxygen atmosphere [160]. However, no quantitative information has been provided so far to understand which structures/compositions are stable in different experimental conditions.

In this chapter, we report an *ab initio* atomistic thermodynamics [161] study of TM clusters supported on MgO, as well as unsupported TM-Mg clusters in an oxygen atmosphere. Gas-phase clusters are often used as model systems to study structural and compositional variability of the clusters at realistic conditions both experimentally and theoretically. Although such models cannot capture the full complexity of the supported nano-catalysts, they provide the necessary knowledge to disentangle various effects determining the catalytic activity. Using a massively parallel *ab initio* cascade genetic algorithm [82], we identify stable and metastable structures of the clusters at a hybrid density functional theory (DFT) level, in order to overcome the difficulties of the standard Local Density Approximation (LDA) and Generalized Gradient Approximation (GGA) exchange-correlation functionals in describing localization of *d*-electrons in TMs, as well as the charge transfer from metal atoms to oxygen [108]. We present an exhaustive and reliable database of small ternary $\text{TM}_x\text{Mg}_y\text{O}_z$ clusters (TM = Cr, Ni, Fe, Co; $x + y \leq 3$, $z = 1, 2, \dots, 12$). Among a variety of TMs, Cr, Ni, Fe, and Co are of special interest to the catalytic research community because of their wide applications viz. in partial oxidation of CH_4 [162, 163, 164, 159, 165, 166], selective oxidation of alkanes [35, 36, 37, 38], alcohols [39, 40], olefins [41], and aromatics [42], selective reduction of nitrogen oxides [43], and oxidation of hydrogen sulfide [44]. MgO is often used as a support in these applications, or as a component of an oxide solid solution catalyst [159]. The high thermal stability and low cost are two important factors that make MgO to be one of the best choices for catalytic applications [160, 167].

A simple descriptor that captures both the nature of the reactive oxygen centers and the tendency of adjacent TM centers to gain electron density is the ligand-to-metal charge transfer excitation energy [168]. For oxides having TM centres in their highest oxidation states, this ligand-to-metal charge transfer excitation energy typically corresponds to the band-gap energy. For a cluster, electron transfer to/from it is more appropriately described by the electron affinity (EA) and ionization potential (IP), respectively. Therefore, the clusters having a high EA and a low IP are the ones having a low fundamental gap ($E_g = \text{EA} - \text{IP}$). Clusters possessing a high EA and/or a low IP may be expected to be better catalysts because they would accept or

donate an electron more readily [90, 138]. Thus, fundamental gap E_g can be considered as an important feature of the clusters that determines their redox properties, and in many cases can serve as a descriptor of the catalytic activity [169, 170, 168, 171, 172, 173, 174, 175].

We therefore analyze the dependence of E_g of the clusters on composition, temperature, and O_2 pressure, and determine the explicit role of different atomic species to modulate the E_g values. Strikingly, we find that the nature of TM plays a negligible role in tuning the E_g in $TM_xMg_yO_z$ clusters. Rather, E_g is strongly correlated with the presence of Mg-coordinated O_2 (i.e., the oxygen atoms directly attached with Mg atom) and is found to be minimum under O -rich conditions (i.e., $z > x+y$, when $T \approx 200K - 450K$ and $p_{O_2} \approx 10^{-6} - 10^{10}$ atm). The analysis of our high-throughput data suggests that the tunability of the cluster chemical properties may be limited at given (T, p_{O_2}) conditions, but is strongly dependent on the conditions.

3.2 Methodology

We have considered first a wide range of $TM_xMg_yO_z$ cluster compositions, where z is determined by thermal equilibrium with the environment at given temperature T and partial oxygen pressure p_{O_2} [176]. In order to get the minimum energy configurations, for each stoichiometry, the total energy is minimized with respect to both geometry and spin state. The low-energy structures (including the global minimum) are generated from an exhaustive scanning of the potential energy surface (PES) using our recent implementation of cascade genetic algorithm (GA) [108, 82]. The term “cascade” means a multi-stepped algorithm where successive steps employ higher level of theory and each of the next level takes information obtained at its immediate lower level. Typically here the cascade GA starts from a DFT with semi-local xc-functionals and goes up to DFT with hybrid xc-functionals. [177] This GA algorithm’s implementation is thoroughly benchmarked and its efficiency is validated (w.r.t more advanced theory) in detail in Ref. [82].

We have performed the DFT calculations using FHI-aims, which is an all electron code with numerical atom centred basis sets [126]. The low-energy GA structures are further optimized at a higher level settings, where energy minimization is performed with vdW-corrected PBE (PBE+vdW) functional, “tight - tier 2” settings, and force tolerance was set to better than 10^{-5} eV/Å. The van der Waals correction is calculated as implemented in Tkatchenko-Scheffler scheme [178]. The total single-point energy is calculated afterwards on top of this optimized

structure via vdW-corrected-PBE0 [124] hybrid xc-functional (PBE0+vdW), with “tight - tier 2” settings [179]. Note that PBE+vdW strongly overestimates the stability of oxide-clusters under O-rich conditions (i.e. with larger z values) as reported for the case of Mg_yO_z clusters [108]. This gives a qualitatively wrong prediction that adsorption of O_2 could be favored over desorption up to a large excess of oxygen. Such behavior is not confirmed by hybrid functionals [e.g. HSE06, PBE0] employed in our calculations. For the data set we have used, the difference in energetics of PBE0 and HSE06 is always within 0.04 eV. The spin states of the clusters are also sometimes different as found by PBE and PBE0/HSE06. Thus, all our results are thoroughly tested and benchmarked w.r.t hybrid xc-functionals (PBE0) using “tight” numerical settings and tier 2 basis set. For estimation of (vertical) electron affinity (VEA), (vertical) ionization potential (VIP), and fundamental gap ($E_g = \text{VEA} - \text{VIP}$) we have used the G_0W_0 @PBE0 approach with “really-tight” numerical settings and tier 4 basis set [126].

The free energy of the isomers [180] is then calculated as a function of T and p_{O_2} for each stoichiometry using the *ab initio* atomistic thermodynamics (*aiAT*) approach. The concept of *aiAT* was successfully applied initially for bulk semiconductors [105, 150], and later applied to the study of oxide formation at the surface of some TMs and other materials [151, 152, 106, 107]. We have recently extended this approach to clusters in a reactive atmosphere [108, 82, 181, 182]. From different cluster compositions and structures with the lowest free energy the thermodynamic phase diagram can be constructed as a function of T and p_{O_2} . At a given T , p_{O_2} , and x, y , the stable stoichiometry of a $\text{TM}_x\text{Mg}_y\text{O}_z$ cluster is determined via *aiAT*, i.e., by minimizing the Gibbs free energy of formation $\Delta G_f(T, p_{\text{O}_2})$.

$$\Delta G_f(T, p_{\text{O}_2}) = F_{\text{TM}_x\text{Mg}_y\text{O}_z}(T) - F_{\text{TM}_x\text{Mg}_y}(T) - z \times \mu_{\text{O}}(T, p_{\text{O}_2}) \quad (3.1)$$

Here, $F_{\text{TM}_x\text{Mg}_y\text{O}_z}(T)$ and $F_{\text{TM}_x\text{Mg}_y}(T)$ are the Helmholtz free energies of the $\text{TM}_x\text{Mg}_y\text{O}_z$ and the pristine TM_xMg_y cluster, respectively [183]. $\mu_{\text{O}}(T, p_{\text{O}_2}) = \frac{1}{2}\mu_{\text{O}_2}$ is the chemical potential of oxygen. The chemical potential of oxygen is calculated by using following equation:

$$\begin{aligned} \mu_{\text{O}_2}(T, p_{\text{O}_2}) = & -k_B T \ln \left[\left(\frac{2\pi m}{h^2} \right)^{\frac{3}{2}} (k_B T)^{\frac{5}{2}} \right] + k_B T \ln p_{\text{O}_2} - k_B T \ln \left(\frac{8\pi^2 I_A k_B T}{h^2} \right) \\ & + \frac{h\nu_{\text{OO}}}{2} + k_B T \ln \left[1 - \exp \left(-\frac{h\nu_{\text{OO}}}{k_B T} \right) \right] + E^{\text{DFT}} - k_B T \ln \mathcal{M} + k_B T \ln \sigma \end{aligned} \quad (3.2)$$

$$\Delta\mu_{\text{O}}(T, p_{\text{O}_2}) = \frac{1}{2} \left(\mu_{\text{O}_2}(T, p_{\text{O}_2}) - E_{\text{O}_2}^{\text{DFT}} - \frac{h\nu_{\text{OO}}}{2} \right) \quad (3.3)$$

In the above equations, m is the mass, I_A is the moment of inertia, \mathcal{M} is the spin multiplicity, and σ is the symmetry number for oxygen molecule. ν_{OO} is the O-O stretching frequency and $\frac{h\nu_{OO}}{2}$ is the zero point energy of the oxygen molecule. Pressure dependency in the free energy of formation ΔG comes in $\Delta\mu_O$ expression only. Therefore, the pressure axes are calculated according to the relation between μ_{O_2} , with p_{O_2} as shown in Equation 3.2 and 3.3. The structures and compositions, which exhibit the lowest free energy of formation ΔG in the experimentally accessible (T, p_{O_2}) region, is the most stable one under that (T, p_{O_2}) region. As explained in Ref. [82], $F_{TM_xMg_yO_z}(T)$ and $F_{TM_xMg_y}(T)$ are calculated as the sum of DFT total energy, DFT vibrational free energy (up to harmonic approximation), translational, rotational, symmetry and spin-degeneracy free-energy contributions. The dependence of $\mu_O(T, p_{O_2})$ on T and p_{O_2} is calculated using the ideal (diatomic) gas approximation with the same DFT functional as for the clusters. The phase diagram for a particular $TM_xMg_yO_z$ is constructed by identifying the lowest free-energy structures at each T, p_{O_2} .

3.3 Results and Discussions

3.3.1 Global minimum (GM) structures of $TM_xMg_yO_z$ clusters

An exhaustive set of $TM_xMg_yO_z$ ($x + y \leq 3; y \neq 0$) clusters are generated including all the possible structural and composition motifs, oxidation states, electronic spin and symmetry. For instance, in Figure 3.1, we have shown the global optimized structures of $TM_1Mg_2O_z$, $TM_2Mg_1O_z$ ($z = 1..8$) set of clusters and their corresponding spin multiplicity. The spin multiplicity of the clusters are changed with size of clusters.

3.3.2 Determination of Gibbs free energy of formation as function of temperature and pressure via *ab initio* atomistic thermodynamics

In the next step, *aiAT* is employed to study the effect of T and p_{O_2} on the stability of all sets of clusters ($TM_xMg_yO_z$). Here, total energies are the primary requirement to evaluate formation energy (ΔG_f), which is directly amenable to electronic structure calculation. After calculating the total energies, equation 3.1 allows to directly plot the phase diagrams for each set of clusters as a function of the oxygen chemical potential ($\Delta\mu_O$) at finite $T = 300K$, as shown in Figure 3.2a. This yields a line in the phase diagram corresponding to each cluster,

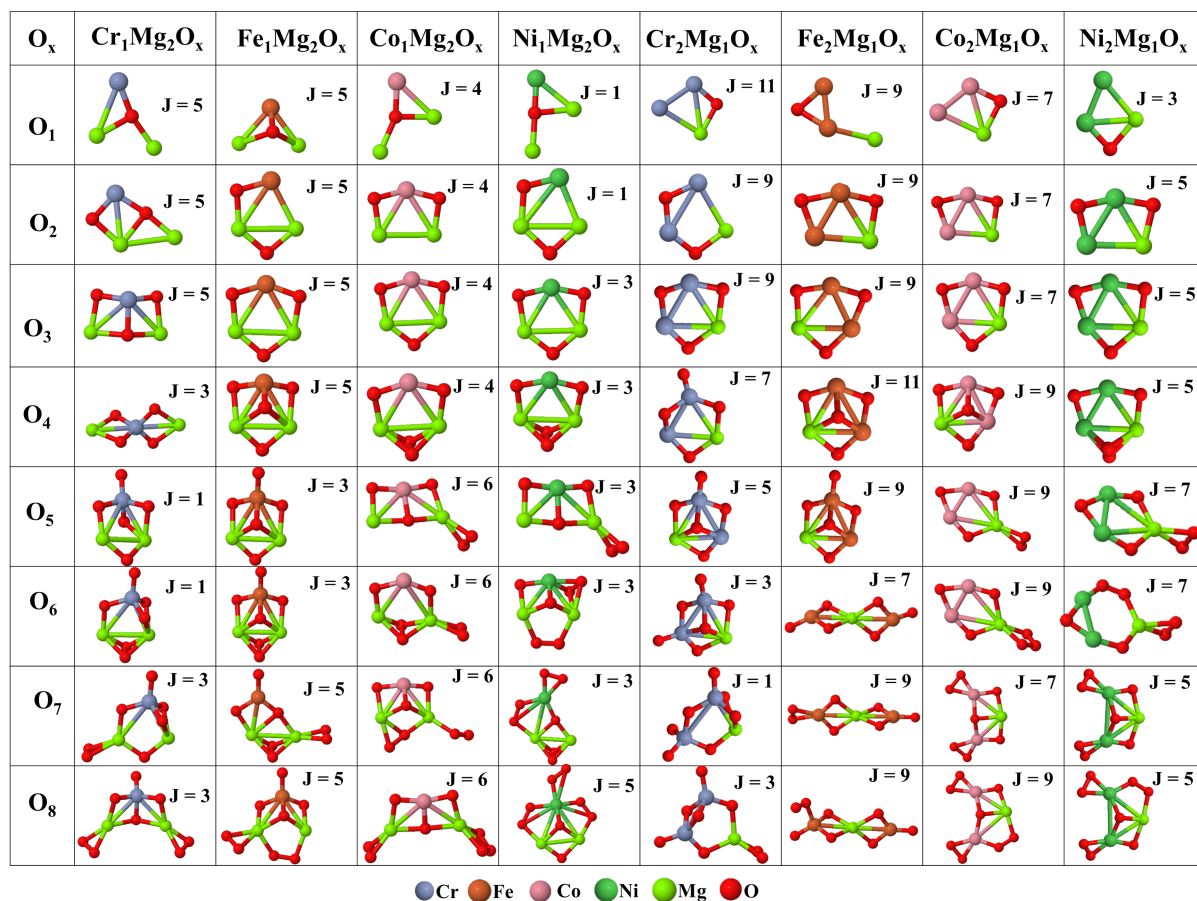


Figure 3.1: The GM structures in PES of $\text{TM}_x\text{Mg}_y\text{O}_z$ clusters are scanned via cGA. In $\text{TM}_x\text{Mg}_y\text{O}_z$ clusters, TM = Cr, Fe, Co and Ni and $x, y = (1,2), Z = (1..8)$. The geometries are optimized with PBE+vdW, and J is calculated using HSE06+vdW.

and at any $\Delta\mu_{\text{O}}$ the composition with the lowest lying line in the phase diagram is the most stable one under the environment conditions (T and p_{O_2}). Using Equation 3.2 the pressure axis can be determined at any specific T by varying the chemical potential ($\Delta\mu_{\text{O}}$) of O_2 . In Figure 3.2a, the pressure axis (top x-axis) is included at 300K. The black dotted lines denote the limiting conditions (left for the lower limit and right for higher limit) of physically acceptable chemical potentials (detailed discussion is given in chapter 2). The different color shaded area indicates the most stable phases within the range of $\Delta\mu_{\text{O}}$. In Figure 3.2a, we can see in the low range of pressure, $\text{Ni}_1\text{Mg}_1\text{O}_2$ and $\text{Ni}_1\text{Mg}_1\text{O}_4$ are the most stable conformers. On increasing the pressure, $\text{Ni}_1\text{Mg}_1\text{O}_6$ and $\text{Ni}_1\text{Mg}_1\text{O}_7$ become the most stable compositions, that exhibit the lowest formation energy around the ambient condition ($T = 300\text{K}, p_{\text{O}_2} = 1\text{atm}$) of oxygen gas. However, in the high range of pressure $\text{Ni}_1\text{Mg}_1\text{O}_8$ and $\text{Ni}_1\text{Mg}_1\text{O}_{10}$ are the most preferable configurations in the phase diagram. This 2D phase diagram provides first valuable insight into the structure and composition of the clusters at realistic environmental conditions.

In Figure 3.2b, we have plotted ΔG_f as a function of T by fixing the pressure of O_2 at 1 atm.

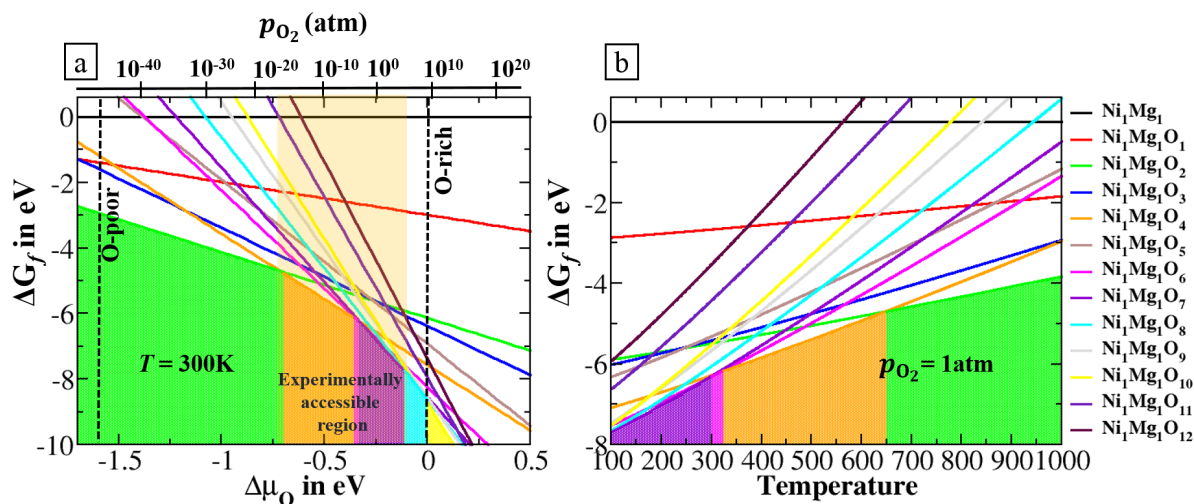


Figure 3.2: In Figure (a), the formation energy (ΔG_f) of globally optimized clusters ($Ni_1Mg_1O_x$) is varied with $\Delta\mu_O$ at $T = 300$ K. The top axis represents the pressure scale at 300 K. The black dotted lines indicate O-poor and O-rich limit. In Figure (b), ΔG_f is varied with T at 1 atm pressure of O_2 . Total energies are calculated using HSE06+vdW [13]. Colored areas are for the guideline to identify which phase is the most stable for the different range of pressure (a) and temperature (b).

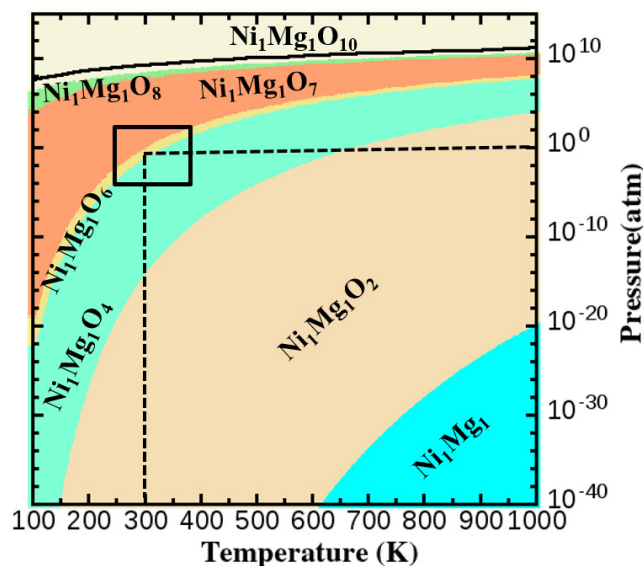


Figure 3.3: 3D phase diagram is constructed for most stable $Ni_1Mg_1O_x$ clusters at various T and p_{O_2} under thermodynamic equilibrium. The top black line represents the O-rich limit: beyond this limit O_2 molecules start to condense on the clusters. The rectangular box represents the ambient conditions ($T = 300$ K, $p_{O_2} = 1$ atm), and the dashed-dotted lines indicate the normal conditions in the phase diagram. The vibrational free energy is calculated under harmonic approximations.

Here, at low T , $Ni_1Mg_1O_7$ and $Ni_1Mg_1O_6$ are energetically preferable, while as we increase

the T , $\text{Ni}_1\text{Mg}_1\text{O}_4$, and $\text{Ni}_1\text{Mg}_1\text{O}_2$ become the most stable phases. It is obvious that the same configurations are observed ($\text{Ni}_1\text{Mg}_1\text{O}_6$ and $\text{Ni}_1\text{Mg}_1\text{O}_7$) around the ambient condition ($T = 300$ K, $p_{\text{O}_2} = 1$ atm) from both the phase diagrams. In Figure 3.3, the dependence of T and p_{O_2} are combined in a 3D phase diagram, which provides the more direct insight to identify that which composition is more stable in different range of T and p_{O_2} . Here, the negative values of formation energy are plotted along the z-axis (pointing out from the page). In 3D phase diagram, near ambient conditions (T and p_{O_2}) $\text{Ni}_1\text{Mg}_1\text{O}_4$, $\text{Ni}_1\text{Mg}_1\text{O}_6$ and $\text{Ni}_1\text{Mg}_1\text{O}_7$ are thermodynamically preferred compositions (phases within the rectangular box). At high T and low p_{O_2} $\text{Ni}_1\text{Mg}_1\text{O}_2$ and Ni_1Mg_1 are the most stable phases, while at high pressure $\text{Ni}_1\text{Mg}_1\text{O}_8$ and $\text{Ni}_1\text{Mg}_1\text{O}_{10}$ compositions become more favorable. Hence, we observe a general trend that O-rich clusters are more stable at low T and ambient to high pressure, whereas at high T and low p_{O_2} , O-deficient clusters are more stable.

3.3.3 Validation of functional

To see the effect of functional on our model system, we have plotted the phase diagrams of $\text{Ni}_1\text{Mg}_2\text{O}_z$ clusters with different functionals (viz. PBE, HSE06). The phase diagrams of clusters are not correctly estimated using DFT local/semi-local functionals as these functionals underestimate the binding energy of oxygen atom. As the model system of our choice is bimetallic oxides, therefore, advanced hybrid functional is inevitable to address both the structural and thermodynamic stability of the system. In Figure 3.4, we can see there is quite a difference in phase diagrams for the same set of cluster ($\text{Ni}_1\text{Mg}_2\text{O}_z$) with different functionals (Figure 3.4a and 3.4b are plotted with PBE+vdW and Figure 3.4c and 3.4d with HSE06+vdW [13]). In Figure 3.4a, at 300 K $\text{Ni}_1\text{Mg}_2\text{O}_3$ conformer, is the most stable phase in the low range of pressure (10^{-10} to 10^{-6} atm). With the increase in pressure, $\text{Ni}_1\text{Mg}_2\text{O}_5$, $\text{Ni}_1\text{Mg}_2\text{O}_9$ and $\text{Ni}_1\text{Mg}_2\text{O}_{11}$ compositions become favorable in the phase diagram, sequentially. Same trend for stable phases can be observed by decreasing the T at a fixed pressure value as shown in 3.4b. Similarly, we have plotted the 2D and 3D phase diagrams by using more advanced hybrid functional (HSE06+vdW). Here, we have calculated the electronic energies of $\text{Ni}_1\text{Mg}_2\text{O}_z$ clusters by using HSE06+vdW functional. Unlike PBE+vdW results, in Figure 3.4c, $\text{Ni}_1\text{Mg}_2\text{O}_3$ is the most stable phase in the range 10^{-10} to 10^{-4} atm of pressure and $\text{Ni}_1\text{Mg}_2\text{O}_4$ is the most stable one in the range 10^{-4} to 10^2 atm. 3D view shows that $\text{Ni}_1\text{Mg}_2\text{O}_3$ phase is stable in all range of pressure above 450 K, whereas in lower range of T and higher range of pressure $\text{Ni}_1\text{Mg}_2\text{O}_4$

is the favorable one. In view of this, we have carried out all the calculations using hybrid functional (HSE06+vdW).

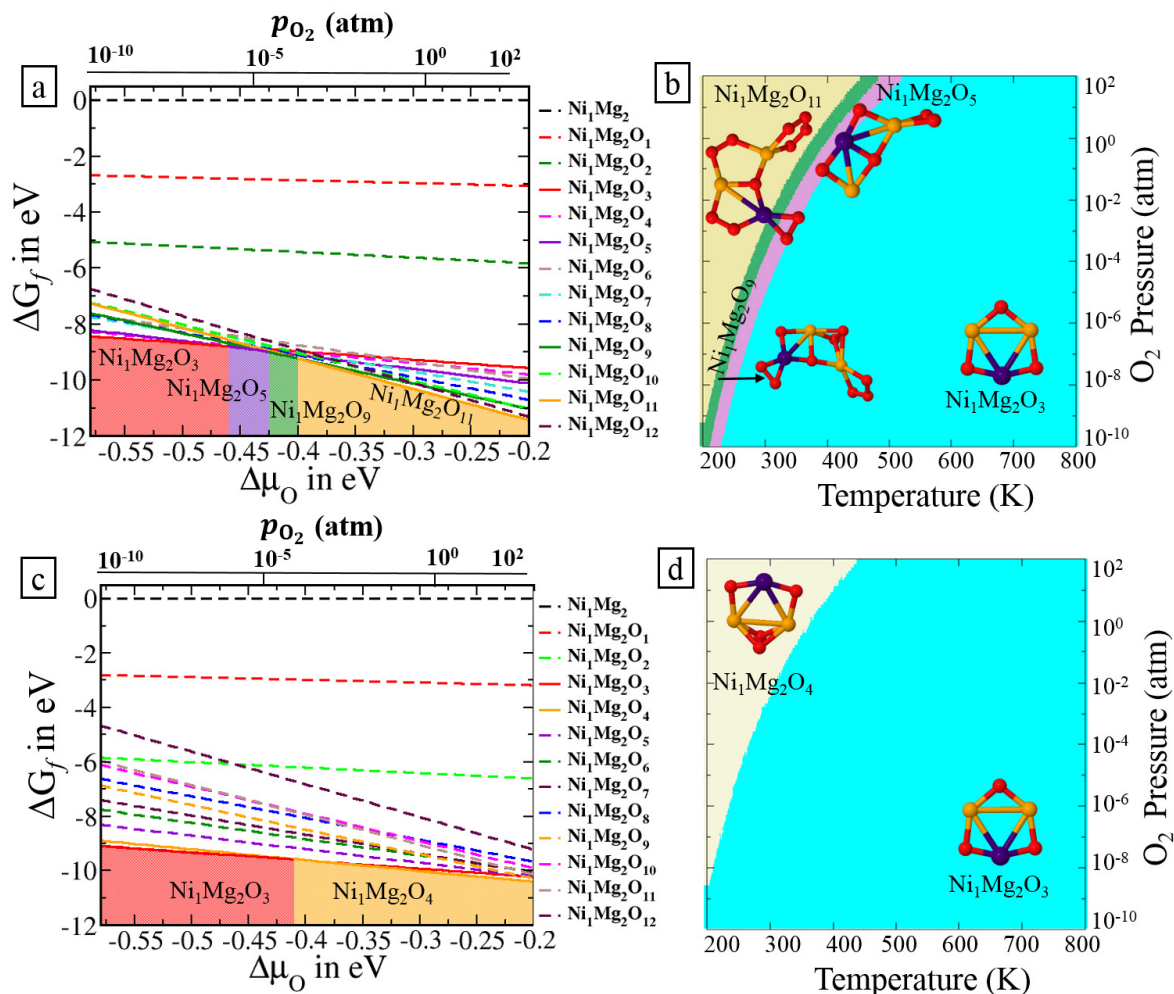


Figure 3.4: In Figure (a) and (c), ΔG_f varies as a function of chemical potential of oxygen at 300 K. Total energy of geometries are calculated using PBE+vdW and HSE06+vdW, respectively. Colored areas identify the stable phases. In Figure (b) and (d), 3D phase diagrams are shown corresponding to the 2D phase diagrams of $\text{Ni}_1\text{Mg}_2\text{O}_x$ clusters.

3.3.4 Determination of the stable phases of $\text{TM}_x\text{Mg}_y\text{O}_z$ clusters

Following this thermodynamic phase diagrams are calculated for all possible combinations of $x + y \leq 3$ ($y \neq 0$) in $\text{TM}_x\text{Mg}_y\text{O}_z$ clusters, and the most stable compositions and configurations are identified. In Figure 3.5(a-d) we show phase diagrams of a set of $\text{TM}_1\text{Mg}_2\text{O}_z$ clusters, where four different TMs viz. Cr, Co, Ni, Fe are investigated, respectively. The most stable configurations and the respective stable phases are shown within a window of experimentally

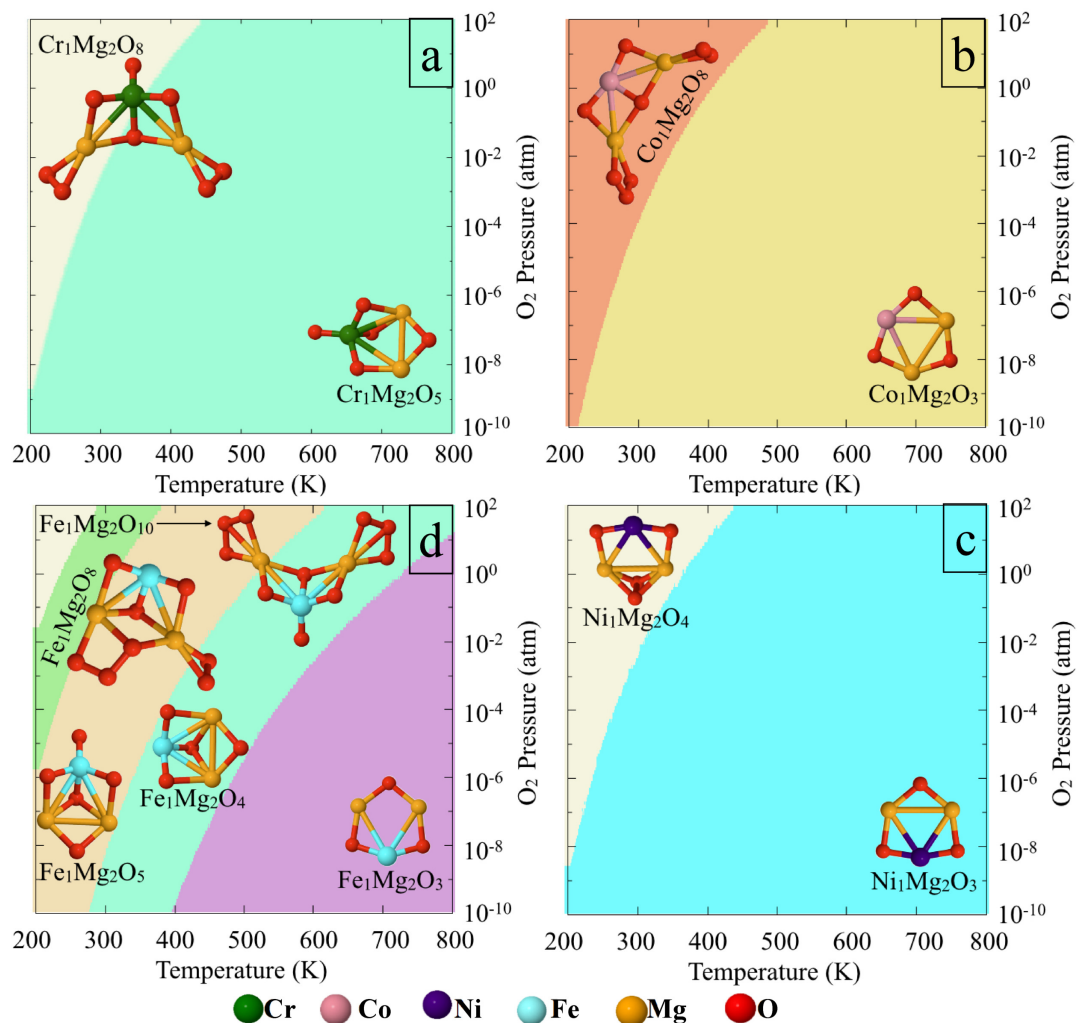


Figure 3.5: The most stable $\text{TM}_x\text{Mg}_y\text{O}_z$ clusters at various temperatures and pressures under thermodynamic equilibrium. In $\text{TM}_x\text{Mg}_y\text{O}_z$ clusters, TM = Cr (a), Co (b), Ni (c) and Fe (d). The geometries are optimized with PBE+vdW, and the electronic energy is calculated using HSE06+vdW. The vibrational free energy is computed under harmonic approximations.

achievable environmental conditions (T , p_{O_2} window). From Figure 3.5a, we see for TM = Cr and $x = 1$, $y = 2$ at low T and high p_{O_2} , $\text{Cr}_1\text{Mg}_2\text{O}_8$ is the most stable phase, while at high T and low p_{O_2} $\text{Cr}_1\text{Mg}_2\text{O}_5$ is the most stable phase. For TM = Co and Ni (see Figure 3.5b and Figure 3.5c) the stable phases are respectively $\text{Co}_1\text{Mg}_2\text{O}_8$, $\text{Co}_1\text{Mg}_2\text{O}_3$, and $\text{Ni}_1\text{Mg}_2\text{O}_4$, $\text{Ni}_1\text{Mg}_2\text{O}_3$. However for TM = Fe (see Figure 3.5d) at low T and high p_{O_2} there are a lot of competing isomers viz. $\text{Fe}_1\text{Mg}_2\text{O}_{10}$, $\text{Fe}_1\text{Mg}_2\text{O}_8$ and $\text{Fe}_1\text{Mg}_2\text{O}_5$. At a moderate T and moderate p_{O_2} i.e. $T \approx 300$ K, $p_{\text{O}_2} \approx 10^{-6}$ atm there is competition between two phases viz. $\text{Fe}_1\text{Mg}_2\text{O}_4$ and $\text{Fe}_1\text{Mg}_2\text{O}_5$. At high T and low p_{O_2} the most stable phase is $\text{Fe}_1\text{Mg}_2\text{O}_3$. Thus, we observe a general trend that usually O-rich clusters are more stable at low T and moderate to high p_{O_2} (i.e. upto $\approx 10^{10}$ atm).

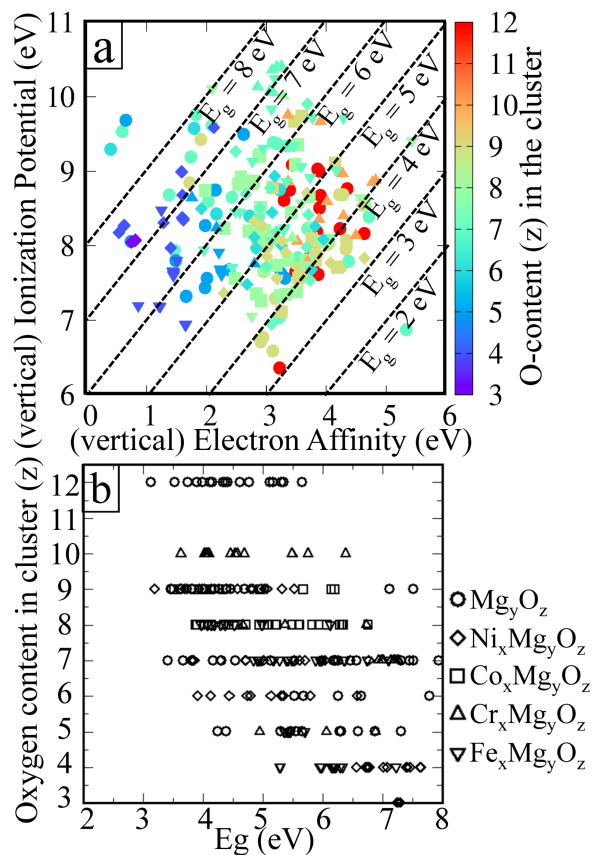


Figure 3.6: (a) VIP vs VEA for the low energy isomers stable at an experimentally achievable environmental condition for all different cluster sizes ($x + y \leq 3$). The symbols represent the nature of the TM atoms in the clusters, while the colour is set as per the amount of oxygen content (as shown by the colour bar) in the cluster. The loci of constant E_g are indicated by diagonal lines. (b) E_g vs oxygen content (z) is plotted for all the stable isomers at realistic conditions (see text for details).

The electronic structure of the clusters determines their reactivity, and can serve as a descriptor of the catalytic activity. Under reaction conditions, the catalyst comprises of a wide range of structures including different number of atoms with various oxidation states, all of which could be active to some extent in the catalytic reaction. Therefore, after identifying the most stable compositions (i.e., specific x , y , and z in stable phases of $\text{TM}_x\text{Mg}_y\text{O}_z$), we have studied electronic structure of not only the global minimum isomer of that given composition but also all the low-energy isomers lying within an energy window of 0.5 eV from the global minimum [184].

In Figure 3.6a we show VEA and VIP values (obtained by G_0W_0 @PBE0) of all such thermodynamically stable isomers. Typically we have included data for $\text{TM}_1\text{Mg}_1\text{O}_z$, $\text{TM}_1\text{Mg}_2\text{O}_z$, $\text{TM}_2\text{Mg}_1\text{O}_z$ with $\text{TM} = \text{Cr}, \text{Co}, \text{Ni}, \text{Fe}$. We have also included data for clusters without TM atoms, i.e., Mg_yO_z ($y = 1-3$) clusters. The symbols are selected as per the type of the TM

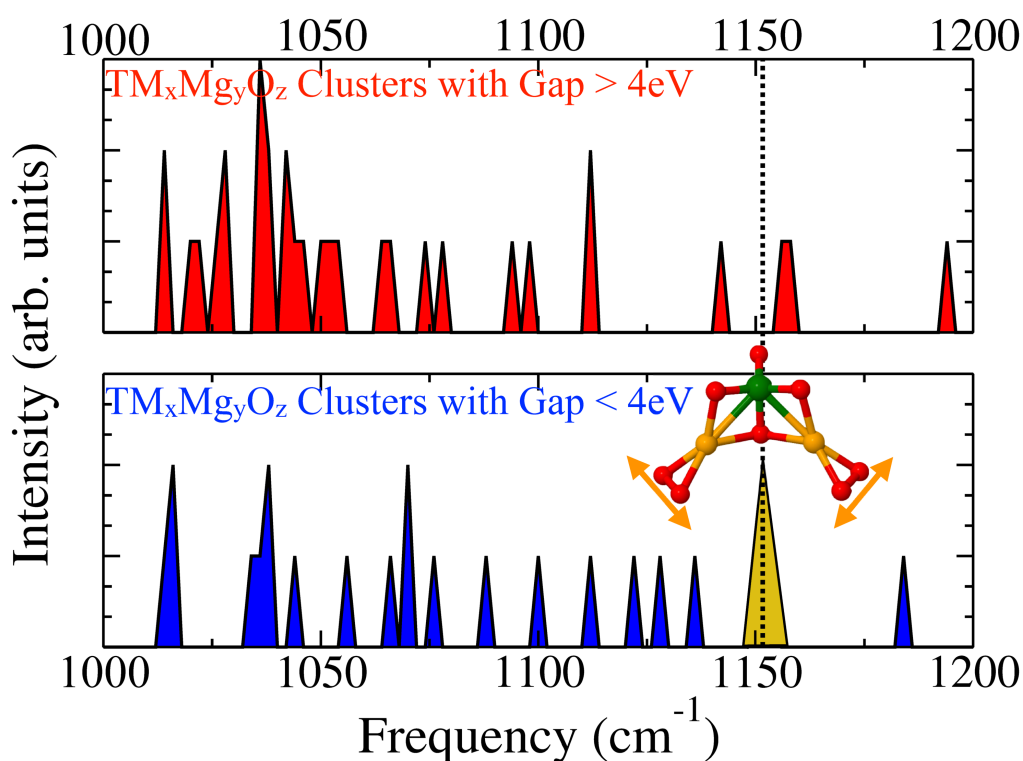


Figure 3.7: Histogram of vibrational frequencies ranging from 1000–1200 cm^{-1} for clusters (i) gap $>$ 4 eV (top panel) (ii) gap \leq 4 eV (bottom panel).

atoms in the clusters, while the colour of the symbols are selected based on the amount of oxygen content in the cluster. The diagonal lines are drawn to represent the corresponding constant E_g , which is evaluated as the absolute difference between VIP and VEA. Geometry coordinates and E_g are provided in supporting information. In Figure 3.6a the E_g for the clusters are widely scattered at all different sizes and nature of TM atoms. In Figure 3.6b we have explicitly shown E_g with different no. of oxygen content (z) in the clusters. Clearly, it is not following any trends except that the E_g for O-deficient clusters (i.e. $z \leq x + y$) are consistently in the higher side (see, bluish points in the Figure 3.6a and the region around low oxygen content ($z \approx 3-5$)). Thus, for sure it can be concluded from Figure 3.6 that O-deficient clusters (mostly stable at high T and low p_{O_2}) are not good for catalysis. However, for O-rich clusters (i.e. $z \geq x + y$) both high and low E_g are found (see Figure 3.6b around $z \geq 6$). This observation hints towards the fact that some structural feature in these O-rich clusters might act as active site that dominates the low E_g value. Moreover, the invariance of the E_g values for different TM clusters with same O-content emphasizes that it is not the nature of TM atoms but probably some active centers originating from oxygen moieties that affect the fundamental gap. Note that it

is common understanding that the former (i.e., nature of the TM atoms) is solely responsible for making the material a good catalyst [166, 165, 162, 163, 164, 159]. We have next divided our clusters into two sets viz., (i) having low gap (≤ 4 eV) and (ii) having high gap (> 4 eV). Following this, the vibrational frequencies (corresponding O-vibrations) of all the structures are carefully analyzed. In Figure 3.7, we show the histogram of vibrational frequencies by including an average of all vibrational spectra ranging $1000\text{--}1200\text{ cm}^{-1}$. Clearly the peak corresponding to the frequency 1151 cm^{-1} of the O_2 moiety bonded to the Mg atom, is missing for all clusters with the $E_g > 4$ eV (see in Figure 3.7). This means clusters with low E_g have some correlation with this Mg coordinated O_2 moieties, while clusters with higher E_g do not have this structural feature. To unravel the particular role of these O_2 moieties in the E_g , we

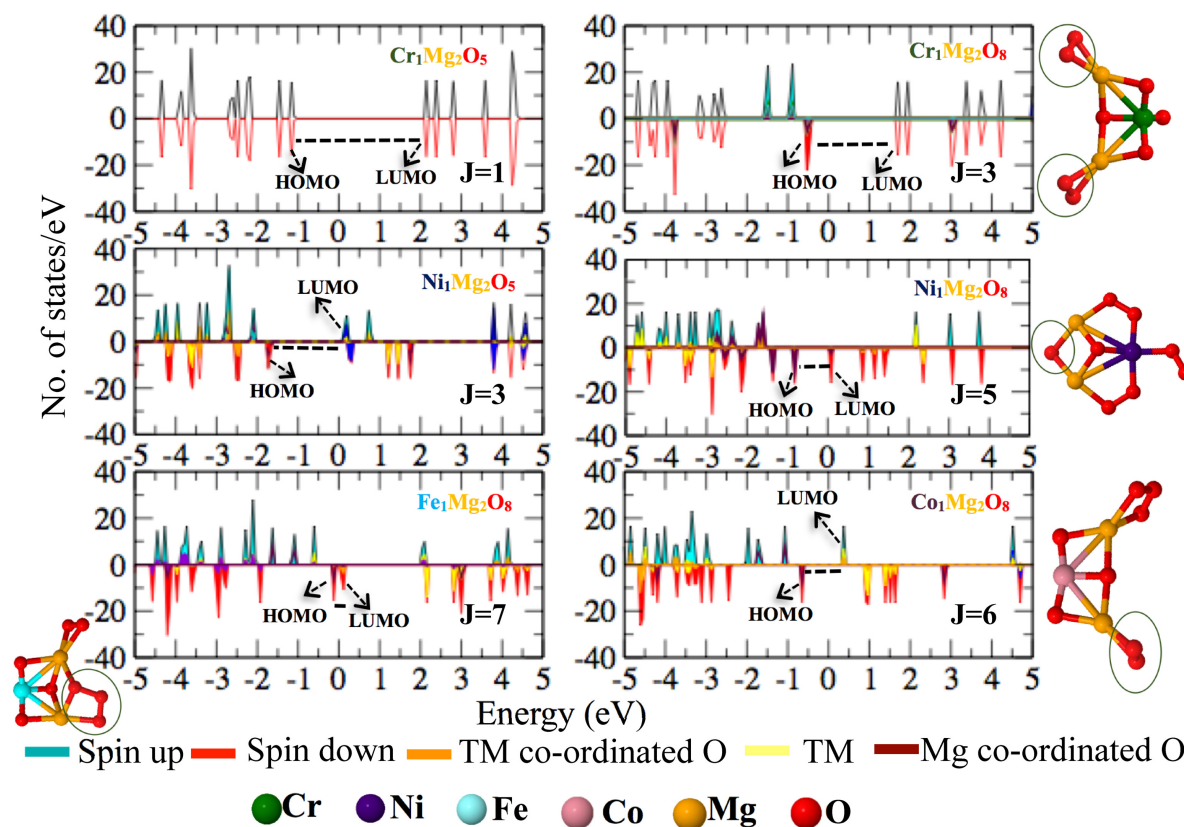


Figure 3.8: Atom-projected spin polarised density of states of different $\text{TM}_x\text{Mg}_y\text{O}_z$ clusters. The corresponding *spin multiplicity* (J) is also given in the respective plots. Oxygen atoms responsible for lowering the fundamental gap of a particular cluster are marked by dark green circle.

examined the density of states (DOS) profiles for different $\text{TM}_x\text{Mg}_y\text{O}_z$ clusters in Figure 3.8. We can see the HOMO-LUMO gap in $\text{Cr}_1\text{Mg}_2\text{O}_8$ is smaller than in $\text{Cr}_1\text{Mg}_2\text{O}_5$. Presence of spin-polarised states near fermi-energy (E_f) leads to the reduced HOMO-LUMO gap in the oxygen-rich phase. Further, comparing top panel in Figure 3.8 we observe that the presence of

TM (Cr) atom has minimal effect on the spin polarized states near E_f . These states occur only due to the extra oxygen atoms in $\text{Cr}_1\text{Mg}_2\text{O}_8$, whereas they are absent in case of $\text{Cr}_1\text{Mg}_2\text{O}_5$. To further understand if our observation is coincidental for Cr clusters or not, we have plotted the same for Ni clusters in Figure 3.8 (middle panel). We again observe the HOMO-LUMO gap to be smaller in case of oxygen-rich phase, i.e., $\text{Ni}_1\text{Mg}_2\text{O}_8$ in comparison to $\text{Ni}_1\text{Mg}_2\text{O}_5$. Including the insights from the atom-projected DOS, we conclude that the spin-polarized states are indeed the states of Mg-coordinated oxygen atoms in the O-rich clusters, which have caused a reduced E_g in these clusters. Next in Figure 3.8 (bottom panel), we see the O-rich phases of Fe and Co clusters respectively, which are having smaller E_g in comparison to their O-reduced phases. Again the atom-projected DOS indicate that the Mg coordinated O-atoms are playing pivotal role in the states near E_f and hence, are responsible for the reduced E_g in these clusters. The $\text{Fe}_1\text{Mg}_2\text{O}_8$ cluster has the lowest E_g among all because of the presence of spin-polarized $3d$ states of Fe near E_f . However, it can easily be seen from the comparison of $z = 5$ and $z = 8$ clusters that it is not the nature of TM atoms, but the states of Mg coordinated O atoms in the O-rich phases of each $\text{TM}_x\text{Mg}_y\text{O}_z$ cluster that play the crucial role in controlling the E_g . Irrespective to any specific TM atoms, TM has always states at the LUMO level, whereas the HOMO keeps on shifting depending on oxygen content in the cluster. Under O-rich condition, the clusters usually have O_2 (containing loosely bound electrons) coordinated with Mg atom. This gives rise to occupied states near E_f yielding a smaller E_g . Closing this section, we

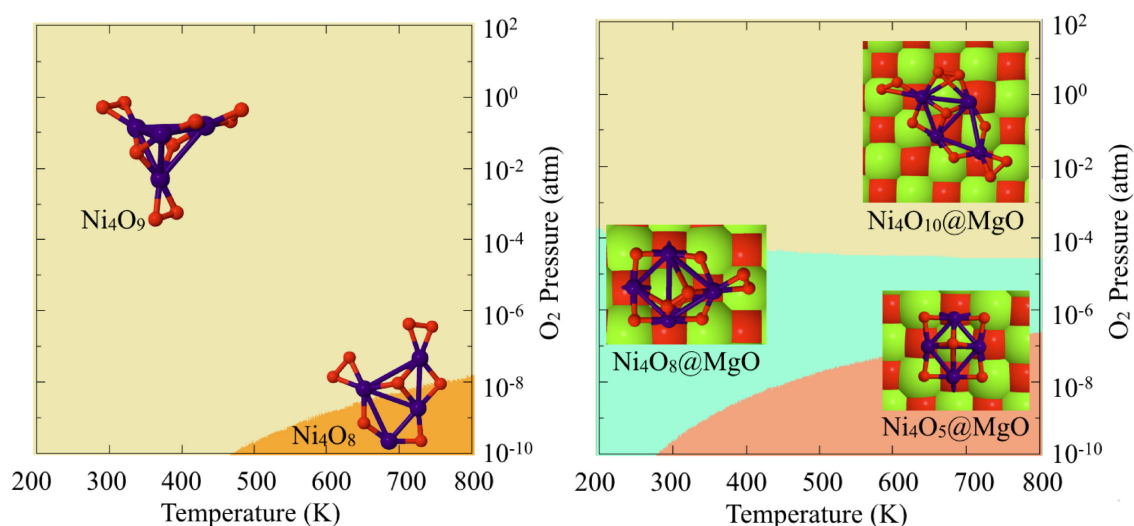


Figure 3.9: T - p_{O_2} phase diagram (see text) of Ni_4 clusters under oxygen atmosphere with (right) and without (left) MgO substrate. The red, navyblue, and green spheres represent O, Ni and Mg respectively.

demonstrate that an MgO support stabilizes further the excess of O on a metal-oxide cluster.

Figure 3.9 shows a comparison between the phase diagrams of Ni_4O_y clusters in the gas phase and supported on $\text{MgO}(100)$. Clearly, the oxygen-rich Ni_4O_8 and Ni_4O_{10} phases are stabilized by the support. Interestingly, at very low O chemical potentials clusters with less oxygen are stabilized. Thus, the support increases the variability of O content in supported oxide clusters at realistic temperature and pressure conditions.

3.4 Conclusion

In summary, we have used a robust first-principles approach to understand the stability and electronic structure of ternary $\text{TM}_x\text{Mg}_y\text{O}_z$ clusters at realistic temperatures and oxygen partial pressures. The low-energy isomers of different composition are determined by cascade genetic algorithm. Following that, the stable compositions are found by minimizing Gibbs free energy of formation using *aiAT* methodology (within harmonic approximation for the vibrational contributions). On analyzing the electronic structure of the clusters, we establish that the presence of Mg-coordinated-O in O-rich clusters (i.e. $z > x + y$) correlates with low E_g , whereas the nature of TM atoms is insignificant. We further note that these Mg coordinated O_2 moieties have unpaired electrons that give rise to multiple degenerate spin states. The latter play key role in producing a reduced E_g from the O_2 moieties at an environmental condition $T \approx 200\text{K} - 450\text{K}$ and $p_{\text{O}_2} \approx 10^{-6} - 10^{10}$ atm; while at higher temperature and lower pressure the stable clusters have less O-content. These observations lead us to argue that the chemical (redox) properties of mixed metal oxide clusters are sensitive to the oxygen content controlled by T and p_{O_2} rather than to the specific transition metal type. We hope that this finding will be helpful for understanding experiments with gas-phase and supported metal clusters at realistic (T , p_{O_2}) conditions, and for designing new functional nano-materials.

Electronic structures and catalytic activity of charged bimetallic oxide clusters

4.1 Introduction

Transition metals (TMs) are well known for their efficient homogeneous and heterogeneous catalytic activity [166, 165]. In heterogeneous catalysis, transition metal (TM) oxide nanoparticles (typically clusters consisting of a well-defined number of atoms) comprise a large family of catalysts that are used for selective oxidation of various hydrocarbons [35, 36, 37, 38, 39, 40, 41, 42, 43, 44]. From very recent studies, it has been revealed that the reactivity and selectivity of homogeneous metal oxides can be enhanced drastically upon doping and / or mixing with other metal atoms [47, 48, 49, 50]. The most active and selective TM oxides sometimes involve mixtures of multiple metal oxides [51, 52, 53], the performance of which is typically quite different from that of the component oxides. The catalytic activity in mixed oxide systems, can be explored by the stoichiometry, size and the structure of the catalyst. These bimetallic oxide clusters possess intriguing electronic properties to enhance the chemical reactivity of the composite systems. From previous chapter, we have conveyed (and validated by forming a huge data-set of $\text{TM}_x\text{Mg}_y\text{O}_z$ (TM = Co, Ni, Fe, Cr and $x+y \leq 3$) clusters) one central message; that catalytic reactivity of this type of bimetallic oxide system is expected to be correlated more strongly with oxygen rich environment than the choice of any specific TM atoms [153]. The latter is, however, conventionally believed to play the lead role in catalysis. The present work, therefore, originates addressing this open question that out of four chosen TM atoms viz. Fe, Cr, Co, Ni, which one should be the best choice for catalysis and why? It's interesting to understand the explicit role of TM despite one should aim for O-rich environment condition for synthesis of these catalysts. In the former chapter, we have introduced

$\text{TM}_x\text{Mg}_y\text{O}_z$ clusters but not commented anything on the thermodynamic stability of charged clusters. In view of this, in this chapter, we study the charged clusters to gain insights on how an excess or deficiency of charge density will influence its thermodynamic stability as well as catalytic properties. Note that in heterogeneous catalysis, TM nano-particles, at various charge states, exhibit significant variations as a function of size in their physico-chemical nature and electronic properties. In the presence of a realistic reactive atmosphere (i.e. temperature (T), pressure(p) and doping), clusters change their stoichiometry by adsorbing the ligands (usually oxygen) from the environment, under certain conditions [82]. This new composition (with specific active sites) may work as active (functional) material. Therefore, one has to understand the functional properties of clusters in a technologically relevant atmosphere. However, the unambiguous identification of active sites, detailed insight of elementary steps of the reaction process, the selectivity and the stability of intermediate products are sometimes a daunting task due to the complexity involved in catalytic processes.

In this chapter, we have generated a large data set $[\text{TM}_x\text{Mg}_y\text{O}_z]^{+/0/-}$ (TM = Cr, Fe, Co, Ni with $x + y \leq 5$) (even bigger than the former publication [153] $\text{TM}_x\text{Mg}_y\text{O}_z$ (TM = Cr, Fe, Co, Ni with $x + y \leq 3$)) consisting of all the neutral as well as charged clusters to analyze their thermodynamic stability. Following this, we have explicitly calculated the activation barrier of bimetallic clusters to abstract the first C–H bond from the methane. This step is considered to be a rate determining step for a catalyst to convert methane into valuable chemical products [56, 185, 186, 187, 188, 31, 33, 189, 190]. Numerous interesting studies for C–H bond activation of methane at room-temperature by various (noble-metals [189, 190, 191, 192], homonuclear [30, 31, 32, 33, 34] and heteronuclear [54, 193, 194, 187, 186, 195] metal oxides) gas phase clusters have been reported. Among them, noble metal based bimetallic clusters (i.e. $\text{RhAl}_3\text{O}_4^+$, $\text{RhAl}_2\text{O}_4^-$, $\text{PtAl}_2\text{O}_4^-$, AuV_2O_6^+ and $\text{AuTi}_3\text{O}_{7,8^-}$) exhibit high activity for methane activation [54, 55, 56, 57, 58]. However, high cost and the limited availability limits their commercialization. Therefore, currently, researchers are extensively focused to find the most promising substitutes based on non-noble active transition metals with high activity, low cost, and formidable abundance. From the literature, to the best of our knowledge, there are not many reports on this topic until date. We find only Li et al. have studied the activation of methane on transition-metal doped magnesium oxide clusters [195]. In view of this, we aim to address the activity of non-noble metal (Cr, Fe, Co and Ni) based MgO clusters. By analyzing the barrier height of first C–H bond activation of methane on different cluster configurations,

we have established a direct correlation of the fundamental gap with the activation barrier of a catalyst. Here, in addition to that, we have addressed the presence of active centres in these bimetallic oxide clusters to facilitate the first C–H bond dissociation in the context of methane activation. Moreover, we have explicitly provided the information of the governing factors (including the role of TMs, electronic structures and the charged states) on the active centre to improve its reactivity for methane oxidation. Further, the aim of the study is to address the role of charged states on the thermodynamic stability of the clusters and their efficiency in reducing the activation barrier for the reaction kinetics for methane oxidation.

4.2 Methodology

We have generated a large data set of bimetallic oxide $[\text{TM}_x\text{Mg}_y\text{O}_z]^{+/0/-}$ clusters (TM = Cr, Fe, Co, Ni with $x + y \leq 5$) at different charge states (+, 0, -). We have varied the value of z (no. of oxygen atoms) from zero to the saturation value, where no more oxygen atom can be absorbed by the cluster. As a first step, we have used a massively parallel cascade genetic algorithm (cGA) to thoroughly scan the potential energy surface (PES) to determine all possible low-energy structures (including the global minimum). All the DFT calculations are carried out using FHI-aims code [126], which is an all electron calculation using numeric atom centered basis set. The low energy structures obtained from the cGA are further optimized at higher level settings. In this step vdW-corrected (Tkatchenko-Scheffler scheme [178]) PBE+vdW [121] exchange and correlation (ϵ_{xc}) functional is used. The atomic forces are converged up to 10^{-5} eV/Å using “tight” settings with “tier 2” basis set as implemented in FHI-aims code. The atomic zero-order regular approximation (ZORA) is considered for the scalar relativistic correction [126, 196]. Finally, the total single point energy is calculated on top of this optimized structure using vdW-corrected-PBE0 [124] hybrid ϵ_{xc} functional (PBE0+vdW), with “tight - tier 2” settings. It is reported that PBE+vdW highly overestimates stability of clusters containing larger concentration of O-atoms [108]. This results in a qualitatively wrong prediction of O₂ adsorption for O-rich cases. Such behaviour is not confirmed by hybrid functionals [e.g HSE06 [123], PBE0] as employed in our calculations. The difference in energetics of PBE0 and HSE06 is always within 0.04 eV [153]. The spin states of the clusters are also different as found by PBE and PBE0/HSE06. In view of this, we have used hybrid ϵ_{xc} functional (PBE0) with tight numerical settings and tier 2 basis set to compute the formation energies of various

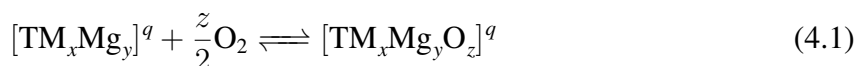
configurations [see details in the next section].

To examine the fundamental gap (E_g) of all the clusters, we have used state-of-the-art many-body perturbation theory within the GW approximation. We have calculated E_g at the level of $G_0W_0@PBE0$ with “really-tight” numerical settings and tier 4 basis set [126]. To determine the structure of the transition state (TS) and to find the minimum energy path for first C–H bond activation of methane on bimetallic clusters, we have used FHI-aims code using PBE ϵ_{xc} functional as implemented in aims-chain feature for doing the nudged elastic band method (NEB) calculations. We have analyzed the vibrational frequencies of TS to confirm the one imaginary frequency in the direction of the reaction coordinate.

4.3 Results and Discussions

4.3.1 Determination of the stable phases of $[\text{TM}_x\text{Mg}_y\text{O}_z]^{+/0/-}$ clusters

After generating the structures of all the low energy isomers of $[\text{TM}_x\text{Mg}_y\text{O}_z]^{+/0/-}$ clusters (TM = Cr, Fe, Co, Ni with $x + y \leq 5$) using cascade genetic algorithm, we study the thermodynamic stability of gas-phase $[\text{TM}_x\text{Mg}_y\text{O}_z]^{+/0/-}$ clusters in an oxygen atmosphere using the *ab initio* atomistic thermodynamics (*aiAT*) approach. Here we assume, when a bimetallic cluster is exposed in a reactive atmosphere of gas-phase O_2 , it will react with the atmosphere depending on environmental conditions (*viz.* T , p_{O_2} and doping (by doping we mean fixing of chemical potential of the electron (μ_e)) via the following equation:



q is the electric charge of the cluster. Here, we have used “+” for cationic clusters with charge +1, “0” for neutral, and “–” for the anionic clusters with charge –1. Since the ligand O_2 is a neutral species, the charge q remains the same during the reaction [197]. Using *aiAT*, we determine the Gibbs free energy of formation of all the $[\text{TM}_x\text{Mg}_y\text{O}_z]^{q}$ structures as a function of T , p_{O_2} , and chemical potential of electron (μ_e). The most preferred composition at a given T , p_{O_2} and μ_e , relevant for the experiments, will be the one that is having the minimum Gibbs free energy of formation at that experimental conditions. This is shown in the following equation:

$$\begin{aligned} \Delta G_f(T, p_{\text{O}_2}) = & F_{[\text{TM}_x\text{Mg}_y\text{O}_z]^{q}}(T) - F_{[\text{TM}_x\text{Mg}_y]^{0}}(T) \\ & - z \times \mu_{\text{O}}(T, p_{\text{O}_2}) + q \times \mu_e \end{aligned} \quad (4.2)$$

Here, $F_{[\text{TM}_x\text{Mg}_y\text{O}_z]^q}(T)$ and $F_{[\text{TM}_x\text{Mg}_y]^0}(T)$ are the Helmholtz free energies of the cluster+ligands $[\text{TM}_x\text{Mg}_y\text{O}_z]^q$ and the pristine $[\text{TM}_x\text{Mg}_y]^0$ cluster, respectively. The clusters are at their ground state configuration with respect to geometry and spin state. The term $\mu_{\text{O}}(T, p_{\text{O}_2})$ is the chemical potential of an oxygen atom ($\mu_{\text{O}} = \frac{1}{2}\mu_{\text{O}_2}$). The range of μ_e is taken from bulk MgO. The Valence Band Maximum (VBM) is the Fermi level of bulk MgO which is located at -7.5 eV as estimated from HSE06 functionals [181]. The free energy of each stoichiometry (cluster+ligands, pristine cluster) and the chemical potential of O_2 was evaluated from the corresponding partition functions including translational, rotational, vibrational, electronic and configurational degree of freedom. The dependence of $\mu_{\text{O}}(T, p_{\text{O}_2})$ on T and p_{O_2} is calculated using the ideal (diatomic) gas approximation with the same DFT functional as for the clusters. The details of this methodology can be found in Ref. [82]. Following this, a three dimensional (3D) phase diagram for all possible combinations of $x + y \leq 5$ ($y \neq 0$) of $[\text{TM}_x\text{Mg}_y\text{O}_z]^{+/0/-}$ clusters is constructed to identify the lowest free energy composition and structure at a specific T , p_{O_2} and μ_e condition (see Figure 4.1 where one specific case for $x = 2, y = 2$ is shown). From these type of phase diagrams, the stable compositions at a given environmental condition of $[\text{TM}_x\text{Mg}_y\text{O}_z]^q$ clusters can be determined. Here, on x-axis $\Delta\mu_{\text{O}}$ is varied in accordance with the corresponding T and p_{O_2} . On y-axis μ_e is varied from valence band maximum to conduction band minimum of the bulk MgO. On z-axis the negative $\Delta G_f(T, p_{\text{O}_2})$ values are plotted so that only the most stable phases are visible from the top. In Figure 4.1 (a-d), the phase diagrams of $[\text{TM}_2\text{Mg}_2\text{O}_z]^{+/0/-}$ clusters are shown as one of the representative cases for four different TMs viz. Cr, Fe, Co, and Ni, respectively. From Figure 4.1(a-d), it can be inferred that at lower values of μ_e (i.e. close to HOMO level at -7.5 eV; implying p-type doping condition) neutral clusters are more stable, whereas at higher values of μ_e (i.e. close to LUMO level at 0 eV; implying n-type doping) anionic clusters get more stabilized. For example, in case of TM = Cr, we see from Figure 4.1a that at fixed $T = 300$ K for values μ_e suitable for p-type doping and at lower values of p_{O_2} , $(\text{Cr}_2\text{Mg}_2\text{O}_8)^0$ is the most stable phase, whereas, as we increase the p_{O_2} , $(\text{Cr}_2\text{Mg}_2\text{O}_{10})^0$ is the most preferable phase in the phase diagram. However, if we set μ_e to the values suitable to n-type doping at lower p_{O_2} , $(\text{Cr}_2\text{Mg}_2\text{O}_8)^-$ is the stable phase and on increasing the p_{O_2} , $(\text{Cr}_2\text{Mg}_2\text{O}_{10})^-$ is favorable at ambient p_{O_2} and $(\text{Cr}_2\text{Mg}_2\text{O}_{12})^-$ becomes stable configuration at higher p_{O_2} . This trend of enhanced stability of neutral and anionic clusters, respectively for lower and higher values of μ_e (i.e. at a given doping condition) with varying p_{O_2} is also followed by other TMs (viz. Figure 4.1b-d, for Fe, Co and Ni, respectively). We

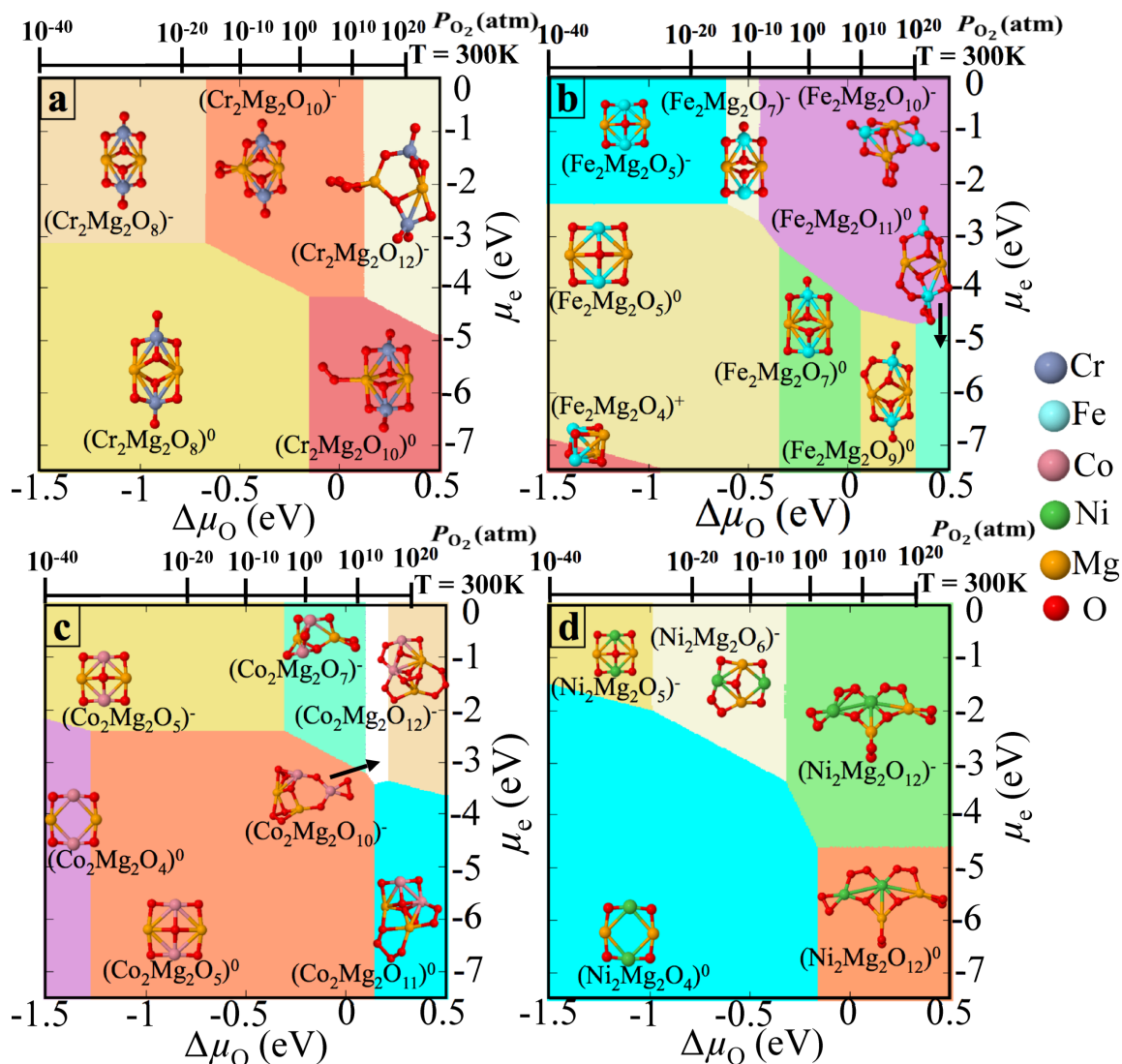


Figure 4.1: 2D view of 3D phase diagrams obtained for neutral and ionic $[\text{TM}_2\text{Mg}_2\text{O}_z]^{+0/-}$ clusters in the reactive atmosphere of O_2 . Coloured regions show the most stable compositions in wide range of pressures and μ_e under thermodynamic equilibrium. In $(\text{TM}_2\text{Mg}_2\text{O}_z)^{+0/-}$ clusters, TM = Cr (a), Fe (b), Co (c) and Ni (d). The top axis is representing the pressure of oxygen at $T = 300$ K.

have further noticed from these phase diagrams that at ambient environmental condition (i.e. $T = 300$ K, $p_{\text{O}_2} = 1$ atm) non-stoichiometric O-rich clusters are the most stable phases in all the cases. Following the representative case with $x = 2$ and $y = 2$, we have verified all possible combinations of x and y by limiting $x + y \leq 5$; to see the trends at other sizes. We have found that the observed trend in thermodynamic stability holds at other values of x, y as well and are in line the representative case i.e. (i) positively charged clusters are not stable throughout the phase diagram and (ii) non-stoichiometric O-rich phases (with charge $0/-$) are more favorable at ambient conditions. After identification of all the stable (and / or meta-stable) configurations at a realistic environmental condition it's now important to understand their catalytic properties

from electronic structure analysis.

4.3.2 Identification of the active center to abstract first C–H bond from CH₄

In order to calculate the activation barrier (E_a) for the C–H bond dissociation of methane (CH₄) molecule, we have initially checked the active sites to extract the first H-atom from methane molecule. We have tried different sites, and have found that O-site with higher negative charge density is the most favorable site to break the first C–H bond. In Figure 4.2, we have shown an example where we have placed CH₄ at the Ni-site and then optimized the structure. After optimization, we have found that CH₄ molecule favored the Mg-site which is bonded to the O-atom with higher charge density. In Figure 4.3, we have shown the structures of those clusters which have been considered to calculate E_a for C–H bond dissociation. Also, we have indicated the hirshfeld charge of all the atoms in the clusters. In Figure 4.3a, 4.3b, and 4.3d,

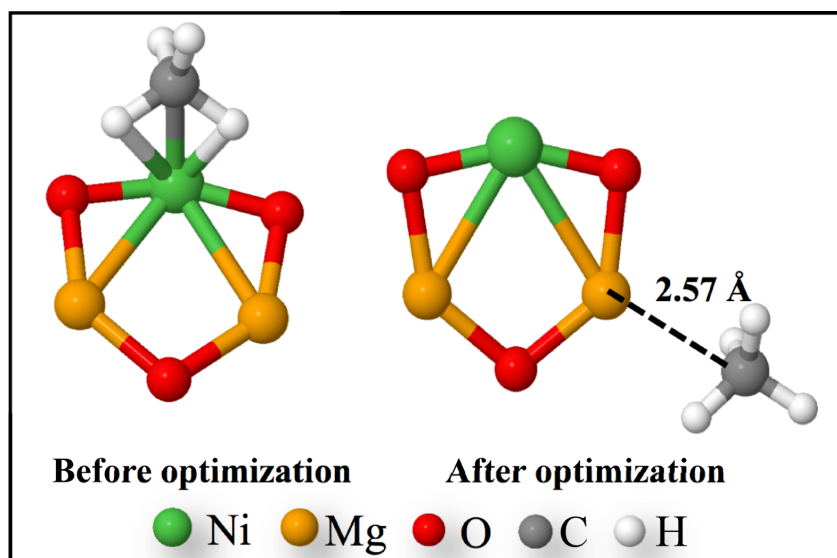


Figure 4.2: Structure of Ni₁Mg₂O₃ cluster with methane before optimization (left one) and after optimization (right one).

higher negative charge densities are corresponding to the O-atoms which are only coordinated to the Mg-atoms. In all the cases, Mg-atoms have more positive charge density as compared to Ni-atoms in the cluster. In Figure 4.3c, all the O-atoms have almost same negative charge because of symmetry in the positions, and in Figure 4.3e, the O-atoms in the top plane bonded with Mg-atoms have more negative charge as compared to the O-atoms in the below planes.

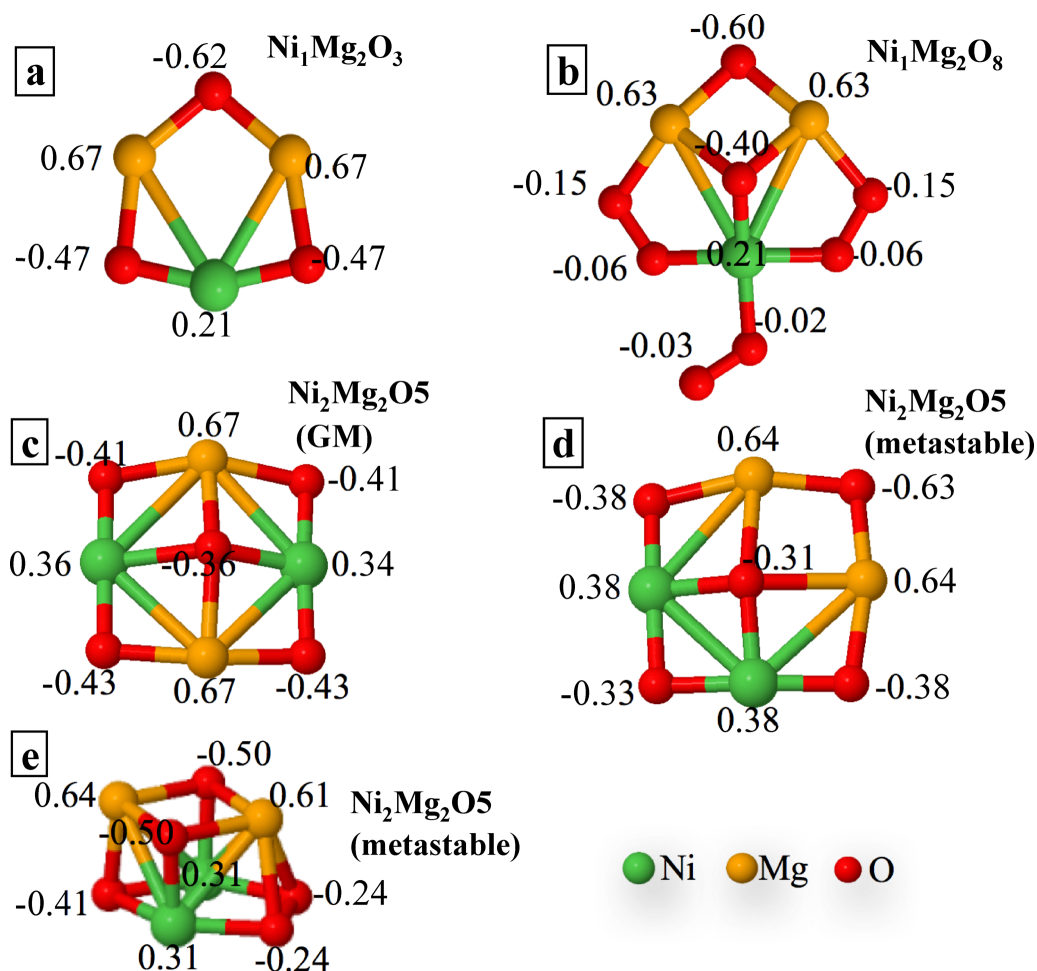


Figure 4.3: Structure of the global minimum (GM) for $\text{Ni}_1\text{Mg}_2\text{O}_3$, $\text{Ni}_1\text{Mg}_2\text{O}_8$ and $\text{Ni}_2\text{Mg}_2\text{O}_5$ clusters in (a), (b), (c), respectively. In (d) and (e), meta-stable structure of $\text{Ni}_2\text{Mg}_2\text{O}_5$ cluster with the charge corresponding to each atom. The partial charge density on each atom is calculated from the Hirshfeld charge analysis.

From Figures 4.3 and 4.3, we have a clear idea of the active sites where the cleaving of the C–H bond of CH_4 will be favorable. O-atom site with higher negative charge density is the best choice to activate the C–H bond of CH_4 . This O-atom is coordinated to Mg-atoms that have the higher positive charge and makes a favorable site to adsorb CH_3 when CH_3 –H bond breaks. To confirm the above mentioned analysis, we have performed the NEB to calculate E_a by considering both configurations, with higher negative charge (in Figure 4.4a) and lower negative charge (in Figure 4.4b) on O-atom site. In Figure 4.4a, the activation energy to cleave C–H bond is 82.44 kJ/mol while in Figure 4.4b, it is 115.68 kJ/mol. Also, cleaving of C–H bond at O-atom site with higher negative charge is an exothermic process (see the Figure 4.4a), whereas at the site of lower negative charge is an endothermic process (see the Figure 4.4b).

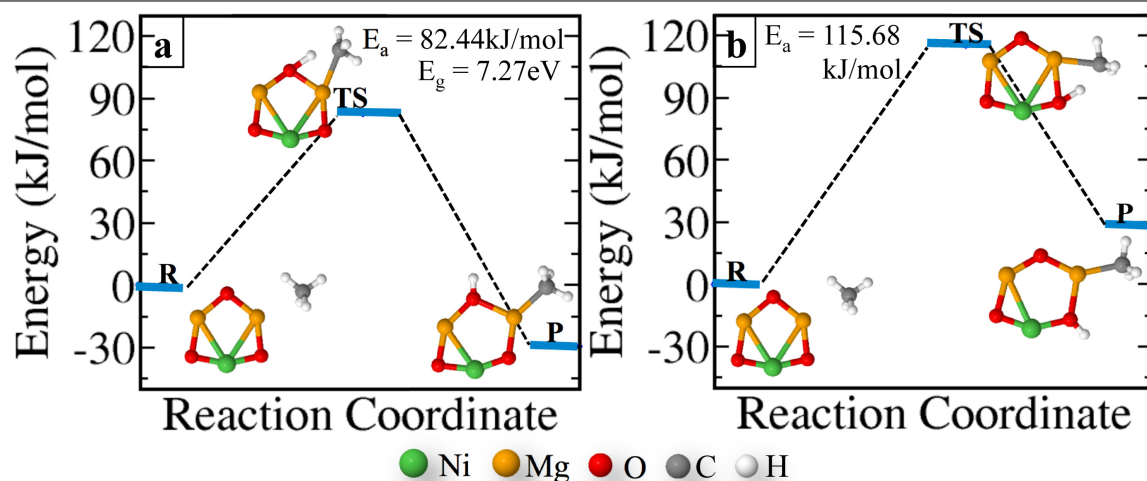


Figure 4.4: Potential energy surfaces for first C–H bond activation by $\text{Ni}_1\text{Mg}_2\text{O}_3$ cluster at the O-atom with the higher negative charge (a), and the lesser negative charge (b).

4.3.3 Correlation of fundamental gap (E_g) vs C–H bond activation barrier (E_a) of a catalyst

A catalyst is expected to be more effective, if it can accept or donate electrons more easily [90, 198]. Therefore, if a particular cluster has simultaneously high electron affinity (EA) and low ionisation potential (IP), it is expected to act as a good catalyst. This means the cluster should have a low fundamental gap (E_g), which is simply the difference between IP and EA. Over the past, E_g is been assumed in many instances to act as one of the descriptors to correlate reactivity of a catalyst [153, 168, 171, 90, 198, 199, 200, 201], for TMs based MgO clusters (viz. $\text{TM}_x\text{Mg}_y\text{O}_z$), we presumably for the first time, study the correlation of E_g with the catalytic activity. We, therefore, first try to investigate how a smaller E_g of $[\text{TM}_x\text{Mg}_y\text{O}_z]^{+/0/-}$ clusters is correlated with the C–H bond activation barrier (E_a) for oxidation of methane. This step is considered to be a decisive step for a catalyst to convert methane into valuable chemical products. To do that we have taken three different isomers of $\text{Ni}_2\text{Mg}_2\text{O}_5$ clusters as shown in Figure 4.5. The electronic charge density at each atom is also shown, whose relevance is discussed later. The structure in Figure 4.5a is the global minimum (GM) isomer, whereas the other two are low energy isomers lying within 2 eV from the GM. These three structures are used to estimate the C–H bond activation energy. In Figure 4.6, we have shown six different cases for the C–H bond activation on various configurations of $\text{Ni}_2\text{Mg}_2\text{O}_5$ cluster. We have compared the E_a values for the GM structure with one of the meta-stable isomers (see Figure 4.6a and c). We see a smaller E_a is associated with the meta-stable isomer than the GM as

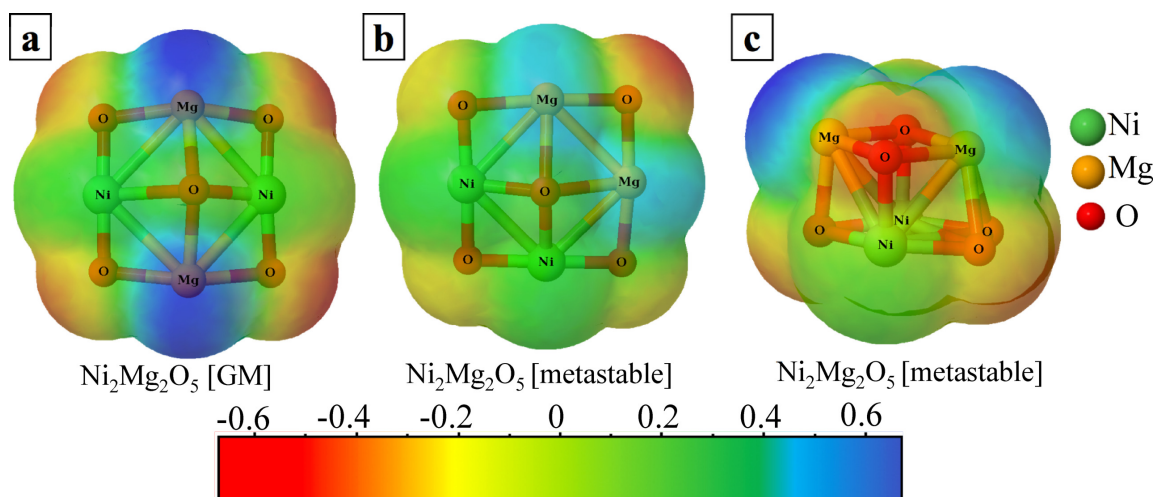


Figure 4.5: Electronic structures of $\text{Ni}_2\text{Mg}_2\text{O}_5$ cluster (global minimum (a), meta-stables (b) and (c)). Coloured surface represents the hirshfeld charge density in the cluster.

a catalyst. Therefore, the meta-stable isomer should be a better catalyst than the GM structure and this observation is inline to the E_g values of the respective clusters. The E_g of the meta-stable structure is indeed lower than the E_g of the GM structure. This clear correlation between E_g and E_a holds for most of the cases with a few exceptions, where they do not follow exactly the same trend. For example, if some structural feature of a specific catalyst starts working as active centre, it enhances its catalytic activity drastically. Let's focus on the third isomer shown in Figure 4.5c and compare it with the structure as in Figure 4.5b. The catalytic behaviour of these two respective clusters is shown in Figure 4.6e and 4.6c. We see [Ref: Figure 4.6e and 4.6c] the former structure [i.e. Figure 4.6c] is having a smaller E_g but not E_a than the latter structure as shown in Figure 4.6b.

The reason can easily be understood from identifying the active site present in the structure shown in Figure 4.5b by analyzing its hirshfeld charge distribution. But before this let us note a few important points. We find that the methane molecule gets adsorbed to the Mg-atom site (see Figure 4.2). This is due to the presence of more positive charge density into Mg atoms than the nearby TM atoms (see Figure 4.3 and Figure 4.6 for $\text{Ni}_2\text{Mg}_2\text{O}_5$ cluster). After C–H bond activation, the H atom favors that O-atom site which is more negatively charged as compared to other O-atoms in the cluster (see Figure 4.2, 4.3 and 4.4 for details) and CH_3 molecule gets adsorbed at Mg-site. Note that, the C–H bond activation energy depends on the charge density of the O-atom, where the H-atom tends to make a bond after dissociating from CH_4 . Therefore, in Figure 4.6, for the GM structure, all the O-atoms have an approximately equally distributed charge ($\approx -0.41e$) due to the nature of the symmetry in the position of atoms. On the

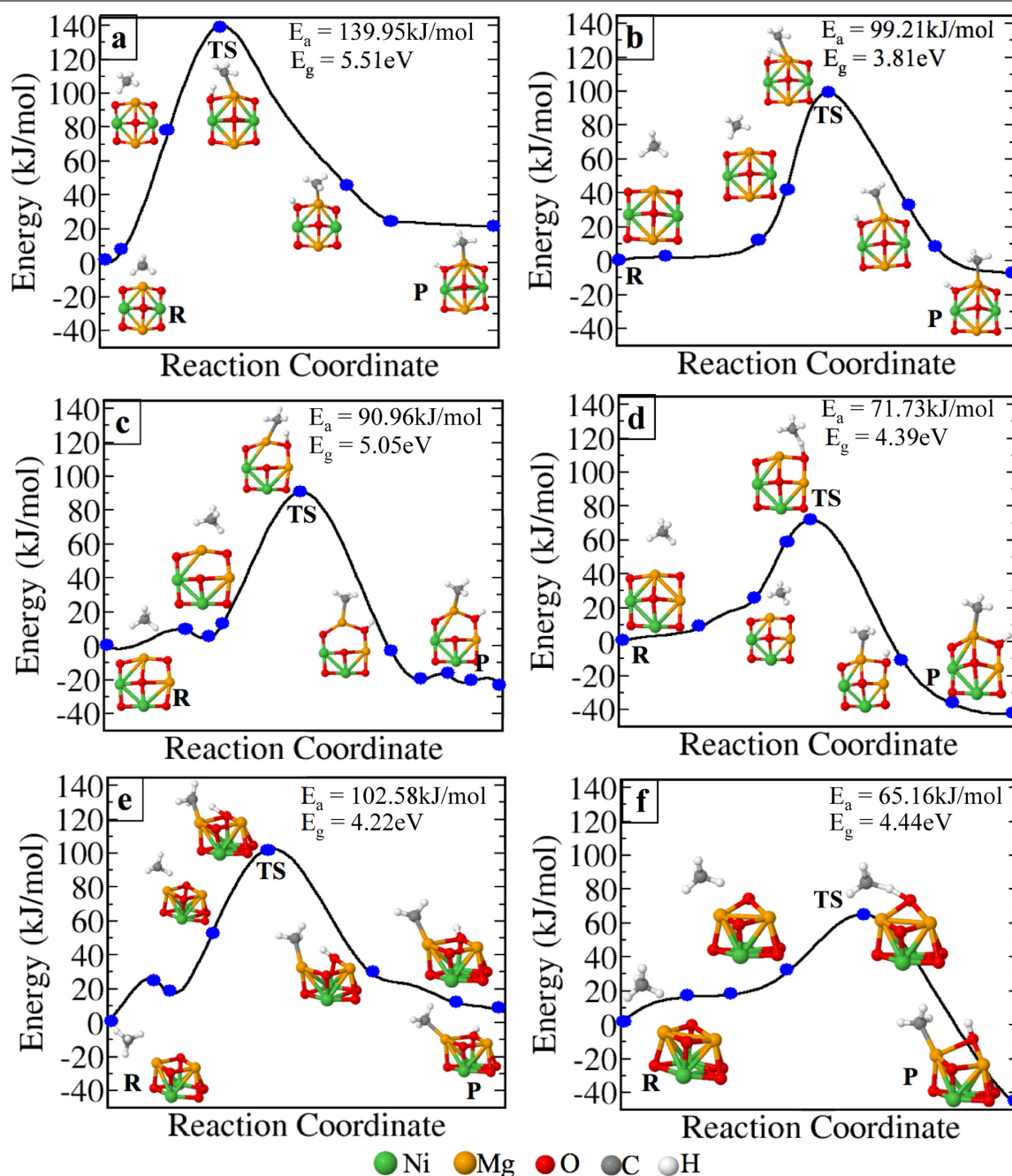


Figure 4.6: Minimum energy pathway of first C–H bond activation of methane on GM of neutral ($\text{Ni}_2\text{Mg}_2\text{O}_5$)⁰ cluster (a), negatively charged ($\text{Ni}_2\text{Mg}_2\text{O}_5$)⁻ (b), meta-stable structure of ($\text{Ni}_2\text{Mg}_2\text{O}_5$) cluster in neutral state (c and e), and meta-stable structure of $\text{Ni}_2\text{Mg}_2\text{O}_5$ cluster in negatively charge state (d and f). Reaction coordinate of initial (R), final (P), transition state (TS) and intermediates are shown. Activation barriers (E_a) for all cases are also indicated in the respective graphs in kJ/mol. The fundamental gap E_g of the clusters in all cases are shown in eV.

other hand, the meta-stable structures are somewhat asymmetric in nature. Thus, it has some O-atoms, where localized negative charge exists. This makes the site to act as an active centre. In Figure 4.5b and 4.5c, such cases are shown. Note that in Figure 4.5b, one O-atom with charge

density $\approx -0.63e$ is present to act as an active site, whereas in Figure 4.5c two such localized orbitals are noticed both with charge $\approx -0.50e$. The latter structure is less active than the former as two O-sites effectively reduces the overall activity as in the former structure with one active O-site (Figure 4.5b). Therefore, both the meta-stable structures are having smaller E_a and E_g than the GM structure. But the former one is supposed to be more effective with a reduced E_a than the latter one despite having a smaller gap than the former. We have obtained the better activity for C–H bond activation on Ni-based bimetallic clusters than the cationic gold cluster (Au_3^+) reported by Lang. et al. (131.33 kJ/mol) [189]. However, the activity of these clusters are slightly less as compared to the noble metal based bimetallic oxide clusters [56, 57].

From the phase diagram (as in Figure 4.1), the most stable phases are either neutral clusters (under p-typed doped condition) or negatively charged clusters (under n-type doped condition). Therefore, we have also shown the activation energy to break the C–H bond by negatively charged clusters. In fact we have noticed that the charged clusters are more effective in doing the same. In case of GM (see in Figure 4.6a and b), E_a for C–H bond activation by a negatively charged cluster is obtained to be much lower (99.21 kJ/mol) than the neutral one (139.95 kJ/mol). The trend in E_g for the $(\text{Ni}_2\text{Mg}_2\text{O}_5)^{-1}$ and $(\text{Ni}_2\text{Mg}_2\text{O}_5)^0$ are also in agreement with the respective E_a values. Further, we have also noticed a remarkable reduction in C–H bond activation barrier E_a by negatively charged meta-stable clusters (see in the Figure 4.6d and 4.6f). On adsorbing one electron the clusters possess localized charge, which acts as active centre to reduce the C–H bond activation barrier. Therefore, this analysis concludes that a smaller value of E_g is usually associated with a lowered C–H bond activation barrier E_a . The latter gets further reduced if the structure is also having one active centre with localized charged density. Note that, it's computationally very expensive to calculate E_a values of all the stable configurations of $[\text{TM}_x\text{Mg}_y\text{O}_z]^{+/0/-}$ clusters to understand their catalytic activity. However, a very good qualitative description can be drawn for the same, from comparing the respective E_g values (estimated with $\text{G}_0\text{W}_0@\text{PBE0}$) of all the isomers relevant at a realistic experimental conditions.

4.3.4 E_g is a descriptor for catalytic activity

We have considered all the neutral and ionic (-ve) clusters of the dataset ($[\text{TM}_x\text{Mg}_y\text{O}_z]^{0/-}$) to plot their E_g as shown in Figure 4.7(a-d). Here, we see the E_g of negatively charged clusters (red points) are tending to have smaller values than that of neutral clusters (black points). However,

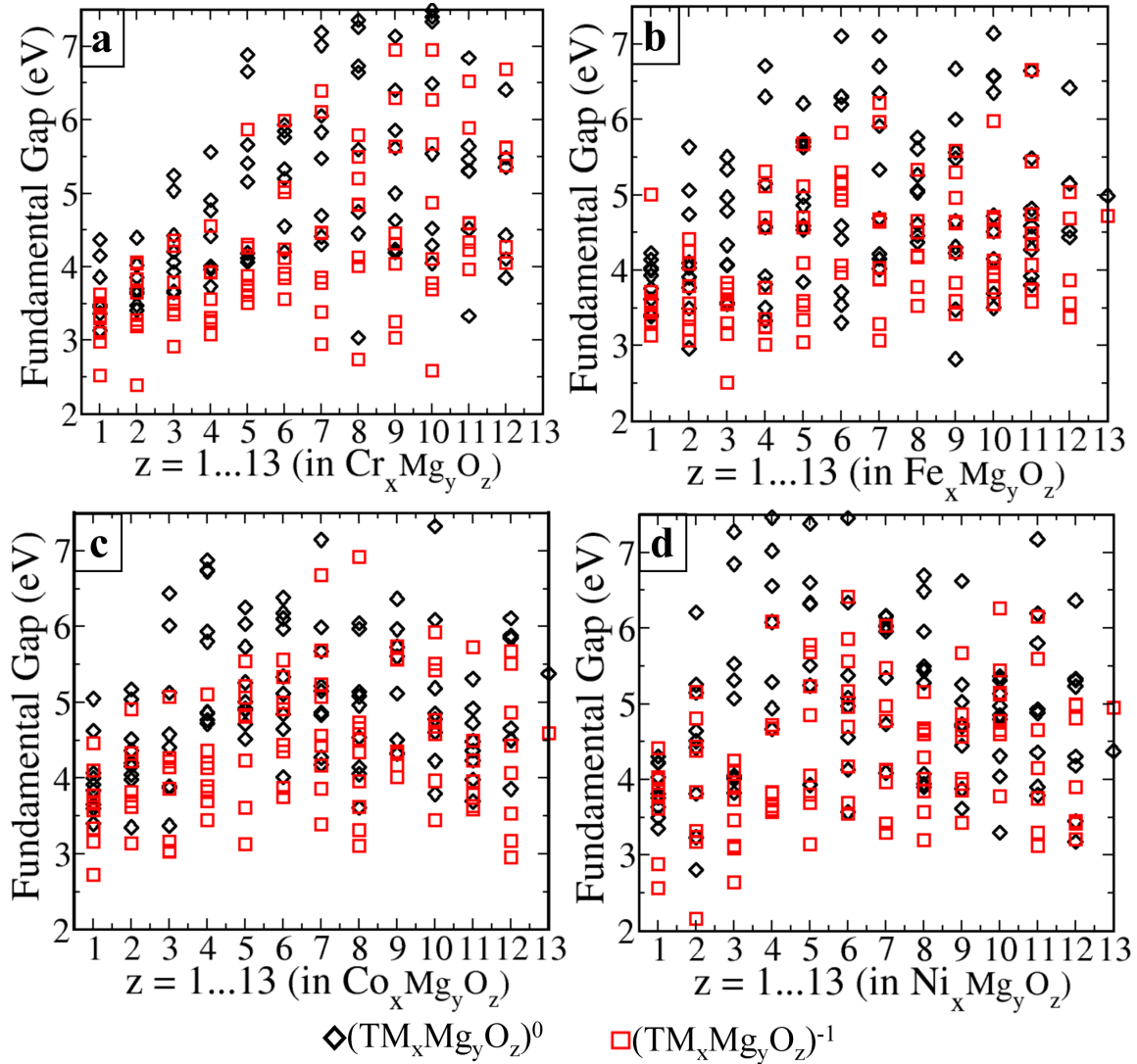


Figure 4.7: E_g ($G_0W_0@PBE0$) of all the charged and neutral $[TM_xMg_yO_z]^{0/-}$ clusters of the dataset are shown for TM = Cr (a), Fe (b), Co (c) and Ni (d) as a function of the oxygen content (z), which is varied from 1..13.

it should be mentioned here that there are some scattered red points showing larger E_g . We have manually checked those data-points (clusters) and found that the corresponding E_g of the neutral cluster is even higher. Note that this figure gives only overall qualitative trend but not any quantitative information of individual clusters to identify the E_g for neutral cluster and the same with one additional electron. By examine fundamental gap of all data points, we have found that the negatively charged clusters are consistently having smaller E_g than its neutral counterpart (except for only few cases). Therefore, for sure the negatively charged clusters are expected to be a better catalyst than the neutral clusters.

In addition to this, note that these data points are distributed in such a way that there is no specific trends of E_g for the choice of any specific TM atoms. This observation is inline

to our former publication [153], where we have shown that higher catalytic reactivity is correlated more strongly with the oxygen content in the cluster than with any specific TM type. However, despite TM atoms do not have much role to control the E_g , they give rise to different structural motifs in the $\text{TM}_x\text{Mg}_y\text{O}_z$ clusters with respective TM components [see Figure 3.1]. For some TMs, the structures contain molecular O_2 , whereas in some other cases, this O_2 gets dissociated and got adsorbed in atomic form. This is due to the presence of different no. of unpaired electrons in the outer shell of the TM atoms, giving rise to different types of structural features. This may play significant role in catalysis as active centres. It is therefore important to understand these structural difference in $\text{TM}_x\text{Mg}_y\text{O}_z$ clusters with various TM atoms.

4.3.5 Structural analysis: Radial distribution function of $\text{TM}_x\text{Mg}_y\text{O}_z$ clusters

In order to present a quantitative understanding of the structural motifs, in Figure 4.8 (a-d), we have shown the radial distribution function (RDF) for various $\text{TM}_x\text{Mg}_y\text{O}_z$ clusters with four different TM atoms (viz. Cr, Fe, Co and Ni and $z = [1..13]$). Note that, in general, there are three types of molecular O_2 adsorption in O-rich bimetallic $\text{TM}_x\text{Mg}_y\text{O}_z$ clusters viz. at atop site of metal atom, parallel site and cross bridge site [202, 203]. Bond length of O_2 moiety is highly dependent on the kind of adsorption at various mentioned sites. This is to be ≈ 1.33 Å, 1.35 Å and 1.57 Å for atop, parallel and cross bridge site, respectively (see Figure 4.8e). It should be mentioned here that the calculated bond length for isolated molecular oxygen O_2 is 1.22 Å, whereas the same for O_2^{-1} (superoxo) and O_2^{-2} (peroxo) are 1.36 Å, 1.6 Å, respectively. Thus, a superoxo moiety is formed when O_2 is adsorbed at atop and parallel sites, whereas a peroxo moiety is formed at cross bridge site. The bond length of O_2^{-1} (1.36 Å) is approximately equal to the bond length of O_2 moieties at atop (1.33 Å) and parallel site (1.35 Å). However, the bond length of O_2 moieties at cross site is comparable to the bond length of O_2^{-2} . Oxygen ions O_2^{-1} and O_2^{-2} are the reactive species that enhance the reaction of methane oxidation on bimetallic oxide clusters as catalyst [204]. In Figure 4.8, the first order peaks (orange coloured) in all cases correspond to the O_2 adsorption at atop and parallel sites. This first order peaks (orange coloured) are more intense (see Figure 4.8c and Figure 4.8d) for Co and Ni based bimetallic clusters. However, in case of Cr and Fe based clusters, the second order peaks (blue coloured) represent the (TM-O) bond length where one dangling oxygen atom is bonded only to the TM atom. If we see the structures in Figure 3.1, this TM-O case is totally

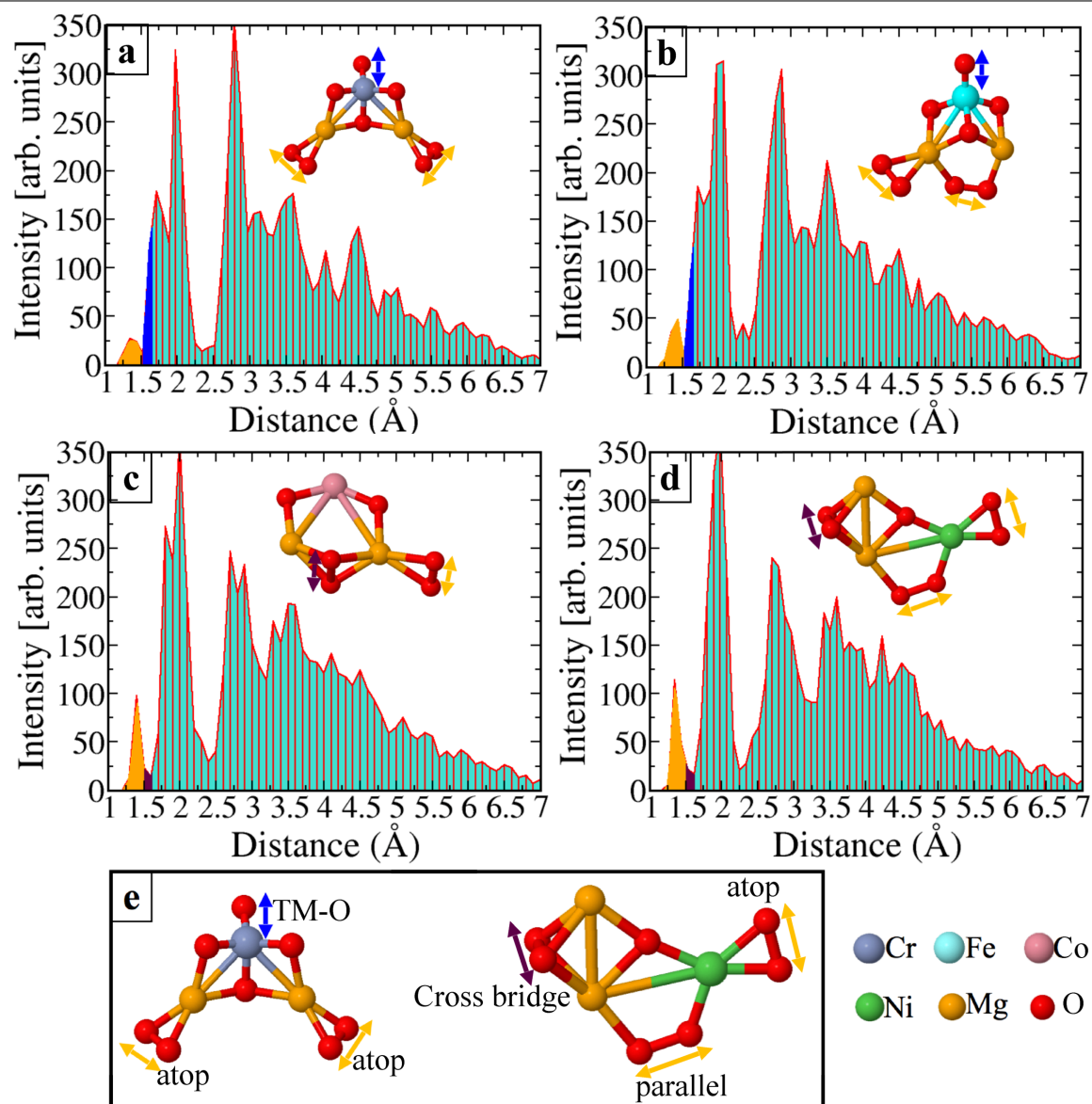


Figure 4.8: The radial distribution function for $\text{TM}_x\text{Mg}_y\text{O}_z$ [TM = Cr (a), Fe (b), Co (c) and Ni (d)] using all the data for all possible combination of x and y with $x + y \leq 5$ and $z=1..11$ set of clusters.

absent in Co and Ni based bimetallic clusters. Therefore, this blue coloured peaks are absent in Figure 4.8c and 4.8d. This signifies that in Cr and Fe based bimetallic clusters, a dissociative adsorption of O_2 is more favorable. On the other hand, in Co and Ni based bimetallic clusters a molecular adsorption of O_2 is favored. Note that the latter is the prerequisite for methane oxidation reaction. Further, we have noticed another peak of very reduced intensity (maroon colour) next to orange coloured peak as in Figure 4.8c and 4.8d. This peak represents the bond length of O_2 moieties bonded at cross-bridge site (bond length is same as TM-O bond). Note that O_2 moieties bonded at cross-bridge site have more electronic interaction with metal atoms in clusters as compared to O_2 moieties at atop site. Therefore, the bond length of cross-bridge

O₂ moiety is comparatively higher than atop moieties. However, with the increase of the no. of TM atoms in the clusters, dissociative adsorption of oxygen gets increased. This information should be very useful in the kinetic study to propose a reaction mechanism.

4.4 Conclusion

In summary, we have presented a robust methodology to study the catalytic activity of small TM based bimetallic oxide clusters. As a first step we have used a massively parallel cascade genetic algorithm to determine all the low energy isomers. The thermodynamic stability of such structures are determined by minimizing their Gibbs free energy of formation using *ab initio* atomistic thermodynamics method. A smaller C–H bond activation barrier is noticed when the cluster possesses both a smaller fundamental gap alongwith an active centre for higher catalytic activity. The negatively charged clusters are in general more promising candidates for having smaller activation barrier with high stability. The role of TMs towards controlling the activation barrier is less. However, the nature of TMs determine the favorable type of O₂ adsorption. Since Co and Ni based clusters favor molecular O₂ adsorption, they are expected to have a better catalytic performance amongst various TM_xMg_yO_z clusters.

Effect of nitrogen doping on the stability and electronic properties of (meta-)stable $(\text{TiO}_2)_n$ clusters

5.1 Introduction

Accurate prediction of the structure of clusters as a catalyst, under reaction conditions, is the most fundamental challenge to get a detailed understanding of the active sites and their importance. First principles based state-of-the-art global optimization methods viz. genetic algorithm (GA)[144, 145, 146, 147, 148], basin-hopping (BH)[205], parallel tempering[206], particle-swarm optimization (PSO)[207], stochastic tunneling[208], simulated annealing (SA)[209] etc. can predict the catalysts' structure. Moreover, if we have some primary information such as the elemental constituents in the catalyst and its reaction conditions (e.g. temperature and pressure, doping concentration, etc.), accurate prediction of the equilibrium state is in principle possible via *ab initio* thermodynamics [82]. However, this situation becomes complicated for real catalysis if we look deep into the practical correlation of the predicted structure and its relevance with the concerned catalytic reactivity. The structures closer to the global minimum (based on ground state total energies) have higher occurrence probability at a finite temperature, but that does not ensure these structures are responsible for the observed activity [88]. On the other hand, metastable isomers of the catalyst are definitely not as stable as its global minimum structure but may lead to having higher activity due to presence of active sites. Moreover, under reaction conditions, the catalyst comprises of a wide range of structures all of which could be active to some extent in the catalytic reaction [87]. Over the past, in most of the theoretical studies of clusters, it is assumed that experimentally probed clusters are in their ground state conditions due to thermodynamic equilibrium [107, 210, 211, 212, 213]. Contrary to this, few experimental and theoretical studies have revealed that the experimentally detected clusters are

the metastable isomers, rather than the ground-state ones [214, 215, 138, 90]. Here we present a robust theoretical approach to study the active sites of a cluster by taking a prototypical model system for Transition-metal (TM) oxides, in particular titanium dioxide (TiO_2), owing to its ubiquity, low cost, stability, nontoxicity, catalytic activity and environment friendly nature.

TiO_2 has a great significance in photocatalysis from the perspective of industrial applications [216, 217, 218, 219, 220, 221, 222, 223, 224]. However, the wide band gap of TiO_2 that only absorbs the UV light of the solar spectrum, limits its efficiency in technological applications. Previous works suggest that the non-metal doping enhances the photoactivity of nanoclusters of TiO_2 [225, 226, 227, 228, 229, 230]. The higher photocatalytic activity and stronger optical response are noticed with an increase of the N-doping concentration in TiO_2 nanophotocatalyst [231, 154, 226, 155, 229, 232, 156, 233, 157, 158, 162]. Xiaobo *et al.* have revealed additional electronic states for non-metal dopants (N, C and S), above the valence band edge of pure TiO_2 nanomaterials using X-ray photoelectron spectroscopy (XPS) [229], which lead the substantial modification in the optical properties. On the contrary, in theoretical study of Shevlin *et al.*, no response in visible region is reported for N-doped TiO_2 clusters[8]. The viable reason of this discrepancy of theoretical and experimental finding is, in the theoretical work they have addressed only the most stable substitutional N-defects, whereas in the XPS spectra both substitutional and interstitial (meta)stable defects are detected [229].

Therefore, it is well known these days that electronic properties of nanoclusters highly depend on structural configuration and particularly for the catalysis purpose, metastable structures are promising choice rather than the global minimum structure [214, 88, 138, 212]. Note that previous studies have suggested that clusters possessing a high vertical electron affinity (VEA) or a low vertical ionization potential (VIP) are the promising choice as a photocatalyst. This is due to their ability to accept or donate an electron more readily [138, 90, 214, 234, 235]. We have, therefore, implemented a suite of massively parallel cascade genetic algorithms (GA). The first is the conventional energy-based GA [viz. $(\text{GA})_E$] as described in detail in Ref [82]. This will give us all the local isomers close to energy based global minimum. The second GA is tailored explicitly to find metastable structures having specific bias for a property [viz. $(\text{GA})_P$]. This specific property is used to evaluate the fitness function for $(\text{GA})_P$. If this property is high vertical electron affinity, we call it $(\text{GA})_P^{\text{EA}}$, whereas if it is low vertical ionization potential we represent it as $(\text{GA})_P^{\text{IP}}$. As a test case, we have shown the performance of these three GAs [viz. $(\text{GA})_E$, $(\text{GA})_P^{\text{EA}}$, $(\text{GA})_P^{\text{IP}}$] for pristine $(\text{TiO}_2)_n$ clusters at various sizes in Figure 5.1. It is clearly

shown that while $(\text{GA})_E$ searches low energy clusters, $(\text{GA})_P$ focuses on some metastable part of the PES to optimize some specific properties. More details and validity of this implementation can be found in Ref [90]. Here, we have applied these three GAs to build a database of pristine as well as doped $(\text{TiO}_2)_n$ clusters with $n = 4 - 10, 15, 20$. Note that we have investigated three different configurations of N-doped $(\text{TiO}_2)_n$ nanoclusters to modify electronic properties at sub-nanometer scale: (a) N replaces O-atom making a substitutional defect (N_O) , (b) N as interstitial $(\text{NO})_O$, and (c) $(\text{N}_2)_O$ where both N substitution as well as interstitial share the same site.

In this chapter, as a first step from an exhaustive scanning, we have considered three types of (un)doped $(\text{TiO}_2)_n$ clusters: (i) clusters having the minimum ground state total energy (ii) clusters with high vertical electron affinity (VEA), and (iii) clusters possessing the low vertical ionization potential (VIP). Note that despite (meta)stable structures are promising candidates for catalysis, their free energy of formation should not be too far away from the free energy based global minimum. Therefore, we determine the thermodynamic stability of these structures by minimizing its Gibbs' free energy of formation as a function of charge state at realistic conditions (e.g. temperature (T), oxygen partial pressure (p_{O_2}), doping) [82, 236, 237, 238, 239]. This facilitates us to estimate the probability of occurrence of these (meta)stable structures. Following this, a few clusters, that are thermodynamically stable as well as possess active sites, are selected and their electronic structures are accurately analyzed using GW calculations. Further, we have performed the OER and HER on these clusters to understand the catalytic performance and active sites of stable and metastable configurations. We have also examined the electrochemical potential/pH (Pourbaix) diagram to understand the relative electrochemical stability of these N-doped (meta)stable clusters in aqueous environments. The electrochemical stability is a crucial factor to determine the performance and durability of these systems as a function of electrode potential and pH. In this way, we have systematically studied doped $(\text{TiO}_2)_n$ clusters for application in electrocatalytic water splitting.

5.2 Methodology

All density functional theory (DFT) calculations have been performed using FHI-aims code, which is an all electron code with numeric, atom-centered basis set [126]. To find the preferred site for different types of defects $[\text{N}_O, (\text{NO})_O$ and $(\text{N}_2)_O]$ in the clusters, we have employed

cascade GA [82, 90]. While running GA, the optimization is done with vdW-corrected [178] PBE [121] functional [PBE+vdW]. We have used “tight - tier 2” settings [126], and force tolerance is set to 10^{-5} eV/Å. We have reported in our previous studies [108, 212, 82, 215, 213] that PBE+vdW energetics give qualitatively wrong prediction for the stability of oxide systems. Therefore, inside cascade GA, right after optimization, we run a single point energy calculation via vdW-corrected-PBE0 [124] hybrid exchange correlation functional (PBE0+vdW), with “tight - tier 2” settings to determine the fitness function of various defect configurations. Note that for property based cascade GA i.e. $(GA)_P$ the VEA/VIP values are obtained via delta-scf method [90] at the level of PBE0+vdW. Note that an accurate choice of functional for estimation of the fitness function of different clusters is essential for a meaningful scanning of the PES. We have thoroughly validated this in Ref [108, 82, 90].

After getting the low energy N-doped $(TiO_2)_n$ ($n = 4 - 10, 15, 20$) configurations for all the sets of clusters ($(GA)_E$, $(GA)_P^{EA}$ and $(GA)_P^{IP}$ based clusters), we study the thermodynamic stability of the N-doped $(TiO_2)_n$ clusters in an oxygen atmosphere using the *ab initio* atomistic thermodynamics (*aiAT*) approach. Using this approach, we can determine the stability of defect states by minimizing the Gibbs’ free energy of formation at different T and p_{O_2} . We have used many-body perturbation theory within the GW approximation to evaluate the fundamental gap (E_g) and excitation energy (E_x) of all the defect configurations. “Really-tight” numerical settings and tier 4 basis set [126] are used to calculate E_g at the level of $G_0W_0@PBE0$.

5.3 Results and Discussions

5.3.1 VEA, VIP and Relative energy of pristine $(TiO_2)_n$ clusters

As mentioned above, to study N-doped $(TiO_2)_n$ clusters, as a first step, a robust scanning of the potential energy surface (PES) is done by $(GA)_E$, $(GA)_P^{EA}$, and $(GA)_P^{IP}$ based algorithm. This helps in building a large data set (global minimum and metastable clusters) to provide a realistic description of structures and electronic properties. Moreover, it helps us to identify all possible energetically favorable positions of N related defects (either substitution, interstitial or combination of both) in $(TiO_2)_n$ clusters. In Figure 5.1(a-c), we have plotted VEA, VIP and relative energy of undoped clusters which are scanned by $(GA)_E$, $(GA)_P^{EA}$ and $(GA)_P^{IP}$ algorithm, respectively. Each GA has scanned the different regions of the configuration space. The energy based algorithm [$(GA)_E$] has scanned the clusters with minimum energy (bluish

points in Figure 5.1a), whereas the property based algorithms $[(\text{GA})_p^{\text{EA}}$ and $(\text{GA})_p^{\text{IP}}$] have scanned the clusters with higher energy than that obtained by $(\text{GA})_E$ as shown in Figure 5.1b and 5.1c.

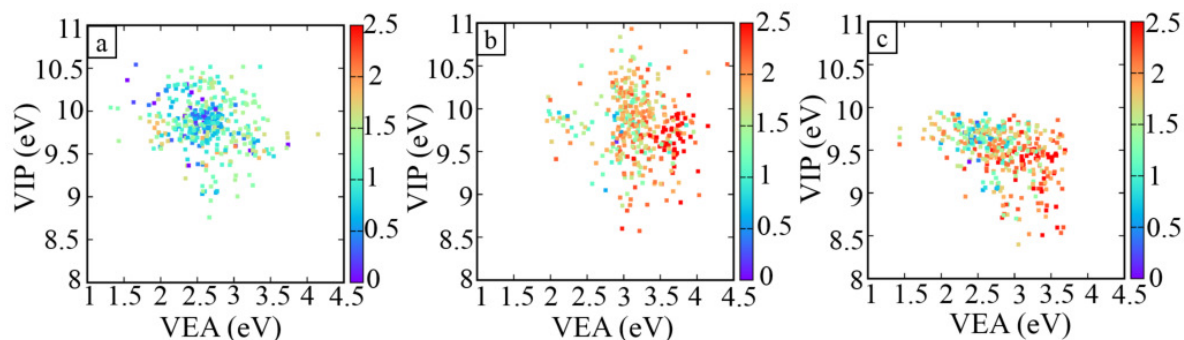


Figure 5.1: VIP vs VEA for the low-energy isomers of (a) $(\text{GA})_E$, (b) $(\text{GA})_p^{\text{EA}}$ and (c) $(\text{GA})_p^{\text{IP}}$ based clusters. The color bar represents the relative energy. The single point energy is calculated with PBE0+vdW, whereas VIP and VEA are determined with G0W0@PBE0.

5.3.2 Density of states for undoped $(\text{TiO}_2)_{10}$ cluster

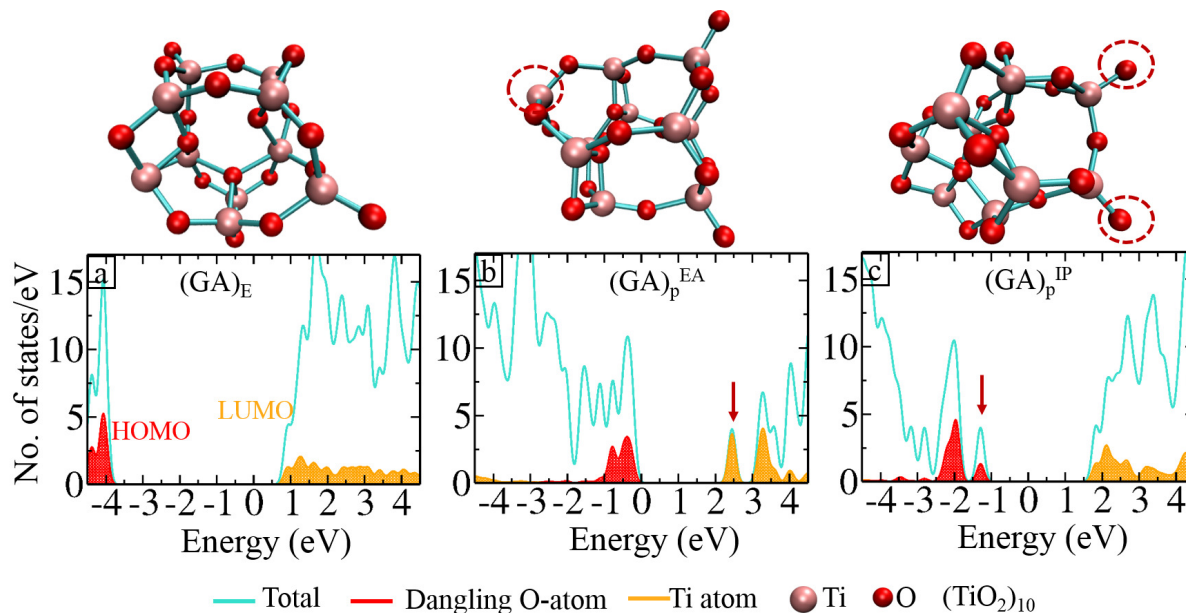


Figure 5.2: TDOS and PDOS for $(\text{TiO}_2)_{10}$ cluster.

In Figure 5.2, we have shown the total density of states (TDOS) and atom-projected density of states (PDOS) that are mainly contributing at HOMO and LUMO level. At HOMO level, states are highly localized to the dangling O-atoms, whereas LUMO states are localized to the Ti-atom, which is at the maximum distance from the dangling O. Low energy based cluster

shows the higher HOMO-LUMO gap in comparison to property based clusters. The reduction in the gap is attributed to the highly localized peaks near LUMO and HOMO level, in case of $(GA)_p^{EA}$ and $(GA)_p^{IP}$ based clusters, respectively.

5.3.3 Structural details to form $(N)_O$, $(NO)_O$ and $(N_2)_O$ in $(TiO_2)_n$ clusters

In Figure 5.3(a-c), we have shown the favorable defect sites as $(N)_O$, $(NO)_O$ and $(N_2)_O$ in N-doped $(TiO_2)_{10}$ cluster, respectively. We have found that O-site with high coordination is

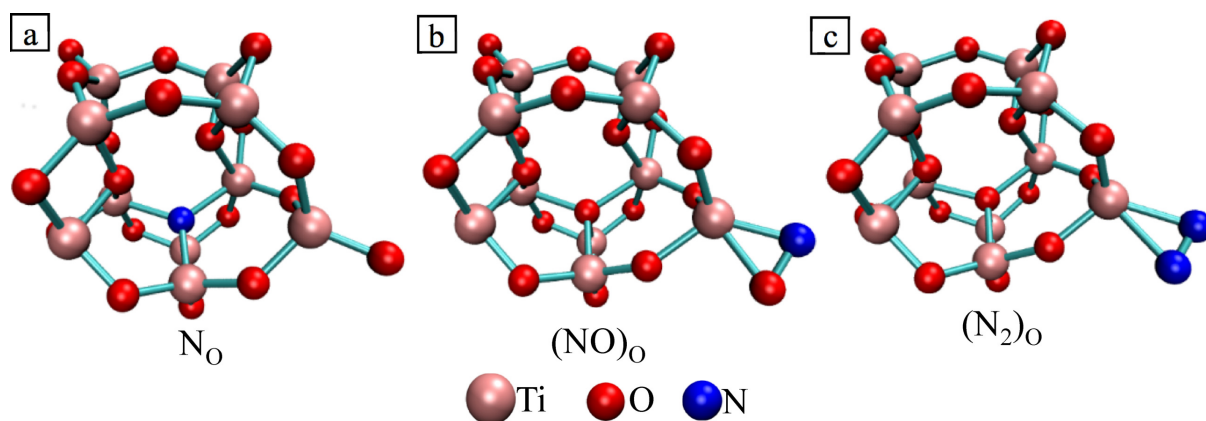


Figure 5.3: Energetically preferable position of different types of defects in N-doped $(TiO_2)_{10}$ cluster: (a) N_O , (b) $(NO)_O$ and (c) $(N_2)_O$.

preferable for substitutional defect. This finding is in good agreement with the previous simulation study [8]. Note that from the perspective of electronic configuration, N-atom has three unpaired electrons in the outermost shell, whereas O-atom has only two electrons. Therefore, the N-atom will favor more folded O-site to attain the maximum coordination number in the clusters. For interstitial case, we have observed that interstitial N-atom prefers to form the bond with dangling O-atoms because these oxygen atoms have the localized states at the HOMO level. The interaction of $(NO)_O$ doping affects the HOMO states, which may lead to substantial modification in their electronic properties. Moreover, since N-atom has unpaired electrons, it has tendency to share the electrons with more electronegative atom (dangling O-atom is having less coordination number). Likewise $(NO)_O$, $(N_2)_O$ also favors the dangling O-site (see Figure 5.3). By getting various cluster configurations from GA, we determine the thermodynamic stability of the clusters at finite T , p_{O_2} as discussed in the following section.

5.3.4 Thermodynamic stability of (N)_O, (NO)_O and (N₂)_O in (TiO₂)_n clusters

We address the thermodynamic stability of different types of charged defects ($[(N)_O]^q$, $[(NO)_O]^q$ and $[(N_2)_O]^q$ with $q = -2, -1, 0, +1, +2$) in an oxygen atmosphere using *aiAT*. The phase diagrams are obtained by determining the Gibbs free energy of formation of all N-doped clusters as a function of T , p_{O_2} and chemical potential of an electron (μ_e) by using the following equations:

(i) The formation energy of (N)_O in the charge state q is given by:

$$E_f(N_O^q) = E[N\text{Ti}_n\text{O}_{2n-1}]^q - E[\text{Ti}_n\text{O}_{2n}]^0 + \mu_O - \mu_N + q\mu_e \quad (5.1)$$

(ii) The formation energy for interstitial N i.e. (NO)_O is:

$$E_f((NO)_O^q) = E[N\text{Ti}_n\text{O}_{2n}]^q - E[\text{Ti}_n\text{O}_{2n}]^0 - \mu_N + q\mu_e \quad (5.2)$$

(iii) Similarly, the formation energy for (N₂)_O can be written as:

$$E_f((N_2)_O^q) = E[N_2\text{Ti}_n\text{O}_{2n-1}]^q - E[\text{Ti}_n\text{O}_{2n}]^0 + \mu_O - 2\mu_N + q\mu_e \quad (5.3)$$

where, $\mu_N = \Delta\mu_N + \frac{1}{2}E[N_2] + \frac{h\nu_{NN}}{4}$ and $\mu_O = \Delta\mu_O + \frac{1}{2}E[O_2] + \frac{h\nu_{OO}}{4}$. Here, $E[N\text{Ti}_n\text{O}_{2n-1}]^q$, $E[N\text{Ti}_n\text{O}_{2n}]^q$, $E[N_2\text{Ti}_n\text{O}_{2n-1}]^q$ and $E[\text{Ti}_n\text{O}_{2n}]^0$ are the total energies corresponding to (N)_O, (NO)_O, (N₂)_O doped and undoped clusters, respectively. $E[O_2]$ and $E[N_2]$ are the total energies of O₂ and N₂ molecules, respectively. μ_e is varied from valence band maximum to conduction band minimum of the bulk TiO₂. ν_{OO} and ν_{NN} are the stretching frequencies of O–O and N–N bonds, respectively. The formation energies of charged and neutral defects depend on μ_O , which incorporates the effect of T and p_{O_2} . $\Delta\mu_O$ as a function of T and p_{O_2} is calculated as follows [82]:

$$\begin{aligned} \Delta\mu_O(T, p_{O_2}) = & \frac{1}{2} \left[-k_B T \ln \left[\left(\frac{2\pi m}{h^2} \right)^{\frac{3}{2}} (k_B T)^{\frac{5}{2}} \right] + k_B T \ln p_{O_2} - k_B T \ln \left(\frac{8\pi^2 I_A k_B T}{h^2} \right) \right. \\ & \left. + k_B T \ln \left[1 - \exp \left(\frac{-h\nu_{OO}}{k_B T} \right) \right] - k_B T \ln \mathcal{M} + k_B T \ln \sigma \right] \end{aligned} \quad (5.4)$$

where m is the mass, I_A is the moment of inertia of O₂ molecule, \mathcal{M} is the spin multiplicity and σ is the symmetry number. Similarly, μ_N is estimated by the formation of N₂ molecule, i.e., $\Delta\mu_N = -0.25$ eV at ambient condition [213, 240].

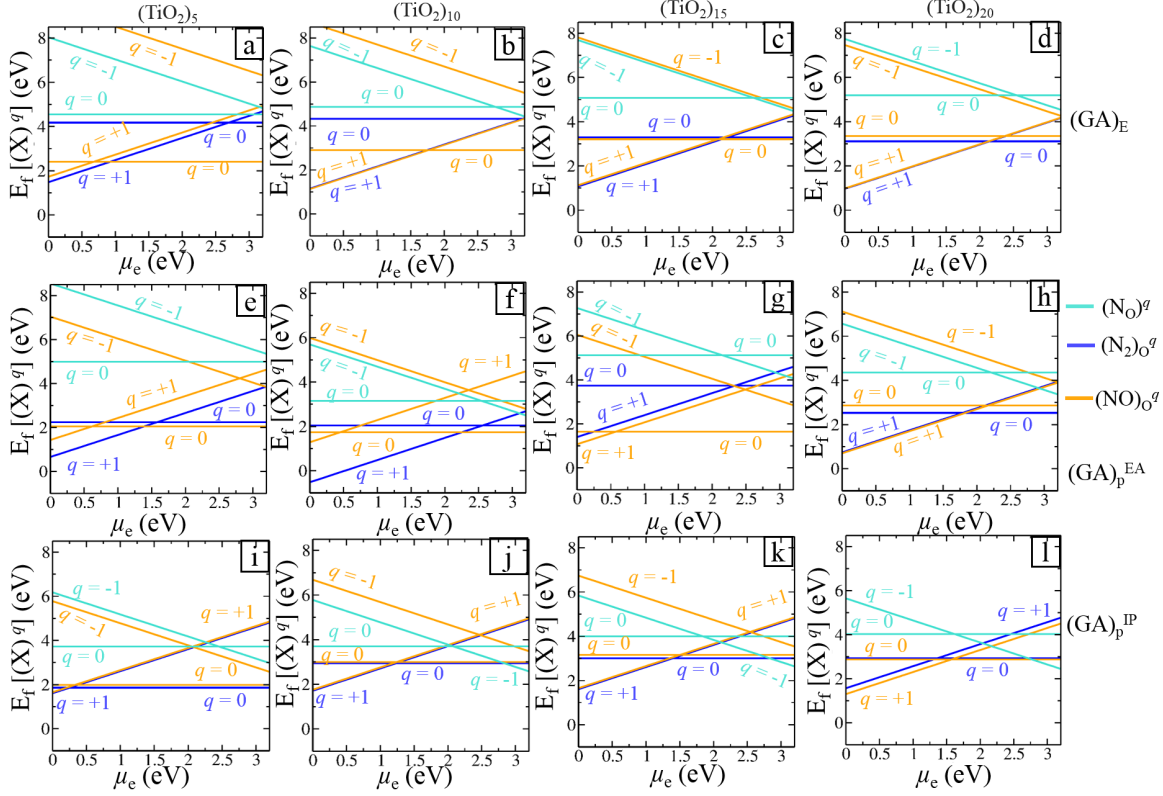


Figure 5.4: 2D phase diagrams of N-doped $(\text{TiO}_2)_{10}$ clusters at $T = 300$ K and $p_{\text{O}_2} = 1$ atm. The formation free energy is shown as a function of the chemical potential of an electron (μ_e). The upper, middle and lower panel represent the phase diagrams of $(\text{GA})_{\text{E}}$, $(\text{GA})_{\text{p}}^{\text{EA}}$ and $(\text{GA})_{\text{p}}^{\text{IP}}$ based clusters, respectively, for size: (a, e, i) $n = 5$, (b, f, j) $n = 10$, (c, g, k) $n = 15$, (d, h, l) $n = 20$.

5.3.4.1 2D phase diagrams

In Figure 5.4, we have shown the 2D phase diagrams of N-doped $(\text{TiO}_2)_{10}$ clusters at ambient condition ($T = 300$ K and $p_{\text{O}_2} = 1$ atm). In the upper, middle and lower panel, phase diagrams are shown for $(\text{GA})_{\text{E}}$, $(\text{GA})_{\text{p}}^{\text{EA}}$ and $(\text{GA})_{\text{p}}^{\text{IP}}$ based clusters, respectively. In $(\text{GA})_{\text{E}}$ clusters for $n = 5$, at lower values of μ_e (p-type doping region), $(\text{N}_2)_{\text{O}}^{+1}$ is the most stable state with the minimum formation energy, whereas at higher values of μ_e (n-type doping region) $(\text{NO})_{\text{O}}^0$ phase becomes stable (see Figure 5.4a). For $n = 10, 15$ and 20 , $(\text{N}_2)_{\text{O}}^{+1}$ and $(\text{NO})_{\text{O}}^{+1}$ states have the same formation energy near p-type doping. Near n-type doping region, $(\text{NO})_{\text{O}}^0$ is the most stable for $n = 10$ and 15 , whereas $(\text{N}_2)_{\text{O}}^0$ is stable for $n = 20$ (see the Figure 5.4(b-d)). In $(\text{GA})_{\text{p}}^{\text{EA}}$ case, near p-type doping region $(\text{N}_2)_{\text{O}}^{+1}$ is the most stable phase for $n = 5, 10$, and near n-type doping region $(\text{NO})_{\text{O}}^0$ becomes favorable as shown in Figure 5.4(e-f). For $n = 15$, $(\text{NO})_{\text{O}}^{+1}$ and $(\text{NO})_{\text{O}}^0$ are the stable phases in p-type and n-type doping region, respectively. Note that for $n = 20$, $(\text{N}_2)_{\text{O}}^{+1}$ and $(\text{NO})_{\text{O}}^{+1}$ phases are overlapping in p-type doping region. Near n-type doping

region, $(\text{N}_2)_\text{O}^0$ becomes the most stable. In N-doped $(\text{GA})_\text{P}^\text{IP}$ clusters, $(\text{NO})_\text{O}^{+1}$ and $(\text{N}_2)_\text{O}^{+1}$ both phases have nearly same formation energy and are stable in p-type doping region for size $n = 5, 10$ and 15 . However, for size $n = 20$, $(\text{NO})_\text{O}^{+1}$ is the most stable phase in p-type doping region. In n-type doping region, for $n = 5$, $(\text{N}_2)_\text{O}^0$ phase is most stable. For size = $10, 15$ and 20 , N_O^{-1} state is the most stable state having the minimum formation energy.

5.3.4.2 3D phase diagrams

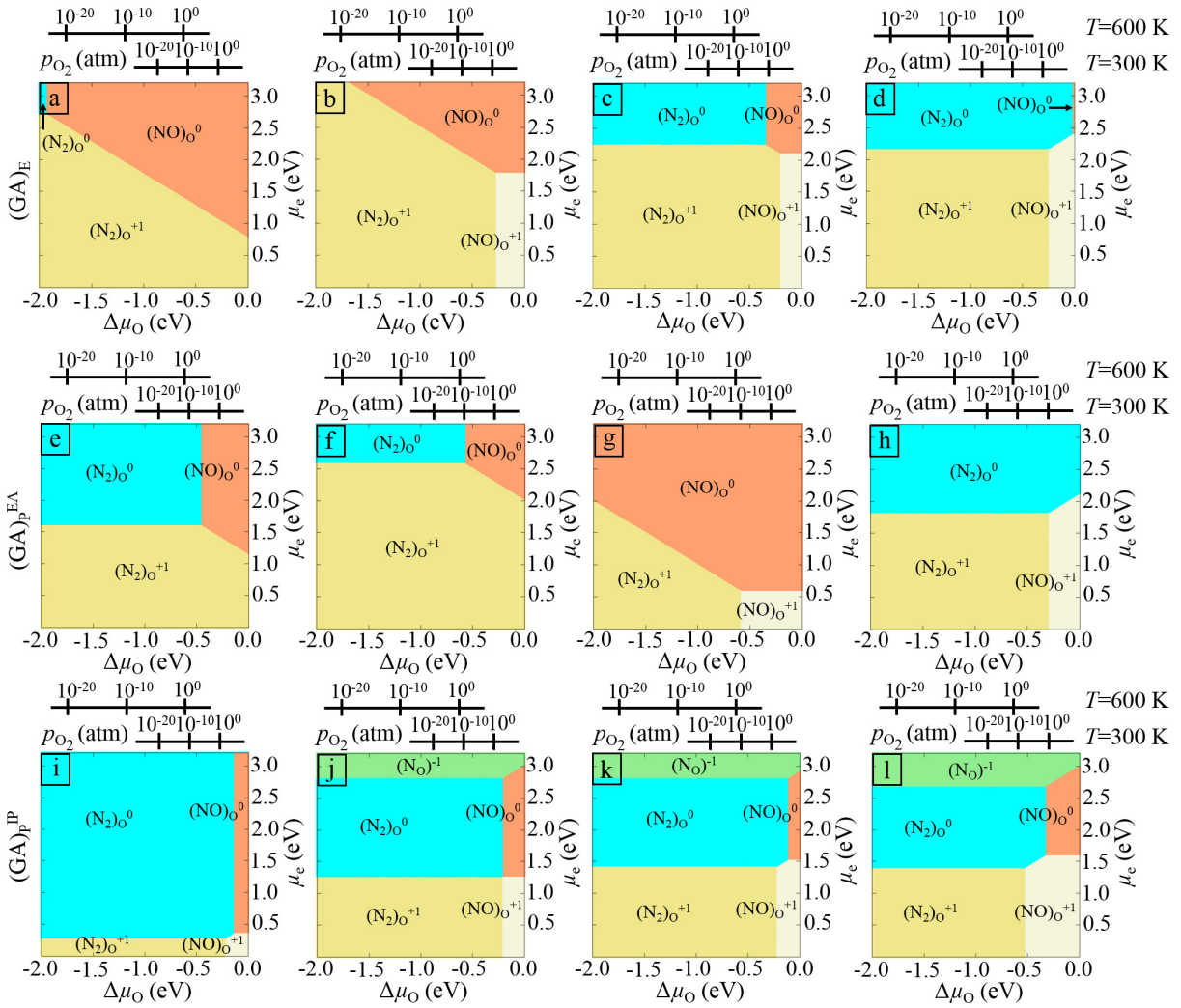


Figure 5.5: 2D view of 3D phase diagrams obtained for N-doped $(\text{GA})_\text{E}$ [upper panel], $(\text{GA})_\text{P}^\text{EA}$ [middle panel] and $(\text{GA})_\text{P}^\text{IP}$ [lower panel] clusters in different charge states for size $n = 5$ (a, e, i), 10 (b, f, j), 15 (c, g, k) and 20 (d, h, l). Colored regions show the most stable defect states at realistic conditions (T , p_{O_2} and μ_e). The top axes are representing the pressure scale of O_2 at $T = 300\text{K}$ and 600K .

3D phase diagrams of $(\text{GA})_\text{E}$ clusters for size $n = 5, 10, 15, 20$ are shown in Figure 5.5(a-d), sequentially. At lower values of μ_e (p-type doping), $(\text{N}_2)_\text{O}^{+1}$ defect is predominant for a wide range of $\Delta\mu_\text{O}$. However, $(\text{NO})_\text{O}^{+1}$ defect is also observed at a higher range of pressure for size

$n = 10, 15, 20$. At higher values of μ_e (n-type doping), $(N_2)_O^0$ defect is stable at lower range of pressure except for $n = 10$ case. However, at feasible pressure, $(NO)_O^0$ defect is found to be the most stable. Hence, we can summarize that interstitial defects $[(NO)_O$ and $(N_2)_O]$ are most stable in $(GA)_E$ based $(TiO_2)_n$ clusters. However, substitutional defect N_O has higher formation energy at ambient condition ($T = 300$ K, $p_{O_2} = 1$ atm), that can be seen clearly in 2D phase diagrams as shown in Figure 5.4(a-d). Note that until date, theoretical calculations are limited to non-metal doping (that to substitution only) in TiO_2 clusters closer to energy based global minimum [228, 8]. It is therefore of profound interest to address the stability and electronic structure of property based doped clusters (i.e. clusters generated from $(GA)_P^{EA}$, and $(GA)_P^{IP}$ algorithms). The latter may have a better correlation with the experimentally detected clusters.

Likewise $(GA)_E$ clusters, the property based clusters follow almost the same trend at lower values of μ_e [see Figure 5.5(e-l)]. However, $(N_2)_O^0$ phase is most probable in n-type region (higher μ_e), whereas a slight portion of $(NO)_O^0$ defect is apparent at high pressures for $n = 5, 10$ and 15 cases (see Figure 5.5(e-h)). Interestingly, we notice that substitutional phase i.e., N_O^{-1} is only visible in n-type doping region along with interstitial phases for doped clusters (scanned via $(GA)_P^{IP}$) having size $n = 10, 15, 20$ (see Figure 5.5(j-l)). We can make a key conclusion from Figure 5.5 that N interstitial defects ($(N_2)_O^{0/+1}$, $(NO)_O^{0/+1}$) are most prominent at a given T and p_{O_2} in N-doped TiO_2 clusters. Further, we have explored the fundamental gap and excitation energy of (un)doped TiO_2 clusters to see their applicability in photocatalysis.

5.3.5 Fundamental gap and excitation energy of (un)doped $(TiO_2)_n$ clusters

Next, setting formation energy of global minimum at 0 eV of the respective class of configurations (viz. pristine, N_O , $(NO)_O$ and $(N_2)_O$), we have considered all the structures within an energy window of 3 eV generated via $(GA)_E$, $(GA)_P^{EA}$ and $(GA)_P^{IP}$ for further analysis of their electronic structure. The number 3 eV is chosen assuming this is large enough window for consideration of metastable isomers and anything beyond this is very less likely to appear in real experiments.

We have then determined the fundamental gap (E_g) and excitation energy of all the N-doped $(TiO_2)_n$ clusters and compared with pristine counterpart (see Figure 5.6a). These are computed at the level of $G_0W_0@PBE0$. Note that the difference of vertical electron affinity (VEA) and vertical ionization potential (VIP) gives the fundamental gap[168]. We can also define it as

the energy required to make a pair of free charge carriers i.e. quasiparticle gap. If a particular cluster has simultaneously high vertical electron affinity (VEA) and low vertical ionization potential (VIP), it possesses the low fundamental gap ($\text{VIP} - \text{VEA}$). Furthermore, this candidate would be the very active cluster as it can accept or donate an electron readily [90, 198, 212]. It is experimentally reported that photoelectron spectroscopy of negatively charged clusters gives information about the energy gap between the highest occupied molecular orbital (HOMO) and lowest unoccupied molecular orbital (LUMO) for neutral clusters [7]. Therefore, the excitation energy for neutral species can be determined by their negatively charged species. The extra electron in the anion cluster occupies the LUMO of the neutral cluster, and thus, yields the first band peak, whereas the next peak of the band corresponds to ionization energy of the HOMO-1 of the charged cluster. Therefore, to calculate the excitation energy of (un)doped clusters, we

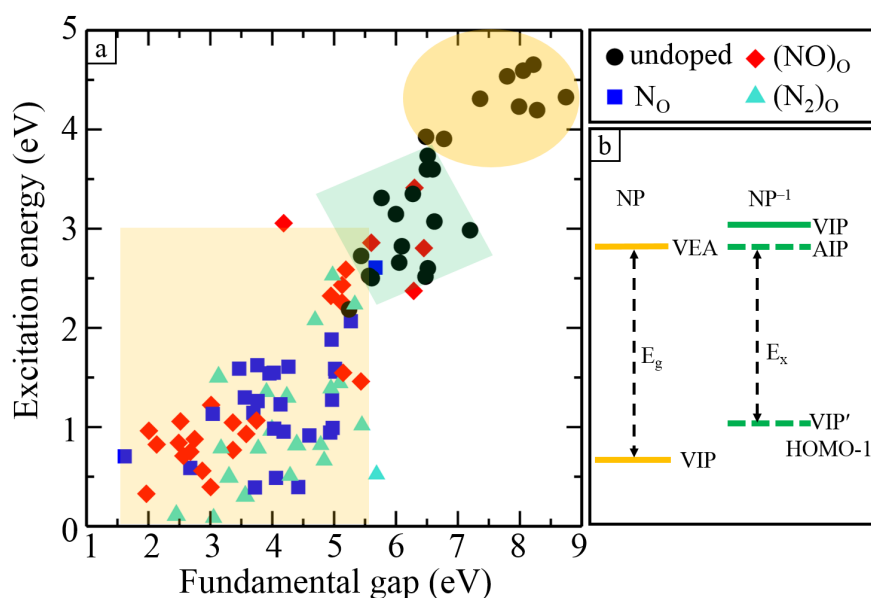


Figure 5.6: (a) Fundamental gap (E_g) vs. excitation energy (E_x) (G_0W_0 @PBE0) for all the (un)doped $(\text{TiO}_2)_n$ [$n = 4 - 10, 15, 20$] clusters. (b) In the schematic, yellow lines refer to the vertical ionization potential and vertical electron affinity of the neutral cluster (NP), while the green line refers to the vertical ionization potential of negatively charged cluster. The dashed green lines define VIP' (the energetic cost of extracting an electron from the HOMO-1 level of the NP^{-1}) and AIP (adiabatic ionization potential corresponds to the HOMO level of the NP^{-1}).

have taken the difference of ionization potential of HOMO-1 level of anion cluster and electron affinity of the neutral clusters as shown in the schematic diagram in Figure 5.6b. Note that the adiabatic ionization potential (AIP) of the anion cluster defines the vertical electron affinity (VEA) of the neutral clusters. We notice that the experimental results of undoped clusters are

Cluster size	E_x [(GA) _E]	E_x [(GA) _P ^{EA}]	E_x [(GA) _P ^{IP}]	E_{exp}	E_{TD}	E_{HL}
(TiO ₂) ₄	4.33	2.98	2.60	2.60	3.30	3.15
(TiO ₂) ₅	4.19	2.51	2.82	2.85	3.06	4.54
(TiO ₂) ₆	4.23	2.65	2.18	3.00	3.23	4.53
(TiO ₂) ₇	4.65	3.07	2.52	3.10	2.88	3.96
(TiO ₂) ₈	4.59	3.59	2.50	3.13	-	3.58
(TiO ₂) ₉	4.30	3.59	3.35	3.13	-	3.84
(TiO ₂) ₁₀	4.54	2.73	3.15	3.31	3.14	4.49

Table 5.1: Theoretically calculated excitation energy (E_x), experimental excitation energy (E_{exp}) [7], singlet transition energy (E_{TD}) [8], and HOMO-LUMO energy E_{HL} [9, 10] corresponding to (TiO₂)_n clusters. All the values are in eVs.

consistent with the clusters generated via (GA)_P rather than (GA)_E (see Table 5.1). This means the experimentally observed clusters are metastable and any conventional total energy based global minimum search algorithm will fail to detect them. In Figure 5.6a, we have shown the fundamental gap vs. excitation energy of (un)doped clusters for each set of clusters ((GA)_E, (GA)_P^{EA} and (GA)_P^{IP}). The region enclosed by circle corresponds to the undoped (GA)_E clusters, having the large values for fundamental gap and excitation energy. Note that the same undoped clusters scanned via (GA)_P show the lower values as compared to the (GA)_E clusters (see enclosed diamond shape region). As the undoped clusters possess high excitation energy, this limits their applications for the photocatalysis. Interestingly, in N-doped clusters, each types of defect (viz. substitution, interstitials) reduce the fundamental gap (E_g) and excitation energy (E_x) substantially (see the rectangular shaded area in Figure 5.6a). The reduction in the fundamental gap and excitation energy could be ascribed to the presence of the dopant states, which lead to the new HOMO–LUMO levels in the clusters.

5.3.6 VIP and VEA of (un)doped clusters with respect to the water redox potentials

Note that only reduction in the fundamental gap can not assure the hydrogen generation via photocatalytic water splitting. The potential of free charge carriers (VIP, VEA) should have appropriate position to straddle the redox potentials of water for hydrogen evolution reaction

(HER) and oxygen evolution reaction (OER). In order to analyze the ability of the clusters to drive the reduction of protons and the oxidation of water, four redox half-reactions are involved. Among these, two reactions are governed by exciton, and the other two by free electron and hole[241, 242, 243]. In our case study, we have considered the latter one. Free charge carriers with the necessary chemical potential can in principle drive the water splitting half-reactions. The redox half-reactions are given below with the convention of reduction reactions[242]:



here NP is the neutral cluster, and NP⁻¹, NP⁺¹ represent the photocatalyst with a free electron in the conduction band and hole in the valence band, respectively. In equation 5 and 6, free electron act as a reductant and free hole will acts as an oxidant, respectively. The free energies of half-reactions are given in equation 7 and 8:

$$\Delta E(6) = E(\text{NP}^{-1}) - E(\text{NP}) = -EA \quad (5.7)$$

$$\Delta E(7) = E(\text{NP}) - E(\text{NP}^{+1}) = -IP \quad (5.8)$$

$\Delta E(6)$ and $\Delta E(7)$ are equal to negative of adiabatic electron affinity and ionization potential, respectively. Note that we have used vertical approximation that ignores the nuclear relaxation and yields vertical potential. For water splitting photocatalyst, the VIP (energy required to extract an electron from the HOMO) level must be located below the OER potential (O₂/H₂O), whereas the VEA (the energy released while adding the electron to LUMO) level must be above the HER potential (H⁺/H₂) as shown in the schematic diagram of Figure 5.7a. Using the information of VIP and VEA, one can calculate the reduction potentials associated with the free charge carriers. Specifically, we use many body perturbation theory to calculate the thermodynamic driving force for the water splitting half-reactions 5 and 6. Experimental potential values are given relative to the Standard Hydrogen Electrode (SHE) (pH = 0). In practice, the required overall potential difference is larger than 1.23 eV to overcome energetic losses and kinetic barriers. In Figure 5.7(b-d), we show the G₀W₀@PBE0 predicted vertical potentials relative to the SHE to obtain the potential candidates for photocatalytic water splitting. The colored area (as in Figure 5.7(b-d)) represents the suitable region for overall water splitting. For N_O dopant

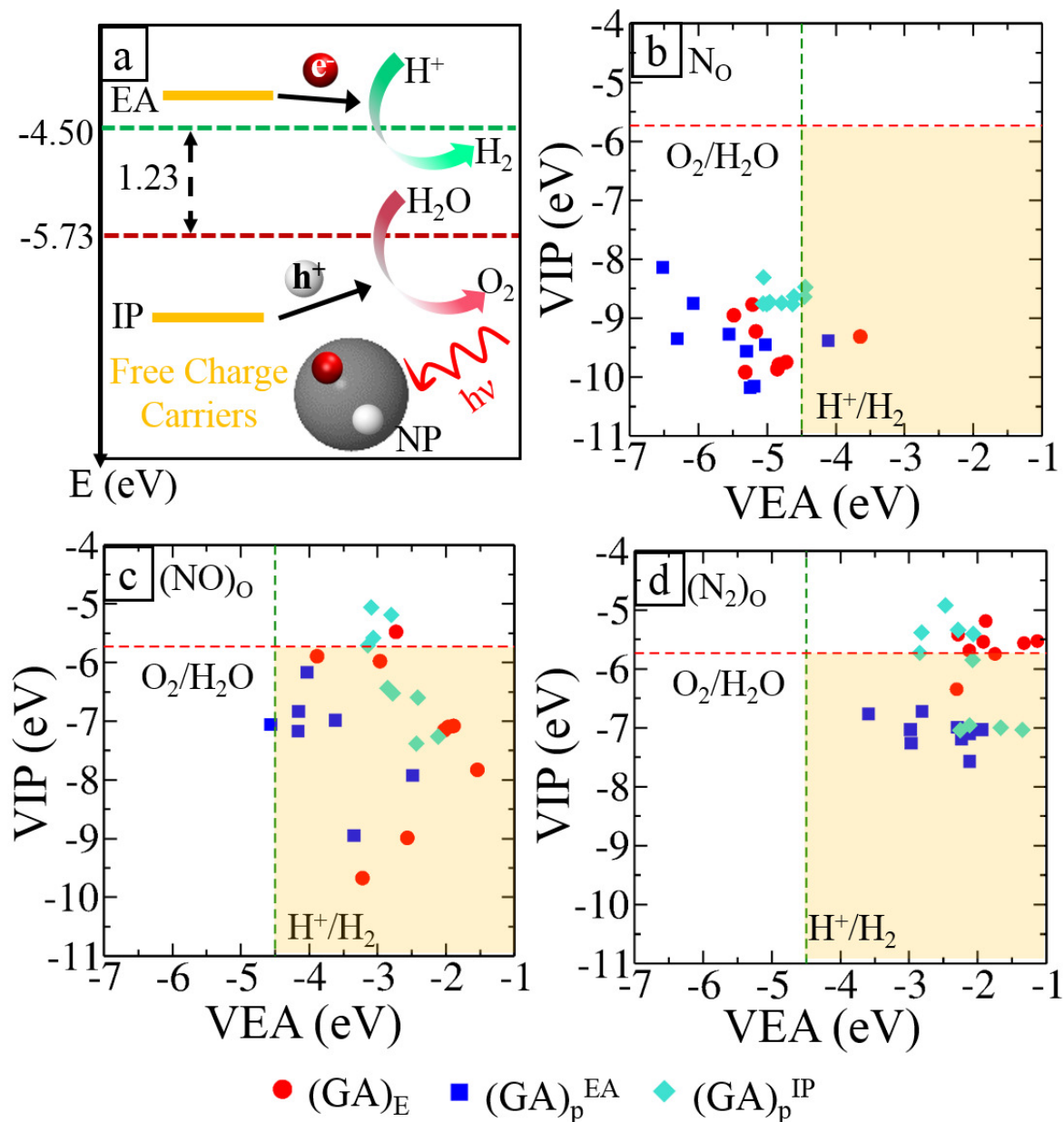


Figure 5.7: (a) The schematic diagram shows how the (standard) reduction potentials (VIP and VEA) of the ideal photocatalyst (cluster) straddle the HER and OER potentials. The schematic shows the free charge carriers scenario, where the excited electron and hole are spatially separated within the particle due to negligible coulombic interaction. $h\nu$ defines the energy of the photon absorbed by the cluster. e^- and h^+ stand for electron and hole, respectively. VIP refers to the cluster's ground-state ionization potential, whereas VEA to the ground-state electron affinity. VIP and VEA for doped clusters: (b) N_O , (c) $(NO)_O$, and (d) $(N_2)_O$. The dashed green and red lines represent the standard redox potentials for water reduction (H^+/H_2) and oxidation potential (O_2/H_2O) at $pH = 0$, respectively.

case, all the candidates (generated via $(GA)_E$ and $(GA)_p$) have only the suitable VIP for OER as shown in Figure 5.7(b). Hence, the N_O doped clusters are not potential candidates for overall

water splitting except two $[(\text{GA})_{\text{E}}$ and $(\text{GA})_{\text{P}}^{\text{EA}}$ of size 9 and 10, respectively]. In the case of $(\text{NO})_{\text{O}}$ doping, maximum points lie within a suitable region for both the potentials (see Figure 5.7(c)). In Figure 5.7(d), for $(\text{N}_2)_{\text{O}}$ doping, all the $(\text{GA})_{\text{P}}^{\text{EA}}$ clusters are inside the colored region whereas majority of $(\text{GA})_{\text{E}}$ and few $(\text{GA})_{\text{P}}^{\text{IP}}$ clusters are lying above the water oxidation potential level ($\text{O}_2/\text{H}_2\text{O}$). The latter are appropriate for HER. Among different doped configurations, $(\text{NO})_{\text{O}}$ is the promising choice for photocatalytic water splitting (see Figure 5.7). Note that maximum isomers scanned via $(\text{GA})_{\text{P}}^{\text{EA}}$ are found to be suitable for photocatalytic water splitting followed by the isomers generated by $(\text{GA})_{\text{P}}^{\text{IP}}$ and $(\text{GA})_{\text{E}}$ for all the doped configurations. This further validates the importance of a dedicated algorithm viz. $(\text{GA})_{\text{P}}$ to capture the metastability triggered reactivity.

5.3.7 Electronic structure of doped $(\text{TiO}_2)_{10}$ clusters

To have in-depth understanding on the role of dopants in reducing the fundamental gap and their applicability in photocatalytic water splitting, we have analyzed the electronic density of states (DOS). The total DOS (TDOS) and partial DOS (PDOS) of $(\text{GA})_{\text{P}}^{\text{EA}}$ based doped $(\text{TiO}_2)_{10}$ clusters are shown in Figure 5.8. Note that we have shown the PDOS of only those atoms, which have the major contribution at HOMO–LUMO levels. In undoped $(\text{TiO}_2)_{10}$ cluster, orbitals of dangling O-atoms contribute to HOMO level, whereas the LUMO level is mainly attributed by the Ti-atoms that have the maximum distance from dangling O. In case of N-substitutional doping $(\text{N})_{\text{O}}$, N is 4-folded and tightly bonded with Ti-atoms, that results in deep states far away from the Fermi-level (see lower panel of Figure 5.8a, e and f). Further, the charge density is calculated on N-site (-0.38) which is comparable to charge density on substitutional O-atom site (-0.40) of undoped case. This signifies that it will act as a deep donor site. We have also noticed the unoccupied deep mid gap states, which are associated with the dangling O-atoms and their bonded Ti-atoms. Consequently, the fundamental gap (E_g) is reduced in the N_{O} doped structures, where N is highly coordinated to Ti (see in Figure 5.8a). The aforementioned states shift the LUMO towards Fermi level and thus, N_{O} doped clusters are not suitable for HER (see Figure 5.8e and 5.8f), which can also be observed from Figure 5.7b. In case of $(\text{NO})_{\text{O}}$ doping, we find the occupied N-states above the HOMO level, which are overlapped with the states of bonded atoms to the dopant as shown in Figure 5.8b, d and g. Since oxygen is more electronegative than nitrogen, nitrogen might transfer charge to the bonded oxygen. As a result, dopant acts as a donor, and introduces occupied states near the HOMO. Therefore, in Figure

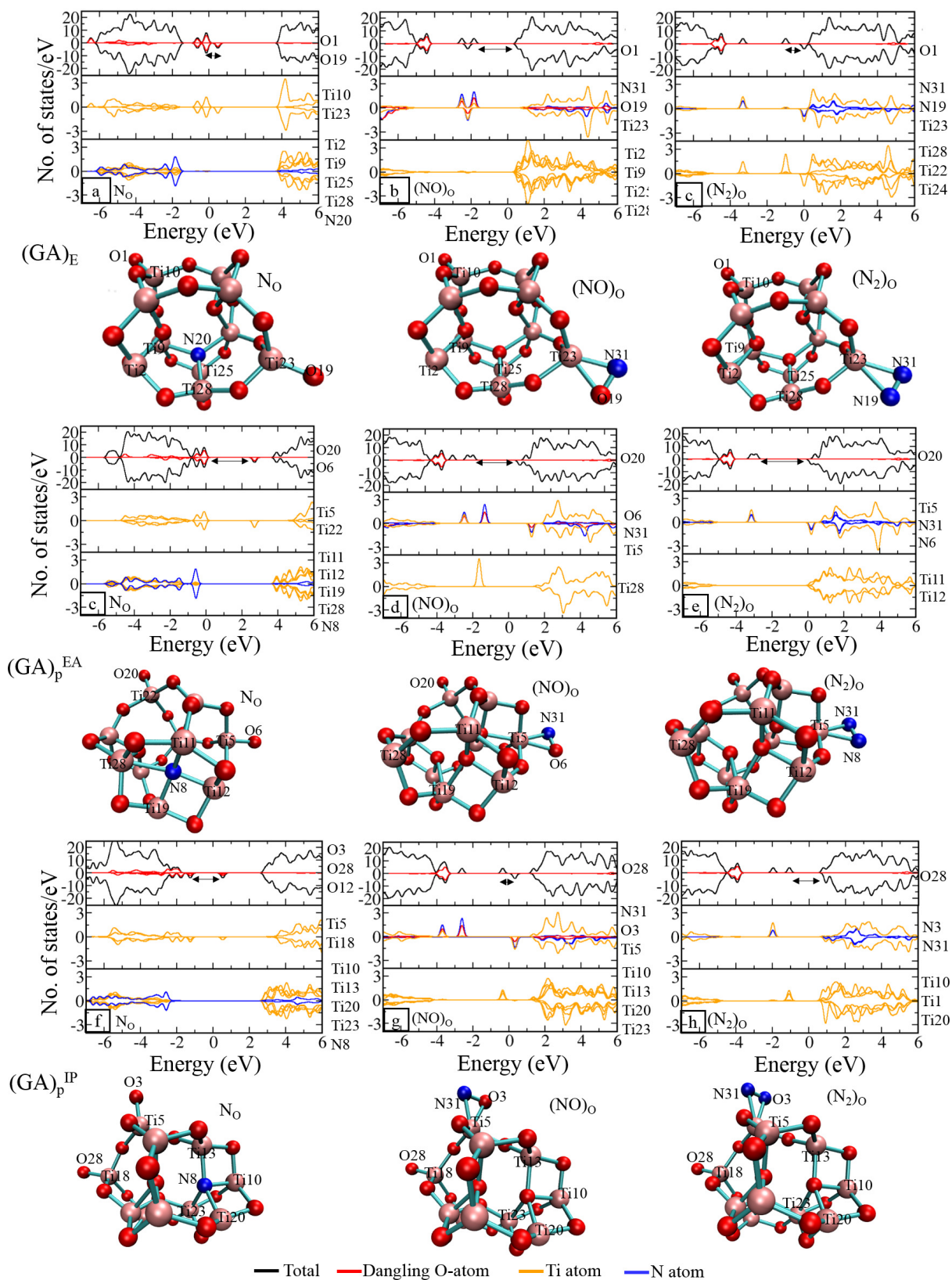


Figure 5.8: TDOS and PDOS of $(\text{GA})_{\text{P}}^{\text{EA}}$ based doped $(\text{TiO}_2)_{10}$ clusters: (a) NO , (b) $(\text{NO})_{\text{O}}$, (c) $(\text{N}_2)_{\text{O}}$. The respective electronic configuration of doped state is shown below the DOS. Double headed arrows are representing the HOMO-LUMO gap.

5.4b, for p-type doping, the formation energy of $(\text{NO})_O$ defect with +1 charge state is minimum. In few cases of $(\text{GA})_P^{\text{IP}}$ based clusters, the manifestation of deep occupied mid gap states of Ti-atoms deteriorates their oxidation potential (see Figure 5.8g). Similarly, for $(\text{N}_2)_O$ doping,

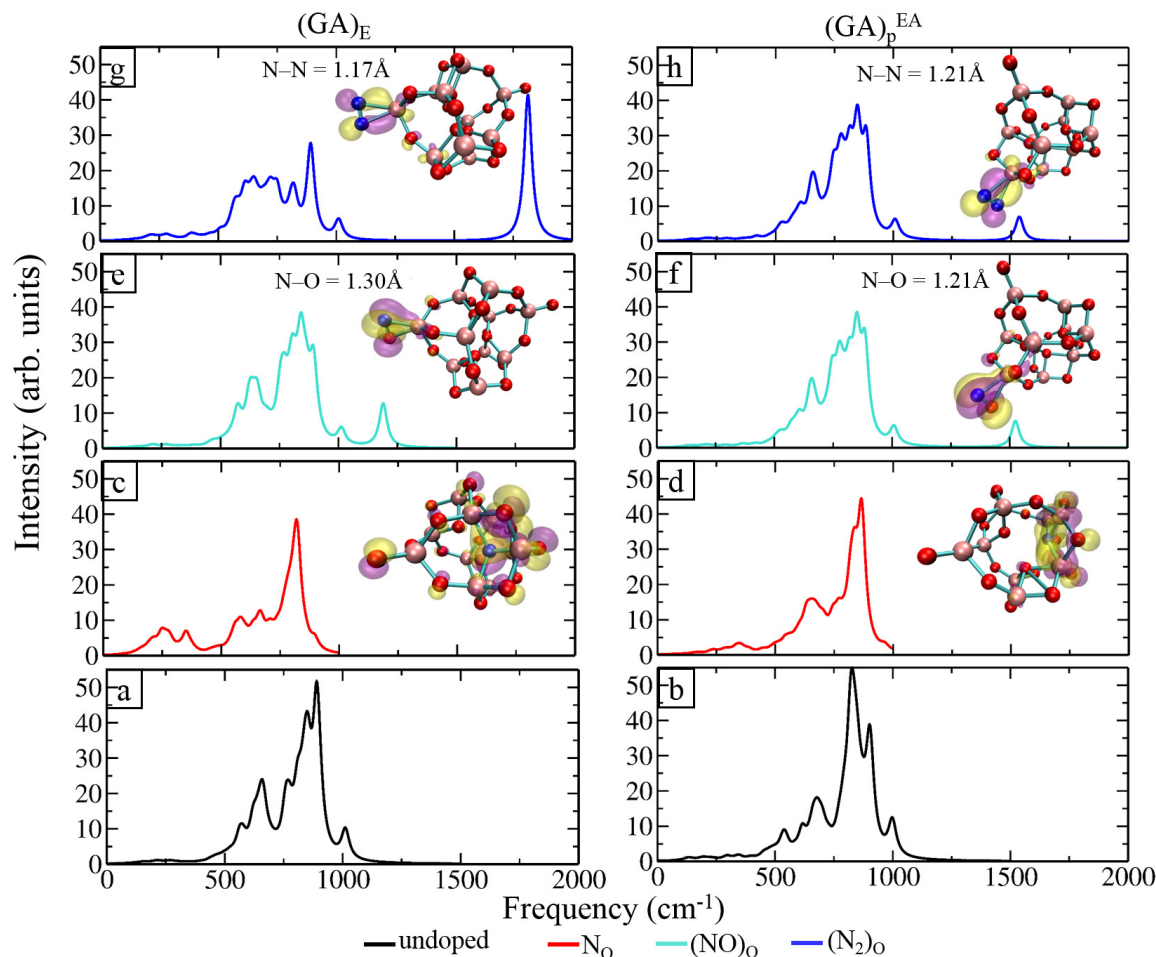


Figure 5.9: IR spectra of $(\text{GA})_E$ (left column) and $(\text{GA})_P^{\text{EA}}$ (right column) based $(\text{TiO}_2)_{10}$ clusters: (a, b) undoped, (c, d) NO , (e, f) $(\text{NO})_O$ and (g, h) $(\text{N}_2)_O$.

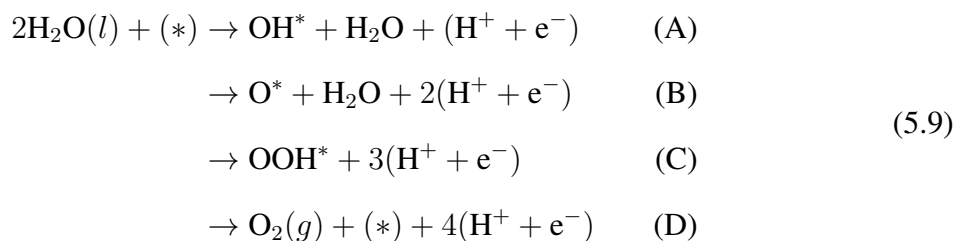
N-atoms yield the occupied states, which are overlapped with states of bonded Ti as shown in Figure 5.8c, 5.8e and 5.8h. $(\text{N}_2)_O$ transfers the charge to the Ti, which results in the strong bonding between N_2 entity and Ti-atom. However, in $(\text{GA})_E$ clusters, we observe the occupied mid gap states of Ti-atom in $(\text{N}_2)_O$ dopant case (see Figure 5.8c). As a result, their oxidation power is degraded. Therefore, all the points of $(\text{N}_2)_O$ dopant for $(\text{GA})_E$ based clusters are lying above the OER potential in Figure 5.7d. Hence, $(\text{N}_2)_O$ dopant in $(\text{GA})_E$ clusters is not a desirable choice for overall water splitting.

In the next step, we have simulated the infrared (IR) spectra to determine the characteristic vibrational modes which are induced by the dopant sites in the clusters. For the concise de-

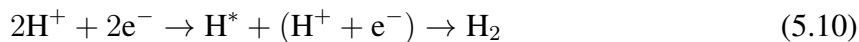
scription, we have considered representative cases as $(GA)_E$ and $(GA)_P^{EA}$ based clusters of size $n = 10$. In $(N)_O$ dopant cases, the spectrum has shifted to the lower frequency in comparison to the undoped cluster (see Figure 5.9(a-d)). Contrary to this, in the IR spectra of $(NO)_O$ and $(N_2)_O$ doped clusters, we have noticed the additional peaks above the highest peak of undoped cluster as shown in Figure 5.9(e-h). The N–O and N–N moieties are found to be responsible for the new emerging peaks in the spectra. In addition to this, we have seen the localized electron density at N–O and N–N moieties, which confirms that these moieties are the active centres in the clusters. However, in $(N)_O$ dopant cases, the electron density is not localized at a particular site. These observations would be helpful for future experiments to recognize the different type of dopant sites in the $(TiO_2)_n$ clusters.

5.3.8 Evaluation of OER and HER

In next step, the study of OER and HER is carried out on (un)doped (meta)stable $(TiO_2)_{10}$ clusters according to the four steps and single step mechanisms, respectively. The OER process involves four sequential proton-coupled electron transfer (PCET) steps in which the intermediate states hydroxyl (OH^*), atomic oxygen (O^*), and hydroperoxo (OOH^*) are formed as follows:



The HER takes place through proton reduction:



where $(*)$ is an active site on the cluster. The detailed description of the procedure is given in Ref. [244, 245]. For every reaction step, we have optimized the geometries of the intermediate configurations to compute their ground-state and zero point energies. The free energy variation at each reaction step is calculated as $\Delta G = \Delta E + \Delta E_{ZPE} - T\Delta S + \Delta G_U + \Delta G_{pH}$, where ΔE is the difference of total energy, ΔE_{ZPE} is the difference in the zero-point energy, ΔS is the change in entropy, T is temperature (300 K). ΔG_U and ΔG_{pH} are the contributions from the electrode potential (E_{SHE}) and pH value. We have calculated the free energy of the intermediates at zero electrode potential (E_{SHE}) and pH = 0 [246]. The E_{ZPE} and TS for each reaction intermediates

are calculated as $E_{\text{ZPE}} = \frac{1}{2} \sum_i h\nu_i$ and $TS = \sum_i h\nu_i \frac{1}{\exp\left(\frac{h\nu_i}{k_B T}\right) - 1} - k_B T \sum_i \ln \left[1 - \exp\left(-\frac{h\nu_i}{k_B T}\right) \right]$, where h , ν_i and k_B are Planck constant, vibrational frequencies and Boltzmann constant, respectively. Following this, the theoretical overpotential (η) of OER is obtained, which provides insight on the relative catalytic performance of different configurations. The difference between potentials corresponding to the change in free energy and the overall thermodynamic reaction potential (1.23 V), provides the lower bound for the overpotential as given in Eq. 5.11.

$$\eta = \max(\Delta G_A, \Delta G_B, \Delta G_C, \Delta G_D)/e - 1.23\text{V} \quad (5.11)$$

Further, the adsorption energies of H-atom and H₂O molecule on doped clusters are determined as follows:

$$E_{\text{ad}} = E_{\text{catalyst+mol}} - E_{\text{mol}} - E_{\text{catalyst}} \quad (5.12)$$

Where, E_{catalyst} , E_{mol} and $E_{\text{catalyst+mol}}$ are the total energies of catalyst, adsorbate and catalyst

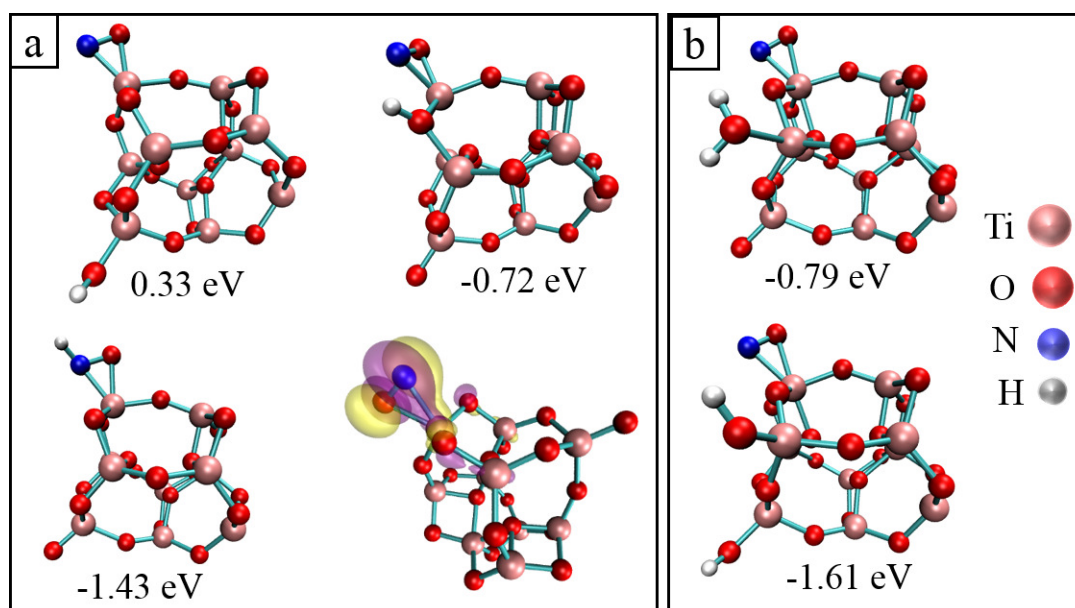


Figure 5.10: (a, b) Geometries, electron density profile and binding energies of single H-atom and water molecule adsorbed on (NO)_O doped (TiO₂)₁₀ cluster, respectively.

with adsorbate, respectively. The adsorption of H-atom favors (NO)_O-site as the electron density is highly localized at the dopant site (see Fig. 5.10(a)). The (NO)_O-site leads to a gain in adsorption energy from -0.72 eV to -1.43 eV. This observation matches with earlier reported results on TiO₂(001) surface, that the presence of N-dopant promotes the water dissociation via proton transfer from the H₂O molecule to the N-doped site [245]. Moreover, the dissociative adsorption of H₂O molecule is observed to be more favorable than the molecular adsorption (see Fig. 5.10(b)). The step with higher positive free energy between two reaction

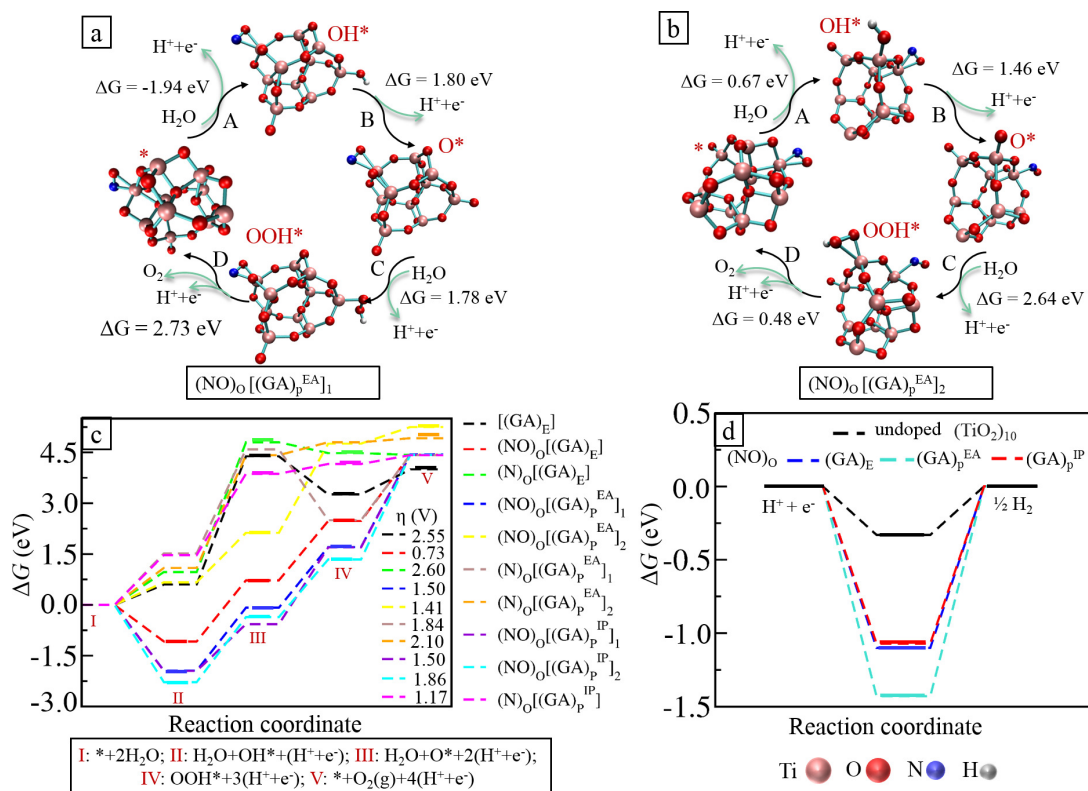


Figure 5.11: (a, b) OER cycles on two different Ti-sites of $(\text{NO})_0$ doped $(\text{GA})_p^{\text{EA}}$ based $(\text{TiO}_2)_{10}$ cluster. In Fig. 5.12, we have shown the OER cycles on other configurations. (c, d) Reaction free energy diagrams of the OER and HER on N-doped $(\text{TiO}_2)_{10}$ clusters at an electrode potential $E_{\text{SHE}} = 0$ V, respectively. At zero potential, $(\text{H}^+ + \text{e}^-)$ can be expressed as $\frac{1}{2}\text{H}_2$.

steps in the mechanism determines the overall thermodynamics of the OER and is called the rate-determining step (RDS). It is observed that the RDS of the OER is located on the second (Eq. 5.9B) or the fourth (Eq. 5.9D) PCET step. In the cases, where the formation of hydroxyl (OH^*) intermediate is energetically less favorable (positive value of ΔG_A), the dissociation of OH^* is the RDS of the OER. Contrary to this, if formation of OH^* is favorable then the last step, the dissociation of OOH^* (Eq. 5.9D) is the RDS. Only $(\text{NO})_0$ doped $(\text{GA})_p^{\text{EA}}$ cluster holds the RDS of the formation of OOH^* (Eq. 5.9C) with a ΔG value of 2.64 eV as shown in Fig. 5.11(b). For the same configuration, different Ti-sites give different value of ΔG_A . In Fig. 5.11(a), we find the negative value of ΔG_A , whereas in Fig. 5.11(b) (with different Ti-site), we obtain positive value. In the former case, the Ti-site is away from the dopant site, while in latter case, it is close to the dopant site, which results in lower overpotential. The calculated overpotential (η) values of OER on pristine (2.55 eV) and $(\text{N})_0$ (2.60 eV) doped $(\text{GA})_E$ cluster are found to be higher than that of N-doped property based clusters as shown in Fig. 5.11(c). A large decrement in ΔG for HER on $(\text{NO})_0$ doped $(\text{TiO}_2)_{10}$ clusters indicates a preferable

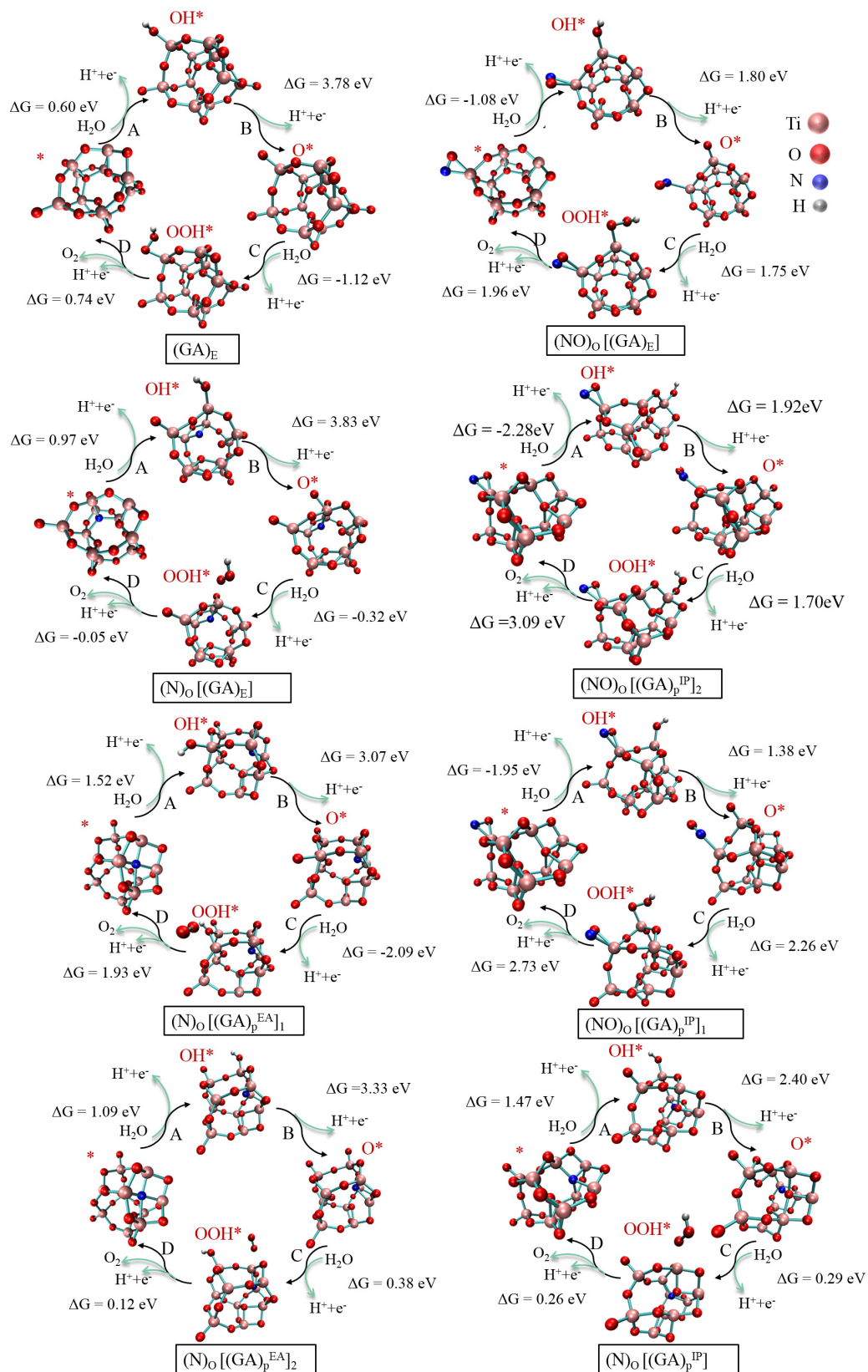


Figure 5.12: OER cycles on different configurations of $(\text{GA})_E$, $(\text{GA})_P^{\text{EA}}$ and $(\text{GA})_P^{\text{IP}}$ based $(\text{TiO}_2)_{10}$ clusters.

hydrogen adsorption strength due to highly localized charge density at the active site (see Fig. 5.11(d)). Therefore, doped clusters show higher HER activity than undoped clusters. Hence, based on the reaction free energy profiles, a conclusion can be drawn that N-doped clusters exhibit higher OER and HER catalytic activity than the undoped counterpart due to the smaller ΔG value of the RDS, which results in lower overpotential.

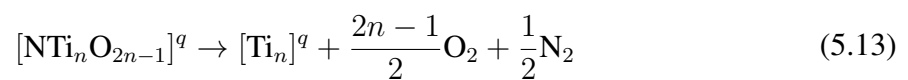
5.3.9 Electrochemical phase (Pourbaix) diagram and phase probability analysis

The electrochemical phase (Pourbaix) diagram is simulated by varying the chemical potential of reaction ($\Delta\mu$) for considered species over the specified electrochemical conditions ($E_{\text{SHE}} \in [-3, 3]$ V and $\text{pH} \in [0, 16]$). $\Delta\mu$ is calculated using the Thermodynamic and Nernst equations.

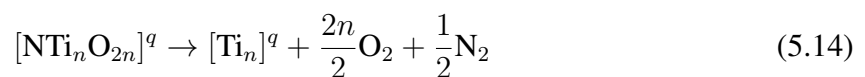
5.3.9.1 Thermodynamic energies

The reaction equations between N-doped $(\text{TiO}_2)_n$ clusters and the references (i.e., Ti_n , O_2 , and N_2) can be written as:

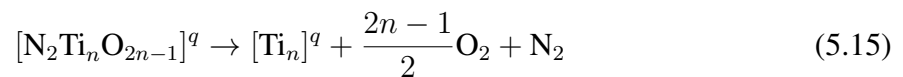
(i) Reaction path for $(\text{N})_{\text{O}}$ doped clusters:



(ii) Reaction path for $(\text{NO})_{\text{O}}$ doped clusters:



(iii) Reaction path for $(\text{N}_2)_{\text{O}}$ doped clusters:



Then, their formation energy (E_f) can be calculated using the following equations:

(i) The formation energy for substitutional N is:

$$E_f(\text{N}_{\text{O}}^q) = E[\text{NTi}_n\text{O}_{2n-1}]^q - E[\text{Ti}_n]^q + (2n-1)\mu_{\text{O}} - \mu_{\text{N}} \quad (5.16)$$

(ii) The formation energy for interstitial N i.e. $(\text{NO})_{\text{O}}$ is:

$$E_f((\text{NO})_{\text{O}}^q) = E[\text{NTi}_n\text{O}_{2n}]^q - E[\text{Ti}_n]^0 + (2n)\mu_{\text{O}} - \mu_{\text{N}} \quad (5.17)$$

(iii) Similarly, the formation energy for (N₂)_O can be written as:

$$E_f((N_2)_O^q) = E[N_2Ti_nO_{2n-1}]^q - E[Ti_n]^0 + (2n - 1)\mu_O - 2\mu_N \quad (5.18)$$

To maintain a consistent energy scale for different set of clusters [i.e., (GA)_E, (GA)_P^{EA}, (GA)_P^{IP}], we use the energy of Ti₁₀ cluster as our reference state. To determine E_f, we have included the DFT vibrational, translational and rotational free energies in O₂ and N₂ gases for accurate thermodynamical simulation.

5.3.9.2 Electrochemical reaction paths and chemical potentials of reaction

The chemical potentials of clusters and aqueous ions are used to calculate Δμ's. To calculate the Δμ's, Ti⁺⁺ is considered as the electrochemical reference, therefore, it always resides at the right side of the reaction paths designed here. Further, we have noted the electrochemical reaction paths for different type [i.e., (GA)_E, (GA)_P^{EA}, (GA)_P^{IP}] of N-doped (TiO₁₀)_n clusters, that connect all the considered species [e.g., metal, oxides, water, and aqueous ions] with each other. Using these paths, the chemical potentials of reaction Δμ(E_{SHE}, pH) as function of electrode-potential and solution-pH are determined. Using Δμ values, the relative electrochemical stabilities of all the considered species are described at any defined electrochemical condition. It is important to note that the chemical potentials for aqueous ions are concentration dependent. Therefore, the chemical potential of an aqueous ion (e.g., ion I) is calculated at a specified concentration ([I]) using the following expression:

$$\mu(I) = \mu^0 + RT\ln([I]) \quad (5.19)$$

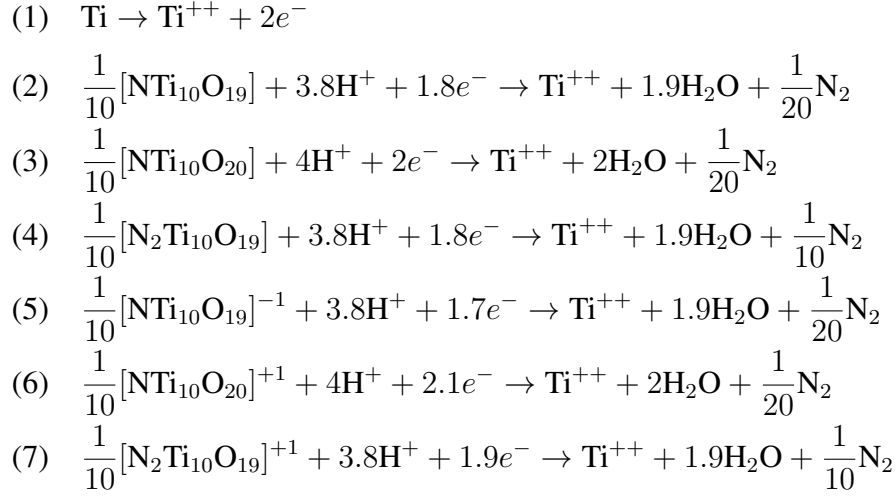
where *R* is the gas constant [8.31446 J/(mol K)] and μ⁰ is the chemical potential of ion I at the standard condition (298.15 K, 1.0 bar, 1.0 mol/L, and pH=0). [I] is the aqueous-ion activity approximated to be the concentration of the ion I. The considered experimental value of μ⁰ for water is -2.458 eV. For H⁺ ion, μ⁰ at the standard condition (298.15 K, pH=0, 1.0 bar) equals 0 for standard hydrogen electrode (SHE). Hence, μ for H⁺ can be written as [247, 248]:

$$\mu(I) = RT\ln([H^+]) = -RT\ln(10) \cdot \text{pH} \quad (5.20)$$

The standard chemical potential (μ⁰ = -3.26 eV) of aqueous ion (Ti⁺⁺) in solution is used from Pourbaix & Bard's data [249, 250]. For clusters, the standard chemical potential (μ) equals E_f. Reaction paths and the corresponding reaction energies (Δμ), where μ(Ti) and μ(H⁺) are the

references (i.e., zero) for the chemical potentials at standard condition, and the standard hydrogen potential is the reference for the electrode potential E_{SHE} (in V):

Reaction Paths:



The $\Delta\mu$ for every reaction path is determined by evaluating the corresponding Nernst equation at specified pH values and electrode potential E_{SHE} .

$$(1a) \quad \Delta\mu(\text{Ti} - \text{Ti}^{++}) = \mu(\text{Ti}) - \mu(\text{Ti}^{++}) + 2eE_{\text{SHE}} = -\mu(\text{Ti}^{++}) + 2eE_{\text{SHE}}$$

$$\begin{aligned}
 (2a) \quad \Delta\mu(\text{NTi}_{10}\text{O}_{19} - \text{Ti}^{++}) &= \frac{1}{10}\mu(\text{NTi}_{10}\text{O}_{19}) - \mu(\text{Ti}^{++}) - 0.1\mu_{\text{N}} \\
 &\quad - 1.9\mu(\text{H}_2\text{O}) - 3.8RT\ln(10) \cdot \text{pH} - 1.8eE_{\text{SHE}}
 \end{aligned}$$

$$\begin{aligned}
 (3a) \quad \Delta\mu(\text{NTi}_{10}\text{O}_{20} - \text{Ti}^{++}) &= \frac{1}{10}\mu(\text{NTi}_{10}\text{O}_{20}) - \mu(\text{Ti}^{++}) - 0.1\mu_{\text{N}} \\
 &\quad - 2\mu(\text{H}_2\text{O}) - 4RT\ln(10) \cdot \text{pH} - 2eE_{\text{SHE}}
 \end{aligned}$$

$$\begin{aligned}
 (4a) \quad \Delta\mu(\text{N}_2\text{Ti}_{10}\text{O}_{19} - \text{Ti}^{++}) &= \frac{1}{10}\mu(\text{NTi}_{10}\text{O}_{20}) - \mu(\text{Ti}^{++}) - 0.2\mu_{\text{N}} \\
 &\quad - 1.9\mu(\text{H}_2\text{O}) - 3.8RT\ln(10) \cdot \text{pH} - 1.8eE_{\text{SHE}}
 \end{aligned}$$

$$\begin{aligned}
 (5a) \quad \Delta\mu([\text{NTi}_{10}\text{O}_{19}]^{-1} - \text{Ti}^{++}) &= \frac{1}{10}\mu(\text{NTi}_{10}\text{O}_{19})^{-1} - \mu(\text{Ti}^{++}) - 0.1\mu_{\text{N}} \\
 &\quad - 1.9\mu(\text{H}_2\text{O}) - 3.8RT\ln(10) \cdot \text{pH} - 1.7eE_{\text{SHE}}
 \end{aligned}$$

$$\begin{aligned}
 (6a) \quad \Delta\mu([\text{NTi}_{10}\text{O}_{20}]^{+1} - \text{Ti}^{++}) &= \frac{1}{10}\mu(\text{NTi}_{10}\text{O}_{20})^{+1} - \mu(\text{Ti}^{++}) - 0.1\mu_{\text{N}} \\
 &\quad - 2\mu(\text{H}_2\text{O}) - 4RT\ln(10) \cdot \text{pH} - 2.1eE_{\text{SHE}}
 \end{aligned}$$

$$\begin{aligned}
 (7a) \quad \Delta\mu([\text{N}_2\text{Ti}_{10}\text{O}_{19}]^{+1} - \text{Ti}^{++}) &= \frac{1}{10}\mu(\text{NTi}_{10}\text{O}_{20})^{+1} - \mu(\text{Ti}^{++}) - 0.2\mu_{\text{N}} \\
 &\quad - 1.9\mu(\text{H}_2\text{O}) - 3.8RT\ln(10) \cdot \text{pH} - 1.9eE_{\text{SHE}}
 \end{aligned}$$

Moreover, the involved steps of the adopted scheme are described in Ref. [248, 251] to predict the electrochemical stability. Here, the hybrid functional (PBE0) is used to include the

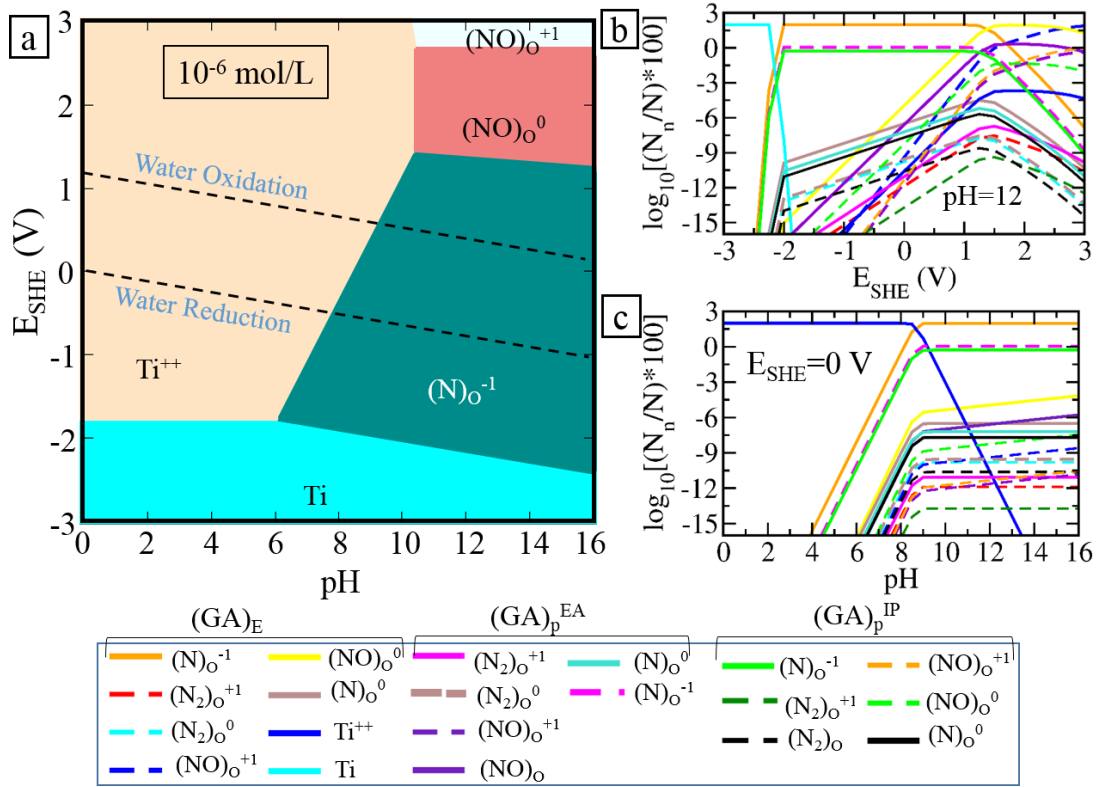


Figure 5.13: (a) Pourbaix diagram with aqueous ion concentration of 10^{-6} mol/L is obtained using PBE0 functional including vibrational contributions. The two inclined parallel black dashed lines show the electrode potentials for the water oxidation ($2\text{H}_2\text{O} - 4e^- \rightarrow \text{O}_2 + 4\text{H}^+$, upper one) and reduction ($2\text{H}_2\text{O} + 2e^- \rightarrow \text{H}_2 + 2\text{OH}^-$, lower one). (b, c) Logarithm of concentration (in %) of various configurations with respect to E_{SHE} (pH = 12) and pH ($E_{\text{SHE}} = 0$ V).

screened nonlocal exact exchange interaction, which is indispensable to draw the Pourbaix diagram accurately. The Pourbaix diagram at a moderate aqueous ion concentration $[I]$ of 10^{-6} mol/L is simulated for N-doped $(\text{TiO}_2)_{10}$ clusters for all sets [i.e., $(\text{GA})_E$, $(\text{GA})_P^{EA}$, $(\text{GA})_P^{IP}$] as shown in Fig. 5.13(a). $(\text{NO})_O^{+1}$, $(\text{NO})_O^0$ and $(\text{N})_O^{-1}$ phases of $(\text{GA})_E$ based clusters appear as the most stable one in the Pourbaix diagram at $\text{pH} > 6.0$, below which they will dissolve into Ti^{++} ions. $(\text{NO})_O^{+1}$ and $(\text{NO})_O^0$ are stable, when E_{SHE} resides above the oxidation potentials of water. We have finally performed probability analysis, to quantitatively reveal the existence of multiple-phase near the phase boundaries. The thermodynamic probabilities of the relevant species are varied between 0 to 1 near the phase boundary in a Pourbaix diagram. Therefore, it is important to compute the concentration of various configuration at different conditions of pH and E_{SHE} , to determine the occurrence probability of metastable states. If N is the total number

of all possible species in the aqueous medium and $\Delta\mu_n$ is the reaction chemical potential of specific type n configuration, then the number of n -type configurations, N_n , can be expressed as:

$$N_n = \left(N - \sum_{m \neq n} N_m \right) \frac{1}{e^{\beta\Delta\mu_n} + 1} \quad (5.21)$$

where $\beta = 1/k_B T$ and N_m is any other considered configuration type. Similar equation can be written for each configuration, and their solution will provide the concentration at different conditions of pH and E_{SHE} [237, 252].

$$\frac{N_n}{N} = \frac{e^{-\beta\Delta\mu_n}}{1 + \sum_m e^{-\beta\Delta\mu_m}} \quad (5.22)$$

Note that the 100% occurrence of a configuration in the medium corresponds to the value of logarithmic percentage concentration as 2. We have considered two types of electrochemical conditions: (i) E_{SHE} as a variable at fixed pH (=12) and (ii) pH as a variable at fixed E_{SHE} (=0 V) as shown in Fig. 5.13(b) and 5.13(c), respectively. The main observation from the probability profiles is the coexistence of multiple (stable and metastable) phases near the phase boundaries [Ti – (N)_O^{−1}, (N)_O^{−1} – (NO)_O⁺¹ in Fig. 5.13(b) and Ti⁺⁺ – (N)_O^{−1} in Fig. 5.13(c)]. We deduce that the (N)_O^{−1}, (NO)_O⁰ and (NO)_O⁺¹ states of (GA)_P^{EA} and (GA)_P^{IP} based clusters achieve significant concentration near the phase boundaries (see Fig. 5.13(b) and 5.13(c)). However, (N₂)_O conformers have comparatively less concentration at the phase boundaries. Hence, at operating conditions, the electrocatalytic active metastable states can contribute significantly in the overall activity of catalyst as their occurrence probability is comparable with stable phases.

5.4 Conclusion

In summary, we have presented a robust methodology to design clusters with desired properties: favorable formation energy, high vertical electron affinity (VEA), and low vertical ionization potential (VIP). For this purpose, we have implemented a suite of massively parallel cascade genetic algorithm to predict the accurate structures of N-doped (TiO₂)_n (n = 4 – 10, 15, 20) clusters viz. N_O, (NO)_O, (N₂)_O. From exhaustive scanning, we reveal that N-substitutional (N_O) dopant prefers to occupy oxygen site which is highly coordinated with Ti-atoms, whereas interstitial dopants [viz. (NO)_O and (N₂)_O] reside at the dangling oxygen site. Further, we have analyzed the thermodynamic stability of different doped configurations in various charge states at finite T and p_{O_2} using *ab initio* atomistic thermodynamics approach. We have found

that $(\text{NO})_O$ and $(\text{N}_2)_O$ are the most favorable phases in a wide range of T and p_{O_2} . We have noticed a significant reduction in the fundamental gap and excitation energy for doped clusters, which accounts for their application in electrocatalytic water splitting. N-doped clusters act as an efficient electrocatalyst for water splitting than the undoped counterpart due to the smaller ΔG value of the rate determining step, which results in lower overpotential. In the OER, the dissociation of OH^* and OOH^* are found to be the rate determining step, which correlates to the free energy of initial step of OER. Moreover, the doped clusters show high activity towards HER than the undoped clusters. Further, from Pourbaix diagram, $(\text{NO})_O^{+1}$, $(\text{NO})_O^0$ and $(\text{N})_O^{-1}$ phases of $(\text{GA})_E$ based clusters appear as the most stable one. The probability profiles show the coexistence of multiple (stable and metastable) phases near the phase boundary. Therefore, the metastable states can contribute significantly to the overall activity of the catalyst at the environmental conditions. Hence, to capture the metastability triggered reactivity, the adapted methodology will be helpful to design the rational nanoparticles for efficient water splitting.

Shape dependent catalytic activity of Ru nanoparticles

6.1 Introduction

Active metal catalysts are the key in chemical industry for sustainable production of multitude of chemical resources [253, 254, 255]. Among the various metal catalyst architectures, supported metal catalysts (i.e. metal nanoparticles (NPs) dispersed on heterogeneous supports) have been studied extensively [253, 254, 256, 257, 258, 259, 260, 261]. Their performance is often governed by the nature of metal-support interaction, which is strongly related to their structures [259, 260]. In this context, the long-standing concerns are, downsizing the metal NPs to few nanometers or even sub-nanometer scale for maximizing the atom utilization efficiency [257, 258]; controlling the shape of metal NPs to create more active surfaces [255, 261, 262]; and designing the functionalized supports, that strongly influence the local electronic structure of the materials [253, 263]. These parameters independently dictate the intrinsic activity and selectivity of many supported metal catalysts [254, 256, 263, 264]. However, tuning the size/shape of metal NPs and electronic structure of the material synergistically remain a significant challenge, but crucial for the rational development of active metal catalysts [62]. Primary amines are crucial intermediates for various applications such as production of polymers, pharmaceuticals, dyes and detergents [265, 266, 267]. The catalytic reductive amination of carbonyl compounds is a viable and valuable approach to form the primary amines [255, 259]. In particular, the reductive amination of biomass derived furfural gives the most valuable derivatives (furfurylamine) that are highly desirable in chemical industry. Moreover, catalytic hydrogenation of heteroarenes is a fundamentally important reaction in many synthetic chemical processes [268, 269, 270, 271]. For instances, direct hydrogenation of quinoline derivatives are immensely important for the selective production of 1,2,3,4-tetrahydroquinolines, a core structural motif in numerous pharmaceuticals,

agrochemicals and fine chemicals [272, 273, 274, 275, 276]. To date, most of the practical heterogeneous systems for transformation of carbonyl compounds and N-heteroarenes are mainly based on support catalysts of noble metals such as Pt, Pd, Rh, Au, Ru and Ir [277, 278, 279, 280, 281, 282, 283, 284, 285, 286]. Unfortunately, these noble metal catalysts are often hampered by lack of regioselectivity [287], low functional group tolerance [288], and poor recyclability [289]. Particularly, in most cases the catalysts are difficult to recycle because of deactivation/poisoning of the metal NPs by strong interaction with the heteroatoms [285, 289, 290]. Nowadays, Ru-based nanomaterials are of pivotal importance in numerous catalytic applications (synthetic-organic processes, ammonia synthesis, Fischer-Tropsch reactions, CO methanation oxidation water splitting, etc.), which is also the cheapest in price among the noble metals [255, 253, 259, 291, 292, 293, 294]. Herein, we first report a new specific flat-shaped fcc Ru nanoparticle that possesses the active sites with weak electron-donating ability, which facilitate the reductive amination of furfural. Further, in the pursuit of a high-performance Ru catalyst for hydrogenation of N-heteroarenes, we have focused on the nitrogen-containing carbon (N-carbon) as a functionalized support, in which incorporated N-atoms can strongly affect the physico-chemical and catalytic properties owing to the metal-support electronic interaction [295, 296]. Huge efforts have been devoted in recent years to the development of more active N-carbon modified metal-based materials including Ru ones [254, 296, 297, 298]. However, the electronic structure of these materials including activity-structure relationship has not yet been clarified, which is vital for designing more efficient catalysis. Computational study played an important role in understanding and predicting chemical reactivity of various catalytic materials for many valuable chemical reactions. Therefore, we have performed the density functional theory (DFT) calculations to provide activity-structure relationship for different types of Ru nanoclusters.

6.2 Methodology

All the spin-polarized density functional theory (DFT) calculations are carried out using the projector augmented wave (PAW) pseudopotential as implemented in the Vienna *ab initio* Simulation Package (VASP) [127, 128, 129]. We have employed the Perdew-Burke-Ernzerhof (PBE) exchange-correlation functional within generalized gradient approximation (GGA) [121] for the calculations. The cut-off energy is set to 500 eV for the plane wave basis sets to expand

the Kohn-Sham orbitals. The threshold value is specified up to 0.1 meV to achieve the self-consistency in the total energy. The Brillouin zone integrations are performed at the Γ point for all DFT calculations. To study the reductive amination of furfural over Ru-nanocatalysts, we have modeled the flat-shaped fcc Ru nanocluster with (111) facet and spherical-shaped hcp nanocluster containing 37 and 36 atoms, respectively. We have performed the calculations to find the full reaction path for transformation of quinoline to 1,2,3,4-tetrahydroquinoline over flat-shaped hcp Ru and Ru δ^- nanoclusters consisting 54 atoms. The supercell size is chosen 25 Å to prevent the interaction between the adjacent periodic images of the nanocluster. A 6×6 graphite supercell comprising three atomic layers with randomly doped N-atoms has been constructed to model the catalyst's support (N-doped carbon framework). A vacuum region in the perpendicular direction of supported cluster is set to 15 Å to minimize the effect of the periodic slab under periodic boundary conditions. The structures are fully relaxed until all the forces on each ion is lower than 0.001 eV/Å using conjugate gradient minimization. The climbing-image nudged elastic band (CI-NEB) method is used to locate the transition states (TSs) along the minimum energy path [140, 109]. The force tolerance is set to 0.02 eV/Å for CI-NEB calculations. Vibrational analysis is performed to verify that each of the transition state has an imaginary frequency along the minimum energy and rest of the configurations have the real frequencies. The adsorption energy (E_{ad}) of the adsorbate molecules is calculated as:

$$E_{ad} = E_{adsorbate+cluster} - E_{adsorbate} - E_{cluster} \quad (6.1)$$

where, $E_{cluster}$, $E_{adsorbate}$ and $E_{adsorbate+cluster}$ are the total energy of the nanocluster, the adsorbate in the gas phase and the adsorbate adsorbed on the nanocluster, respectively.

6.3 Results

6.3.1 Elucidating the role of catalyst's shape for reductive amination of furfural

6.3.1.1 Interaction of reactants with catalyst

As it has been suggested that the chemical transformation of furfural to other products significantly depends on the affinity of the reactants to the catalysts [299]. Therefore, first, we have determined the adsorption energies (E_{ad}) of the reactants (NH_3 , H_2 , furfural) and product

(furfurylamine) molecules on both the flat and spherical-shaped Ru nanoclusters. As a result, the spherical-shaped hcp Ru nanocluster clearly shows more stability for all the configurations due to higher adsorption strength than the flat-shaped fcc nanocluster as shown in Figure 6.1. Moreover, on comparing the adsorption energies of different adsorbed configurations of furfural molecule, we observe considerably weak interaction between furfural and flat-shaped Ru catalyst, in comparison to the conventional shaped Ru nanocluster and previously reported values (-1.83 eV on flat Pd(111) and -1.37 eV on Ru(001)) [299, 300]. It is noted, that the adsorption energy for furfural is obtained to be significantly lower on the flat-shaped fcc nanocluster (-0.21 eV), when the carbonyl group is tilted away from the catalyst surface with slightly stretched C–O bond up to 1.25 Å (see the Figure 6.2a). The interaction of the furfural is increased on the fcc nanocluster (-0.70 eV) due to strong bonding of carbonyl oxygen to top Ru-site via bond length of O–Ru 2.09 Å (see the Figure 6.2b). In the latter case, the bond length of C–O significantly stretches from 1.22 Å to 1.34 Å, and the negative charge density (-0.22) is comparatively less than the tilted carbonyl oxygen in the former case. It is important to note that the most stable configuration of furfural entails the furan ring lying flat on the cluster as well the carbonyl oxygen plays significant role in the adsorption strength (see Figure 6.2b and 6.2c). In isolated

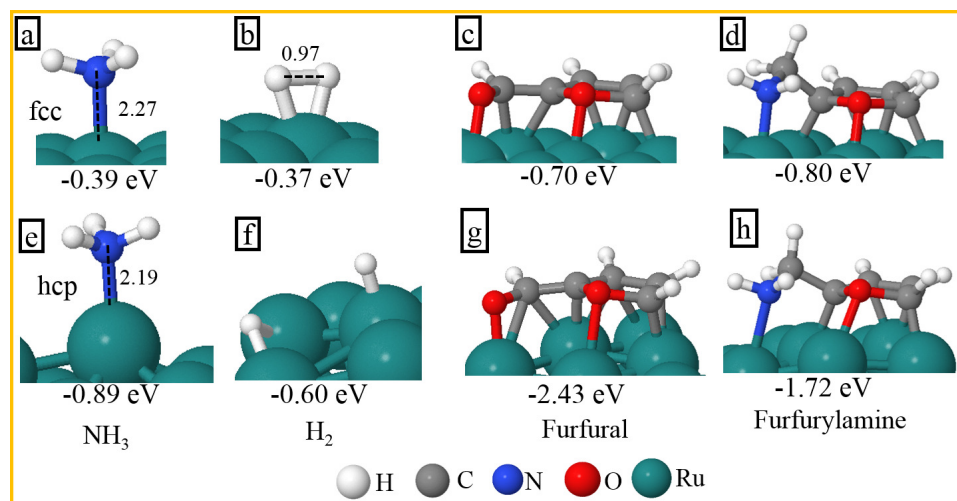


Figure 6.1: Side view of DFT-optimized adsorption configurations of reactants and products on flat-shaped fcc (upper panel) and spherical-shaped hcp clusters (lower panel). Bond lengths are labelled in Å.

furfural molecule, the carbonyl oxygen exhibits more localized negative charge density (-0.23) than the furan ring oxygen (-0.04) as shown in Figure 6.2d and 6.2e. In Table 6.1, the hirshfeld charge density of each atom for furfural molecule in different adsorbed configurations is given, from where we find that hcp nanocluster donates more charge to furfural due to which its gets

highly stabilized upon adsorption. Contrary to this, the flat-shaped Ru nanocluster possesses active sites with weak charge donating ability, which could be responsible for facile reductive amination of furfural to furfurylamine.

Atom	Hirshfeld charge			
	Isolated Furfural	Furfural on flat fcc Ru cluster (in Figure 6.1c)	Furfural on flat fcc Ru cluster (in Figure 6.1d)	Furfural on spherical hcp Ru cluster (in Figure 6.1e)
O1	-0.04	-0.06	-0.05	-0.07
O2	-0.23	-0.25	-0.22	-0.22
C3	0.04	-0.05	-0.06	-0.03
C4	-0.07	-0.08	-0.08	-0.10
C5	-0.05	-0.07	-0.08	-0.09
C6	0.04	0.01	0.05	0.02
C7	0.08	0.03	0.03	-0.01

Table 6.1: Hirshfeld charge density of furfural molecule.

6.3.1.2 Determination of activation barrier

Aiming to achieve better understanding, we further determine the energy barriers of the elementary steps and obtained reaction paths for reductive amination of furfural over flat-shaped fcc and spherical-shaped hcp Ru nanoclusters. This process constitutes five elementary steps as illustrated in Figure 6.3. The first step is the formation of O–H bond with carbonyl O-atom by cleaving the first N–H bond of NH_3 , yielding an intermediate (hydroxyalkyl), which is then followed by the addition of the second H atom to this intermediate, forming an adsorbed H_2O moiety. Subsequently, the bond formation between C and NH results in imine. After that by hydrogenation of imine, furfurylamine is formed in two elementary steps. Initially, we have evaluated the energy barrier for first step by considering three configurations of furfural on flat-shaped fcc nanocluster to determine the effect of different orientation of carbonyl group to initialize the reaction path (see in Figure 6.4). For parallelly adsorbed furfural, the activation barrier comes out to be 0.54 eV to scission the N–H bond of NH_3 . However, we notice comparatively lesser barriers (0.36 eV and 0.44 eV), when the carbonyl group is tilted away from the surface. Here, the bond length of Ru–O is substantially extended to 3.55 Å and 3.10

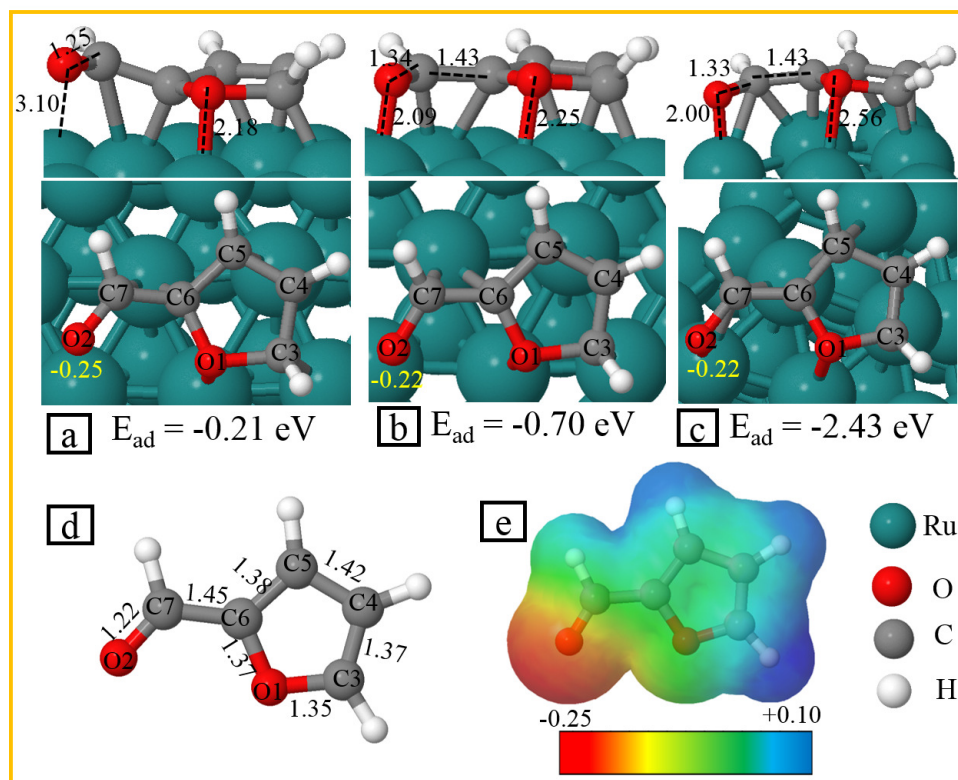


Figure 6.2: Side and top view of DFT-optimized adsorption configurations of furfural on flat-shaped fcc Ru nanocluster (a, b) and spherical-shaped hcp Ru nanocluster (c). The adsorption energy of furfural and hirshfeld charge density of O-atom (in yellow color) in carbonyl are shown with respective configuration. (d) Optimized geometry structure, and (e) hirshfeld charge density for isolated furural molecule. The dashed lines represent the bond lengths (labelled in Å).

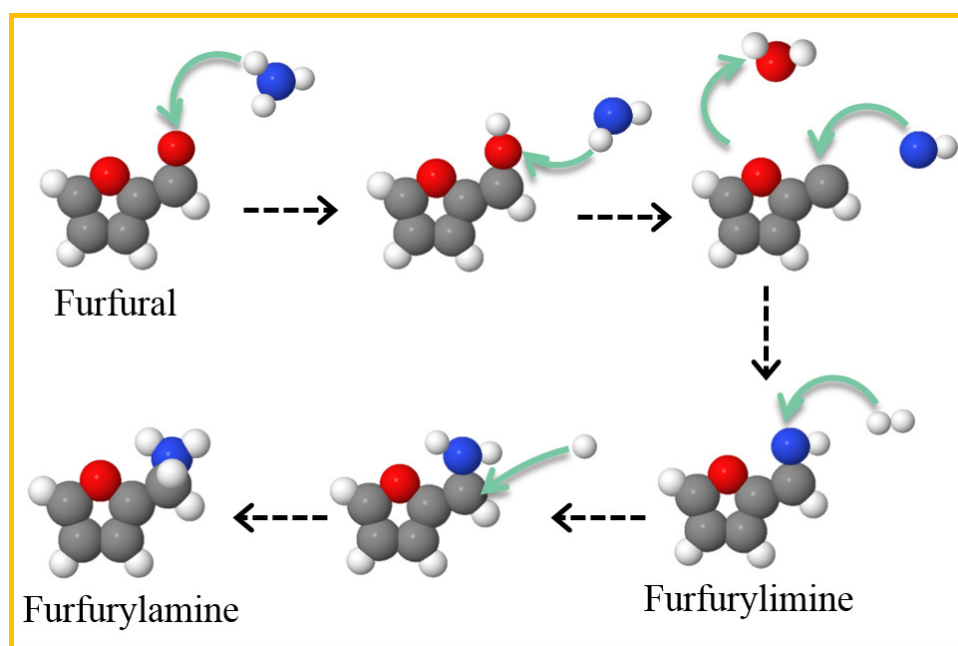


Figure 6.3: Illustration of elementary steps for reductive amination of furfural.

Å than the former case (2.16 Å) (as shown in Figures 6.4a, 6.4b and 6.4c). In bent configuration of carbonyl group, oxygen (O) atom has more localized negative charge density than the parallel configuration, due to which the NH₃ molecule slightly tilt towards the O-atom. This leads in slight lengthening of the N–H bond, which initializes the reductive amination over flat-shaped Ru catalyst. In Figure 6.5a and 6.5b, the complete reaction paths on the nanoclus-

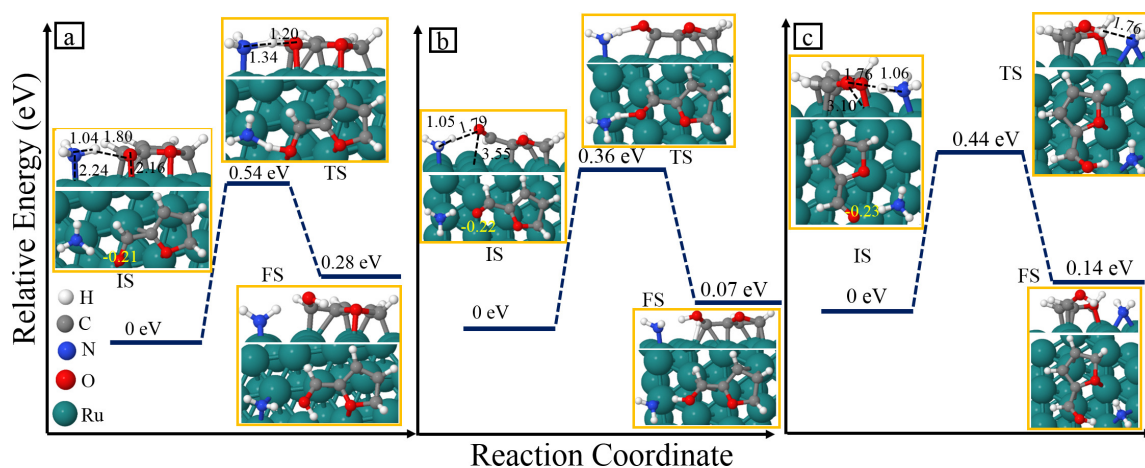


Figure 6.4: Reaction profiles of first elementary step with side and top view of initial state (IS), transition state (TS) and final state (FS) on flat-shaped fcc nanocluster by considering flat (a) and bent (b, c) configuration. The dashed lines represent the bond lengths (labeled in Å).

Reaction step	E _a on flat-shaped fcc Ru nanocluster (eV)	E _a on spherical-shaped hcp Ru nanocluster (eV)
2-4	0.54	0.69
4-6	1.24	1.83
7-9	0.64	0.71
10-12	0.20	0.91
12-14	0.50	1.07

Table 6.2: Activation barrier (E_a) of elementary reaction steps for the reductive amination of furfural.

ters corresponding to both the flat-shaped fcc (upper panel) and spherical-shaped hcp (lower panel) nanoclusters are shown, respectively. All the free energies are set with respect to the sum of total energy of furfural on catalyst, hydrogen and ammonia molecules in the gaseous phase. The first step starts with abstracting the first H-atom from the NH₃ via carbonyl oxygen. This step preferably occurs over fcc Ru nanocluster due to less activation barrier than hcp nanocluster. The second step (4-6) of pathway, to abstract the second H-atom from NH₂

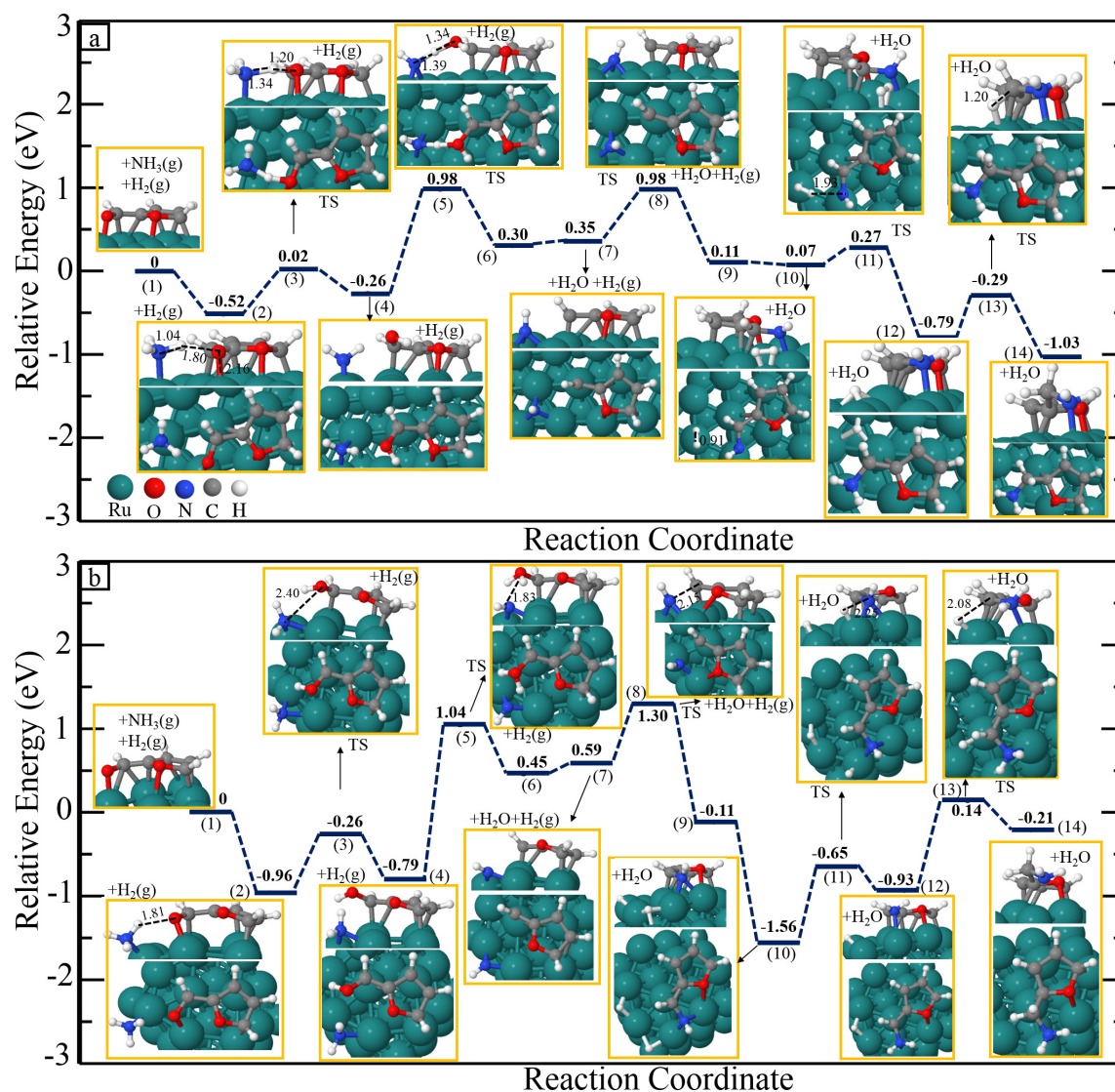


Figure 6.5: Reaction profile of furfural conversion to furfurylamine over flat-shaped (upper panel) and spherical-shaped (lower panel) Ru nanocluster. The side and top view of initial state (IS), transition state (TS) and final state (FS) structures of all the elementary steps on flat-shaped fcc nanocluster are shown. The dashed lines represent the bond lengths (labeled in Å).

group by the carbonyl oxygen to form the H_2O moiety, needs to overcome the highest activation barrier regardless of the type of nanocluster. This step may proceed in different way such as, formation of H_2O followed by scission of $\text{C}-\text{OH}$, which we have not considered here. In the third step, the formation of $\text{C}-\text{NH}$ bond results in intermediate product imine, and this is a thermodynamically unstable configuration. Note that hydrogenated derivatives degrades the selectivity of the catalyst, therefore, one should minimize its formation. Activation barriers show that imine is more readily to be formed over flat shaped Ru nanocluster. Moreover, the hydrogenation of imine to form furfurylamine on flat-shaped fcc nanocluster occurs easily due

to smaller activation barriers. We have summarized all the activation barriers in the given Table 6.2. The activation barrier corresponding to each step of spherical-shaped hcp nanocluster is slightly higher than that of the flat-shaped fcc nanocluster. More importantly, all the initial, final and intermediate configurations on spherical-shaped hcp nanoclusters exhibit the higher adsorption strength than the flat-shaped fcc nanocluster, which leads to deter the conversion of furfural to furfurylamine. Thus, the transformation of furfural is more readily over flat-shaped fcc nanocluster due to availability of less electron donating active sites. In addition, to predict the selectivity of the modeled nanoclusters, the activation barrier for ring hydrogenation of product molecule is also determined. We find that hydrogenation of the furan ring on the fcc nanocluster is an arduous step due to strong C–C bond, thus, this step requires the higher activation barrier (≈ 1.0 eV). Therefore, it can be inferred that the flat-shaped fcc Ru nanocluster favors selective reductive amination by preventing the formation of by products due to ring hydrogenation. Hence, we can make a key conclusion from the above discussion that the shape of Ru-catalyst is the prevalent factor to govern the catalytic properties.

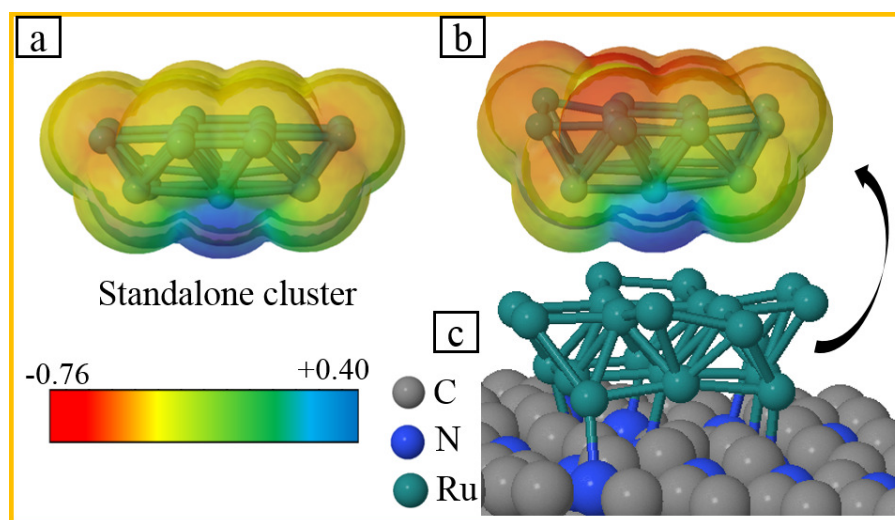


Figure 6.6: Optimized geometry structure and Hirshfeld charge density for (a) standalone and (b) supported hcp Ru nanocluster. (c) The side view of DFT-optimized structure of hcp Ru nanocluster on N-carbon support.

6.3.2 Role of support on catalytic activity of Ru nanoclusters

The synergistic effect and electronic property of the support provide the outstanding catalytic performance for chemoselective hydrogenation of several N-heteroarenes with low per metal usage. Therefore, we have modeled a flat-shaped hcp Ru nanocluster supported on top of the N-

carbon frame (Figure 6.6). On analyzing the Hirshfeld charge density of fully relaxed structure, we have found that N-atoms of the support are bound strongly with the Ru-atoms through electron donation and thereby increasing the negative charge density of Ru surface. Hence, N-doped carbon frame significantly altered the catalytic properties by providing the additional charge to the catalyst. In addition, the structural change in the carbon rings occurs due to the interaction of N-atoms with carbon atoms, which profoundly alters the physico-chemical properties of the support materials.

6.3.3 Role of charge state on catalytic activity of Ru nanoclusters

Next, we have estimated the adsorption energies (E_{ad}) of the quinoline (1a) molecule on top of a neutral Ru nanocluster and compared the same with a negatively charged $Ru^{\delta-}$ nanocluster. The latter is our representative model system of Ru nanocluster on N-carbon frame. The different adsorbed configurations of 1a molecule on Ru and $Ru^{\delta-}$ surfaces are shown in Figure 6.7. The 1a adsorbs on Ru surface with overall higher E_{ad} in the range -1.51 eV – -1.85 eV as shown in Figure 6.7a-c (depending on the site of the nanocluster). The E_{ad} for $Ru^{\delta-}$ surface is in the range -1.41 eV – -1.67 eV (Figure 6.7 d-e) for all possible configurations. This reduction in E_{ad} indicates the weak interaction of the N-heterocyclic ring of 1a with $Ru^{\delta-}$ surface, which prevents the poisoning of the catalyst. Moreover, the high adsorption energies are noticed if the N-atom of 1a is bonded with the Ru-atom with relatively positive charge density (in case of Figure 6.7a and 6.7d). However, less adsorption energies are observed for the cases of N-atom bonded at bridge site (see Figure 6.7b and 6.7e) and Ru-atom with more negative charge density (see Figure 6.7c and 6.7f). The weak binding of N-containing ring on catalyst leads to facilitate the reduction of C–N bond of quinoline. It is important to note that on top of the Ru cluster, we have obtained higher (in negative value) dissociative adsorption ($E_{ad} = -1.12$ eV) for H_2 molecule than the molecular adsorption ($E_{ad} = -0.42$ eV) on Ru nanocluster (see in Figure 6.8). This adsorbed H_2 molecule gets dissociated easily into atomic H and the corresponding activation barrier is estimated to be very minimal ($E_{ad} = 0.03$ eV). The presence of dissociated H-atoms on the catalyst further promotes the hydrogenation of quinoline. In order to understand the effect of charge state on performance of Ru catalysts, the energy barriers of elementary steps of 1a hydrogenation over Ru and $Ru^{\delta-}$ surfaces are calculated and the corresponding reaction paths are obtained (see Figure 6.9). All the free energies are set from a reference of 1a with one adsorbed H-atom on Ru and two H_2 molecules in the gaseous phase. The activation barrier

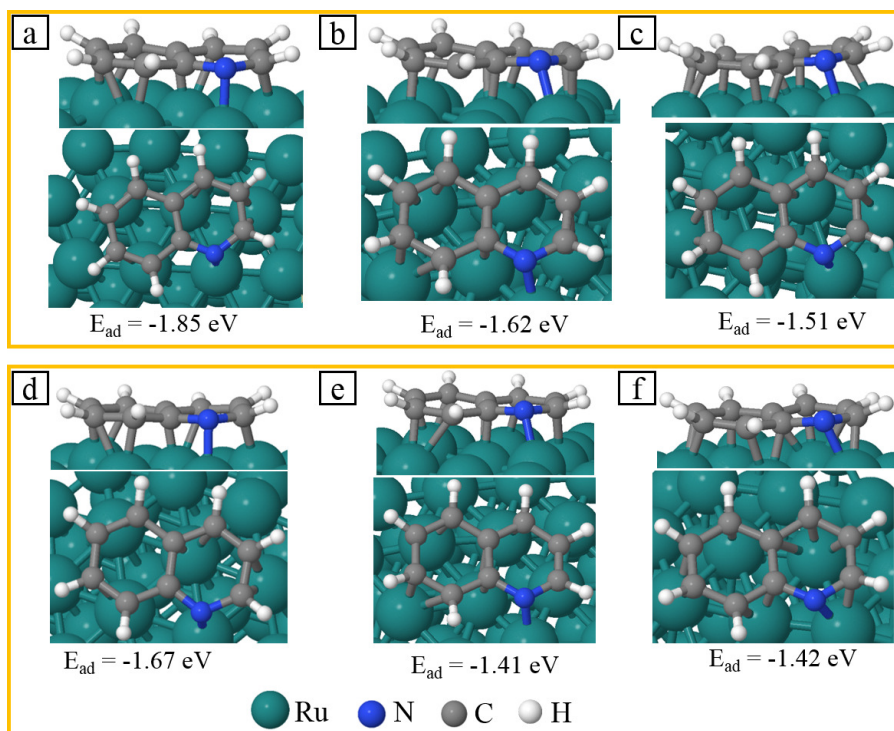


Figure 6.7: Side and top view of DFT-optimized adsorption configurations of quinoline (1a) on neutral Ru nanocluster (a, b, c) and negatively charged $\text{Ru}^{\delta-}$ nanocluster (d, e, f). The adsorption energy (E_{ad}) of 1a is shown with respective configuration.

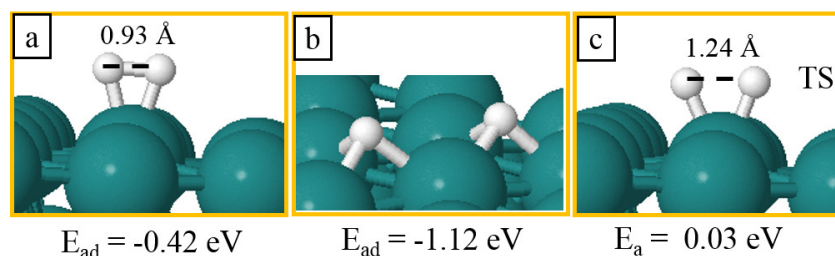


Figure 6.8: (a, b) Side view of DFT-optimized adsorption configuration of H_2 molecule, and (c) transition state of H_2 dissociation step on flat-shape Ru nanocluster.

(E_a) to react the first H-atom to the N-atom of heterocyclic ring (step I) from the Ru surface is smaller on $\text{Ru}^{\delta-}$ (≈ 0.23 eV) than that of on Ru (≈ 0.69 eV). This clearly indicates the facile reduction of the N-atom with more localized negative charge density. Also, the next consecutive step (II) of hydrogenation proceeds easily on $\text{Ru}^{\delta-}$ (having $E_a \approx 0.72$ eV; see Table 6.3), due to weak interaction of the adjacent C-atom of N-heterocyclic ring with the Ru surface. However, in case of neutral Ru, the H-atom has lesser number of sites as these sites are blocked by heterocyclic ring's atoms. Therefore, in latter case we have observed the higher E_a (1.15 eV) than the former case (for $\text{Ru}^{\delta-}$ (0.72 eV)). Owing to these hydrogenation steps, the N-heterocyclic ring is observed to get tilted (some part is displaced upward) from the surface

in such a way so that the interaction with the Ru surface becomes weaker. We find this to

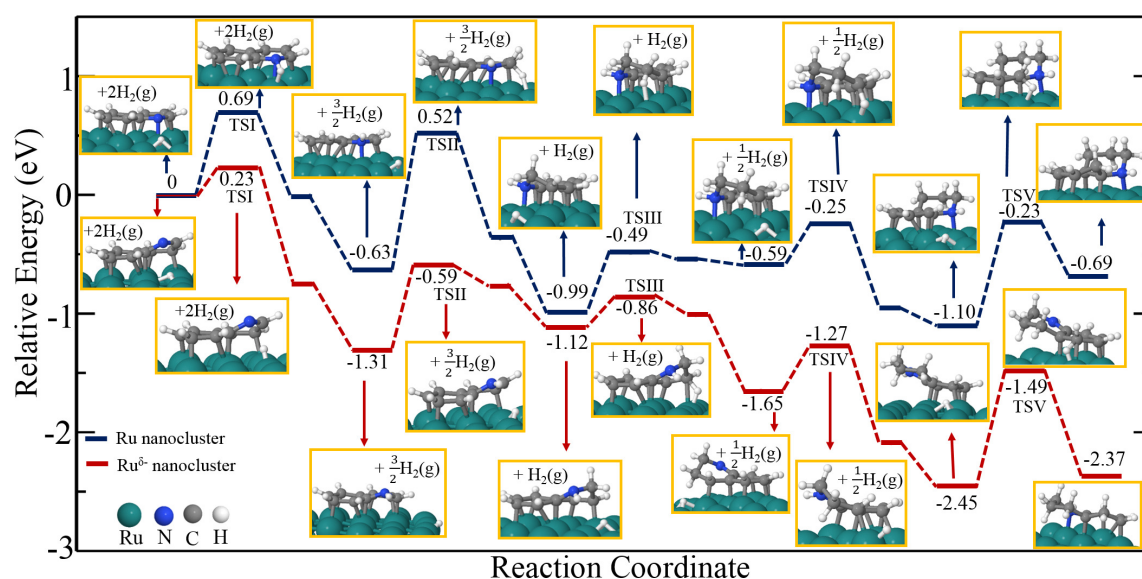


Figure 6.9: Reaction profile of quinoline conversion to 1,2,3,4-tetrahydroquinoline over flat-shaped hcp Ru and $\text{Ru}^{\delta-}$ nanocluster. The side view of initial state (IS), transition state (TS) and final state (FS) structures of all the elementary steps are shown.

be more significant on $\text{Ru}^{\delta-}$ nanocluster than the neutral counterpart. Since on $\text{Ru}^{\delta-}$ surface, some part of the N-heterocyclic gets more tilted, the C-atom's interaction gets reduced with the Ru-atoms, which results in favorable hydrogenation. The adjacent H-atom (dissociative adsorbed H-atom) could move easily on the Ru surface to reach the C-atom of N-heterocyclic ring (see the Figure 6.10). This in turn helps to have lesser activation barrier E_a for the next two steps (III and IV) of the hydrogenation on $\text{Ru}^{\delta-}$ surface (Table 6.3). However, note that the activation barrier for the hydrogenation of step (V) of benzene ring is observed to be higher on the $\text{Ru}^{\delta-}$ surface than the neutral one. Figure 6.11 infers that there is preferential selective

Reaction step	E_a on neutral hcp Ru nanocluster (eV)	E_a on negatively charged hcp Ru nanocluster (eV)
1 st	0.69	0.23
2 nd	1.15	0.72
3 rd	0.50	0.26
4 th	0.34	0.38
For Benzene Ring Hydrogenation	0.87	0.96

Table 6.3: Activation barrier (E_a) of elementary reaction steps for hydrogenation of quinoline (1a) on Ru and $\text{Ru}^{\delta-}$ nanoclusters.

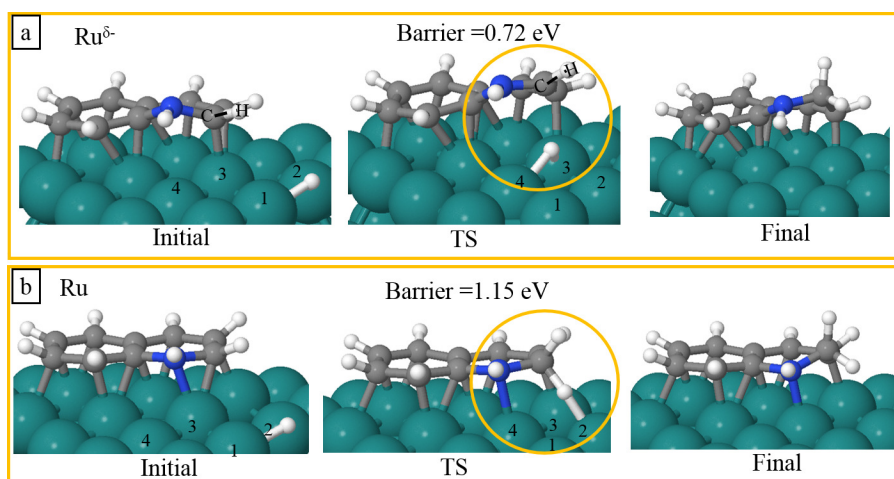


Figure 6.10: (a, b) Side view of initial state (IS), transition state (TS) and final state (FS) for second step of hydrogenation on negatively charged Ru^{δ-} and neutral Ru nanocluster, respectively.

hydrogenation of N-heterocyclic ring of 1a the sites rich in negative charge density. The lower E_a for the hydrogenation of N-heterocyclic ring is ascribed to its weak interaction with the electron-rich Ru surface, which initiates high performance of the flat-shaped hcp Ru catalyst.

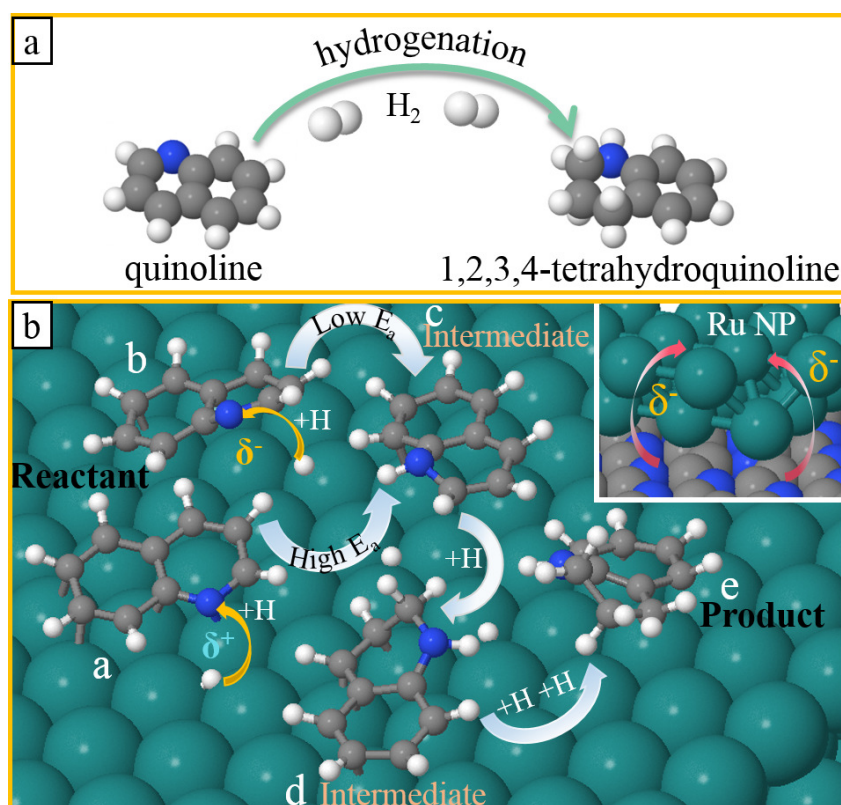


Figure 6.11: Schematic representation of reaction processes for hydrogenation of quinoline over Ru catalyst. The electron rich site is highly active to initialize the hydrogenation process. The detailed configurations for full reaction paths on flat-shaped hcp Ru and Ru^{δ-} nanoparticles are illustrated in Figure 6.9.

6.4 Conclusions

In summary, we have addressed that the shape of Ru nanoparticles is an important factor in determining their catalytic performance. It is noticed that the adsorption energy plays pivotal role to predict the catalytic activity of these nanoparticles to convert carbonyl and imine compounds into other products. The weaker adsorption drives their selective transformation into other valuable derivatives. Our results reveal that flat-shaped fcc nanoparticles with weak charge donating ability possess more active sites than the conventional shaped Ru, that are responsible for facile reductive amination of furfural to fufurylamine. For the first time, the strong electron donating power of Ru catalyst due to charge transfer from a N-carbon support is revealed by DFT calculations. This catalyst exhibits high catalytic activity due to weak adsorption energies of quinoline at the electron-rich Ru surface. Moreover, weak adsorption energies of quinoline at the electron-rich Ru surface prevents poisoning caused by its adsorption and provides excellent reusability. The low activation barriers for the hydrogenation steps of N-heterocyclic ring correlate with high catalytic activity. Hence, we suggest that the shape-controlled characterization and modeling of Ru nanocatalysts would build a strong foundation for tailoring and optimizing their catalytic performance in various important reactions.

Conclusions and future aspects

An efficient modeling of catalytic materials requires the throughout understanding of catalytic process at each length and time scale from electronic level to macroscopic level. The best way to approach a vast problem is to divide it into subproblems and deal one by one, by integrating the developed methods and techniques. The advancement and rational design of catalytic materials ultimately depend, on understanding of the system at atomic level that mainly involved the individual molecular processes. Under realistic conditions catalytic materials come into contact with reactive molecules of surrounding phase. Due to adaptive nature of catalyst, the operating conditions significantly influence the catalyst surface and induce the changes in local structure, composition and morphology of the catalyst. Moreover, catalysts change their stoichiometry by adsorbing the ligands from the reactive atmosphere. The newly formed configurations can play major role in the observed activity of catalyst. Therefore, the working framework becomes incredibly complex and dynamical. This indicates the necessity of comprehensively explore the low energy isomers to address their impact in catalysis. The advanced property based genetic algorithm in the framework of density functional theory is highly efficient to accurately predict the global minimum as well as metastable structures. *Ab initio* atomistic thermodynamics allows to account the effect of temperature and pressure, which is of crucial importance for modeling and performance of advanced catalysts. In particular, small cluster is considered as the prototypical system to fully understand the active sites which makes it one of the enduring research topics. Therefore, the aim of our work is to design the metal/metal-oxides nanoclusters for catalytic applications (e. g. C–H bond activation, overall water splitting, reduction and hydrogenation) and thoroughly explore their electronic and catalytic properties at finite temperature and pressure. Further, the performance of clusters are enhanced by mixing/doping different add-atoms, charge defect, changing the shape and tuning the morphology of support. The significant efforts have been dedicated for efficient designing of metastable structures and

their role in catalysts' performance. The calculations that I have carried out for designing efficient catalytic materials are: (a) clusters designing via property based cascade genetic algorithm (b) ground state geometry, electronic structure (c) stability using *ab initio* atomistic thermodynamics, fundamental gap using GW approximation (d) transition state and reaction pathways using the Nudge Elastic Band method.

Following these methods, the extensive study have carried out on bimetallic $[\text{TM}_x\text{Mg}_y\text{O}_z]^{+/0/-}$ clusters (TM = Cr, Fe, Co, Ni with $x + y \leq 5$) in an oxygen (O)-environment. The composition, atomic structure, stability, electronic properties and catalytic activity of $\text{TM}_x\text{Mg}_y\text{O}_z$ clusters at realistic temperature T and partial oxygen pressure p_{O_2} are explored by using robust methodologies. The low-energy isomers of the different clusters are identified by employing a massively parallel cascade genetic algorithm (cGA) in the framework of density functional theory. The thermodynamic stability of the tailored clusters is determined by minimizing their Gibbs free energy of formation using the *ab initio* atomistic thermodynamics. Our results reveal that the neutral and anionic clusters are the most stable phases in the wide range of temperature and pressure. By analyzing a huge data set, we find that the fundamental gap E_g of these clusters is strongly correlated with Mg-coordinated O_2 moieties. This is in contrast to the conventional belief that O-atoms are mainly responsible to reduce the fundamental gap. Also, we have noticed that near ambient conditions O-rich clusters are the most stable, whereas at higher temperature and lower pressure, O-deficient clusters become favorable. Following these findings, further we have extended our interest to explore the explicit role of TM in these clusters. The TM gives rise to different structural motifs (O_2^- and O_2^{2-}) in the cluster, which may act as the active centers for oxidative coupling of methane. The metastable and negatively charged clusters have shown better catalytic activity for C–H bond activation because of their unique structural and electronic properties. By taking the inspiration from higher activity of metastable cluster, our further study is extensively dedicated to efficiently design the metastable clusters. For this, we have considered N-doped $(\text{TiO}_2)_n$ clusters as prototypical system to drive the overall water splitting. This requires fixing various parameters viz. (i) favorable formation energy, (ii) low fundamental gap, (iii) low excitation energy and (iv) high vertical electron affinity (VEA) and low vertical ionization potential (VIP). In order to fix these parameters, we have used a suite of genetic algorithms [viz. searching clusters with conventional minimum total energy ($(\text{GA})_E$); searching clusters with specific property i.e. high VEA ($(\text{GA})_P^{\text{EA}}$), and low VIP ($(\text{GA})_P^{\text{IP}}$)] to model the N-doped $(\text{TiO}_2)_n$ ($n = 4 - 10, 15, 20$) (meta)stable clusters. From exhaustive scan-

ning of potential energy surface, we have addressed that N-substitution ((N)_O) prefers to reside at highly coordinated oxygen site to maximize its coordination, whereas N-interstitial ((NO)_O) and split-interstitial ((N₂)_O) favor the dangling oxygen site. Interestingly, we find that each types of defect (viz. substitution, interstitials) reduce the fundamental gap and excitation energy substantially. However, (NO)_O and (N₂)_O doped clusters are the potential candidates for overall water splitting, whereas N_O is congenial only for oxygen evolution reaction (OER). The relative efficiency for generating structures for overall water splitting is $(GA)_P^{EA} > (GA)_P^{IP} > (GA)_E$ for all the doped configurations. Hence, to capture the metastability triggered reactivity, the adapted methodology is useful to design the efficient nanoclusters. Further, we have explored the role of clusters' shape on the catalytic activity of Ru catalyst. Our results show that flat-shaped fcc nanoparticles with weak charge donating ability possess more active sites than the conventional shaped Ru, that are responsible for facile reductive amination of furfural to fufurylamine. In addition to shape, support also play the pivotal role to determine the activity of Ru catalysts. We observe that N-carbon support transfer the significant amount of charge to the Ru nanocluster that leads to increment in electron donating capacity of Ru catalyst. The weak adsorption of reactant molecules are noticed on Ru nanoclusters that facile the transformation of carbonyl and imine compounds into valuable products. Hence, this study suggests the necessity to acquire clear understanding of underlying factors that govern the performance of catalyst prior to their synthesis.

Future aspects. The work presented in this thesis elucidates the electronic structure, thermodynamic stability and catalytic activity of complex oxide clusters at realistic conditions. Our findings provide the in-depth understanding that how the charged defects, shape, size, doping and ligand influence the catalytic properties of the clusters. The present work can be further extended to include the support effect on the modeled bimetallic oxide clusters and to see how the catalytic properties of the corresponding system varies. Moreover, the designed clusters can be used to perform many other chemical processes (oxidation, reduction and dehydrogenation etc.). The methods used here can be employed to understand the effect of finite temperature and pressure on other catalysts' performance. Also, the adopted strategy opens up new directions for rational designing of new catalyst. Doping, alloying, changing the shape and tuning the support provide the tremendous opportunities to enhance the performance of the catalyst. Hence, designing functional materials based on these approaches can be studied in detail for more insights. The property based algorithm assists us to target the structures which possess

the active centers. This not only helps in designing the most stable structure but also target the highly active low energy metastable isomers of the catalyst. The modeled clusters can further be modified to accommodate more complexities like ternary and quaternary component based catalysts. In order to get the complete picture of dynamic changes of operating catalysts, we need to include the adaptive methods such as Microkinetics and kinetic Monte Carlo simulations. Further, it is essential to find the suitable descriptor to predict the catalytic activity of large data set of bimetallic oxide clusters. In our study, we have found that the fundamental gap and binding energy are more appropriate to predict the activity of designed catalyst. In addition to that we can develop the machine learning methods for cluster designing and predicting the catalytic properties to reduce the computational cost.

The van't Hoff equation

$$\frac{d \ln K}{dT} = \frac{\Delta H^\ddagger}{RT^2} \quad (\text{A.1})$$

ΔH^\ddagger is the enthalpy for the equilibrium. K is the equilibrium constant of the reaction.

The van't Hoff equation use to describe the temperature dependence of equilibrium constant:

Let's consider the two states of reaction A and B in equilibrium: $A \longrightarrow B$. The equilibrium condition at constant T and p :

$$\mu_A = \mu_B$$

$$\mu_A^\ddagger + kT \ln p_A = \mu_B^\ddagger + kT \ln p_B$$

$$\ln \left(\frac{p_B}{p_A} \right) = \frac{-(\mu_B^\ddagger - \mu_A^\ddagger)}{kT} = -\frac{\Delta \mu^\ddagger}{kT}$$

The pressure based equilibrium constant: $K_p = \frac{p_B}{p_A}$.

$$\ln K_p = -\frac{\Delta \mu^\ddagger}{kT}$$

By taking the derivative:

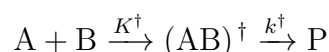
$$\left(\frac{d \ln K_p}{dT} \right) = -\frac{d}{dT} \left(\frac{\Delta \mu^\ddagger}{kT} \right) = -\frac{d}{dT} \left(\frac{\Delta H^\ddagger - T \Delta S^\ddagger}{kT} \right)$$

where H, S and μ indicate an enthalpy, entropy and free energy per molecule or per mole. If ΔH^\ddagger and ΔS^\ddagger do not depend on temperature:

$$\left(\frac{d \ln K_p}{dT} \right) = \frac{\Delta H^\ddagger}{kT^2}$$

Calculating rate coefficients from Transition State Theory

Let's consider the reaction $A + B \xrightarrow{k_2} P$ to calculate the rate coefficient k_2 by applying the transition state theory. The transition state theory depends on two main assumption: (i) Reactants and activated complex are in equilibrium, (ii) Decomposition of activated complex to form the product.



where, K^\ddagger is the equilibrium constant between the reactants and activated complex $(AB)^\ddagger$ for the first step. k^\ddagger rate coefficient for the second step, in which transition state forms the product.

$$K^\ddagger = \frac{[(AB)^\ddagger]}{[A][B]}$$

where, $[(AB)^\ddagger] = K^\ddagger[A][B]$ represents the concentrations of activated complexes. The overall rate of reaction can be written by decomposition rate of transition state to product:

$$\frac{d[P]}{dt} = k^\ddagger[(AB)^\ddagger] = k^\ddagger K^\ddagger[A][B]$$

$$k_2 = k^\ddagger K^\ddagger$$

Equilibrium constant K^\ddagger can be expressed in terms of partition functions.

$$K^\ddagger = \left(\frac{Q_{(AB)^\ddagger}}{Q_A Q_B} \right) \exp(-\Delta E^\ddagger / kT)$$

where, ΔE^\ddagger is an energetic difference between the transition state and the reactants. $Q_{(AB)^\ddagger}$, Q_A , and Q_B are the partition functions for the activated complex and reactants. The total partition function of a molecules contains the translation, rotational, vibrational and electronic configurations terms. The general expression of this:

$$Q = Q_{trans} \times Q_{rot} \times Q_{vibr} \times Q_{el}$$

For the activated state, we can divide it into two parts:

$$Q_{(AB)^\ddagger} = Q_{rc} \times Q_{oth}$$

Q_{rc} is the partition function corresponds to the one degree of freedom (vibration) along the reaction coordinate. Contribution of other degree of freedoms includes in Q_{oth} . The expression of Q_{rc} partition function:

$$Q_{rc} = \sum_{n=0}^{\infty} \exp\left(-\frac{nh\nu}{k_B T}\right)$$

This can be written as:

$$Q_{rc} = \frac{1}{1 - \exp\left(-\frac{nh\nu}{k_B T}\right)}$$

For the small value of ν , we can write it as follow:

$$Q_{rc} \approx \frac{1}{1 - 1 + \frac{h\nu}{k_B T}} = \frac{k_B T}{h\nu}$$

Chemical potential of oxygen

The partition function of an ideal gas containing of N indistinguishable O_2 molecules in a confined volume V :

$$q_N = \frac{1}{N!} [q]^N = \frac{1}{N!} [q^{trans} \times q^{rot} \times q^{vib} \times q^{conf} \times q^{elect}]^N \quad (A.2)$$

Chemical potential in term of partition function:

$$\mu_{O_2}(T, p_{O_2}) = \frac{G}{N} = \frac{1}{N} [-k_B T \ln q_N + pV] \quad (A.3)$$

By combining equation [A.2](#) and [A.3](#):

$$\begin{aligned} \mu_{O_2}(T, p_{O_2}) = & \frac{1}{N} [-k_B T \ln \left[\frac{1}{N!} (q^{trans})^N \right] - k_B T \ln [(q^{rot})^N] - k_B T \ln [(q^{vib})^N] \\ & - k_B T \ln [(q^{conf})^N] - k_B T \ln [(q^{elect})^N] + pV] \end{aligned} \quad (A.4)$$

Derivation of partition functions of different motions:

(i) q^{trans} : Let's consider an ideal gas consisting of N non-interacting indistinguishable molecules filled in a cylinder of volume V .

$$q_N = \frac{1}{h^f N!} \int e^{\beta E} d^f q d^f p \quad (A.5)$$

For a single particle $f = 3$, $N = 1$. Transnational partition function:

$$\begin{aligned}
q^{trans} &= \frac{1}{h^3} \int e^{\beta E} d^3q d^3p \\
&= \frac{V}{h^3} \int e^{\frac{\beta P^2}{2m}} d^3p \\
&= \frac{V}{h^3} \int_0^\infty \int_0^\pi \int_0^{2\pi} e^{\frac{\beta P^2}{2m}} p^2 dp \sin\theta d\theta d\phi \\
&= \frac{V}{h^3} \int_0^\infty 4\pi e^{\frac{\beta P^2}{2m}} p^2 dp \\
&= \frac{4\pi V}{h^3} \frac{\Gamma 3/2}{2\left(\frac{\beta}{2m}\right)^{3/2}}
\end{aligned} \tag{A.6}$$

$$\text{since, } \int_0^\infty e^{-\alpha x^2} x^n dx = \frac{\Gamma n + 1/2}{2(\alpha)^{n+1/2}}$$

$$q^{trans} = V \left(\frac{2\pi m K_B T}{h^2} \right)^{3/2} = \frac{V}{\lambda^3}$$

where, $\lambda = \frac{h}{\sqrt{2\pi m k_B T}}$, is the thermal de broglie wavelength

Hence the partition function for N-particles:

$$q_N = \frac{[q^{trans}]^N}{N!} = \frac{1}{N!} \left(\frac{V}{\lambda^3} \right)^N \tag{A.7}$$

$$\mu_{O_2}^{trans} = \frac{1}{N} \left[-k_B T \ln \left[\frac{1}{N!} (q^{trans})^N \right] + pV \right]$$

by using stirling formula : $\ln N! = N \ln N - N$

$$\begin{aligned}
&= \frac{1}{N} \left[k_B T (N \ln N - N) - k_B T N \ln q^{trans} + pV \right] \\
&= \frac{1}{N} \left[k_B T (N \ln N - N) - k_B T N \ln q^{trans} + pV \right]
\end{aligned}$$

since, $pV = N k_B T$

$$\begin{aligned}
&= \frac{1}{N} \left[k_B T (N \ln N) - N k_B T - k_B T N \ln q^{trans} + N k_B T \right] \\
&= \frac{k_B T N}{N} \left[\ln N - \ln q^{trans} \right] = -k_B T \ln \frac{q^{trans}}{N}
\end{aligned} \tag{A.8}$$

$$\begin{aligned}
q^{trans} &= V \left(\frac{2\pi m K_B T}{h^2} \right)^{3/2} \\
&= -k_B T \ln \left[\frac{V}{N} \left(\frac{2\pi m K_B T}{h^2} \right)^{3/2} \right]
\end{aligned}$$

since, $pV = N k_B T$; $\frac{V}{N} = \frac{k_B T}{p}$

$$\mu_{O_2}^{trans} = -k_B T \ln \left[\left(\frac{2\pi m}{h^2} \right)^{3/2} \frac{(k_B T)^{5/2}}{p} \right] \tag{A.9}$$

(ii) q^{rot} and q^{conf} :

$$q^{rot} = \sum g_j e^{-\beta E_j} \quad (\text{A.10})$$

where, $g_j = (2j + 1)$ term is the degeneracy factor.

$$E_j = \frac{j(j+1)\hbar^2}{2I} \quad (\text{A.11})$$

for higher values of T and I : $j+1 \approx j$ and $2j+1 \approx 2j$. When, the spacing of the rotational levels become smaller as compared to $k_B T$ then \sum in q^{rot} can be changed into \int .

$$\begin{aligned} q^{rot} &= \int_0^\infty 2j e^{-\frac{j^2 \hbar^2}{2Ik_B T}} dj \\ &\text{since, } \int_0^\infty e^{-\alpha x^2} x^n dx = \frac{\Gamma(n+1/2)}{2(\alpha)^{n+1/2}} \\ &= 2 \times \frac{\Gamma 1}{2 \left(\frac{\hbar^2}{2Ik_B T} \right)^{1+1/2}} \\ q^{rot} &= \frac{8\pi^2 I k_B T}{h^2} \end{aligned} \quad (\text{A.12})$$

Note that this expression is valid only for linear molecules. For non-linear cases one need to consider all three eigenvalues of inertial tensor (I_A , I_B and I_C). This term couples with the classical symmetry number (σ) which represents the number of indistinguishable orientations of the molecule.

$$q^{rot} = \frac{8\pi^2 I k_B T}{\sigma h^2} \quad (\text{A.13})$$

$$\begin{aligned} \mu_{O_2}^{rot} &= -k_B T \ln q^{rot} \\ \mu_{O_2}^{rot} &= -k_B T \ln \left(\frac{8\pi^2 I k_B T}{\sigma h^2} \right) = -k_B T \ln \left(\frac{8\pi^2 I k_B T}{h^2} \right) - k_B T \ln \left(\frac{1}{\sigma} \right) \end{aligned} \quad (\text{A.14})$$

(iii) q^{vib} :

The vibrational contribution of partition function is obtained under harmonic approximation.

$$q^{vibrational} = \sum_i \sum_{n=0}^\infty e^{-\beta(n+\frac{1}{2})\hbar\omega_i} \quad (\text{A.15})$$

By expanding the geometric series for $n = 0, 1, 2 \dots \infty$.

$$\sum_{n=0}^\infty e^{-\beta(n+\frac{1}{2})\hbar\omega} = e^{-\frac{\beta\hbar\omega}{2}} + e^{-\frac{3\beta\hbar\omega}{2}} + e^{-\frac{5\beta\hbar\omega}{2}} + \dots = \frac{e^{-\beta\hbar\omega/2}}{1 - e^{-\beta\hbar\omega}} \quad (\text{A.16})$$

$$\begin{aligned} \mu_{O_2}^{vib} &= -k_B T \ln q^{vib} = -k_B T \ln \left[\frac{e^{-\beta\hbar\omega/2}}{1 - e^{-\beta\hbar\omega}} \right] \\ &= -k_B T \left[\ln(e^{-\beta\hbar\omega/2}) - \ln(1 - e^{-\beta\hbar\omega}) \right] \\ &= \frac{\hbar\omega}{2} + k_B T \ln(1 - e^{-\beta\hbar\omega}) \end{aligned} \quad (\text{A.17})$$

Partition function by taking sum over all the modes:

$$\mu_{\text{O}_2}^{vib} = \sum_i \frac{h\nu_i}{2} + \sum_i k_B T \ln \left[1 - e^{-\frac{h\nu_i}{k_B T}} \right] \quad (\text{A.18})$$

where first term is the zero-point energy.

(iv) q^{elect} :

Internal excitation energies of most of molecules are usually higher as compared to $k_B T$, therefore mainly the ground state contributes to the partition.

$$q^{elect} = \sum_i \left(\mathcal{M}_i e^{-\frac{E_i}{k_B T}} \right) \approx \mathcal{M} e^{-\frac{E^{DFT}}{k_B T}} \quad (\text{A.19})$$

$$\mu^{elect} = -k_B T \ln q^{elect} = -k_B T \ln \mathcal{M} + E^{DFT} \quad (\text{A.20})$$

Total partition function of O_2 molecule by combining the equations [A.9](#), [A.14](#), [A.18](#) and [A.20](#):

$$\begin{aligned} \mu_{\text{O}_2}(T, p_{\text{O}_2}) = & -k_B T \ln \left[\left(\frac{2\pi m}{h^2} \right)^{\frac{3}{2}} (k_B T)^{\frac{5}{2}} \right] + k_B T \ln p_{\text{O}_2} - k_B T \ln \left(\frac{8\pi^2 I_A k_B T}{h^2} \right) \\ & + \frac{h\nu_{OO}}{2} + k_B T \ln \left[1 - \exp \left(-\frac{h\nu_{OO}}{k_B T} \right) \right] + E^{DFT} - k_B T \ln \mathcal{M} + k_B T \ln \sigma \end{aligned} \quad (\text{A.21})$$

Bibliography

- [1] Stanisław Waclawek, Vinod VT Padil, and Miroslav Černík. Major advances and challenges in heterogeneous catalysis for environmental applications: a review. *Ecological Chemistry and Engineering S*, 25(1):9–34, 2018.
- [2] Ib Chorkendorff and Johannes W Niemantsverdriet. *Concepts of modern catalysis and kinetics*. John Wiley & Sons, 2017.
- [3] Beatriz Roldan Cuenya. Synthesis and catalytic properties of metal nanoparticles: Size, shape, support, composition, and oxidation state effects. *Thin Solid Films*, 518(12):3127–3150, 2010.
- [4] Peter William Atkins, Julio De Paula, and James Keeler. *Atkins' physical chemistry*. Oxford university press, 2018.
- [5] David J Singh and Lars Nordstrom. *Planewaves, Pseudopotentials, and the LAPW method*. Springer Science & Business Media, 2006.
- [6] Daniel Sheppard, Rye Terrell, and Graeme Henkelman. Optimization methods for finding minimum energy paths. *The Journal of chemical physics*, 128(13):134106, 2008.
- [7] Hua-Jin Zhai and Lai-Sheng Wang. Probing the electronic structure and band gap evolution of titanium oxide clusters $(\text{TiO}_2)_n^-$ ($n= 1-10$) using photoelectron spectroscopy. *Journal of the American Chemical Society*, 129(10):3022–3026, 2007.
- [8] SA Shevlin and SM Woodley. Electronic and optical properties of doped and undoped $(\text{TiO}_2)_n$ nanoparticles. *The Journal of Physical Chemistry C*, 114(41):17333–17343, 2010.

-
- [9] Zheng-wang Qu and Geert-Jan Kroes. Theoretical study of the electronic structure and stability of titanium dioxide clusters $(\text{TiO}_2)_n$ with $n= 1- 9$. *The Journal of Physical Chemistry B*, 110(18):8998–9007, 2006.
- [10] Zheng-wang Qu and Geert-Jan Kroes. Theoretical study of stable, defect-free $(\text{TiO}_2)_n$ nanoparticles with $n= 10- 16$. *The Journal of Physical Chemistry C*, 111(45):16808–16817, 2007.
- [11] Marco Piumetti. A brief history of the science of catalysis-i. *Chimica Oggi-Chemistry Today*, 32:6, 2014.
- [12] Gerhard Ertl. Wilhelm ostwald: Founder of physical chemistry and nobel laureate 1909. *Angewandte Chemie International Edition*, 48(36):6600–6606, 2009.
- [13] Bretislav Friedrich. Fritz haber: Chemist, nobel laureate, german, jew. by dietrich stoltzenberg. *Angewandte Chemie International Edition*, 44(26):3957–3961, 2005.
- [14] Ahmed H Zewail. Femtochemistry: recent progress in studies of dynamics and control of reactions and their transition states. *The Journal of Physical Chemistry*, 100(31):12701–12724, 1996.
- [15] Jens K Nørskov, Felix Studt, Frank Abild-Pedersen, and Thomas Bligaard. *Fundamental concepts in heterogeneous catalysis*. John Wiley & Sons, 2014.
- [16] Petr Ptáček, František Šoukal, and Tomáš Opravil. Introduction to the transition state theory. *Introducing the Effective Mass of Activated Complex and the Discussion on the Wave Function of this Instanton*, page 27, 2018.
- [17] Mohammed Th Hassan. Attomicroscopy: from femtosecond to attosecond electron microscopy. *Journal of Physics B: Atomic, Molecular and Optical Physics*, 51(3):032005, jan 2018.
- [18] Kai F Kalz, Ralph Kraehnert, Muslim Dvoyashkin, Roland Dittmeyer, Roger Gläser, Ulrike Krewer, Karsten Reuter, and Jan-Dierk Grunwaldt. Future challenges in heterogeneous catalysis: understanding catalysts under dynamic reaction conditions. *Chem-CatChem*, 9(1):17–29, 2017.

-
- [19] Xiang Wang, Sheng-Chao Huang, Teng-Xiang Huang, Hai-Sheng Su, Jin-Hui Zhong, Zhi-Cong Zeng, Mao-Hua Li, and Bin Ren. Tip-enhanced raman spectroscopy for surfaces and interfaces. *Chemical Society Reviews*, 46(13):4020–4041, 2017.
- [20] Jean-Michel Andanson and Alfons Baiker. Exploring catalytic solid/liquid interfaces by in situ attenuated total reflection infrared spectroscopy. *Chemical Society Reviews*, 39(12):4571–4584, 2010.
- [21] Santhosh Chenna, Ritubarna Banerjee, and Peter A Crozier. Atomic-scale observation of the Ni activation process for partial oxidation of methane using in situ environmental tem. *ChemCatChem*, 3(6):1051–1059, 2011.
- [22] Masatake Haruta, Tetsuhiko Kobayashi, Hiroshi Sano, and Nobumasa Yamada. Novel gold catalysts for the oxidation of carbon monoxide at a temperature far below 0 c. *Chemistry Letters*, 16(2):405–408, 1987.
- [23] Lichen Liu and Avelino Corma. Metal catalysts for heterogeneous catalysis: from single atoms to nanoclusters and nanoparticles. *Chemical reviews*, 118(10):4981–5079, 2018.
- [24] Indranath Chakraborty and Thalappil Pradeep. Atomically precise clusters of noble metals: emerging link between atoms and nanoparticles. *Chemical reviews*, 117(12):8208–8271, 2017.
- [25] Zhixun Luo, AW Castleman Jr, and Shiv N Khanna. Reactivity of metal clusters. *Chemical reviews*, 116(23):14456–14492, 2016.
- [26] Meiling Xiao, Liqin Gao, Ying Wang, Xian Wang, Jianbing Zhu, Zhao Jin, Changpeng Liu, Hengquan Chen, Gaoran Li, Junjie Ge, et al. Engineering energy level of metal center: Ru single-atom site for efficient and durable oxygen reduction catalysis. *Journal of the American Chemical Society*, 141(50):19800–19806, 2019.
- [27] Federico Calle-Vallejo, Jakub Tymoczko, Viktor Colic, Quang Huy Vu, Marcus D Pohl, Karina Morgenstern, David Loffreda, Philippe Sautet, Wolfgang Schuhmann, and Aliaksandr S Bandarenka. Finding optimal surface sites on heterogeneous catalysts by counting nearest neighbors. *Science*, 350(6257):185–189, 2015.
- [28] Prasenjit Ghosh, Matteo Farnesi Camellone, and Stefano Fabris. Fluxionality of Au clusters at ceria surfaces during CO oxidation: Relationships among reactivity, size,

-
- cohesion, and surface defects from dft simulations. *The Journal of Physical Chemistry Letters*, 4(14):2256–2263, 2013.
- [29] Jacques VÅdrine. Heterogeneous catalysis on metal oxides. *Catalysts*, 7(11):341, Nov 2017.
- [30] Sandra Feyel, Jens Döbler, Robert Höckendorf, Martin K Beyer, Joachim Sauer, and Helmut Schwarz. Activation of methane by oligomeric $(Al_2O_3)_x^+$ ($x= 3, 4, 5$): The role of oxygen-centered radicals in thermal hydrogen-atom abstraction. *Angew. Chem. Int. Ed.*, 47(10):1946–1950, 2008.
- [31] Sandra Feyel, Jens Döbler, Detlef Schröder, Joachim Sauer, and Helmut Schwarz. Thermal activation of methane by tetranuclear $[V_4O_{10}]^+$. *Angew. Chem. Int. Ed.*, 45(28):4681–4685, 2006.
- [32] Detlef Schröder and Jana Roithová. Low-temperature activation of methane: It also works without a transition metal. *Angewandte Chemie International Edition*, 45(34):5705–5708, 2006.
- [33] Zi-Yu Li, Yan-Xia Zhao, Xiao-Nan Wu, Xun-Lei Ding, and Sheng-Gui He. Methane activation by yttrium-doped vanadium oxide cluster cations: Local charge effects. *Chem. Eur. J.*, 17(42):11728–11733, 2011.
- [34] Yan-Xia Zhao, Xiao-Nan Wu, Zhe-Chen Wang, Sheng-Gui He, and Xun-Lei Ding. Hydrogen-atom abstraction from methane by stoichiometric early transition metal oxide cluster cations. *Chem. Comm.*, 46(10):1736–1738, 2010.
- [35] Stefania Albonetti, Fabrizio Cavani, and Ferruccio Trifiro. Key aspects of catalyst design for the selective oxidation of paraffins. *Catal. Rev.*, 38(4):413–438, 1996.
- [36] S Albonetti, F Cavani, F Trifiro, P Venturoli, G Calestani, M Lopez Granados, and JL GarcíAa Fierro. A comparison of the reactivity of “nonequilibrated” and “equilibrated” v–p–o catalysts: structural evolution, surface characterization, and reactivity in the selective oxidation of n-butane and n-pentane. *J. Catal.*, 160(1):52–64, 1996.
- [37] Miguel A Bañares. Supported metal oxide and other catalysts for ethane conversion: A review. *Catal. Today*, 51(2):319–348, 1999.

-
- [38] BK Hodnett. Vanadium-phosphorus oxide catalysts for the selective oxidation of C4 hydrocarbons to maleic anhydride. *Catal. Rev.*, 27(3):373–424, 1985.
- [39] William C Vining, Anthony Goodrow, Jennifer Strunk, and Alexis T Bell. An experimental and theoretical investigation of the structure and reactivity of bilayered vox/tiox/sio2 catalysts for methanol oxidation. *J. Catal.*, 270(1):163–171, 2010.
- [40] Weimin Zhang, Anantha Desikan, and S Ted Oyama. Effect of support in ethanol oxidation on molybdenum oxide. *J. Phys. Chem.*, 99(39):14468–14476, 1995.
- [41] Robert Karl Grasselli. Genesis of site isolation and phase cooperation in selective oxidation catalysis. *Top. Catal.*, 15(2-4):93–101, 2001.
- [42] V Nikolov, D Klissurski, and A Anastasov. Phthalic anhydride from o-xylene catalysis: science and engineering. *Catal. Rev.*, 33(3-4):319–374, 1991.
- [43] Ronald M Heck. Catalytic abatement of nitrogen oxides—stationary applications. *Catal. Today*, 53(4):519–523, 1999.
- [44] Kuo-Tseng Li, Min-Ya Huang, and Wen-Da Cheng. Vanadium-based mixed-oxide catalysts for selective oxidation of hydrogen sulfide to sulfur. *Ind. Eng. Chem. Res.*, 35(2):621–626, 1996.
- [45] Juan Liu, Limin Dong, Wenli Guo, Tongxiang Liang, and Wensheng Lai. CO adsorption and oxidation on N-doped TiO₂ nanoparticles. *The Journal of Physical Chemistry C*, 117(25):13037–13044, 2013.
- [46] Mai-Anh Ha, Jonny Dadras, and Anastassia Alexandrova. Rutile-deposited Pt–Pd clusters: A hypothesis regarding the stability at 50/50 ratio. *ACS Catalysis*, 4(10):3570–3580, 2014.
- [47] Jilai Li, Xiao-Nan Wu, Maria Schlangen, Shaodong Zhou, Patricio González-Navarrete, Shiya Tang, and Helmut Schwarz. On the role of the electronic structure of the heteronuclear oxide cluster [Ga₂Mg₂O₅]⁺ in the thermal activation of methane and ethane: An unusual doping effect. *Angewandte Chemie International Edition*, 54(17):5074–5078, 2015.

-
- [48] Karolina Kwapien, Joachim Paier, Joachim Sauer, Michael Geske, Ulyana Zavyalova, Raimund Horn, Pierre Schwach, Annette Trunschke, and Robert Schlögl. Sites for methane activation on lithium-doped magnesium oxide surfaces. *Angewandte Chemie International Edition*, 53(33):8774–8778, 2014.
- [49] Jilai Li, Shaodong Zhou, Jun Zhang, Maria Schlangen, Thomas Weiske, Dandamudi Usharani, Sason Shaik, and Helmut Schwarz. Electronic origins of the variable efficiency of room-temperature methane activation by homo- and heteronuclear cluster oxide cations $[XYO_2]^+$ (X, Y = Al, Si, Mg): Competition between proton-coupled electron transfer and hydrogen-atom transfer. *Journal of the American Chemical Society*, 138(25):7973–7981, 2016.
- [50] Yan-Xia Zhao, Xiao-Nan Wu, Jia-Bi Ma, Sheng-Gui He, and Xun-Lei Ding. Experimental and theoretical study of the reactions between vanadium-silicon heteronuclear oxide cluster anions with n-butane. *The Journal of Physical Chemistry C*, 114(28):12271–12279, 2010.
- [51] M Baca, A Pigamo, JL Dubois, and JMM Millet. Propane oxidation on mordenite mixed oxide catalysts: study of the phase composition of active and selective catalysts. *Topics in catalysis*, 23(1-4):39–46, 2003.
- [52] Nicola Burriesci, Fabio Garbassi, Michele Petrera, and Guido Petrini. Influence of the bulk and surface properties on the performance of iron-antimony catalysts. *Journal of the Chemical Society, Faraday Transactions 1: Physical Chemistry in Condensed Phases*, 78(3):817–833, 1982.
- [53] Ana Paula Vieira Soares, Manuel Farinha Portela, and Alain Kiennemann. Methanol selective oxidation to formaldehyde over iron-molybdate catalysts. *Catalysis Reviews*, 47(1):125–174, 2005.
- [54] Ya-Ke Li, Zhen Yuan, Yan-Xia Zhao, Chongyang Zhao, Qing-Yu Liu, Hui Chen, and Sheng-Gui He. Thermal methane conversion to syngas mediated by Rh1-doped aluminum oxide cluster cations $RhAl_3O_4^+$. *Journal of the American Chemical Society*, 138(39):12854–12860, 2016.

-
- [55] Ya-Ke Li, Yan-Xia Zhao, and Sheng-Gui He. Selective conversion of methane by Rh1-doped aluminum oxide cluster anions $\text{RhAl}_2\text{O}_4^-$: A comparison with the reactivity of $\text{PtAl}_2\text{O}_4^-$. *The Journal of Physical Chemistry A*, 2018.
- [56] Yan-Xia Zhao, Zi-Yu Li, Yuan Yang, and Sheng-Gui He. Methane activation by gas phase atomic clusters. *Acc. Chem. Res*, 51(11):2603–2610, 2018.
- [57] Zi-Yu Li, Hai-Fang Li, Yan-Xia Zhao, and Sheng-Gui He. Gold (iii) mediated activation and transformation of methane on Au1-doped vanadium oxide cluster cations AuV_2O_6^+ . *Journal of the American Chemical Society*, 138(30):9437–9443, 2016.
- [58] Yan-Xia Zhao, Xiao-Na Li, Zhen Yuan, Qing-Yu Liu, Qiang Shi, and Sheng-Gui He. Methane activation by gold-doped titanium oxide cluster anions with closed-shell electronic structures. *Chemical Science*, 7(7):4730–4735, 2016.
- [59] O Ducreux, J Lynch, B Rebours, M Roy, and P Chaumette. In situ characterisation of cobalt based fischer-tropsch catalysts: A new approach to the active phase. *Studies in surface science and catalysis*, pages 125–130, 1998.
- [60] M Sadeqzadeh, H Karaca, OV Safonova, P Fongarland, S Chambrey, Pascal Roussel, A Griboval-Constant, M Lacroix, D Curulla-Ferré, F Luck, et al. Identification of the active species in the working alumina-supported cobalt catalyst under various conditions of fischer–tropsch synthesis. *Catalysis Today*, 164(1):62–67, 2011.
- [61] Jin-Xun Liu, Hai-Yan Su, Da-Peng Sun, Bing-Yan Zhang, and Wei-Xue Li. Crystallographic dependence of co activation on cobalt catalysts: Hcp versus fcc. *Journal of the American Chemical Society*, 135(44):16284–16287, 2013.
- [62] Kohei Kusada. Discovery of the face-centered cubic ruthenium nanoparticles: Facile size-controlled synthesis using the chemical reduction method. In *Creation of New Metal Nanoparticles and Their Hydrogen-Storage and Catalytic Properties*, pages 59–67. Springer, 2014.
- [63] Hui Wang, Jin-Xun Liu, Lawrence F Allard, Sungsik Lee, Jilei Liu, Hang Li, Jianqiang Wang, Jun Wang, Se H Oh, Wei Li, et al. Surpassing the single-atom catalytic activity limit through paired Pt-O-Pt ensemble built from isolated Pt 1 atoms. *Nature communications*, 10(1):1–12, 2019.

-
- [64] Jutta Rogal and Karsten Reuter. Ab initio atomistic thermodynamics for surfaces: A primer. Technical report, Max-planck-gesellschaft zur foerderung der wissenschaften ev berlin (germany fr) fritz-haber-inst, 2006.
- [65] Jutta Rogal, Karsten Reuter, and Matthias Scheffler. First-principles statistical mechanics study of the stability of a subnanometer thin surface oxide in reactive environments: CO oxidation at Pd (100). *Physical review letters*, 98(4):046101, 2007.
- [66] Iann C Gerber and Philippe Serp. A theory/experience description of support effects in carbon-supported catalysts. *Chemical Reviews*, 2019.
- [67] Hai-Cai Huang, Jing Wang, Jun Li, Yang Zhao, Xiao-Xiao Dong, Jing Chen, Gang Lu, Yuxiang Bu, and Shi-Bo Cheng. A surface modification strategy for promoting the performance of non-noble metal single-atom catalysts in low-temperature co oxidation. *ACS Applied Materials & Interfaces*, 2020.
- [68] Flemming Besenbacher, Ib Chorkendorff, BS Clausen, Bjørk Hammer, AM Molenbroek, Jens Kehlet Nørskov, and Ivan Stensgaard. Design of a surface alloy catalyst for steam reforming. *Science*, 279(5358):1913–1915, 1998.
- [69] Gabor A. Somorjai and Jeong Y. Park. Molecular factors of catalytic selectivity. *Angewandte Chemie International Edition*, 47(48):9212–9228, 2008.
- [70] Mischa Bonn, Christian Hess, Stephan Funk, James H. Miners, Bo N. J. Persson, Martin Wolf, and Gerhard Ertl. Femtosecond surface vibrational spectroscopy of co adsorbed on Ru(001) during desorption. *Phys. Rev. Lett.*, 84:4653–4656, May 2000.
- [71] Masatake Haruta and Masakazu Daté. Advances in the catalysis of au nanoparticles. *Applied Catalysis A: General*, 222(1-2):427–437, 2001.
- [72] Tamao Ishida, Toru Murayama, Ayako Taketoshi, and Masatake Haruta. Importance of size and contact structure of gold nanoparticles for the genesis of unique catalytic processes. *Chemical Reviews*, 2019.
- [73] Xiaoyi Fu, Yuan Wang, Nianzu Wu, Linlin Gui, and Youqi Tang. Shape-selective preparation and properties of oxalate-stabilized pt colloid. *Langmuir*, 18(12):4619–4624, 2002.

-
- [74] Nuria Lopez, TVW Janssens, BS Clausen, Y Xu, Manos Mavrikakis, T Bligaard, and Jens Kehlet Nørskov. On the origin of the catalytic activity of gold nanoparticles for low-temperature CO oxidation. *Journal of Catalysis*, 223(1):232–235, 2004.
- [75] Zhi Li, Shufang Ji, Yiwei Liu, Xing Cao, Shubo Tian, Yuanjun Chen, Zhiqiang Niu, and Yadong Li. Well-defined materials for heterogeneous catalysis: From nanoparticles to isolated single-atom sites. *Chemical Reviews*, 2019.
- [76] Leilei Zhang, Maoxiang Zhou, Aiqin Wang, and Tao Zhang. Selective hydrogenation over supported metal catalysts: From nanoparticles to single atoms. *Chemical reviews*, 2019.
- [77] Xiangwen Liu, Dingsheng Wang, and Yadong Li. Synthesis and catalytic properties of bimetallic nanomaterials with various architectures. *Nano Today*, 7(5):448–466, 2012.
- [78] Alfons M Molenbroek, Jens K Nørskov, and Bjerne S Clausen. Structure and reactivity of Ni–Au nanoparticle catalysts. *The Journal of Physical Chemistry B*, 105(23):5450–5458, 2001.
- [79] LK Ono, D Sulfeld, and B Roldan Cuenya. In situ gas-phase catalytic properties of TiC-supported size-selected gold nanoparticles synthesized by diblock copolymer encapsulation. *Surface science*, 600(23):5041–5050, 2006.
- [80] Bokwon Yoon, Hannu Häkkinen, Uzi Landman, Anke S Wörz, Jean-Marie Antonietti, Stéphane Abbet, Ken Judai, and Ueli Heiz. Charging effects on bonding and catalyzed oxidation of CO on Au₈ clusters on MgO. *Science*, 307(5708):403–407, 2005.
- [81] Beien Zhu, Jun Meng, Wentao Yuan, Xun Zhang, Hangsheng Yang, Yong Wang, and Yi Gao. Reshaping of metal nanoparticles under reaction conditions. *Angewandte Chemie International Edition*, 59(6):2171–2180, 2020.
- [82] Saswata Bhattacharya, Sergey V Levchenko, Luca M Ghiringhelli, and Matthias Scheffler. Efficient ab initio schemes for finding thermodynamically stable and metastable atomic structures: Benchmark of cascade genetic algorithms. *New J. Phys.*, 16(12):123016, 2014.

-
- [83] Hannu Häkkinen. Atomic and electronic structure of gold clusters: understanding flakes, cages and superatoms from simple concepts. *Chem. Soc. Rev.*, 37:1847–1859, 2008.
- [84] Osburg Jin Huang Chai, Zhihe Liu, Tiankai Chen, and Jianping Xie. Engineering ultra-small metal nanoclusters for photocatalytic and electrocatalytic applications. *Nanoscale*, 11:20437–20448, 2019.
- [85] Michikazu Hara, Masaaki Kitano, and Hideo Hosono. Ru-loaded C12A7:e⁻ electride as a catalyst for ammonia synthesis. *ACS Catalysis*, 7(4):2313–2324, 2017.
- [86] Fang Wang, Dongju Zhang, Xiaohong Xu, and Yi Ding. Theoretical study of the CO oxidation mediated by Au₃⁺, Au₃, and Au₃⁻: Mechanism and charge state effect of gold on its catalytic activity. *The Journal of Physical Chemistry C*, 113(42):18032–18039, 2009.
- [87] Huanchen Zhai and Anastassia N. Alexandrova. Fluxionality of catalytic clusters: When it matters and how to address it. *ACS Catalysis*, 7(3):1905–1911, 2017.
- [88] Geng Sun and Philippe Sautet. Metastable structures in cluster catalysis from first-principles: structural ensemble in reaction conditions and metastability triggered reactivity. *Journal of the American Chemical Society*, 140(8):2812–2820, 2018.
- [89] Karsten Reuter, Catherine Stampfl, M. [Verónica Ganduglia-Pirovano], and Matthias Scheffler. Atomistic description of oxide formation on metal surfaces: the example of ruthenium. *Chemical Physics Letters*, 352(5):311 – 317, 2002.
- [90] Saswata Bhattacharya, Benjamin H. Sonin, Christopher J. Jumonville, Luca M. Ghiringhelli, and Noa Marom. Computational design of nanoclusters by property-based genetic algorithms: Tuning the electronic properties of (TiO₂)_n clusters. *Phys. Rev. B*, 91:241115, Jun 2015.
- [91] Nelly M Reilly, Grant E Johnson, and AW Castleman. The reactivity of gas-phase metal oxide clusters: Systems for understanding the mechanisms of heterogeneous catalysts. In *Model Systems in Catalysis*, pages 293–317. Springer, 2010.

-
- [92] Elena F Fialko, Andrey V Kikhtenko, Vladimir B Goncharov, and Kirill I Zamaraev. Similarities between reactions of methanol with Mo_xO_y^+ in the gas phase and over real catalysts. *The Journal of Physical Chemistry B*, 101(30):5772–5773, 1997.
- [93] Christian Hinderling, Derek Feichtinger, Dietmar A Plattner, and Peter Chen. A combined gas-phase, solution-phase, and computational study of C–H activation by cationic iridium (iii) complexes. *Journal of the American Chemical Society*, 119(44):10793–10804, 1997.
- [94] William T Wallace and Robert L Whetten. Coadsorption of CO and O₂ on selected gold clusters: Evidence for efficient room-temperature CO₂ generation. *Journal of the American Chemical Society*, 124(25):7499–7505, 2002.
- [95] Liana D Socaciu, Jan Hagen, Thorsten M Bernhardt, Ludger Wöste, Ulrich Heiz, Hannu Häkkinen, and Uzi Landman. Catalytic CO oxidation by free Au₂⁻: experiment and theory. *Journal of the American Chemical Society*, 125(34):10437–10445, 2003.
- [96] Thorsten M Bernhardt, Liana D Socaciu-Siebert, Jan Hagen, and Ludger Wöste. Size and composition dependence in CO oxidation reaction on small free gold, silver, and binary silver–gold cluster anions. *Applied Catalysis A: General*, 291(1-2):170–178, 2005.
- [97] Mark Brönstrup, Detlef Schröder, Ilona Kretzschmar, Helmut Schwarz, and Jeremy N Harvey. Platinum dioxide cation: Easy to generate experimentally but difficult to describe theoretically. *Journal of the American Chemical Society*, 123(1):142–147, 2001.
- [98] Helmut Schwarz. Chemistry with methane: concepts rather than recipes. *Angewandte Chemie International Edition*, 50(43):10096–10115, 2011.
- [99] Max Born and Robert Oppenheimer. Zur quantentheorie der molekeln. *Annalen der physik*, 389(20):457–484, 1927.
- [100] Charlotte Froese Fischer. General hartree-fock program. *Computer physics communications*, 43(3):355–365, 1987.
- [101] Axel D Becke. A new mixing of hartree–fock and local density-functional theories. *The Journal of chemical physics*, 98(2):1372–1377, 1993.

-
- [102] John C Slater. A simplification of the hartree-fock method. *Physical review*, 81(3):385, 1951.
- [103] Pierre Hohenberg and Walter Kohn. Inhomogeneous electron gas. *Physical review*, 136(3B):B864, 1964.
- [104] Walter Kohn and Lu Jeu Sham. Self-consistent equations including exchange and correlation effects. *Physical review*, 140(4A):A1133, 1965.
- [105] Matthias Scheffler and Udo Scherz. Resonant raman scattering at point defects in gaas. In *Mater. Sci. Forum*, volume 10, pages 353–358. Trans Tech Publ, 1986.
- [106] Karsten Reuter and Matthias Scheffler. Composition and structure of the RuO₂(110) surface in an O₂ and CO environment: Implications for the catalytic formation of CO₂. *Phys. Rev. B*, 68(4):045407, 2003.
- [107] Karsten Reuter, Catherine Stampf, and Matthias Scheffler. Ab initio atomistic thermodynamics and statistical mechanics of surface properties and functions. In *Handbook of Materials Modeling*, pages 149–194. Springer, 2005.
- [108] Saswata Bhattacharya, Sergey V Levchenko, Luca M Ghiringhelli, and Matthias Scheffler. Stability and metastability of clusters in a reactive atmosphere: Theoretical evidence for unexpected stoichiometries of Mg_mO_x. *Phys. Rev. Lett.*, 111(13):135501, 2013.
- [109] Graeme Henkelman and Hannes Jónsson. Improved tangent estimate in the nudged elastic band method for finding minimum energy paths and saddle points. *The Journal of chemical physics*, 113(22):9978–9985, 2000.
- [110] Abdalnour Y Toukmaji and John A Board Jr. Ewald summation techniques in perspective: a survey. *Computer physics communications*, 95(2-3):73–92, 1996.
- [111] Vladimir Fock. Näherungsmethode zur lösung des quantenmechanischen mehrkörperproblems. *Zeitschrift für Physik*, 61(1-2):126–148, 1930.
- [112] John C Slater. Note on hartree’s method. *Physical Review*, 35(2):210, 1930.
- [113] Enrico Fermi. Eine statistische methode zur bestimmung einiger eigenschaften des atoms und ihre anwendung auf die theorie des periodischen systems der elemente. *Zeitschrift für Physik*, 48(1-2):73–79, 1928.

-
- [114] Llewellyn H Thomas. The calculation of atomic fields. In *Mathematical Proceedings of the Cambridge Philosophical Society*, volume 23, pages 542–548. Cambridge University Press, 1927.
- [115] Paul AM Dirac. Note on exchange phenomena in the thomas atom. In *Mathematical Proceedings of the Cambridge Philosophical Society*, volume 26, pages 376–385. Cambridge University Press, 1930.
- [116] Mel Levy. Electron densities in search of hamiltonians. *Phys. Rev. A*, 26:1200–1208, Sep 1982.
- [117] Elliott H. Lieb. Density functionals for coulomb systems. *International Journal of Quantum Chemistry*, 24(3):243–277, 1983.
- [118] Richard M Martin and Richard Milton Martin. *Electronic structure: basic theory and practical methods*. Cambridge university press, 2004.
- [119] Neil W Ashcroft, N David Mermin, et al. Solid state physics [by] neil w. ashcroft [and] n. david mermin., 1976.
- [120] David M Ceperley and Berni J Alder. Ground state of the electron gas by a stochastic method. *Physical review letters*, 45(7):566, 1980.
- [121] John P Perdew, Kieron Burke, and Matthias Ernzerhof. Generalized gradient approximation made simple. *Phys. Rev. Lett.*, 77(18):3865, 1996.
- [122] David Sholl and Janice A Steckel. *Density functional theory: a practical introduction*. John Wiley & Sons, 2011.
- [123] Aliaksandr V Krukau, Oleg A Vydrov, Artur F Izmaylov, and Gustavo E Scuseria. Influence of the exchange screening parameter on the performance of screened hybrid functionals. *The Journal of chemical physics*, 125(22):224106, 2006.
- [124] John P Perdew, Matthias Ernzerhof, and Kieron Burke. Rationale for mixing exact exchange with density functional approximations. *J. Chem. Phys.*, 105(22):9982–9985, 1996.
- [125] Lars Hedin. On correlation effects in electron spectroscopies and the gw approximation. *Journal of Physics: Condensed Matter*, 11(42):R489, 1999.

-
- [126] Volker Blum, Ralf Gehrke, Felix Hanke, Paula Havu, Ville Havu, Xinguo Ren, Karsten Reuter, and Matthias Scheffler. Ab initio molecular simulations with numeric atom-centered orbitals. *Comput. Phys. Commun.*, 180(11):2175–2196, 2009.
- [127] G. Kresse and J. Furthmüller. Efficiency of ab-initio total energy calculations for metals and semiconductors using a plane-wave basis set. *Computational Materials Science*, 6(1):15 – 50, 1996.
- [128] G. Kresse and D. Joubert. From ultrasoft pseudopotentials to the projector augmented-wave method. *Phys. Rev. B*, 59:1758–1775, Jan 1999.
- [129] P. E. Blöchl. Projector augmented-wave method. *Phys. Rev. B*, 50:17953–17979, Dec 1994.
- [130] Hendrik J Monkhorst and James D Pack. Special points for brillouin-zone integrations. *Physical review B*, 13(12):5188, 1976.
- [131] Robert G Parr. Density functional theory of atoms and molecules. In *Horizons of Quantum Chemistry*, pages 5–15. Springer, 1980.
- [132] Alex Willand, Yaroslav O Kvashnin, Luigi Genovese, Álvaro Vázquez-Mayagoitia, Arpan Krishna Deb, Ali Sadeghi, Thierry Deutsch, and Stefan Goedecker. Norm-conserving pseudopotentials with chemical accuracy compared to all-electron calculations. *The Journal of chemical physics*, 138(10):104109, 2013.
- [133] David Vanderbilt. Soft self-consistent pseudopotentials in a generalized eigenvalue formalism. *Physical review B*, 41(11):7892, 1990.
- [134] Peter E Blöchl. Projector augmented-wave method. *Physical review B*, 50(24):17953, 1994.
- [135] Lars Hedin. New method for calculating the one-particle green’s function with application to the electron-gas problem. *Physical Review*, 139(3A):A796, 1965.
- [136] Ferdi Aryasetiawan and Olle Gunnarsson. The gw method. *Reports on Progress in Physics*, 61(3):237, 1998.
- [137] Rex W Godby, Michael Schlüter, and LJ Sham. Self-energy operators and exchange-correlation potentials in semiconductors. *Physical Review B*, 37(17):10159, 1988.

-
- [138] Noa Marom, Minjung Kim, and James R. Chelikowsky. Structure selection based on high vertical electron affinity for TiO_2 clusters. *Phys. Rev. Lett.*, 108:106801, Mar 2012.
- [139] Richard Phillips Feynman. Forces in molecules. *Physical review*, 56(4):340, 1939.
- [140] Graeme Henkelman, Blas P Uberuaga, and Hannes Jónsson. A climbing image nudged elastic band method for finding saddle points and minimum energy paths. *The Journal of chemical physics*, 113(22):9901–9904, 2000.
- [141] H Jónsson, G Mills, and GK Schenter. Reversible work transition state theory: Application to dissociative adsorption of hydrogen. *Surface Science*, 324(2-3):305–337, 1995.
- [142] Ron Elber and M Karplus. A method for determining reaction paths in large molecules: Application to myoglobin. *Chemical Physics Letters*, 139(5):375–380, 1987.
- [143] Ryszard Czerminski and Ron Elber. Reaction path study of conformational transitions in flexible systems: applications to peptides. *The Journal of chemical physics*, 92(9):5580–5601, 1990.
- [144] Anastassia N Alexandrova and Alexander I Boldyrev. Search for the $\text{Li}_n^{0/+1/-1}$ ($n=5-7$) lowest-energy structures using the ab initio gradient embedded genetic algorithm (gega). elucidation of the chemical bonding in the lithium clusters. *Journal of chemical theory and computation*, 1(4):566–580, 2005.
- [145] René A PF Kanters and Kelling J Donald. Cluster: Searching for unique low energy minima of structures using a novel implementation of a genetic algorithm. *Journal of chemical theory and computation*, 10(12):5729–5737, 2014.
- [146] Jack BA Davis, Armin Shayeghi, Sarah L Horswell, and Roy L Johnston. The birmingham parallel genetic algorithm and its application to the direct dft global optimisation of Ir_n ($n=10-20$) clusters. *Nanoscale*, 7(33):14032–14038, 2015.
- [147] Bernhard Bandow and Bernd Hartke. Larger water clusters with edges and corners on their way to ice: Structural trends elucidated with an improved parallel evolutionary algorithm. *The Journal of Physical Chemistry A*, 110(17):5809–5822, 2006.

-
- [148] Farren Curtis, Xiayue Li, Timothy Rose, Alvaro Vazquez-Mayagoitia, Saswata Bhattacharya, Luca M Ghiringhelli, and Noa Marom. Gator: a first-principles genetic algorithm for molecular crystal structure prediction. *Journal of chemical theory and computation*, 14(4):2246–2264, 2018.
- [149] David M Deaven and Kai-Ming Ho. Molecular geometry optimization with a genetic algorithm. *Physical review letters*, 75(2):288, 1995.
- [150] Matthias Scheffler and Jaroslaw Dabrowski. Parameter-free calculations of total energies, interatomic forces and vibrational entropies of defects in semiconductors. *Philos. Mag. A*, 58(1):107–121, 1988.
- [151] X-G Wang, Werner Weiss, Sh K Shaikhutdinov, Michael Ritter, Max Petersen, F Wagner, Robert Schlögl, and Matthias Scheffler. The hematite ($\alpha\text{-Fe}_2\text{O}_3$)(0001) surface: Evidence for domains of distinct chemistry. *Phys. Rev. Lett.*, 81(5):1038, 1998.
- [152] Sung-Hoon Lee, Wolfgang Moritz, and Matthias Scheffler. GaAs (001) surface under conditions of low as pressure: Evidence for a novel surface geometry. *Phys. Rev. Lett.*, 85(18):3890, 2000.
- [153] Shikha Saini, Debalaya Sarker, Pooja Basera, Sergey V. Levchenko, Luca M. Ghiringhelli, and Saswata Bhattacharya. Structure and electronic properties of transition-metal/Mg bimetallic clusters at realistic temperatures and oxygen partial pressures. *J. Phys. Chem. C*, 122(29):16788–16794, 2018.
- [154] Jiwei Ma, Aurélien Habrioux, Yun Luo, Guadalupe Ramos-Sanchez, Laura Calvillo, Gaetano Granozzi, Perla B. Balbuena, and Nicolas Alonso-Vante. Electronic interaction between platinum nanoparticles and nitrogen-doped reduced graphene oxide: effect on the oxygen reduction reaction. *J. Mater. Chem. A*, 3:11891–11904, 2015.
- [155] Xiaofan Zhang, Bingyan Zhang, Zhixiang Zuo, Mingkui Wang, and Yan Shen. N/Si co-doped oriented single crystalline rutile TiO_2 nanorods for photoelectrochemical water splitting. *J. Mater. Chem. A*, 3:10020–10025, 2015.
- [156] Nicholas P. Chadwick, Emily N. K. Glover, Sanjayan Sathasivam, Sulaiman N. Basahel, Shaeel A. Althabaiti, Abdulrahman O. Alyoubi, Ivan P. Parkin, and Claire J. Carmalt.

-
- Photo-activity and low resistivity in N/Nb co-doped TiO₂ thin films by combinatorial aacvd. *J. Mater. Chem. A*, 4:407–415, 2016.
- [157] Hui Zeng, Jingjing Xie, Hao Xie, Bao-Lian Su, Menghu Wang, Hang Ping, Weimin Wang, Hao Wang, and Zhengyi Fu. Bioprocess-inspired synthesis of hierarchically porous nitrogen-doped TiO₂ with high visible-light photocatalytic activity. *J. Mater. Chem. A*, 3:19588–19596, 2015.
- [158] Sainan Liu, Zhenyang Cai, Jiang Zhou, Anqiang Pan, and Shuquan Liang. Nitrogen-doped TiO₂ nanospheres for advanced sodium-ion battery and sodium-ion capacitor applications. *J. Mater. Chem. A*, 4:18278–18283, 2016.
- [159] Yun Hang Hu and Eli Ruckenstein. Binary mgo-based solid solution catalysts for methane conversion to syngas. *Catal. Rev.*, 44(3):423–453, 2002.
- [160] M. Smerieri, J. Pal, L. Savio, L. Vattuone, R. Ferrando, S. Tosoni, L. Giordano, G. Pacchioni, and M. Rocca. Spontaneous oxidation of Ni nanoclusters on MgO monolayers induced by segregation of interfacial oxygen. *J. Phys. Chem. Lett.*, 6(15):3104–3109, 2015. PMID: 26267209.
- [161] Matthias Scheffler and CM Weinert. Chalcogen and vacancy pairs in silicon: electronic structure and stabilities. In H. J. von Bardeleben, editor, *Defects in Semiconductors*, pages 25–30. Trans. Tech. Publ. Ltd, Switzerland, 1986.
- [162] Ryota Inde, Min Liu, Daiki Atarashi, Etsuo Sakai, and Masahiro Miyauchi. Ti(IV) nanoclusters as a promoter on semiconductor photocatalysts for the oxidation of organic compounds. *J. Mater. Chem. A*, 4:1784–1791, 2016.
- [163] Michael K Bates, Qingying Jia, Huong Doan, Wentao Liang, and Sanjeev Mukerjee. Charge-transfer effects in Ni–Fe and Ni–Fe–Co mixed-metal oxides for the alkaline oxygen evolution reaction. *ACS Catal.*, 6(1):155–161, 2015.
- [164] Cong Liu, Thomas R Cundari, and Angela K Wilson. CO₂ reduction on transition metal (Fe, Co, Ni, and Cu) surfaces: In comparison with homogeneous catalysis. *J. Phys. Chem. C*, 116(9):5681–5688, 2012.

-
- [165] John D Aiken and Richard G Finke. A review of modern transition-metal nanoclusters: Their synthesis, characterization, and applications in catalysis. *J. Mol. Catal. Chem.*, 145(1):1–44, 1999.
- [166] Craig L Hill and Christina M Prosser-McCartha. Homogeneous catalysis by transition metal oxygen anion clusters. *Coord. Chem. Rev.*, 143:407–455, 1995.
- [167] Jagriti Pal, Marco Smerieri, Edvige Celasco, Letizia Savio, Luca Vattuone, and Mario Rocca. Morphology of monolayer MgO films on Ag(100): Switching from corrugated islands to extended flat terraces. *Phys. Rev. Lett.*, 112:126102, Mar 2014.
- [168] Andrew Bean Getsoian, Zheng Zhai, and Alexis T Bell. Band-gap energy as a descriptor of catalytic activity for propene oxidation over mixed metal oxide catalysts. *J. Am. Chem. Soc.*, 136(39):13684–13697, 2014.
- [169] Kenichi Fukui, Tejiro Yonezawa, and Haruo Shingu. A molecular orbital theory of reactivity in aromatic hydrocarbons. *J. Chem. Phys.*, 20(4):722–725, 1952.
- [170] Eric V Anslyn and Dennis A Dougherty. *Modern physical organic chemistry*. University science books, 2006.
- [171] Tuhin S Khan, Shelaka Gupta, Md Imteyaz Alam, and M Ali Haider. Reactivity descriptor for the retro diels–alder reaction of partially saturated 2-pyrones: DFT study on substituents and solvent effects. *RSC Adv.*, 6(103):101697–101706, 2016.
- [172] Olga Lopez-Acevedo, Katarzyna A Kacprzak, Jaakko Akola, and Hannu Häkkinen. Quantum size effects in ambient CO oxidation catalysed by ligand-protected gold clusters. *Nat. Chem.*, 2(4):329, 2010.
- [173] Zachary S Fishman, Benjamin Rudshateyn, Yulian He, Bolun Liu, Subhajyoti Chaudhuri, Mikhail Askerka, Gary L Haller, Victor S Batista, and Lisa D Pfefferle. Fundamental role of oxygen stoichiometry in controlling the band gap and reactivity of cupric oxide nanosheets. *J. Am. Chem. Soc.*, 138(34):10978–10985, 2016.
- [174] P Raybaud, J Hafner, G Kresse, and H Toulhoat. Ab initio density functional studies of transition-metal sulphides: II. electronic structure. *J. Phys.: Condens. Matter*, 9(50):11107, 1997.

-
- [175] José A Rodriguez, Tomas Jirsak, and Sanjay Chaturvedi. Reaction of H₂S with MgO(100) and Cu/MgO(100) surfaces: Band-gap size and chemical reactivity. *J. Chem. Phys.*, 111(17):8077–8087, 1999.
- [176] We varied z value starting from 1, 2, 3,... and kept on increasing it until the specific Tm _{x} Mg _{y} O _{z} stoichiometry goes totally outside our phase diagrams, i.e. under no circumstances that stoichiometry can be important at realistic conditions.
- [177] The cascade GA code is a part of the FHI-aims code.
- [178] Alexandre Tkatchenko and Matthias Scheffler. Accurate molecular van der waals interactions from ground-state electron density and free-atom reference data. *Phys. Rev. Lett.*, 102(7):073005, 2009.
- [179] As described in details in ref [82, 90], in our cascade GA, the latter energy is used to evaluate the fitness function, i.e., a mapping of the energy interval between highest-and lowest-energy cluster in the running pool into the interval [0, 1]. obviously, the higher the value of the fitness function for a cluster, the higher is the probability of selecting it for generating a new structure.
- [180] We considered all the isomers within an energy window of 0.5 eV from the global minimum as we have seen that it's very unlikely that isomers above 0.5 eV from the gm would become more stable after including their translational, rotational, vibrational, spin and symmetry free energy contributions to the total energy.
- [181] Saswata Bhattacharya, Daniel Berger, Karsten Reuter, Luca M. Ghiringhelli, and Sergey V. Levchenko. Theoretical evidence for unexpected O-rich phases at corners of MgO surfaces. *Phys. Rev. Materials*, 1:071601, Dec 2017.
- [182] Amrita Bhattacharya and Saswata Bhattacharya. Exploring N-rich phases in Li _{x} N _{y} clusters for hydrogen storage at nanoscale. *J. Phys. Chem. Lett.*, 6(18):3726–3730, 2015. PMID: 26722747.
- [183] The clusters are at their ground state configuration w. r. t. geometry and spin respectively.
- [184] The energy window of 0.5 eV in total energy is carefully chosen such that within this error bar in energetics, the phase diagram will not change significantly in terms of stability of different phases.

-
- [185] Helmut Schwarz, Sason Shaik, and Jilai Li. Electronic effects on room-temperature, gas-phase C–H bond activations by cluster oxides and metal carbides: The methane challenge. *J. Am. Chem. Soc.*, 139(48):17201–17212, 2017.
- [186] Helmut Schwarz, Patricio Gonzalez-Navarrete, Jilai Li, Maria Schlangen, Xiaoyan Sun, Thomas Weiske, and Shaodong Zhou. Unexpected mechanistic variants in the thermal gas-phase activation of methane. *Organometallics*, 36(1):8–17, 2016.
- [187] Jilai Li, Shaodong Zhou, Jun Zhang, Maria Schlangen, Dandamudi Usharani, Sason Shaik, and Helmut Schwarz. Mechanistic variants in gas-phase metal-oxide mediated activation of methane at ambient conditions. *Journal of the American Chemical Society*, 138(35):11368–11377, 2016.
- [188] Xun-Lei Ding, Xiao-Nan Wu, Yan-Xia Zhao, and Sheng-Gui He. C–H bond activation by oxygen-centered radicals over atomic clusters. *Acc. Chem. Res.*, 45(3):382–390, 2011.
- [189] Sandra M Lang, Thorsten M Bernhardt, Valeriy Chernyy, Joost M Bakker, Robert N Barnett, and Uzi Landman. Selective C–H bond cleavage in methane by small gold clusters. *Angew. Chem. Int. Ed.*, 56(43):13406–13410, 2017.
- [190] Sandra M Lang, Thorsten M Bernhardt, Robert N Barnett, and Uzi Landman. Size-dependent binding energies of methane to small gold clusters. *ChemPhysChem*, 11(7):1570–1577, 2010.
- [191] Yu-Min Chen and PB Armentrout. Activation of methane by gas-phase Rh^+ . *J. Phys. Chem.*, 99(27):10775–10779, 1995.
- [192] Christian Adlhart and Einar Uggerud. Reactions of platinum clusters Pt_n^\pm , $n= 1\text{--}21$, with CH_4 : to react or not to react. *Chemical Communications*, (24):2581–2582, 2006.
- [193] Xiao-Nan Wu, Jilai Li, Maria Schlangen, Shaodong Zhou, Patricio González-Navarrete, and Helmut Schwarz. Striking doping effects on thermal methane activation mediated by the heteronuclear metal oxides $[\text{XAlO}_4]^{+\text{--}}$ ($x= \text{V, Nb, and Ta}$). *Chem. Eur. J.*, 23(4):788–792, 2017.

-
- [194] Shaodong Zhou, Jilai Li, Maria Schlangen, and Helmut Schwarz. On the origin of the remarkably variable reactivities of $[\text{AlCeO}_x]^+$ ($x=2-4$) towards methane as a function of oxygen content. *Angew. Chem. Int. Ed.*, 56(1):413–416, 2017.
- [195] Jilai Li, Patricio González-Navarrete, Maria Schlangen, and Helmut Schwarz. Activation of methane and carbon dioxide mediated by transition-metal doped magnesium oxide clusters $[\text{MMgO}]^{+/0/-}$ ($M= \text{Sc-Zn}$). *Chemistry-A European Journal*, 21(21):7780–7789, 2015.
- [196] E van Lenthe, Evert-Jan Baerends, and Jaap G Snijders. Relativistic regular two-component hamiltonians. *J. Chem. Phys.*, 99(6):4597–4610, 1993.
- [197] Elizabeth C Beret, Merel M Wijk, and Luca M Ghiringhelli. Reaction cycles and poisoning in catalysis by gold clusters: A thermodynamics approach. *International Journal of Quantum Chemistry*, 114(1):57–65, 2014.
- [198] Noa Marom, Minjung Kim, and James R Chelikowsky. Structure selection based on high vertical electron affinity for TiO_2 clusters. *Phys. Rev. Lett.*, 108(10):106801, 2012.
- [199] Greg Mills, Mark S Gordon, and Horia Metiu. Oxygen adsorption on Au clusters and a rough Au(111) surface: The role of surface flatness, electron confinement, excess electrons, and band gap. *J. Chem. Phys.*, 118(9):4198–4205, 2003.
- [200] Wojciech Grochala. The generalized maximum hardness principle revisited and applied to atoms and molecules. *Phys. Chem. Chem. Phys.*, 19(46):30964–30983, 2017.
- [201] Hannu Häkkinen and Uzi Landman. Gold clusters (Au_n , $2 < n < 10$) and their anions. *Phys. Rev. B*, 62(4):R2287, 2000.
- [202] Simon Klacar, Anders Hellman, Itai Panas, and Henrik Grönbeck. Oxidation of small silver clusters: A density functional theory study. *J. Phys. Chem. C*, 114(29):12610–12617, 2010.
- [203] Adriana Trincherro, Simon Klacar, Lauro Oliver Paz-Borbón, Anders Hellman, and Henrik Grönbeck. Oxidation at the subnanometer scale. *J. Phys. Chem. C*, 119(20):10797–10803, 2014.

-
- [204] Gennady I Panov, Konstantin A Dubkov, and Eugeny V Starokon. Active oxygen in selective oxidation catalysis. *Catal. Today*, 117(1-3):148–155, 2006.
- [205] David J Wales and Jonathan PK Doye. Global optimization by basin-hopping and the lowest energy structures of lennard-jones clusters containing up to 110 atoms. *The Journal of Physical Chemistry A*, 101(28):5111–5116, 1997.
- [206] Malcolm Sambridge. A parallel tempering algorithm for probabilistic sampling and multimodal optimization. *Geophysical Journal International*, 196(1):357–374, 2013.
- [207] Seth T Call, Dmitry Yu Zubarev, and Alexander I Boldyrev. Global minimum structure searches via particle swarm optimization. *Journal of computational chemistry*, 28(7):1177–1186, 2007.
- [208] Wolfgang Wenzel and Kay Hamacher. Stochastic tunneling approach for global minimization of complex potential energy landscapes. *Physical Review Letters*, 82(15):3003, 1999.
- [209] Jianguang Wang, Li Ma, Jijun Zhao, and Koblar Alan Jackson. Structural growth behavior and polarizability of Cd_nTe_n ($n= 1-14$) clusters. *The Journal of chemical physics*, 130(21):214307, 2009.
- [210] Karsten Reuter and Matthias Scheffler. Composition, structure, and stability of $\text{RuO}_2(110)$ as a function of oxygen pressure. *Phys. Rev. B*, 65(3):035406, 2001.
- [211] Karsten Reuter and Matthias Scheffler. Oxide formation at the surface of late 4d transition metals: insights from first-principles atomistic thermodynamics. *Appl. Phys. A*, 78(6):793–798, 2004.
- [212] Shikha Saini, Debalaya Sarker, Pooja Basera, Sergey V Levchenko, Luca M Ghiringhelli, and Saswata Bhattacharya. Structure and electronic properties of transition-metal/Mg bimetallic clusters at realistic temperatures and oxygen partial pressures. *The Journal of Physical Chemistry C*, 122(29):16788–16794, 2018.
- [213] Pooja Basera, Shikha Saini, Ekta Arora, Arunima Singh, Manish Kumar, and Saswata Bhattacharya. Stability of non-metal dopants to tune the photo-absorption of TiO_2 at realistic temperatures and oxygen partial pressures: A hybrid DFT study. *Scientific reports*, 9(1):1–13, 2019.

-
- [214] Leeor Kronik, Roland Fromherz, Eunjung Ko, Gerd Ganteför, and James R Che-likowsky. Highest electron affinity as a predictor of cluster anion structures. *Nature materials*, 1(1):49, 2002.
- [215] Shikha Saini, Pooja Basera, Ekta Arora, and Saswata Bhattacharya. Unraveling thermodynamic stability, catalytic activity and electronic structure of $[\text{TM}_x\text{Mg}_y\text{O}_z]^{+/0/-}$ clusters at realistic conditions: A hybrid DFT and ab initio thermodynamics study. *The Journal of Physical Chemistry C*, 2019.
- [216] Yeonsig Nam, Jong Hyeon Lim, Kyoung Chul Ko, and Jin Yong Lee. Photocatalytic activity of TiO_2 nanoparticles: a theoretical aspect. *J. Mater. Chem. A*, 7:13833–13859, 2019.
- [217] Wenjing Shi, Weiyi Yang, Qi Li, Shian Gao, Panju Shang, and Jian Ku Shang. The synthesis of nitrogen/sulfur co-doped TiO_2 nanocrystals with a high specific surface area and a high percentage of $\{001\}$ facets and their enhanced visible-light photocatalytic performance. *Nanoscale research letters*, 7(1):590, 2012.
- [218] Siti Nur Aqilah Sulaiman, Mohamad Zaky Noh, Nurul Nadia Adnan, Noriah Bidin, and Siti Noraiza Ab Razak. Effects of photocatalytic activity of metal and non-metal doped TiO_2 for hydrogen production enhancement-a review. In *Journal of Physics: Conference Series*, volume 1027, page 012006. IOP Publishing, 2018.
- [219] Mukes Kapilashrami, Yanfeng Zhang, Yi-Sheng Liu, Anders Hagfeldt, and Jinghua Guo. Probing the optical property and electronic structure of TiO_2 nanomaterials for renewable energy applications. *Chemical reviews*, 114(19):9662–9707, 2014.
- [220] AR Elmaslmane, MB Watkins, and KP McKenna. First-principles modeling of polaron formation in TiO_2 polymorphs. *Journal of chemical theory and computation*, 14(7):3740–3751, 2018.
- [221] Mingzheng Ge, Chunyan Cao, Jianying Huang, Shuhui Li, Zhong Chen, Ke-Qin Zhang, S. S. Al-Deyab, and Yuekun Lai. A review of one-dimensional TiO_2 nanostructured materials for environmental and energy applications. *J. Mater. Chem. A*, 4:6772–6801, 2016.

-
- [222] Pooja Basera, Shikha Saini, and Saswata Bhattacharya. Self energy and excitonic effect in (un)doped TiO₂ anatase: a comparative study of hybrid dft, gw and bse to explore optical properties. *J. Mater. Chem. C*, 7:14284–14293, 2019.
- [223] Jie Zhou, Han Wu, Chun-Yi Sun, Cheng-Ying Hu, Xin-Long Wang, Zhen-Hui Kang, and Zhong-Min Su. Ultrasmall C-TiO_{2-x} nanoparticle/g-C₃N₄ composite for CO₂ photoreduction with high efficiency and selectivity. *J. Mater. Chem. A*, 6:21596–21604, 2018.
- [224] Rosendo Valero, Ángel Morales-García, and Francesc Illas. Theoretical modeling of electronic excitations of gas-phase and solvated TiO₂ nanoclusters and nanoparticles of interest in photocatalysis. *Journal of chemical theory and computation*, 14(8):4391–4404, 2018.
- [225] RYOJI Asahi, TAKESHI Morikawa, Takeshi Ohwaki, Koyu Aoki, and Yasunori Taga. Visible-light photocatalysis in nitrogen-doped titanium oxides. *science*, 293(5528):269–271, 2001.
- [226] Clemens Burda, Yongbing Lou, Xiaobo Chen, Anna CS Samia, John Stout, and James L Gole. Enhanced nitrogen doping in TiO₂ nanoparticles. *Nano letters*, 3(8):1049–1051, 2003.
- [227] James L Gole, John D Stout, Clemens Burda, Yongbing Lou, and Xiaobo Chen. Highly efficient formation of visible light tunable TiO_{2-x}N_x photocatalysts and their transformation at the nanoscale. *The journal of physical chemistry B*, 108(4):1230–1240, 2004.
- [228] DJ Mowbray, Jose Ignacio Martinez, JM García Lastra, Kristian Sommer Thygesen, and Karsten Wedel Jacobsen. Stability and electronic properties of TiO₂ nanostructures with and without B and N doping. *The Journal of Physical Chemistry C*, 113(28):12301–12308, 2009.
- [229] Xiaobo Chen and Clemens Burda. The electronic origin of the visible-light absorption properties of C-, N- and S-doped TiO₂ nanomaterials. *Journal of the American Chemical Society*, 130(15):5018–5019, 2008.

-
- [230] Xiaobo Chen and Clemens Burda. Photoelectron spectroscopic investigation of nitrogen-doped titania nanoparticles. *The Journal of Physical Chemistry B*, 108(40):15446–15449, 2004.
- [231] Ye Cong, Jinlong Zhang, Feng Chen, and Masakazu Anpo. Synthesis and characterization of nitrogen-doped TiO₂ nanophotocatalyst with high visible light activity. *The Journal of Physical Chemistry C*, 111(19):6976–6982, 2007.
- [232] Hiroshi Irie, Yuka Watanabe, and Kazuhito Hashimoto. Nitrogen-concentration dependence on photocatalytic activity of TiO_{2-x}N_x powders. *The Journal of Physical Chemistry B*, 107(23):5483–5486, 2003.
- [233] Daniel Adjei Agyeman, Kyeongse Song, Seung Ho Kang, Mi Ru Jo, Eunbi Cho, and Yong-Mook Kang. An improved catalytic effect of nitrogen-doped TiO₂ nanofibers for rechargeable Li-O₂ batteries; the role of oxidation states and vacancies on the surface. *J. Mater. Chem. A*, 3:22557–22563, 2015.
- [234] Enrico Berardo, Ferdinand Kaplan, Kiran Bhaskaran-Nair, William A Shelton, Michiel J van Setten, Karol Kowalski, and Martijn A Zwijnenburg. Benchmarking the fundamental electronic properties of small TiO₂ nanoclusters by GW and coupled cluster theory calculations. *Journal of chemical theory and computation*, 13(8):3814–3828, 2017.
- [235] Oriol Lamiel-Garcia, Kyoung Chul Ko, Jin Yong Lee, Stefan T Bromley, and Francesc Illas. When anatase nanoparticles become bulklike: Properties of realistic TiO₂ nanoparticles in the 1–6 nm size range from all electron relativistic density functional theory based calculations. *Journal of chemical theory and computation*, 13(4):1785–1793, 2017.
- [236] Ekta Arora, Shikha Saini, Pooja Basera, Manish Kumar, Arunima Singh, and Saswata Bhattacharya. Elucidating the role of temperature and pressure to the thermodynamic stability of charged defects in complex metal-hydrides: A case study of naalh₄. *The Journal of Physical Chemistry C*, 123(1):62–69, 2018.
- [237] Saswata Bhattacharya, Daniel Berger, Karsten Reuter, Luca M Ghiringhelli, and Sergey V Levchenko. Theoretical evidence for unexpected O-rich phases at corners of MgO surfaces. *Physical Review Materials*, 1(7):071601, 2017.

-
- [238] Amrita Bhattacharya and Saswata Bhattacharya. Unraveling the role of vacancies in the potentially promising thermoelectric clathrates $\text{Ba}_8\text{Zn}_x\text{Ge}_{46-x-y}\square_y$. *Phys. Rev. B*, 94:094305, Sep 2016.
- [239] Amrita Bhattacharya and Saswata Bhattacharya. Exploring N-rich phases in Li_xN_y clusters for hydrogen storage at nanoscale. *The Journal of Physical Chemistry Letters*, 6(18):3726–3730, 2015.
- [240] Manish Kumar, Pooja Basera, Shikha Saini, and Saswata Bhattacharya. arxiv:1909.09623, 2019.
- [241] Enrico Berardo and Martijn A Zwijnenburg. Modeling the water splitting activity of a TiO_2 rutile nanoparticle. *The Journal of Physical Chemistry C*, 119(24):13384–13393, 2015.
- [242] Pierre Guiglion, Cristina Butchosa, and Martijn A Zwijnenburg. Polymeric watersplitting photocatalysts; a computational perspective on the water oxidation conundrum. *Journal of Materials Chemistry A*, 2(30):11996–12004, 2014.
- [243] Cristina Butchosa, Pierre Guiglion, and Martijn A Zwijnenburg. Carbon nitride photocatalysts for water splitting: a computational perspective. *The Journal of Physical Chemistry C*, 118(43):24833–24842, 2014.
- [244] Jan Rossmeisl, Z-W Qu, H Zhu, G-J Kroes, and Jens Kehlet Nørskov. Electrolysis of water on oxide surfaces. *Journal of Electroanalytical Chemistry*, 607(1-2):83–89, 2007.
- [245] Stephane Kenmoe and Eckhard Spohr. Photooxidation of water on pristine, s- and n-doped TiO_2 (001) nanotube surfaces: A DFT+U study. *The Journal of Physical Chemistry C*, 123(37):22691–22698, 2019.
- [246] Peng Zhang, Xuejian Xu, Erhong Song, Xiuli Hou, Xuejing Yang, Jianli Mi, Jun Huang, and Catherine Stampfl. Transition metal-doped α -borophene as potential oxygen and hydrogen evolution electrocatalyst: A density functional theory study. *Catalysis Communications*, page 106090, 2020.
- [247] MW Chase. Nist-janaf thermochemical tables 4th ed. *J. of Physical and Chemical Reference Data*, pages 1529–1564, 1998.

-
- [248] Liang-Feng Huang and James M Rondinelli. Electrochemical phase diagrams for Ti oxides from density functional calculations. *Physical Review B*, 92(24):245126, 2015.
- [249] AJ Bard, R Parsons, and J Jordan. Standard potentials in aqueous solution. marcel dekker, new york. *Standard potentials in aqueous solution. Marcel Dekker, New York.*, 1985.
- [250] Marcel Pourbaix. *Atlas of Electrochemical Equilibria in Aqueous Solutions*, Pergamon Press, Oxford, 1966.
- [251] Liang-Feng Huang and James M Rondinelli. Reliable electrochemical phase diagrams of magnetic transition metals and related compounds from high-throughput ab initio calculations. *npj Materials Degradation*, 3(1):1–13, 2019.
- [252] Preeti Bhumla, Manish Kumar, and Saswata Bhattacharya. Theoretical insights into C–H bond activation of methane by transition metal clusters: The role of anharmonic effects. *arXiv preprint arXiv:2004.07432*, 2020.
- [253] Peter Munnik, Petra E de Jongh, and Krijn P de Jong. Recent developments in the synthesis of supported catalysts. *Chemical reviews*, 115(14):6687–6718, 2015.
- [254] Lin He, Florian Weniger, Helfried Neumann, and Matthias Beller. Synthesis, characterization, and application of metal nanoparticles supported on nitrogen-doped carbon: catalysis beyond electrochemistry. *Angewandte Chemie International Edition*, 55(41):12582–12594, 2016.
- [255] Debraj Chandra, Yasunori Inoue, Masato Sasase, Masaaki Kitano, Asim Bhaumik, Keigo Kamata, Hideo Hosono, and Michikazu Hara. A high performance catalyst of shape-specific ruthenium nanoparticles for production of primary amines by reductive amination of carbonyl compounds. *Chemical science*, 9(27):5949–5956, 2018.
- [256] Masaaki Kitano, Yasunori Inoue, Youhei Yamazaki, Fumitaka Hayashi, Shinji Kanbara, Satoru Matsuishi, Toshiharu Yokoyama, Sung-Wng Kim, Michikazu Hara, and Hideo Hosono. Ammonia synthesis using a stable electrider as an electron donor and reversible hydrogen store. *Nature chemistry*, 4(11):934, 2012.

-
- [257] Stefan Vajda, Michael J Pellin, Jeffrey P Greeley, Christopher L Marshall, Larry A Curtiss, Gregory A Ballentine, Jeffrey W Elam, Stephanie Catillon-Mucherie, Paul C Redfern, Faisal Mehmood, et al. Subnanometre platinum clusters as highly active and selective catalysts for the oxidative dehydrogenation of propane. *Nature materials*, 8(3):213–216, 2009.
- [258] Lin-Wei Chen, Lei Tong, Hang Nan, Sheng-Qi Chu, and Hai-Wei Liang. Sub-2 nm Ir nanoclusters immobilized on mesoporous nitrogen-doped carbons as efficient catalysts for selective hydrogenation. *ACS Applied Nano Materials*, 2(10):6546–6553, 2019.
- [259] Tasuku Komanoya, Takashi Kinemura, Yusuke Kita, Keigo Kamata, and Michikazu Hara. Electronic effect of ruthenium nanoparticles on efficient reductive amination of carbonyl compounds. *Journal of the American Chemical Society*, 139(33):11493–11499, 2017.
- [260] Peter Claus, Angelika Brückner, Christian Mohr, and Herbert Hofmeister. Supported gold nanoparticles from quantum dot to mesoscopic size scale: effect of electronic and structural properties on catalytic hydrogenation of conjugated functional groups. *Journal of the American Chemical Society*, 122(46):11430–11439, 2000.
- [261] Ayman M Karim, Vinay Prasad, Giannis Mpourmpakis, William W Lonergan, Anatoly I Frenkel, Jingguang G Chen, and Dionisios G Vlachos. Correlating particle size and shape of supported Ru/ γ -Al₂O₃ catalysts with nh₃ decomposition activity. *Journal of the American Chemical Society*, 131(34):12230–12239, 2009.
- [262] An-Xiang Yin, Wen-Chi Liu, Jun Ke, Wei Zhu, Jun Gu, Ya-Wen Zhang, and Chun-Hua Yan. Ru nanocrystals with shape-dependent surface-enhanced raman spectra and catalytic properties: controlled synthesis and DFT calculations. *Journal of the American Chemical Society*, 134(50):20479–20489, 2012.
- [263] Charles T Campbell. Electronic perturbations. *Nature chemistry*, 4(8):597–598, 2012.
- [264] Mark A Newton, Carolina Belver-Coldeira, Arturo Martínez-Arias, and Marcos Fernández-García. Dynamic in situ observation of rapid size and shape change of supported Pd nanoparticles during CO/NO cycling. *Nature materials*, 6(7):528–532, 2007.

-
- [265] KS Hayes. Industrial processes for manufacturing amines. *Applied Catalysis A: General*, 221(1-2):187–195, 2001.
- [266] Sebastian Imm, Sebastian Baehn, Lorenz Neubert, Helfried Neumann, and Matthias Beller. An efficient and general synthesis of primary amines by ruthenium-catalyzed amination of secondary alcohols with ammonia. *Angewandte Chemie International Edition*, 49(44):8126–8129, 2010.
- [267] Irina Delidovich, Peter JC Hausoul, Li Deng, Rebecca Pfülltzenreuter, Marcus Rose, and Regina Palkovits. Alternative monomers based on lignocellulose and their use for polymer production. *Chemical reviews*, 116(3):1540–1599, 2016.
- [268] Duo-Sheng Wang, Qing-An Chen, Sheng-Mei Lu, and Yong-Gui Zhou. Asymmetric hydrogenation of heteroarenes and arenes. *Chemical reviews*, 112(4):2557–2590, 2012.
- [269] Mario P Wiesenfeldt, Zackaria Nairoukh, Toryn Dalton, and Frank Glorius. Selective arene hydrogenation for direct access to saturated carbo- and heterocycles. *Angewandte Chemie International Edition*, 58(31):10460–10476, 2019.
- [270] William C Wertjes, Emma H Southgate, and David Sarlah. Recent advances in chemical dearomatization of nonactivated arenes. *Chemical Society Reviews*, 47(21):7996–8017, 2018.
- [271] Feng Chen, Wu Li, Basudev Sahoo, Carsten Kreyenschulte, Giovanni Agostini, Henrik Lund, Kathrin Junge, and Matthias Beller. Hydrogenation of pyridines using a nitrogen-modified titania-supported cobalt catalyst. *Angewandte Chemie*, 130(44):14696–14700, 2018.
- [272] Jack D Scott and Robert M Williams. Chemistry and biology of the tetrahydroisoquinoline antitumor antibiotics. *Chemical Reviews*, 102(5):1669–1730, 2002.
- [273] Vellaisamy Sridharan, Padmakar A Suryavanshi, and J Carlos Menendez. Advances in the chemistry of tetrahydroquinolines. *Chemical reviews*, 111(11):7157–7259, 2011.
- [274] Caizhi Wu, Jiayu Liao, and Shaozhong Ge. Cobalt-catalyzed enantioselective hydroboration/cyclization of 1, 7-enynes: Asymmetric synthesis of chiral quinolinones containing quaternary stereogenic centers. *Angewandte Chemie International Edition*, 58(26):8882–8886, 2019.

-
- [275] Ivañ Sorribes, Lichen Liu, Antonio Domeñech-Carboñ, and Avelino Corma. Nanolayered cobalt–molybdenum sulfides as highly chemo- and regioselective catalysts for the hydrogenation of quinoline derivatives. *ACS Catalysis*, 8(5):4545–4557, 2018.
- [276] Basudev Sahoo, Carsten Kreyenschulte, Giovanni Agostini, Henrik Lund, Stephan Bachmann, Michelangelo Scalone, Kathrin Junge, and Matthias Beller. A robust iron catalyst for the selective hydrogenation of substituted (iso) quinolones. *Chemical science*, 9(42):8134–8141, 2018.
- [277] Silvia Gomez, Joop A Peters, Jan C van der Waal, Wuzong Zhou, and Thomas Maschmeyer. Preparation of benzylamine by highly selective reductive amination of benzaldehyde over Ru on an acidic activated carbon support as the catalyst. *Catalysis letters*, 84(1-2):1–5, 2002.
- [278] J Bódis, Leonardus Lefferts, TE Müller, R Pestman, and JA Lercher. Activity and selectivity control in reductive amination of butyraldehyde over noble metal catalysts. *Catalysis letters*, 104(1-2):23–28, 2005.
- [279] Bo Dong, Xingcui Guo, Bo Zhang, Xiufang Chen, Jing Guan, Yunfei Qi, Sheng Han, and Xindong Mu. Heterogeneous Ru-based catalysts for one-pot synthesis of primary amines from aldehydes and ammonia. *Catalysts*, 5(4):2258–2270, 2015.
- [280] Yoichi Nakamura, Kenichi Kon, Abeda Sultana Touchy, Ken-ichi Shimizu, and Wataru Ueda. Selective synthesis of primary amines by reductive amination of ketones with ammonia over supported Pt catalysts. *ChemCatChem*, 7(6):921–924, 2015.
- [281] Licheng Bai, Xin Wang, Qiang Chen, Yifan Ye, Haoquan Zheng, Jinghua Guo, Yadong Yin, and Chuanbo Gao. Explaining the size dependence in platinum-nanoparticle-catalyzed hydrogenation reactions. *Angewandte Chemie International Edition*, 55(50):15656–15661, 2016.
- [282] Yutong Gong, Pengfei Zhang, Xuan Xu, Yi Li, Haoran Li, and Yong Wang. A novel catalyst Pd@ompg-C₃N₄ for highly chemoselective hydrogenation of quinoline under mild conditions. *Journal of catalysis*, 297:272–280, 2013.
- [283] Alena Karakulina, Aswin Gopakumar, İsmail Akçok, Bastien L Roulier, Thomas LaGrange, Sergey A Katsyuba, Shoubhik Das, and Paul J Dyson. A rhodium nanoparticle–

-
- lewis acidic ionic liquid catalyst for the chemoselective reduction of heteroarenes. *Angewandte Chemie International Edition*, 55(1):292–296, 2016.
- [284] Dong Ren, Lin He, Lei Yu, Ran-Sheng Ding, Yong-Mei Liu, Yong Cao, He-Yong He, and Kang-Nian Fan. An unusual chemoselective hydrogenation of quinoline compounds using supported gold catalysts. *Journal of the American Chemical Society*, 134(42):17592–17598, 2012.
- [285] Deming Zhu, Hongbin Jiang, Lei Zhang, Xueli Zheng, Haiyan Fu, Maolin Yuan, Hua Chen, and Ruixiang Li. Aqueous phase hydrogenation of quinoline to decahydroquinoline catalyzed by ruthenium nanoparticles supported on glucose-derived carbon spheres. *ChemCatChem*, 6(10):2954–2960, 2014.
- [286] Yi-Gang Ji, Kai Wei, Teng Liu, Lei Wu, and Wei-Hua Zhang. “naked” iridium (iv) oxide nanoparticles as expedient and robust catalysts for hydrogenation of nitrogen heterocycles: Remarkable vicinal substitution effect and recyclability. *Advanced Synthesis & Catalysis*, 359(6):933–940, 2017.
- [287] Minfeng Fang and Roberto A Sánchez-Delgado. Ruthenium nanoparticles supported on magnesium oxide: A versatile and recyclable dual-site catalyst for hydrogenation of mono- and poly-cyclic arenes, n-heteroaromatics, and s-heteroaromatics. *Journal of catalysis*, 311:357–368, 2014.
- [288] Yu Zhang, Jie Zhu, Yun-Tao Xia, Xiao-Tao Sun, and Lei Wu. Efficient hydrogenation of nitrogen heterocycles catalyzed by carbon-metal covalent bonds-stabilized palladium nanoparticles: Synergistic effects of particle size and water. *Advanced Synthesis & Catalysis*, 358(19):3039–3045, 2016.
- [289] Hannelore Konnerth and Martin HG Prechtel. Selective hydrogenation of n-heterocyclic compounds using Ru nanocatalysts in ionic liquids. *Green Chemistry*, 19(12):2762–2767, 2017.
- [290] Lei Zhang, Xiaoyan Wang, Ying Xue, Xiaojun Zeng, Hua Chen, Ruixiang Li, and Shanling Wang. Cooperation between the surface hydroxyl groups of Ru–SiO₂@mSiO₂ and water for good catalytic performance for hydrogenation of quinoline. *Catalysis Science & Technology*, 4(7):1939–1948, 2014.

-
- [291] Sarwat Iqbal, Simon A Kondrat, Daniel R Jones, Daniël C Schoenmakers, Jennifer K Edwards, Li Lu, Benjamin R Yeo, Peter P Wells, Emma K Gibson, David J Morgan, et al. Ruthenium nanoparticles supported on carbon: an active catalyst for the hydrogenation of lactic acid to 1, 2-propanediol. *ACS Catalysis*, 5(9):5047–5059, 2015.
- [292] Masaaki Kitano, Shinji Kanbara, Yasunori Inoue, Navaratnarajah Kuganathan, Peter V Sushko, Toshiharu Yokoyama, Michikazu Hara, and Hideo Hosono. Electride support boosts nitrogen dissociation over ruthenium catalyst and shifts the bottleneck in ammonia synthesis. *Nature communications*, 6(1):1–9, 2015.
- [293] Wei-Zhen Li, Jin-Xun Liu, Jun Gu, Wu Zhou, Si-Yu Yao, Rui Si, Yu Guo, Hai-Yan Su, Chun-Hua Yan, Wei-Xue Li, et al. Chemical insights into the design and development of face-centered cubic ruthenium catalysts for fischer–tropsch synthesis. *Journal of the American Chemical Society*, 139(6):2267–2276, 2017.
- [294] Sumei Han, Qinbai Yun, Siyang Tu, Lijie Zhu, Wenbin Cao, and Qipeng Lu. Metallic ruthenium-based nanomaterials for electrocatalytic and photocatalytic hydrogen evolution. *Journal of Materials Chemistry A*, 7(43):24691–24714, 2019.
- [295] Rosa Arrigo, Manfred E Schuster, Zailai Xie, Youngmi Yi, Gregor Wowsnick, Li L Sun, Klaus E Hermann, Matthias Friedrich, Patrick Kast, Michael Haillvecker, et al. Nature of the N-Pd interaction in nitrogen-doped carbon nanotube catalysts. *ACS Catalysis*, 5(5):2740–2753, 2015.
- [296] Kevin N Wood, Ryan O’Hayre, and Svitlana Pylypenko. Recent progress on nitrogen/carbon structures designed for use in energy and sustainability applications. *Energy & Environmental Science*, 7(4):1212–1249, 2014.
- [297] Mingming Li, Fan Xu, Haoran Li, and Yong Wang. Nitrogen-doped porous carbon materials: promising catalysts or catalyst supports for heterogeneous hydrogenation and oxidation. *Catalysis Science & Technology*, 6(11):3670–3693, 2016.
- [298] Tianjin Li, Hongfei Lin, Xinping Ouyang, Xueqing Qiu, and Zechen Wan. In situ preparation of Ru@N-doped carbon catalyst for the hydrogenolysis of lignin to produce aromatic monomers. *ACS Catalysis*, 9(7):5828–5836, 2019.

-
- [299] Vassili Vorotnikov, Giannis Mpourmpakis, and Dionisios G Vlachos. DFT study of furfural conversion to furan, furfuryl alcohol, and 2-methylfuran on Pd(111). *Acs Catalysis*, 2(12):2496–2504, 2012.
- [300] He Dong, Ying Zheng, and P Hu. A DFT study of direct furfural conversion to 2-methylfuran on the Ru/Co₃O₄ surface. *Physical Chemistry Chemical Physics*, 21(3):1597–1605, 2019.

List of Publications

1. **Shikha Saini**, Debalaya Sarker, Pooja Basera, Sergey V. Levchenko, Luca M. Ghiringhelli, and Saswata Bhattacharya, “Structure and Electronic Properties of Transition-metal/Mg Bimetallic Clusters at Realistic Temperatures and Oxygen Partial Pressures”, *The Journal of Physical Chemistry C* **122**, 16788 (2018).
2. **Shikha Saini**, Pooja Basera, Ekta Arora, and Saswata Bhattacharya, “Unraveling Thermodynamic Stability, Catalytic Activity and Electronic Structure of $[\text{TM}_x\text{Mg}_y\text{O}_z]^{+/0/-}$ clusters at Realistic Conditions: A Hybrid DFT and Ab initio Thermodynamics Study”, *The Journal of Physical Chemistry C* **123**, 15495 (2019).
3. Ekta Arora, **Shikha Saini**, Pooja Basera, Manish Kumar, Arunima Singh, and Saswata Bhattacharya, “Elucidating the Role of Temperature and Pressure to the Thermodynamic Stability of Charged Defects in Complex Metal-Hydrides: A Case Study of NaAlH_4 ”, *The Journal of Physical Chemistry C* **123**, 62 (2019).
4. Pooja Basera, **Shikha Saini**, Ekta Arora, Arunima Singh, Manish Kumar, and Saswata Bhattacharya, “Stability of non-metal Dopants to Tune the Photo-absorption of TiO_2 at Realistic Temperatures and Oxygen Partial Pressures: A Hybrid DFT Study”, *Scientific Reports* **9**, 11427 (2019).
5. Pooja Basera, **Shikha Saini**, Ekta Arora, Arunima Singh, Manish Kumar, and Saswata Bhattacharya, “Self Energy and Excitonic Effect in (un)doped TiO_2 Anatase: A Comparative Study of Hybrid DFT, GW and BSE to Explore Optical Properties”, *Journal of Materials Chemistry C* **7**, 14284 (2019).
6. Parswajit Kalita, **Shikha Saini**, Parasmani Rajput, S. N. Jha, D. Bhattacharyya, Sunil Ojha, Devesh K. Avasthi, Saswata Bhattacharya, and Santanu Ghosh, “Oxygen Vacancy Mediated Cubic Phase Stabilization at Room Temperature in Pure Nano-Crystalline Zir-

-
- conia Films: A Combined Experimental and First-Principles Based Investigation”, *Physical Chemistry Chemical Physics*, **21**, 22482 (2019).
7. Pooja Basera, Manish Kumar **Shikha Saini**, and Saswata Bhattacharya, “Reducing Lead-toxicity in MAPbI₃: Why Sn Substitution Should be Preferred to Pb Vacancy for Optimum Solar Cell Efficiency”, *Physical Review B* **101**, 054108 (2020).
 8. Manish Kumar, Pooja Basera, **Shikha Saini**, and Saswata Bhattacharya, “Role of Defects in Photocatalytic Water Splitting: Monodoped vs Codoped SrTiO₃”, *The Journal of Physical Chemistry C*, **19** 10272, (2020).
 9. Arunima Singh, Pooja Basera, **Shikha Saini**, Manish Kumar, and Saswata Bhattacharya, “Importance of Many-Body Dispersion in the Stability of Vacancies and Antisites in Free-standing Monolayer of MoS₂ from First-Principles Approaches”, *The Journal of Physical Chemistry C* **124**, 1390 (2020).
 10. **Shikha Saini**, Pooja Basera, M. Kumar, P. Bhumla, and Saswata Bhattacharya, “Unravelling Electronic Structure of N-doped TiO₂ from Property Based Cascade Genetic Algorithm for Efficient Photocatalysis”, *Journal of Physics: Materials*, 2020 (accepted).
 11. Manish Kumar, Pooja Basera, **Shikha Saini**, and Saswata Bhattacharya, “Theoretical Insights of Codoping to Modulate Electronic Structure of TiO₂ and SrTiO₃ for Enhanced Photocatalytic Efficiency”, *Scientific Reports*, **10**, 15372 (2020).
 12. Shailesh Pathak, **Shikha Saini**, Kishore Kondamudi, Sreedevi Upadhyayula and Saswata Bhattacharya, “Promotion of the Reaction Performance of Iron Oxide Catalyst by Tuning Metal-Support Interaction at Nanoscale”, *Applied Catalysis B: Environmental*, 2020 (accepted).
 13. Debraj Chandra, **Shikha Saini**, Asim Bhaumik, Keigo Kamata, Saswata Bhattacharya and Michikazu Hara, “Electronic Effect in a Highly Efficient Ruthenium Catalyst Designed in Nanoporous N-functionalized Carbon for Selective Hydrogenation of Heteroarenes”, (*manuscript under review*).
 14. Sonit Balyan, **Shikha Saini**, Puneet Gupta, Tuhin Suvra Khan, Kamal Kishore Pant, Saswata Bhattacharya and M. Ali Haider, “Unravelling the Reactivity of Metastable

Molybdenum Carbide Nanoclusters in C–H Activation Steps for Methane Dehydroaromatization", (*manuscript under review*).

Conference Proceedings

1. **Shikha Saini**, Pooja Basera, Ekta Arora, Saswata Bhattacharya, "Electronic Structure and Thermodynamic Stability of Ternary Oxide Clusters ($\text{Ni}_1\text{Mg}_1\text{O}_x$)", AIP Conference Proceedings, 2115, 030190 (2019).
2. **Shikha Saini**, Pooja Basera, and Saswata Bhattacharya, "Thermodynamic Stability and Electronic Structure of Bimetallic Clusters ($\text{TM}_x\text{Mg}_y\text{O}_z$)", Materials today: proceedings (2019). DOI: 10.1016/j.matpr.2019.06.657
3. Pooja Basera, **Shikha Saini**, Ekta Arora, Arunima Singh, Saswata Bhattacharya, "Electronic, Magnetic and Optical Properties of C, N-doped TiO_2 Anatase: A Hybrid Density Functional Study", AIP Conference Proceedings, 2115, 030394 (2019).
4. Pooja Basera, **Shikha Saini**, Ekta Arora, Arunima Singh, and Saswata Bhattacharya, "Ab-initio Study on Opto-Electronic Properties of Non-metal Doped TiO_2 " Materials today: proceedings (2019). DOI: 10.1016/j.matpr.2019.05.393

Personal Data

Name: Shikha Saini
Affiliation: Department of Physics, Indian Institute of Technology Delhi
Date of Birth: 01/01/1991
Nationality: Indian
Sex: Female
Marital Status: Single
Email: shikha.saini.india@gmail.com

Profile

Shikha Saini is a research scholar, working with Dr. Saswata Bhattacharya since July 2015 in the department of physics, Indian Institute of Technology Delhi. She works in an interdisciplinary area of condensed matter physics with broad research interest in designing the new materials and understanding their physicochemical properties using state-of-the-art Density Functional Theory (DFT) and beyond approaches. She uses the cascade genetic algorithm to model the electronic structures of complex metal oxide clusters which have the significant impact in heterogeneous catalysis. She employs *ab initio* atomistic thermodynamics, phonopy and molecular dynamics approaches to capture the effect of operational conditions (finite temperatures and pressures, defect/doping). She is proficient to predict the structure-property relations of various type of nanoclusters (single metal, metal oxides, bimetallic oxides, doped oxides etc.) by employing highly sophisticated quantum chemistry methods (viz. HSE06, PBE0, GW, BSE, etc.). To predict the catalytic active materials and examine their performance, she uses the Nudged Elastic Band (NEB) method. The designed materials have a wide range of applica-

tions in preeminent processes viz. methane activation, hydrogen evolution reaction (HER) and oxygen evolution reaction (OER), photocatalysis, CO oxidation, hydrogenation, conversion of biomass to fuels.

Education

- 2015 – 2020 Ph.D in Physics, Department of Physics
Indian Institute of Technology Delhi, Hauz Khas, New Delhi 110016, INDIA.
Thesis title: *Designing Clusters for Efficient Catalytic Activity at a Realistic Condition from First-Principles Simulation.*
Course work grade: A-, Ph.D. viva voce: 21 September 2020
- 2011 – 2013 MSc. Physics, H. N. B. Garhwal University, Srinagar Uttarakhand–246174
India (A Central University). Specialization: Solid state physics.
First class with 79.46%.
- 2008 – 2011 BSc. Physics, H. N. B. Garhwal University, Srinagar Uttarakhand–246174
India (A Central University). First Class with 73.27%.

Research Interest

- Clusters and catalysts
- Photocatalysis
- Defects in semiconductor
- Perovskite materials for solar cell applications
- Finite temperature modelling

Expertise and Technical Skill

Methods	Ground state electronic structure calculations: DFT and beyond, Genetic algorithm, Phonopy, Nudged elastic band, Finite temperature modelling, Molecular dynamics simulations, <i>Ab-initio</i> atomistic thermodynamics, Excited state calculations: GW, BSE.
Programming	Shell, Python, C, Matlab, LaTeX .
Electronic structure Code	FHI-AIMS, VASP, DMOL3.
Operating system and Software	Unix, Linux, Window, Xmgrace, Gnuplot, Matplotlib, Molden, VMD, JMOL, VESTA.
Languages	English, Hindi.
Misc.	Academic research, Teaching, Coding, Consultation, Learning and Publishing.

Awards and Academic Recognitions

- International Travel Support (ITS) awarded by Science and Engineering Research Board, Government of India.
- Presented Contributed Oral Talk in ACCMS10, at City University of Hong Kong, Hong Kong.
- Nominated two times for CSIR Travel Grant by CSIR Human Resource Development Group, Government of India (2019, 2020).
- Recipient of Best Poster Award in ASM 2019, at IIT Delhi, India.
- Recipient of Best Poster Award in IWNEBD:2018 conference, at IIT Mandi, India.
- Recipient of Best Oral Presentation Award in ICN: 3I-2017, at IIT Roorkee, India.
- CSIR Research Fellowship for Ph.D from CSIR, India.
- All India Rank 61 in GATE examination.
- All India Rank 310 in joint entrance screening test (JEST).

-
- Tutor in ASM 2019, at IIT Delhi, India.
 - Active volunteer in ASM 2019, at IIT Delhi, India.

Conferences Attended

- 2nd Indian Materials Conclave and 31st AGM (MRSI AGM 2020), 11st-14th February 2020, at CSIR – Central Glass & Ceramic Research Institute, Kolkata 700032, India. (Poster Presentation)
- 10th International Conference of The Asian Consortium on Computational Materials Science (ACCMS-10), 22nd-26th July 2019, at City University of Hong Kong, Hong Kong. (Oral Presentation)
- Workshop and Symposium on Advanced Simulation Methods: DFT, MD and Beyond (ASM2019), 6–10th March 2019, at Indian Institute of Technology Delhi, India. (poster Presentation)
- 63rd DAE Solid State Physics Symposium (DAE SSPS 2018), 18th-22nd December 2018, at Guru Jambheshwar University of Sci. & Tech., Hisar, Haryana, India. (Poster Presentation)
- 2nd International Conference on Condensed Matter & Applied Physics (ICC-2017), 24–25th November 2017, at Govt. Engineering College Bikaner, India. (Poster Presentation)
- International Conference on Nanotechnology: Ideas, Innovations & Initiatives (ICN:3I 2017), 06–08th December 2017, at IIT Roorkee, Uttarakhand, India. (Oral Presentation)
- International Workshop on Nano/Micro 2D-3D Fabrication, Manufacturing of Electronic Biomedical Devices & Applications (IWNEBD-2018), 31st October–2nd November 2018, at IIT Mandi, H.P, India. (Poster presentation)
- International Conference On Nano Science & Engineering Applications (ICONSEA–2018), 4–6th October 2018, at CNST, IST, JNTU Hyderabad, India . (Oral Presentation)